UNIVERSITY OF LIVERPOOL

Exploring the mechanical behaviour of granular materials considering particle shape characteristics: a discrete element investigation

Thesis submitted in accordance with the requirements of the University of Liverpool for the degree of Doctor in Philosophy

by

Shivaprashanth Kumar Kodicherla
B.Eng (Civil Engineering)., M.Tech (Geoenvironmental Engineering)

February 2021

Declaration of Authorship

I, declare that this thesis titled, and the work presented herein are my own. I confirm that:

- This work was done wholly or mainly while in candidature for a research degree at this University.
- Where any part of this thesis has previously been submitted for a degree or any other qualification at this university or any other institution, this has been clearly stated.
- Where I have consulted the published work of others, this is always clearly ascribed.
- Where I have quoted from the work of others, the source is always mentioned. Except for such quotations, this thesis is entirely my work.
- I have acknowledged all the main sources of help and support for the successful completion of the project.
- Where the thesis is based on work done by myself jointly with others, I have made exactly what was done by others and what I have contributed myself.

Sign: _____

Date: _____

Abstract

Discrete element method (DEM) is a useful numerical tool for analysing complex mechanical behaviour of granular materials as it considers the interaction at discrete contact points. In general, most of the DEM software packages use spherical particles by default because of easy contact detection and less computational cost. However, researchers confirmed that particle shape plays a significant role in exploring the mechanical behaviour of granular materials. Due to upgraded computation resources, nowadays it is possible to simulate the mechanical behaviour of granular materials considering true geometric shapes of particles. The key objective of the current research is to investigate the mechanical behaviour of granular materials considering particle shape characteristics. For that purpose, two basic geotechnical laboratory tests, i.e., direct shear test and triaxial test, are considered in this thesis.

The current research uses a commercial DEM code-named Particle Flow Code (PFC) developed by Itasca. An attempt was made to generate realistic particle shapes considering their major plane of orientations using a built-in clump mechanism in PFC. A series of DEM simulations were performed to investigate the sensitivity of the macroscopic specimen response to some specific parameter (e.g., particle numbers, loading rate). Based on the sensitivity analysis, selected microscopic parameters were selected to validate the DEM model with the experimental direct shear test results.

To investigate the effects of particle elongations on the mechanical behaviour of granular materials, a series of simulations of direct shear tests and triaxial tests were performed using a range of dimensionless elongation parameters. The evolution of elongated particles was investigated at macro-and micro- scale levels. Moreover, the relationships between elongation parameter and critical state parameters were established.

A series of triaxial test simulations were performed considering two morphological descriptors and their mechanical behaviour was investigated at the macro- and micro-scale levels. In addition, a triaxial test environment was implemented to investigate the mechanical response of granular materials under different loading paths (i.e., axial compression (AC), axial extension (AE), lateral compression (LC) and lateral extension (LE)). The grain-scale interactions in terms of coordination number and deviator fabric were also investigated. Furthermore, the relationships were established among strength, dilatancy and state parameter concerning critical states.

Keywords: Discrete element method; particle geometry; shear strength; critical state; microscopic behaviour.

Acknowledgements

My first and foremost thanks to my primary supervisor, Dr. Guobin Gong at Xi'an Jiaotong – Liverpool University (XJTLU), and co-supervisor, Prof. Kristian Krabbenhoft at the University of Liverpool (UoL), who has been my inexhaustible source of ideas throughout my PhD. I also would like to express my deep gratitude to my co-supervisors at XJTLU: Dr. Lei Fan and Dr. Charles K.S. Moy for their constant encouragement and guidance, the freedom they offered to develop my ideas are especially appreciated. My exceptional thanks would go to Dr. Stephen Wilkinson for reviewing articles and providing beneficial suggestions during the entire study period.

I am grateful to the National Natural Science Foundation of China (Grant No: NSFC 51578499 and 51825803) and Xi'an Jiaotong – Liverpool University (RDF-14-02-44, RDF-15-01-38 and RDF-18-01-23) for providing me with a three-year fully-funded PhD studentship.

I would like to express my deep-felt gratitude to my parents who are always there with me at times of happiness and hardships. Special thanks should be mentioned here for my brother Raja Pranav Kumar whose round-the-clock support and enthusiasm boosted my morale. I owe too much to my dear wife Swarna Rani and my daughter Prerana for their steadfast love and never-ending support during my research. I especially thank my daughter for her understanding and positive attitude during the periods of low spirits.

I thank God almighty for his abundant blessings in all my endeavours. Lastly, I express my deepest thanks and regards to all those who have supported me directly or indirectly during this entire research journey.

List of Journal Articles

- Kodicherla, S.P.K., Gong, G., Fan, L., Charles, L. & He, J. (2018) Effects of preparation methods on inherent fabric anisotropy of reconstituted sand samples. *Cogent Engineering*. 5(1), 1- 14. (Published)
- Kodicherla, S.P.K., Gong, G., Yang, Z.X., Krabbenhoft, K., Fan, L., Charles K.S. Moy. & Wilkinson, S. (2019) The influence of particle elongations on direct shear behaviour of granular materials using DEM. *Granular Matter*. 21(4). (Published)
- Kodicherla, S.P.K., Gong, G., Fan, L., Wilkinson, S. & Charles K.S. Moy. (2020) DEM investigations of the effects of particle morphology on granular material behaviour using a multi-sphere approach. Journal of *Rock mechanics and Geotechnical Engineering*. (Published)
- Kodicherla, S.P.K., Gong, G., Fan, L., Wilkinson, S. & Charles K.S. Moy. (2020) Discrete element modelling of strength and critical state characteristics of granular materials under AC and AE stress path tests. *Particuology*. (Published)
- Kodicherla, S.P.K., Gong, G. & Wilkinson, S. (2020) Exploring the relationship between particle shape and critical state parameters for granular materials using DEM. *SN Applied Sciences*. (Published)

List of Conference Proceedings

- Kodicherla, S.P.K., Gong, G., Fan, L., Charles, L. & Krabbenhoft, K. (2018) Direct shear test simulations using DEM. *Indian Geotechnical Conference (IGC), Bangalore, India.* (Published)
- Gong, G., Kodicherla, S.P.K., Fan, L., Charles, L. & Krabbenhoft, K. (2019) Noncoaxiality between stress and strain rate in planar granular materials. *Asian Conference on Civil, Material and Environmental Sciences (ACCMES), Hokkaido, Japan.* (Published)
- Kodicherla, S.P.K., Gong, G., Fan, L. & Charles, L. (2019) Effects of particle morphology on the macroscopic behaviour of ellipsoids: A discrete element investigation. *The 2nd International Conference on Sustainable Buildings and Structures (ICSBS), Organized by Department of Civil Engineering, Xi'an Jiaotong – Liverpool University (XJTLU), P.R China.* (Published)

Dedicated to my whole family

Table of Contents

Declaration of Authorship iii
Abstract v
Acknowledgements vii
List of Journal Articles viii
List of Conference Proceedings ix
Table of Contents xi
List of Symbols/Abbreviations xv
List of Figures xviii
List of Tables xxiv
Chapter 1 Introduction **25**

1.1 Background 25
1.2 Objectives and scope of the thesis 26
1.3 Outline of the thesis 27

Chapter 2 Review of DEM simulations and its terminology **29**

2.1 Introduction 29
2.2 Review of computer algorithms and state of the art review 30
2.3 Discrete Element Method (DEM) 30
2.3.1 Calculation cycle 31
2.3.2 Timestep determination 36
2.3.3 Local damping 38
2.3.4 Linear contact model 39
2.3.5 Principle of clump formation 43
2.4 Stress tensor 45
2.5 Microscopic parameters 46
2.5.1 Coordination number (CN) 46
2.5.2 Fabric tensor 46
2.5.3 Strong and weak force subnetworks 48
2.6 Developments in particle geometries in DEM 49

2.7 Summary 50

Chapter 3 Experimental and numerical validation of direct shear test 52

3.1 Introduction 52

3.2 Review of literature 53

3.3 Description of the physical direct shear test apparatus and procedure 55

3.4 Generation of realistic particles 57

3.5 Numerical simulations 59

3.6 Sensitivity analysis 61

3.6.1 Sensitivity to the number of particles 61

3.6.2 Sensitivity to the interparticle friction coefficient 66

3.6.3 Sensitivity to loading rate 67

3.6.4 Sensitivity to damping constant 69

3.6.5 Sensitivity to the ratio between normal and shear stiffness 71

3.7 Comparison between the experimental and DEM results 73

3.7.1 Stress-strain behaviour 73

3.7.2 Coordination number (CN) 76

3.7.3 Evolution of fabric anisotropy 79

3.8 Summary 82

Chapter 4 Influence of particle elongations on the direct shear behaviour 83

4.1 Introduction 83

4.2 Review of literature 84

4.3 Methodology for particle elongation 86

4.4 Simulation details 88

4.5 Macroscopic behaviour 91

4.6 Evolution of fabric anisotropy and microscopic behaviour 94

4.7 Distribution of force chain networks 98

4.8 Stress- dilatancy relationship 99

4.9 Critical State Soil Mechanics (CSSM) framework 102
4.10 Summary 105

Chapter 5 Influence of particle elongations on triaxial behaviour 107

5.1 Introduction 107
5.2 Review of literature 108
5.3 Particle shape characteristics 113
5.4 Simulation details 115
5.5 Macroscopic behaviour 116
5.6 Microscopic behaviour 121
5.6.1 Coordination number (CN) 121
5.6.2 Evolution of deviator fabric 121
5.7 Relationships between critical state and shape parameters 122
5.8 Summary 126

Chapter 6 Influence of particle morphology on triaxial behaviour 127

6.1 Introduction 127
6.2 Review of literature 128
6.3 Methodology 132
6.4 Simulation details 135
6.5 Simulation results 135
6.5.1 Macroscopic behaviour 136
6.5.2 Evolution of the angles of internal friction 140
6.5.3 Microscopic behaviour 142
6.6 Establishing the micro-macro relationship 149
6.7 Summary 152

Chapter 7 Influence of loading paths on critical state behaviour 153

7.1 Introduction 153
7.2 Review of literature 154
7.3 Evaluation of density index (I_D) 158
7.4 Triaxial loading paths 159

7.5 Simulation details 162
7.6 Simulation results 165
7.6.1 Macroscopic behaviour 165
7.6.2 Comparison of drained triaxial loading paths 168
7.6.3 Evolution of critical state characteristics 169
7.6.4 DEM analysis of the state parameter 171
7.6.5 Relationship between the strength and state parameter 172
7.6.6 Relationship between dilatancy and state parameter 174
7.6.7 Evolution of microscopic quantities 176
7.7 Summary 178
Chapter 8 Summary and Conclusions 180
8.1 Summary 180
8.1 Principal findings 180
8.1.1 Direct shear test 180
8.1.2 Triaxial shear test 182
8.2 Future perspectives 184
Bibliography 186
Appendix - A: Summary of DEM results for different loading paths 211
Appendix - B: Servo-mechanism in PFC 213
Appendix - C: Direct shear test – PFC code 214
Appendix -D: Triaxial shear test – PFC code 229

List of Symbols/Abbreviations

Symbols/Abbreviation		Description
DEM	:	*Discrete Element Method*
PFC	:	*Particle Flow Code*
A_R	:	*Aspect ratio*
C_X	:	*Convexity*
S_W	:	*Sphericity*
O_R	:	*Overall regularity*
p'	:	*Mean effective stress,* $(\sigma_1+\sigma_2+\sigma_3)/3$
p_0'	:	*Initial mean effective stress*
q	:	*Deviator stress,* $(\sigma_1-\sigma_3)$
σ_{ij}	:	*Stress tensor*
CN	:	*Coordination number*
ϕ_{ij}	:	*Fabric tensor*
ϕ^s_{ij}	:	*Strong fabric tensor*
ϕ^w_{ij}	:	*Weak fabric tensor*
f^n_{avg}	:	*Average normal contact force*
ϕ_d	:	*Deviator fabric,* $\phi_1-\phi_3$
ϕ_m	:	*Mean principle fabric,* $\phi_m=(\phi_1+\phi_2+\phi_3)/3=1/3$
C_u	:	*Coefficient of uniformity*
C_c	:	*Coefficient of curvature*
d_{60}	:	*Grain diameter corresponds to 60% finer*
d_{10}	:	*Grain diameter corresponds to 10% finer*
d_{30}	:	*Grain diameter corresponds to 30% finer*

d_{eq}	:	*Equivalent diameter,* $\sqrt{\frac{6V}{\pi}}$
k^*	:	*Normal-to-shear stiffness ratio*
E^*	:	*Effective modulus, Pa*
E	:	*Young's modulus*
ν	:	*Poisson's ratio*
ρ	:	*Notional particle density* $\left(kg/m^3\right)$
Λ	:	*Dimensionless elongation parameter*
e	:	*Void ratio*
e_o	:	*Initial void ratio*
ϕ_p	:	*Peak state angle of shearing resistance*
ϕ_c	:	*Critical state angle of shearing resistance*
D	:	*Dilation rate*
D_p	:	*Dilation rate at peak state*
D_c	:	*Dilation angle at critical state*
k	:	*Fitting parameter*
CSL	:	*Critical state line*
p_a	:	*Atmospheric pressure*
e_Γ	:	*Intercept of the critical state line*
λ_c	:	*Slope of the critical state line*
ς	:	*Material constant*
ε_1	:	*Axial strain, %*
ε_v	:	*Volumetric strain, %*
e_c	:	*Critica state void ratio*
M	:	*Critical stress ratio*
ξ	:	*Ratio between largest to the smallest sphere*
β	:	*The maximum sphere-sphere intersection angle*
μ	:	*Interparticle friction coefficient*

CSSM	:	*Critical- state soil mechanics*
CST	:	*Critical-state theory*
ψ	:	*State parameter*
ψ_0	:	*Initial state parameter*
Ψ	:	*Angle of dilation*
Ψ_p	:	*Peak angle of dilation*
ACST	:	*Anisotropic critical state theory*
I_D	:	*Density index*
ICL	:	*Isotropic consolidation line*
e_{min}	:	*Minimum void ratio*
e_{max}	:	*Maximum void ratio*
AC	:	*Axial compression*
AE	:	*Axial extension*
LC	:	*Lateral compression*
LE	:	*Lateral extension*
REV	:	*Representative elementary volume*
δ_{ij}	:	*Kronecker delta*
σ_n	:	*Normal stress, kPa*
τ	:	*Shear stress, kPa*
SEM	:	*Scanning electron microscope*
S_c	:	*Sliding index*
σ_1	:	*Major principal stress*
σ_2	:	*Intermediate principal stress*
σ_3	:	*Minor principal stress*
e_{up}	:	*Void ratio corresponds to upper consolidation line*
e_{low}	:	*Void ratio corresponds to lower consolidation line*
η	:	*Stress ratio,* q / p'
η_p	:	*Peak stress ratio,* $(q / p')_{peak}$

List of Figures

Figure 2.1 Calculation cycle in PFC 32
Figure 2.2 Multiple mass-spring systems 37
Figure 2.3 Behaviour and rheological components of the linear model 39
Figure 2.4 Surface gap for linear contact model 40
Figure 2.5 Relationship of normal stiffness to piece normal stiffness for linear contact model 42
Figure 2.6 Volume of material associated with contact 43
Figure 2.7 Typical contact between two pebbles in DEM 44
Figure 2.8 DEM variants to capture the particle shape: (a) Ellipsoids, (b) Clumps, (c) Polyhedra, (d) NURBS and (e) Level sets 50
Figure 3.1 Direct shear apparatus currently used in the laboratory 56
Figure 3.2 A snapshot of the direct shear test setup used in the laboratory 56
Figure 3.3 A library of generated clumps along with SEM micrographs 59
Figure 3.4 Schematic representation of direct shear test along XZ-plane 60
Figure 3.5 Numerical assemblies for different particle numbers 63
Figure 3.6 Ratio between mean unbalanced force and the mean contact force against shear strain for different particle numbers 64
Figure 3.7 Stress ratio against shear strain for different particle numbers 64
Figure 3.8 Vertical strain against shear strain for different particle numbers .65
Figure 3.9 Particle size distribution curve used 65
Figure 3.10 Stress ratio against shear strain for different interparticle friction coefficients 66
Figure 3.11 Vertical strain against shear strain for different interparticle friction coefficients 67
Figure 3.12 Ratio between mean unbalanced force and mean contact force against shear strain for different loading rates 68
Figure 3.13 Stress ratio against shear strain for different loading rates 68
Figure 3.14 Vertical strain against shear strain for different loading rates 69

Figure 3.15 Ratio between mean unbalanced force and mean contact force against shear strain for different damping constants 70
Figure 3.16 Stress ratio against shear strain for different damping constants. 70
Figure 3.17 Vertical strain against shear strain for different damping constants 71
Figure 3.18 Stress ratio against shear strain for varying stiffness ratios 72
Figure 3.19 Vertical strain against shear strain for varying stiffness ratios 72
Figure 3.20 Comparison of laboratory and DEM simulation results of stress ratio against the shear strain 74
Figure 3.21 Comparison of laboratory and DEM simulation results of vertical strain against shear strains 75
Figure 3.22 Peak stress against normal stress 76
Figure 3.23 CN against the shear strain 77
Figure 3.24 Distribution of contact normal force networks for normal stress of 179 kPa: a) end of one-dimensional compression; b) end of the shear 78
Figure 3.25 Displacement vectors for normal stress of 179 kPa: a) end of one-dimensional compression; b) end of the shear 79
Figure 3.26 Deviator fabric against shear strain for different normal stresses 80
Figure 3.27 Strong deviator fabric against shear strain for different normal stresses 81
Figure 3.28 Weak deviator fabric against shear strain for different normal stresses 81
Figure 4.1 Methodology for particle elongation 87
Figure 4.2 Elongated particles with different Λ 88
Figure 4.3 The initial states of generated packings with different Λ 90
Figure 4.4 Stress ratio against shear strain for different samples 92
Figure 4.5 Vertical strain against shear strain for different samples 93
Figure 4.6 Influence of Λ on the peak and critical state friction angles 93
Figure 4.7 Influence of normal stresses on the shear behaviour of granular assembly (sample S3) 94
Figure 4.8 Influence of Λ on the CN 95

Figure 4.9 Influence of Λ on the deviator fabric 96
Figure 4.10 Influence of major and minor principal fabrics in the strong subnetwork 97
Figure 4.11 Influence of major and minor principal fabrics in the weak subnetwork 98
Figure 4.12 Distribution of contact force chain networks along XZ-plane 99
Figure 4.13 Angle of dilation against the shear strain 100
Figure 4.14 Relationship between $\phi_p - \phi_c$ and Ψ_p 102
Figure 4.15 Critical state lines in the $e - \left(p'/p_a\right)^{\xi}$ space for all samples 103
Figure 4.16 Correlation between e_Γ against Λ 104
Figure 4.17 Correlation between λ_c against Λ 105
Figure 5.1 Elongated particles with varying shape parameters 115
Figure 5.2 Stress ratio against axial strain for different Λ 117
Figure 5.3 Effect of Λ on the angle of internal frictions 118
Figure 5.4 Stress ratio against axial strain for different isotropic stresses 119
Figure 5.5 (a) Evolution of volumetric strain against axial strain; (b) Evolution of void ratio against axial strain; (c) Relationship between void ratio against Λ at different stages of axial strains 120
Figure 5.6 CN against axial strain for different Λ 121
Figure 5.7 Evolution of deviator fabric against axial strain for different Λ 122
Figure 5.8 Relationships between M and shape parameters 123
Figure 5.9 Relationships between e_Γ and shape parameters 125
Figure 5.10 Relationships between λ_c and shape parameters 125
Figure 6.1 Clump representing an ellipsoid generated by MS approach 133
Figure 6.2 A surface representing an ellipsoid 133
Figure 6.3 The effects of varying β and ξ for the ellipsoid clump templates. 134
Figure 6.4 Initial configurations of ellipsoidal assemblies for triaxial simulations 135
Figure 6.5 Evolutions of stress ratio against axial strain for the specimens ξ = 0.4 with different β 137

Figure 6.6 Evolutions of volumetric strain against axial strain for the specimens ξ = 0.4 with different β 137
Figure 6.7 Evolutions of stress ratio against axial strain for the specimen's β = 150° with different ξ 138
Figure 6.8 Evolutions of volumetric strain against axial strain for the specimens β = 150° with different ξ 138
Figure 6.9 Evolutions of the void ratio against axial strain for the specimens ξ = 0.4 with different β 139
Figure 6.10 Evolutions of the void ratio against axial strain for the specimens β = 150° with different ξ 140
Figure 6.11 Effect of β on the angle of internal frictions 141
Figure 6.12 Effect of ξ on the angle of internal frictions 141
Figure 6.13 Evolutions of CN for the specimens ξ = 0.4 with different β 142
Figure 6.14 Evolutions of CN for the specimens β = 150° with different ξ 143
Figure 6.15 Probability distributions of coordination numbers for the specimens ξ = 0.4 with different β 144
Figure 6.16 Probability distributions of coordination numbers for the specimens β = 150° with different ξ 144
Figure 6.17 The contact force chain networks at initial (left), peak (centre) and critical (right) states for β = 100° and β = 160° 146
Figure 6.18 The contact force chain networks at the initial (left), peak (middle) and critical (right) states for ξ = 0.4 and ξ = 0.8 146
Figure 6.19 Proportions of sliding fractions for the specimens ξ = 0.4 with different β 148
Figure 6.20 Proportions of sliding fractions for the specimens β = 150° with different ξ 148

Figure 6.21 Evolutions of ϕ_d / ϕ_m against axial strain for the specimens ξ = 0.4 with different β 149
Figure 6.22 Evolutions of ϕ_d / ϕ_m against axial strain for the specimens β = 150° with different ξ 150
Figure 6.23 Evolutions of ϕ^s_d / ϕ^s_m against axial strain for the specimens ξ = 0.4 with different β 150
Figure 6.24 Evolutions of ϕ^s_d / ϕ^s_m against axial strain for the specimens β = 150° with different ξ 151
Figure 6.25 Relationship between strong fabric parameter ϕ^s_d / ϕ^s_m and stress ratio q / p' 151
Figure 7.1 Evaluation of densification index (I_D) 159
Figure 7.2 Illustration of three-dimensional triaxial drained loading paths (after Springman *et al.* 2013) 161
Figure 7.3 Triaxial drained loading paths in the $q - p'$ space 162
Figure 7.4 Map of clumps along the different plane of orientations: (a) XYZ (b) XZY (c) YXZ (d) YZX (e) ZXY and (f) ZYX 164
Figure 7.5 Macroscopic results of AC test: (a) $\varepsilon_a - \eta$; (b) $\varepsilon_a - \varepsilon_v$; (c) $\varepsilon_a - e$ 166
Figure 7.6 Macroscopic results of AE test: (a) $\varepsilon_a - \eta$; (b) $\varepsilon_a - \varepsilon_v$; (c) $\varepsilon_a - e$ 166
Figure 7.7 Comparison of triaxial stress path results for Series - II and Series - V: (a) $q - \varepsilon_a$; (b) $\varepsilon_v - \varepsilon_a$; (c) $\eta - \varepsilon_a$ 168
Figure 7.8 Stress-strain behaviour of DEM samples sheared under different loading paths (p_o' = 400 *kPa*) 169
Figure 7.9 Critical state characteristics of AC and AE loading paths: (a) $e_c - p'$ (b) $e_c - (p'/p_a)^\zeta$ (c) $q - p'$ 170
Figure 7.10 Critical state line and state parameter (ψ) (after Li & Dafalias 2000) 172

Figure 7.11 Relationship between ϕ_p and ψ_0 173

Figure 7.12 Relationship between $\phi_p - \phi_c$ and ψ_0 174

Figure 7.13 Relationship between D_p and ψ_0 175

Figure 7.14 Relationship between peak strength and peak dilatancy: (a) $\phi_p - D_p$; (b) $\eta_p - D_p$ 176

Figure 7.15 Evolution of *CN* for Series - II and Series - V: (a) $\varepsilon_a - CN$ for *AC* loading path; (b) $\varepsilon_a - CN$; (c) $p' - CN$ at critical state; (d) $p' - CN$ at a critical state. 177

Figure 7.16 Evolution of deviator fabrics for Series - II and Series - V: 178

List of Tables

Table 3.1 Microscopic parameters for the sensitivity analysis 61
Table 3.2 Input parameters for DEM validation 73
Table 4.1 Initial characteristics of the numerical specimens 89

Chapter 1 Introduction

1.1 Background

Granular materials are ubiquitous and closely associated with our daily life. These materials are basically comprised of discrete particles which interact with each other at their microscopic contacts to sustain the external loads applied to them. In general, these materials exhibit many salient features such as dilatancy, anisotropy and nonlinearity because of the heterogeneity and irregularity in nature. It was mentioned that the strength and deformation characteristics of granular materials mainly depends on the particle shape (e.g., Gong & Liu 2017; Kodicherla *et al*. 2019). The physical mechanisms responsible for macroscopic responses of granular materials remain a question often raised by various investigators in the field (Nouguier-Lehon 2010; Yang & Luo 2015; Hohner *et al*. 2015; Zhao & Zhou 2017). There is no generalized particle shape to intrinsically characterize the mechanical responses of granular material that exist in nature. Therefore, particle shape is still worth considering and its influence on the mechanical behaviour of granular materials remains an open topic in the research community.

Nowadays, constitutive relationships have become a standard tool for resolving a wide variety of engineering problems. Due to rapid developments in the computational power and up-gradation of sophisticated numerical models, there is a potential possibility to investigate large-scale practical problems arising in the field. Among the various available numerical methods, discrete element method (DEM) is one of the powerful tools to simulate the mechanical behaviour of granular materials.

The advent of DEM enables researchers to explore more fundamental aspects of soil behaviour (Cundall & Strack 1979). Despite its simplicity, the particulate implementation of DEM captures many salient features of soils (Iwashita & Oda 1998; Thornton 2000; Cundall 2001; O'Sullivan & Cui 2009). In the past decades, there has been a dramatic increase in the number of DEM-related research papers across a variety of scientific disciplines including Geomechanics (O'Sullivan 2014).

1.2 Objectives and scope of the thesis

The primary intention of this thesis is to investigate the effects of particle shape characteristics on the mechanical behaviour of granular materials under commonly used laboratory element tests, i.e., direct shear test and triaxial test using DEM. In general, particle shape characteristic is defined by the terms, i.e., elongation, roundness and texture. The particle elongation indicates the aspect ratio while the roundness describes the angularity of the particle. The texture represents surface characteristics of the particle or in other words, it represents the particle morphological features. As each of these parameters affects the mechanical behaviour of granular materials, it is important to explore further at micro-scale levels. Hence, this thesis is motivated to investigate some of the major parameters used to define the particle shapes with the following targeted objectives:

- To investigate the effectiveness of realistic particle geometry generation approach and the validation of the DEM model with experimental direct shear test results.

- To explore the influence of particle elongations and morphological features on the direct shear and triaxial shear behaviour of granular materials at the macro- and micro-scale levels.

- To explore the influence of strength and critical state behaviour of granular material under different drained loading paths.

1.3 Outline of the thesis

This thesis consists of eight chapters in total. Each chapter is organized as follows:

- In Chapter 2, a brief history of DEM, a review of the computer algorithms and the state of art is presented. The basic principle of DEM and its terminology is also presented in the subsequent sections. In addition, the basic definitions for macroscopic and microscopic parameters are given.

- In Chapter 3, a systematic sensitivity analysis considering a range of microscopic parameters, a procedure for the generation of realistic particle shapes are presented. The validation of the DEM model with experimental direct shear test results using generated clumped particles is presented. Moreover, subsequent microscopic parameters are also investigated.

- In Chapter 4, the influence of particle elongations on the macro- and the micro-scale response of granular materials under the direct shear test condition is explored. The relationships between stress-dilatancy and the critical state parameters are established.

- In Chapter 5, the influence of particle elongations on the critical state behaviour of granular materials under drained triaxial test conditions is investigated. The quantitative relationships are established between the particle shape characteristics and critical state parameters.

- In Chapter 6, the influence of particle morphology on the drained triaxial behaviour of granular materials is examined. The relationship between macro- and micro-scale levels are derived.

- In Chapter 7, the influence of loading paths on the critical state behaviour of granular materials using DEM is investigated. The effects of loading paths on the strength and the critical state lines in the $q-p'$ are investigated. A comprehensive comparison is made among the loading paths and the evolution of critical state characteristics are discussed.

- In Chapter 8, the key findings from the preceding chapters are summarized and the possible future perspectives are suggested.

Chapter 2 Review of DEM simulations and its terminology

2.1 Introduction

In the 21st century, geotechnical engineering has faced various challenges that require effective and sustainable leadership. The key challenges include climate change, energy production, material characterization and water management which will compel the use of advanced and robust numerical modelling techniques. These new challenges will involve more sophisticated constitutive models that explicitly acknowledge the discrete nature of granular materials or soils.

In granular assembly, the transfer/distribution of forces occurs through interactions between the particles. The macroscopic responses of granular materials are non-linear and hysteretic, which mainly depends on the magnitude of stress levels, stress paths and stress history. Such complexities have led to the developments of constitutive models of granular media, which may be analytical, physical (typically photoelastic) or numerical. The analytical models were developed based on the regular arrays of spheres and discs (Duffy & Mindlin 1957; Deresiewicz 1958 (a) & 1958(b); Duffy 1959; Rowe 1962) whereas the physical models were modelled using steel balls, glass beads, aluminium rods and photoelastic discs (Matsuoka & Geka 1983; Oda *et al.* 1985). As compared to analytical and physical models, the most promising way to model the granular material behaviour is through numerical techniques, because all the loading or boundary conditions can be monitored effectively. Moreover, the stresses and strains at any stage within the sample can be extracted, but the accurate determination of the input parameters selected for the modelling is required as it greatly affects the results. A popular commercially available DEM package named Particle Flow Code (PFC),

developed by Itasca Consulting Group (Itasca Consulting Group 2018) is used to perform all the numerical simulations in this thesis. All numerical simulations are executed by a Dell Precision T7500 workstation, which has the following specifications: Intel® Xeon® CPU X5690 @3.47 GHz; 12 cores; 48 GB of RAM; NVIDIA Quadro 4000.

2.2 Review of computer algorithms and state of the art review

Cundall (1978) developed the original version of the two-dimensional DEM program called BALL. In this program, a linear spring contact law was implemented and a user has an option to choose wall boundaries as strain-controlled, stress-controlled or servo-controlled. Later, the BALL program was extended to TRUBAL for reproducing the published work of Rowe (1962) by Cundall & Strack (1979c). BALL was extended to the 3D version TRUBAL by Cundall (1988). In TRUBAL version, nonlinear contact laws were implemented using a complete Hertz normal contact theory and a simplified tangential contact theory of Mindlin (1949). In the last decade, several open-source and commercial DEM packages have been developed to simulate the mechanical behaviour of granular materials and coupled with fluids as well. Some of the currently available open-source DEM options are Oval (Kuhn 2003), YADE (Kozicki & Donzé 2009), LMGC90 (Duboise *et al.* 2011), ESyS Particle (Weatherley *et al.* 2011), Mercury-DPM (Thornton *et al.* 2013), and LIGGGHTS (Kloss & Goniva 2011). Also, some of the commercially available options include PFC by Itasca (Itasca Consulting Group 2018), Chute Maven, EDEM, ELFEN, PASSAGE®, Bulk Flow Analyst™, and Rocky®.

2.3 Discrete Element Method (DEM)

The discrete element method (DEM) is a numerical approach which was originally pioneered by Cundall (1971, 1974). In the very beginning, DEM was applied to solve problems related to rock mechanics. In later stages, Cundall (1978) and Strack & Cundall (1978) and Cundall & Strack (1979 a, b) used

BALL to develop the constitutive relationships for granular soils. The perks of using this approach are that each particle in the cloud of granular assembly and their interactions are explicitly analysed. To reduce the computational cost of the simulations in DEM, the shapes of the particles are simplified as discs in 2D and spheres in 3D. Hence, this allows a large number of particles to be analysed while still capturing the salient response characteristics of granular material behaviour. The unique feature of the DEM is that a user can apply the load and deformations virtually. However, in the physical laboratory tests, it is incredibly difficult to access all the necessary information and the data of the particle-scale mechanism that underlies the complex overall material response.

In DEM, the properties of stressed assembly of rigid particles (e.g., position, velocity and contact forces) are updated at each numerical iteration timestep. The translational and rotational displacements of each particle are obtained by explicitly integrating the governing differential equations based on Newton's second law of motion, while the contact forces between particles are calculated using a well-defined force-displacement contact law (Hertz 1882; Mindlin & Deresiewicz 1953; Cundall & Strack 1979b; Itasca Consulting Group 2018). The interactions between the particles are monitored at each contact and the movement of each particle is traced. It is presumed that the velocity of each particle is constant at each iteration timestep. Since the explicit numerical integration technique is used in DEM, the time-step is required to be very small so that stable numerical solutions can be achieved.

2.3.1 Calculation cycle

The calculation cycle in PFC alternates between the application of Newton's second law of motion to particles and the force-displacements law at the contacts. The force-displacement law is used to obtain the contact forces from the relative displacements calculated at the contacts based on their positions. The contact forces result in the motion of the particles and the motion is

calculated using the second law of motion. Figure 2.1 shows how the calculation cycle revolves during the simulation in PFC. At the onset of each iteration timestep, a set of contact information is updated based on the known positions of the particles and walls. Then, the updated contact force based on the relative motion between two particles is calculated by the force-displacement law through the contact constitutive model and the relative displacement from the previous timestep. Using the law of motion, the position and velocity resulting from the resultant force and moment; which arises due to the contact force acting on the particle, can be resolved. During the simulation, existing contacts (ball-ball or ball-wall) can break automatically and new contacts may be formed. To ensure the existence of quasi-static conditions, the loading rates are usually taken at a very low rate with very small fractions of inertial forces allowed in the assembly.

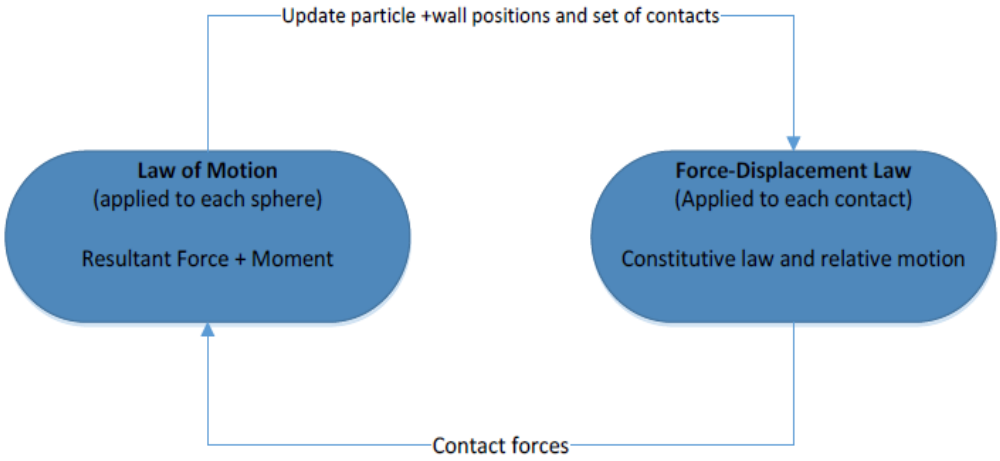

Figure 2.1 Calculation cycle in PFC

(Source: Itasca manual 2018)

Force – displacement law

The force-displacement law is associated with the relative displacement between the particles at contact and the contact forces acting on them. The

contact force vector (F_i) can be decomposed into normal (F_i^n) and shear (F_i^s) components concerning the contact plane, as given below:

$$F_i = F_i^n + F_i^s \tag{2.1}$$

The normal contact force vector (F_i^n) is given as:

$$F_i^n = k^n U^n n^i \tag{2.2}$$

where k^n is the normal stiffness (force/displacement) at the contact evaluated by the implemented contact law, n^i is the unit contact normal and U^n is the overlap of two particles.

When the contact is formed, initially the shear contact force is zero. At each subsequent relative shear-displacement increment of the elastic shear force, the shear displacement increment is added to the current value. The shear component of the contact displacement-increment vector occurring over a timestep of Δt is calculated as:

$$\Delta U_i^s = V_i^s \Delta t \tag{2.3}$$

The shear elastic force-increment vector is given as:

$$\Delta F_i^s = -k^s \Delta U_i^s \tag{2.4}$$

where k^s is the shear stiffness at contact and the value is determined by the implemented contact law. The shear stiffness is the tangent modulus, the new shear contact force is calculated by summing up the old shear force vector

existing at the beginning of the timestep with the shear elastic force-increment vector.

$$F_i^s = (F_j^s)_{old} + \Delta F_i^s \tag{2.5}$$

The value of normal to shear contact force evaluated using Eqns. (2.1) and (2.5), are adjusted to satisfy the contact constitutive relationships.

Law of motion

The motion of a single particle is determined by the resultant force and moment vectors acting upon it. The equations of motion can be described in terms of two vector quantities: one relates to the resultant force to the translational motion and the other one relates to the resultant moment to the rotational motion. The motion of the centre of mass is described in terms of its position- $\mathbf{x}$, velocity- $\dot{\mathbf{x}}$, and acceleration - $\ddot{\mathbf{x}}$. The rotational motion of the particle is described in terms of its angular velocity ω and angular acceleration $\dot{\omega}$.

Translation motion

The equation for translational motion can be written in the vector form as:

$$F = m\left(\ddot{x} - g\right) \tag{2.6}$$

where F is the resultant force. In other words, it is equal to the sum of all externally applied forces acting on a particle; m is the total mass of the particle, and g is the body force acceleration vector (e.g., gravitational loading).

The translational equations of motion are solved for balls and clumps via the second-order Velocity Verlet algorithm (Verlet 1967). This method of

integration offers a second-order accuracy and is often used in the molecular dynamics simulations because, for a conservative system, the energy oscillates around a constant value corresponding to the exact energy of the system. For instance, the previous cycle solved in Eqn. (2.6) at the time t and that the timestep resolved for the current cycle is Δt, the 1/2 step velocity, $\dot{x}^{(t+\Delta t/2)}$, is calculated as:

$$\dot{x}^{(t+\Delta t/2)} = \dot{x}^{(t)} + \frac{1}{2}\left(\frac{F^{(t)}}{m} + g\right)\Delta t \tag{2.7}$$

The position at a time $t+\Delta t$ is updated using the 1/2 step velocity.

$$x^{(t+\Delta t)} = x^{(t)} + \dot{x}^{(t+\Delta t/2)}\Delta t \tag{2.8}$$

During the force-displacement cycle point, the forces are updated for the current cycle, leading to the updated acceleration $\ddot{x}^{(t+\Delta t)}$. The velocity is subsequently updated accordingly:

$$\dot{x}^{(t+\Delta t)} = \dot{x}^{(t+\Delta t/2)} + \frac{1}{2}\left(\frac{F^{(t+\Delta t)}}{m} + g\right)\Delta t \tag{2.9}$$

In PFC, the final velocity update of Eqn. (2.9) occurs as the initial step in the timestep determination cycle point or during the finalization stage when finishing a series of cycles as mentioned above. Thus, if one queries the velocity of a ball or clump after cycle point 10.0, they are querying the 1/2 step velocity $\dot{x}^{(t+\Delta t/2)}$.

Rotational motion

The fundamental equation of rotational motion for a rigid body is given as:

$$L = I\omega \tag{2.10}$$

where L is the angular momentum, I is the inertia tensor and ω is the angular velocity. Euler's equation can be obtained from Eqn. (2.11) by taking the time derivative:

$$M = \dot{L} = I\dot{\omega} + \omega \times L \tag{2.11}$$

where M is the resultant moment acting on the rigid body. This relation refers to a local coordinate system that is attached to the body at its centre of mass.

2.3.2 Timestep determination

To reliably update the model state, one must determine a suitable timestep for the numerical integration of Newton's laws. The accelerations and velocities are assumed to be constant within each timestep. Hence, to minimize the propagation of disturbance to any particles other than its immediate neighbour in the calculation cycle, a small timestep must be identified. At the start of each calculation cycle, PFC estimates the critical timestep and actual timestep is taken as a fraction of this estimated critical value.

The critical timestep estimation is calculated by considering a one-dimensional mass-spring system defined by a point mass (m) and spring stiffness (k) as shown in Figure 2.2. It should be noted that the motion of the point mass is governed by the differential equation, $-kx = m\ddot{x}$. Bathe & Wilson (1976) expressed the critical timestep which corresponds to a second-order finite-difference scheme as follows:

$$t_{crit} = \frac{T}{\pi}; \qquad T = 2\pi\sqrt{m/k} \tag{2.12}$$

where T is the time - period of the system.

Taking the infinite series of point masses and springs (see Figure 2.2 (a)) into consideration, the smallest period will happen when the masses will move in opposite motion synchronically, such that, there is no motion at the centre of each spring. Figure 2.2(b) and Figure 2.2(c) show how the motion of a single mass can be described by two equivalent systems. The mathematical expression for the critical timestep is given as:

$$t_{crit} = 2\sqrt{\frac{m}{4k}} = \sqrt{\frac{m}{k}} \tag{2.13}$$

where k is the stiffness of each spring as shown in figure (see Figure 2.2).

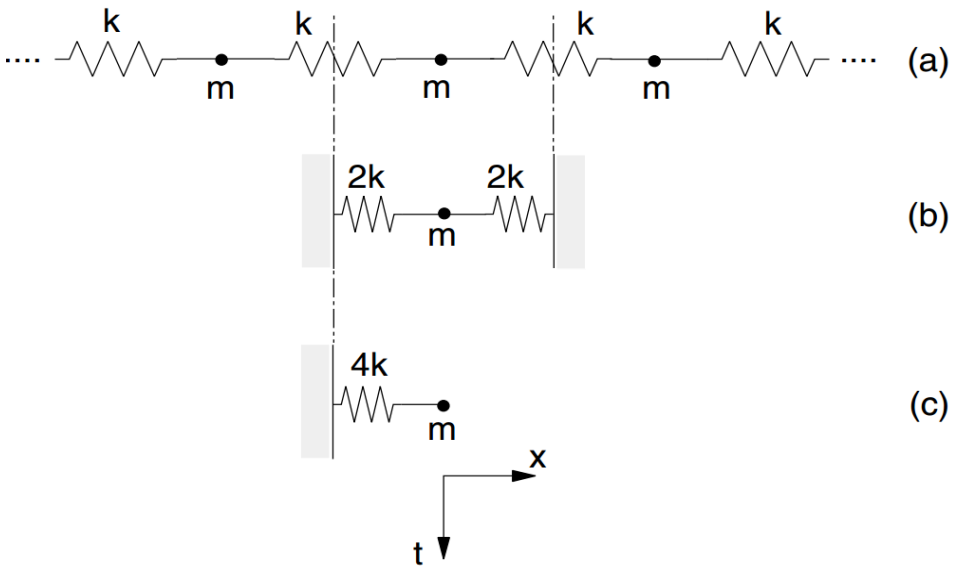

Figure 2.2 Multiple mass-spring systems

(Source: Itasca manual 2018)

These two systems characterize the translational motion. The rotational motion is characterized by the same two systems in which mass '*m*' is replaced by a moment of inertia *I* of a finite-sized particle, and the stiffness is replaced by the rotational stiffness. Thus, a critical timestep for the generalized multiple mass-spring systems can be expressed as:

$$t_{crit} = \begin{cases} \sqrt{m / k^{tran}}, & (translation \quad motion) \\ \sqrt{I / k^{rot}}, & (rotational \quad motion) \end{cases} \tag{2.14}$$

where k^{tran} and k^{rot} are the translational and rotational stiffness's respectively and I is the moment of inertia of the particle.

2.3.3 Local damping

The energy supplied to the particle system is dissipated through frictional sliding or viscous damping. However, these dissipation mechanisms may not be sufficient to arrive at a steady-state solution in a reasonable number of cycles. In PFC, a body-based damping scheme called local damping is available to dissipate additional kinetic energy. The local damping acts on each ball or clump, applying a damping force with a magnitude proportional to the unbalanced force. When the local damping is activated, a damping force/moment F_d, which is proportional to the unbalanced force/moment F_u is applied to particles which are opposite to the corresponding velocity (V) direction is given as:

$$F_d = d \ |F_u| \ sign(V) \tag{2.15}$$

where d is the local damping ratio and *sign* denotes the signum function.

2.3.4 Linear contact model

The linear contact model provides linear and dashpot components that act parallel with each other. The linear component provides linearly elastic (no-tension) frictional behaviour, while the dashpot component provides viscous behaviour (see Figure 2.3). Both components act over a vanishingly small area and thus transmit only a force. This model can be assigned to both ball-ball and ball-facet contacts.

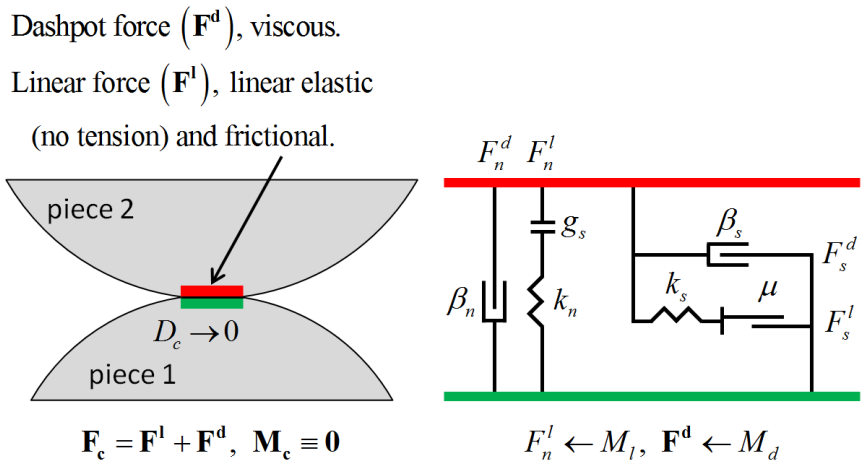

Figure 2.3 Behaviour and rheological components of the linear model

(Source: Itasca manual 2018)

The linear model offers an infinitesimal interface that does not resist relative rotation so that the contact moment equals to zero (i.e., $\mathbf{M}_{\mathrm{c}} \equiv 0$). The contact force is resolved into linear and dashpot components ($\mathbf{F}_{\mathrm{c}} = \mathbf{F}^{\mathrm{l}} + \mathbf{F}^{\mathrm{d}}$). The linear force is produced by linear springs with a constant normal and shear stiffness k_n and k_s, respectively. The dashpot force is produced by dashpots with viscosity given in terms of the normal and shear critical-damping ratios, β_n and β_s respectively. The linear springs act in parallel with the dashpots. A surface gap g_s is defined as the difference between the contact gap, g_c and the reference gap g_r so that when the reference gap is zero, the notional surface coincides with the piece surfaces as shown in Figure 2.4. The contact is active

if and only if the surface gap is less than or equals to zero; the force-displacement law is skipped for inactive contact.

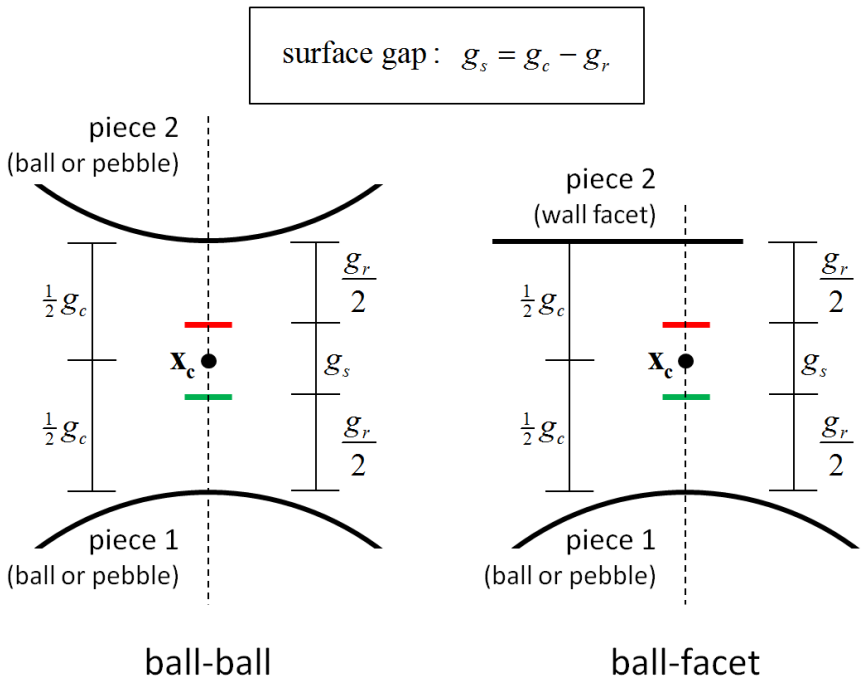

Figure 2.4 Surface gap for linear contact model

(Source: Itasca manual 2018)

The linear springs cannot sustain tensions, and slip is accommodated by imposing a Coulomb limit on the shear force using the friction coefficient, μ. The normal and shear components of the linear force can be denoted by F_n^l and F_s^l, respectively. F_n^l is updated either in an absolute sense based on the surface gap, or incrementally based on the surface-gap increments, with the update type controlled by the normal-force update mode, M_l. It should be mentioned that F_s^l is always updated incrementally based on the relative shear-displacement increments.

The dashpot force is affected by the dashpot mode, M_d, which provides four combinations of normal and shear behaviour. The normal-behaviour model can

be either full or no-tension, where full means that the entire dashpot load is assigned and no-tension means that F_n^d is capped to ensure that the total normal force ($F_n^l + F_n^d$) does not become tensile. The shear-behaviour mode can be either full or slip-cut, where slip-cut means that F_s^d is set to zero if the linear spring is sliding. The contact with the linear model is active if and only if the surface gap ($g_s = g_c - g_r$) is less than or equal to zero. When the reference gap is zero, the notional surfaces coincide with the piece surfaces. The force-displacement law is skipped for inactive contacts.

Surface property inheritance

The linear stiffness and the friction coefficient μ may be inherited from the contacting pieces. For a property to be inherited, the inheritance flag for this property must be set to true, and both contacting pieces must hold a property with the same name.

$$\frac{1}{k_n} = \frac{1}{k_n^{(1)}} + \frac{1}{k_n^{(2)}}$$
$$\frac{1}{k_s} = \frac{1}{k_s^{(1)}} + \frac{1}{k_s^{(2)}} \tag{2.16}$$

where (1) and (2) denote the properties of piece 1 and 2 respectively.

The friction coefficient is inherited using the minimum of the values set for the pieces:

$$\mu = \min\left(\mu^{(1)}, \mu^{(2)}\right) \tag{2.17}$$

The linear stiffnesses are inherited, assuming that both pieces stiffness act in a series as shown in Figure 2.5.

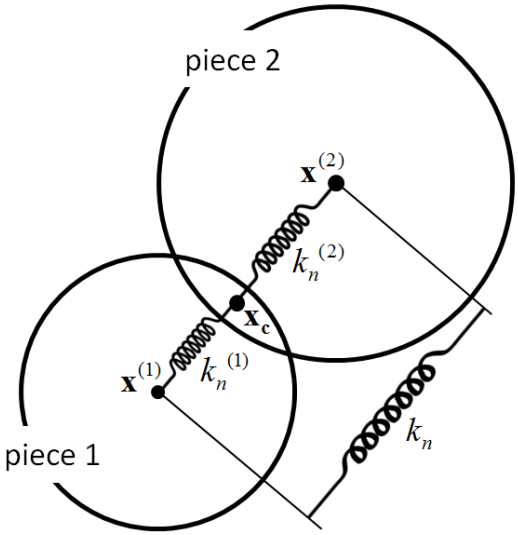

Figure 2.5 Relationship of normal stiffness to piece normal stiffness for linear contact model

(Source: Itasca manual 2018)

Deformability

The deformability of a homogeneous, isotropic, and well-connected granular assembly experiencing small-strain deformation can be fit by isotropic material model, which is described by the elastic constants of Young's modulus (E) and Poisson's ratio (ν). E and ν are emergent properties that can be related to the effective modulus $\left(E^*\right)$ and the normal to shear stiffness ratio $(k^* \equiv k_n / k_s)$ at the contact as follows: E is related to E^*, with E increasing as E^* increases; ν is related to k^*, with ν increases up to a limiting positive value as k^* increases.

$$k_n = AE^* / L \ , \ k_s = k_n / k^* \ , \ [k_n \text{ and } k_s \text{ inheritance: = false}] \tag{2.18}$$

$$\text{with } A = \begin{cases} 2rt, & 2D \quad (t=1) \\ \pi r^2, & 3D \end{cases} , \quad r = \begin{cases} min(R^{(1)}, R^{(2)}), & ball-ball \\ R^{(1)}, & ball-facet \end{cases} \tag{2.19}$$

$$L = \begin{cases} R^{(1)} + R^{(2)}, & ball - ball \\ R^{(1)}, & ball - facet \end{cases} \tag{2.20}$$

These relationships are obtained by specifying E^* and k^* as the arguments of the deformability method. The normal stiffness to the axial stiffness of the volume of material is given in Figure 2.6.

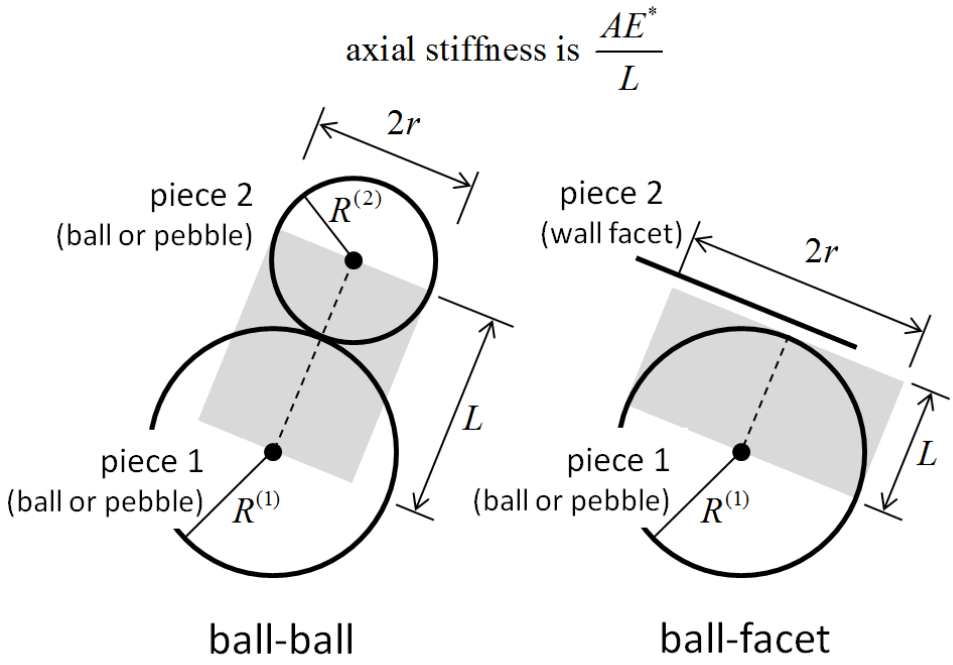

Figure 2.6 Volume of material associated with contact

(Source: Itasca manual 2018)

2.3.5 Principle of clump formation

The clump is a single entity formed by overlapping independent balls (also called pebbles in PFC) at different coordinates to create an irregular particle shape. The overlapping contacts are generally ignored in the calculations, resulting in a saving of computational time as compared to a similar calculation in which all contacts are active. In this sense, a clump differs from a group of

particles that are bonded to one another. Moreover, a clump template may hold the surface description that can be used for the calculation of inertial parameters and clump visualization.

Figure 2.7 shows the contact information of two pebbles in PFC. The clump generally represents by the centres of the pebbles (x_a , x_b), the point of contact (x_c) and the unit-vectors (n_1 , n_2, n_3). The normal n_3 can be given as:

$$n_3 = \frac{x_B - x_A}{|x_B - x_A|} = n_1 \times n_2 \tag{2.21}$$

where n_1 and n_2 lie in the contact plane.

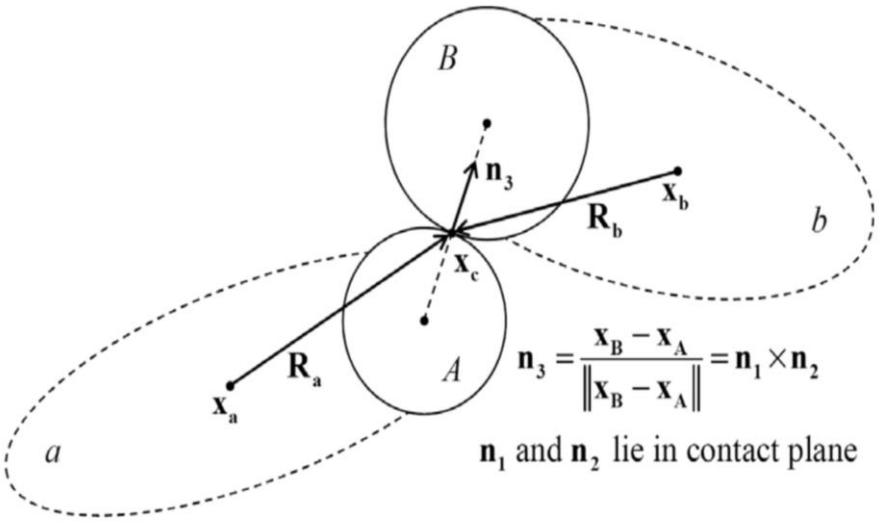

Figure 2.7 Typical contact between two pebbles in DEM

(Source: Itasca manual 2018)

Let 'm' be the mass of a clump and 'x_i^c' be its location of the centre of mass. If N_p is the balls form a clump, the mass of clump can be given as:

$$m = \sum_{p=1}^{N_p} m^p \tag{2.22}$$

$$x_i^c = \frac{1}{m} \sum_{p=1}^{N_p} m^p x_i^p \tag{2.23}$$

where m^p and x_i^p are the mass and centroid of the constituent pebble respectively. The motion of a clump can be expressed in terms of translation motion of a point in the clump and rotation of the entire clump.

2.4 Stress tensor

In a quasi-static regime, for a representative elementary volume (REV), the stress-strain behaviour of a granular assembly can be quantitatively obtained using averaged Cauchy's stress tensor (e.g., Christoffersen *et al.* 1981; Mehrabadi *et al.* 1982):

$$\sigma_{ij} = \frac{1}{V} \sum_{c \in V} f_i^c b_j^c \tag{2.24}$$

where V is the total volume of the REV, f^c and b^c are the contact force and branch vector at each contact point c, respectively. For a clear understanding, a contact force f^c can be decomposed into three components, i.e., f_n^c , f_t^c and f_s^c in the n, t and s directions (in 3D) such that $f^c = f_n^c n + f_t^c t + f_s^c s$. Herein, n, t and s are three orthogonal unit vectors parallel and perpendicular to the contact plane. The mean effective stress and deviator stresses are $p = \sigma_{ii}/3$ and $q = \sqrt{(3/2) s_{ij} s_{ij}}$ with $s_{ij} = \sigma_{ij} - p\delta_{ij}$, respectively, where δ_{ij} is the Kronecker delta.

2.5 Microscopic parameters

2.5.1 Coordination number (CN)

The CN is a fundamental microscopic quantity, which can provide the structural stability of a granular assembly (Thornton 2000; Rothenburg & Kruyt 2004).

$$CN = 2C/N \tag{2.25}$$

where C is the number of contacts and N is the number of particles. The numeric number 2 denotes the fact that each contact is shared by two particles. According to O'Sullivan (2002), higher CN usually corresponds to higher packing density or a lower void ratio (e) and the material strength and stiffness are proportional to the specimen CN in the absence of any particle crushing. It should clearly be stated that the contacts used for clumped particles refer to the clump-to-clump contacts, which means that the contacts between the spheres constituting the clump are ignored or omitted.

2.5.2 Fabric tensor

According to Oda (1972, 1978), the term 'fabric' refers to the spatial arrangement of particles. In other words, it can also be used to quantify the structural anisotropy of granular materials (Oda 1999; Thornton 2000). These measures reflect interparticle connectivity (Satake 1978; Mehrabadi *et al*. 1982; Mehrabadi & Nemat-Nasser 1983; Oda *et al*. 1985), the distribution of void size or orientation (Kuhn 1999; Fu & Dafalias 2015), the distribution of the longer axis for non-spherical particles (Oda *et al*. 1985), or the orientation of particles surfaces (Kuo *et al*. 1998). Satake (1978) suggested that the geometrical anisotropy of a contact network could be characterized by a fabric tensor ϕ_{ij}, which is given as:

$$\phi_{ij} = \frac{1}{N_c}\sum_{k=1}^{N_c} n_i^k \, n_j^k \tag{2.26}$$

where n^k denotes the unit normal contact vector at contact k with $i,j=1,2,3$ (for 3D) and N_c is the number of contacts in the assembly. The similar fabric tensor was also used by Kodicherla *et al.* (2018) for the evaluation of inherent fabric anisotropy of sand particles.

The elements of the second-order fabric tensor ϕ_{11}, ϕ_{22} and ϕ_{33} characterize the distribution of the contact orientation in the direction of reference axes, i.e., x, y, and z-axis. If the assembly of particles is isotropic in the sense of second-order fabric tensor, the fabric tensor can be given in the matrix form as:

$$\phi = \begin{bmatrix} \phi_{11} & \phi_{12} & \phi_{13} \\ \phi_{21} & \phi_{22} & \phi_{23} \\ \phi_{31} & \phi_{32} & \phi_{33} \end{bmatrix} = \begin{bmatrix} 1/3 & 0 & 0 \\ 0 & 1/3 & 0 \\ 0 & 0 & 1/3 \end{bmatrix} \tag{2.27}$$

$$\phi_1 + \phi_2 + \phi_3 = \phi_{11} + \phi_{22} + \phi_{33} = 1 \tag{2.28}$$

The fabric tensor given in Equation (2.26) is a symmetrical second-order tensor, which has three principal values $\phi_{11} = \phi_{22} = \phi_{33} = 1/3$ indicates the average orientation of contacts distributed uniformly in the x, y and z directions.

Although the second-order fabric tensor is the most commonly used approach to quantify the fabric, it may not necessarily identify the important differences between different packing configurations such as face-centred-cubic packing and/or rhombic packing (O'Sullivan *et al.* 2004). Consequently, some researchers like O'Sullivan *et al.* (2004) and Thornton & Zhang (2005) have also been used the fourth-order fabric tensor in their studies, which is given by:

$$\phi_{ijkl} = \frac{1}{N_c}\sum_{N_c} n_i n_j n_k n_l \qquad (i,j,k,l = x,y,z) \tag{2.29}$$

It is cumbersome to visualise the fourth-order fabric tensor. Thus, still, the second-order fabric tensor is used.

2.5.3 Strong and weak force subnetworks

Radjai *et al.* (1998) in a 2D case and Thornton & Antony (1998) in a 3D case demonstrated that the whole contact network can be distinguished into strong and weak subnetworks based on whether the normal contact force is higher or lower than the average normal contact force f^n_{avg}, respectively. The average normal contact force is given as:

$$f^n_{avg} = \frac{1}{N_c}\sum_{1}^{N_c} f^n_i \tag{2.30}$$

where f_i^n is the i^{th} normal contact force in the assembly. Similarly, based on the definition of the fabric tensor mentioned in Eq. (2.26), the associated fabric tensors with the subnetworks can be expressed as:

$$\phi^s_{ij} = \frac{1}{N^s_c}\sum_{k=1}^{N^s_c} n^k_i\, n^k_j, \qquad \phi^w_{ij} = \frac{1}{N^w_c}\sum_{k=1}^{N^w_c} n^k_i\, n^k_j \tag{2.31}$$

where N^s_c and N^w_c are numbers of contacts in the strong and weak subnetworks, respectively. The total number of contacts N_c in the granular assembly is $N_c = N^s_c + N^w_c$. As a result, the relation between the fabric tensor ϕ_{ij} of the whole contact network and those of the strong and weak sub-networks can be expressed as:

$$\phi_{ij} = \frac{N_c^s}{N_c}\phi_{ij}^s + \frac{N_c^w}{N_c}\phi_{ij}^w \tag{2.32}$$

According to Thornton & Sun (1993), for three-dimensional axisymmetric conditions, a deviator fabric (ϕ_d) is given as the difference between major and minor principal fabrics, i.e., $\phi_d = \phi_1 - \phi_3$ has been used to describe the degree of structural anisotropy of granular assembly.

2.6 Developments in particle geometries in DEM

Although the basic formulations for DEM were derived back in the 1970s, the seminal research papers were published in 1979 (Cundall & Strack 1979) and picked- up slowly in the late 1990s (Zhu *et al.* 2007; O'Sullivan 2011). The most commonly used particle shapes in DEM are discs (in 2D) and spheres (in 3D). This is mainly due to computational limitations and easy contact detection during the simulation. However, the characterization of particle shape is crucial when it comes to reproducing quantitative bulk behaviour of granular assemblies (Cho *et al.* 2006; Andrade *et al.* 2012; Jerves *et al.* 2016). Such observations have spurred the development of several DEM variants to capture the particle shapes given in Figure 2.8 (Andrade & Mital 2019). Among these efforts involved in the use of ellipsoids (Rothenburg & Bathurst 1991; Lin & Ng 1997; Ng 2004; Ng 2009; Yan *et al.* 2010), use of clumps or clusters of spherical particles (Favier *et al.* 2001; McDowell & Harireche 2002; Li & McDowell 2018), polyhedra (Hart *et al.* 1988; Nezami *et al.* 2004), non-uniform rational basis splines or NURBS (Lim *et al.* 2014; Lim *et al.* 2016), and level sets (Jerves *et al.* 2016; Kawamoto *et al.* 2016; Kawamoto *et al.* 2018).

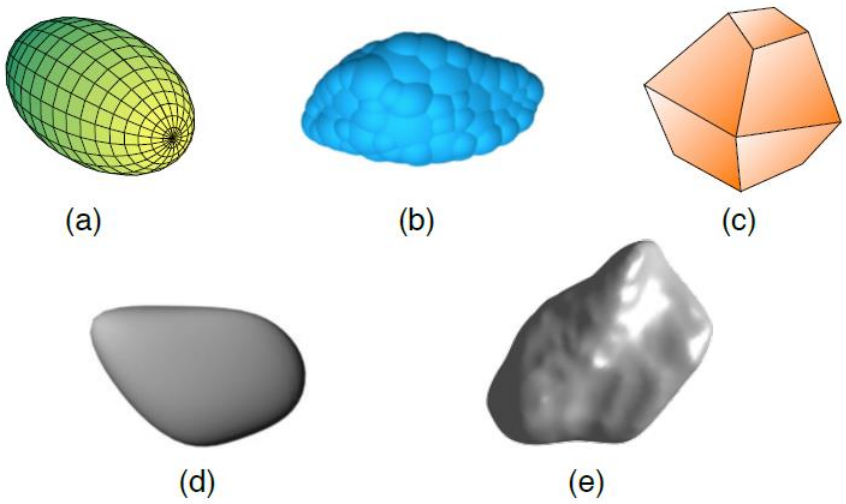

Figure 2.8 DEM variants to capture the particle shape: (a) Ellipsoids, (b) Clumps, (c) Polyhedra, (d) NURBS and (e) Level sets

(Source: Andrade & Mital 2019)

2.7 Summary

The DEM has been considered as a useful tool for exploring the mechanical behaviour of granular materials. The particle mechanics studies are mostly performed by considering the assemblies of spherical particles due to its simplicity and easy contact detection. But some studies (e.g., Cavarretta *et al.* 2010; Kodicherla *et al.* 2019) reported that the particle shape has significant effects on the mechanical behaviour of granular assemblies. The ability of realistic particles mainly depends on the motion and inter-particle contact forces at both macro- and micro-scale levels. A study conducted by Rothenburg & Bathurst (1992) indicates that a smaller angle of repose and reduced shear strength for spherical particles when compared with the non-spherical particles. Thus considering particle shape is an important aspect in modelling behaviour of granular materials. However, there is no generalized particle shape to understand the underlying mechanism between the particles in the literature. Hence, this thesis is targeted at exploring the macroscopic and

microscopic behaviour of granular materials employing different particle shapes using a built-in clump logic in PFC.

Chapter 3 Experimental and numerical validation of direct shear test

3.1 Introduction

In geotechnical engineering, the shear strength of granular materials can be evaluated using the direct shear test in the laboratory. The test was initially used in the 19th century by Alexandre Collin. There exists two kinds of direct shear test apparatus: the cubical specimen (i.e., Cambridge-type) with rigid wall boundaries which was developed by Roscoe (1953), and the cylindrical specimen (i.e., NGI-type) with the wire-reinforced membrane, which provides lateral confinement to the specimen (Bjerrum & Landva 1966). In both tests, the applied vertical and horizontal forces are measured and the ratio of horizontal stress acting in the shear band area and thereby providing a direct measure of the angle of internal friction of granular materials. However, it is still unclear that the exact state of stress within the shear band is unidentified. Alternatively, this problem can be further examined using DEM simulations. In DEM, a user can have great controllability and the same representative samples can be generated multiple times. This would ultimately provide a way to understand the sensitivity of granular materials considering a range of microscopic parameters for further investigation.

In Section 3.2, relevant published literature on both laboratory tests and DEM simulations under the direct shear test condition is reviewed. The description of the physical direct shear test and the procedure is presented in Section 3.3. A brief procedure for the generation of realistic particle shapes is presented in Section 3.4. The procedure for numerical simulations and sensitivity analysis is presented in Section 3.5 and Section 3.6 respectively. A numerical DEM validation with experimental laboratory direct shear test results is presented

in Sections 3.7. In the end, a summary of the overall chapter is presented in Section 3.8.

3.2 Review of literature

In the early stages of two-dimensional DEM simulations employing direct shear test was performed by Masson & Martinez (2001) and Zhang & Thornton (2002). It should be noted that the displacements of the particles in the out-of-plane direction, and the contact forces between the particles in the shear direction also contribute to the overall material response of granular materials. Therefore, three-dimensional DEM analyses are essentially needed to capture the micromechanics along with the localisation.

The macro-and micro-scale response of idealised granular material in the direct shear test apparatus was carried out by Cui & O'Sullivan (2006). The mechanical response of granular materials was considered by combining coupling experimental tests with subsequent DEM simulations. They found that the macro-scale response of the experimental test results was generally in agreement with the simulation results and the peak state angle of shearing resistance slightly underestimated. Moreover, a relative good match was found between the physical tests and the numerical simulations considering the micro-scale response.

The shear behaviour of fresh and coal fouled ballast in the direct shear test using a three-dimensional DEM code i.e., PFC, was explored by Indraratna *et al.* (2014). The ballast particles were modelled using about 10-20 spherical balls clumped together in appropriate sizes. The fouled ballast with various void contamination index (VCI) ranging between 20 and 70% was modelled by injecting a specified number of miniature spherical particles. It was found that the peak shear stress of ballast assembly decreases and the dilation of fouled ballast increases with increasing VCI. The reduced maximum contact force

associated with increased particle contact area due to fouling describes the decreased breakage of fouled ballast.

The direct shear behaviour of coarse sand using three-dimensional DEM considering rolling friction model was investigated by Salazar *et al.* (2015). To incorporate the grain shape characteristics, a rolling friction contact model was applied to the spherical particles. From the analysis of results, it was found that the particles that were up-scaled twice slightly less accurate than the unscaled experimental results.

Wang *et al.* (2015) applied DEM to simulate the irregular ballast stones using a clump mechanism using the direct shear test. A non-linear contact force model with Mohr-Coulomb was implemented to model the interaction of the clumped particles. The results demonstrate that ballast behaviour was in good agreement with experimental behaviour. Also, the shear resistance increases with the normal stress application, indicating that the lateral confinement of ballast bed leading to less vertical settlement and more track stability.

Amirpour Harehdasht *et al.* (2018) studied the micromechanics based assessment of reliability and applicability of boundary measurements in a symmetric direct shear test using a three-dimensional DEM code, i.e., SiGran. The performance of physical direct shear apparatus was optimized by modifying the symmetrical test configuration. The numerical results show quantitative data on different forms of energy consumed during shear and also confirmed the physical and numerical data reported in the literature. The micro-scale results show new evidence that corroborates the further use of the boundary measurements in the physical symmetrical direct shear test.

Wang *et al.* (2018) explored three-dimensional modelling of direct shear test on granular rubber-sand. An excellent agreement was found between the simulation and experimental results, verifying the model's capacity to examine

the mixtures shear behaviour. Moreover, these observations demonstrate the inclusion of rubber particles amends the mixture stiffness, grading and packing at the particulate level, leading to a corresponding variation in the material shear behaviour.

Gong *et al.* (2019) studied the direct shear behaviour of railway ballast mixed with tire-derived aggregates (TDA) and compared those results with DEM. Both laboratory and DEM results confirmed that TDA significantly decreased the peak shear stress and the dilation effect of the ballast-TDA mix. As the content of TDA increased, the coordination number (CN) of TDA increased, while the CN of ballast particles decreased. Moreover, the TDA tended to decrease the occurrence of large contact forces which are greater than 250 N, and thus lowered ballast breakage in the TDA mix.

3.3 Description of the physical direct shear test apparatus and procedure

The laboratory direct shear apparatus consists of a metal box of a square in cross-section (100 *mm* × 100 *mm* × 50 *mm*, as shown in Figure 3.1), split horizontally into two halves at its mid-height. The normal (vertical) load is applied to the specimen and is kept constant throughout the test. A gradually increasing horizontal (shear) load is applied to the lower part of the box until the sample fails in shear. Each sample is tested with different normal loads. The horizontal load is applied at a constant loading rate (0.015 mm/s). The lower half of the box is mounted on the rollers and is pushed forward at a uniform rate by a motorized gear system. The upper half of the box bears against a steel proving ring, the deformation of which is shown on the dial gauge indicating the shearing force. A snapshot of the laboratory direct shear test set-up used is shown in Figure 3.2.

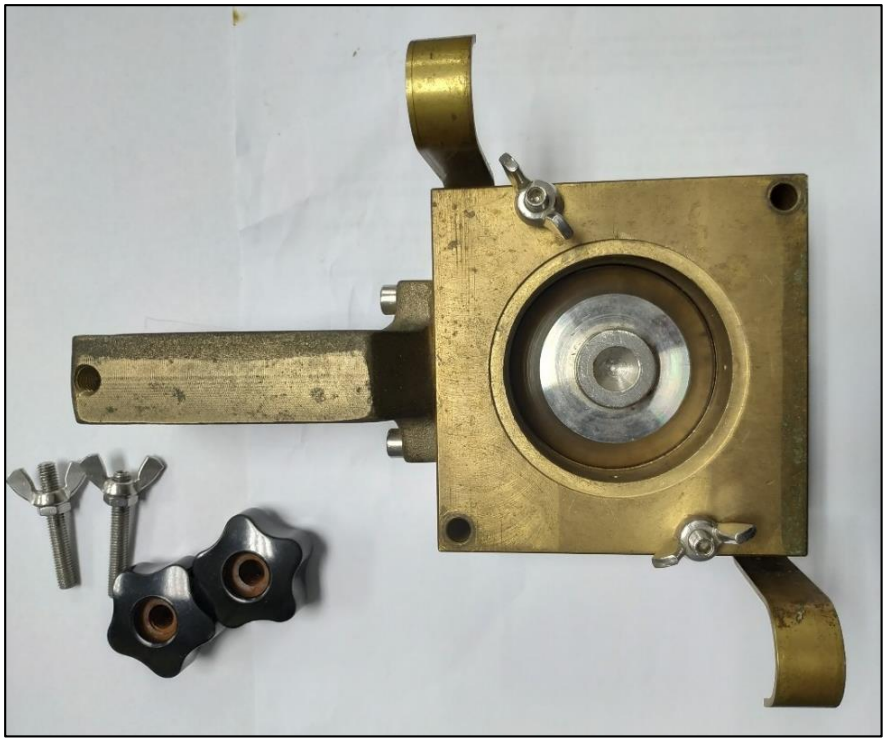

Figure 3.1 Direct shear apparatus currently used in the laboratory

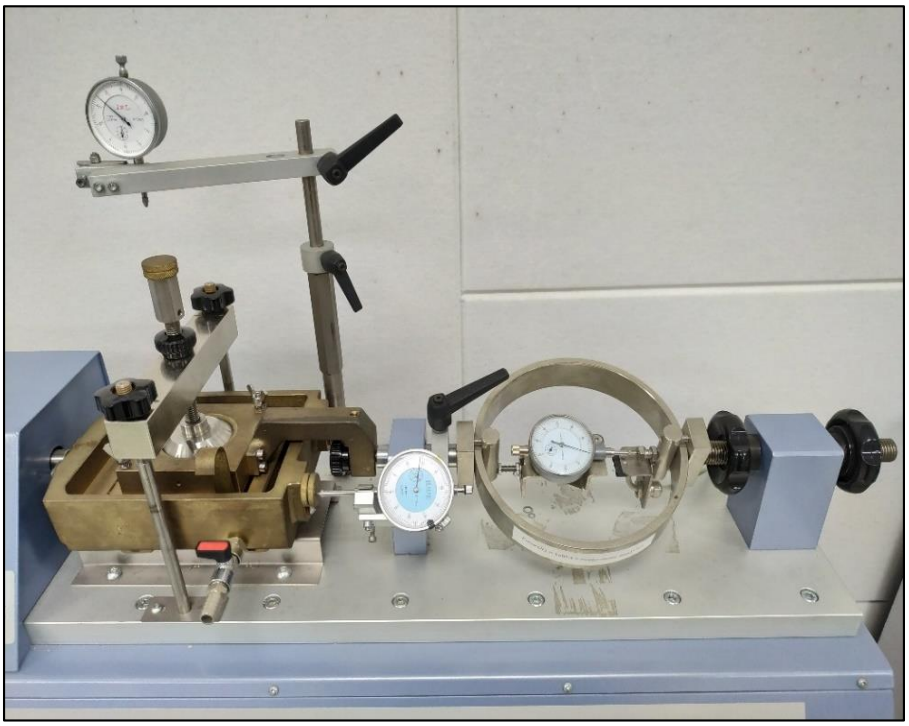

Figure 3.2 A snapshot of the direct shear test setup used in the laboratory

The shear stress, τ, is calculated by dividing the horizontal load measured in the proving ring over the original cross-sectional area of the specimen, while the vertical stress (or normal stress), σ is calculated by dividing the applied vertical load over the original cross-sectional area of the specimen.

The angle of shearing resistance, ϕ, can be calculated as:

$$\phi = \tan^{-1}\left(\tau / \sigma_n\right) \tag{3.1}$$

where τ is shear stress and σ_n is normal stress applied to the specimen. This test has been considered widely by many researchers in the geotechnical investigations, including the recent works by Cui & O'Sullivan (2006); Indraratna *et al.* (2014); Salazar *et al.* (2015); Wang *et al.* (2015); Amirpour Harehdasht *et al.* (2018); Wang *et al.* (2018) and Gong *et al.* (2019).

3.4 Generation of realistic particles

The development of digital imaging technology has supported the growth of advanced 3D imaging methods coupled with numerical models, such as X-ray tomography, laser scanner and X-ray microtomography (Lin & Miller 2005; Ando *et al.* 2012; Mollon & Zhao 2013; Sun *et al.* 2014; Garboczi & Bullard 2016). However, these approaches involve high precision instrumentation and complicated approaches. Alternatively, 2D approaches which are robust and reasonably appropriate can be used as an effective tool for shape characterization and understanding the interaction of contacts of realistic particle shapes using DEM (Vangla *et al.* 2018).

To capture the geometric shape of the particle, about 10 representative sand particles are selected and those are cleaned thoroughly with alcohol to remove any dust particles exist on the surface. The scanning electron microscope (SEM) JSM – 6510 (JEOL) is used to obtain high-quality images for the analysis.

The particles are mounted on a specialized sample holder with adjustable height to optimize the operation. Before placing the particles on the sample holder, the particles are air-dried and coated with a conductive film to reduce thermal damage and to improve the secondary electron signal by the electron beam under a voltage of 15 kV. The surfaces of the particles are sputtered with a thin layer of a gold coating by JEC - 3000FC auto-fine coater. By adjusting the contrast and focusing on the particle with the required magnification, the desired image is obtained. For the representative purposes, magnification is fixed at 30x and subsequently yielded image has pixels of 1024 × 819. To obtain the particle shape/geometry information, it is necessary to apply image processing techniques before analysing the image. The scanning electron microscope (SEM) micrographs are processed using an open-source image processing tool called Image *J* (Schneider *et al.* 2012). A MATLAB based subroutine is adopted to trace the outer periphery of the particle. This image has different features such as pixels, roughness and form features of the particle for further analysis (Vangla *et al.* 2018). A method proposed by Gander *et al.* (1994) is applied to fit the circles to a series of data points along the periphery of particle geometry. Using this approach, the best-fit circles are being found by minimising the sum of the squares of the distances between the points and the circle. A detailed procedure for finding the corner and non-corner regions, particle outline and best-fitted circles were reported in Zheng & Hryciw (2015). It should be noted that this approach provides a way to generate realistic particles using clumps considering the major plane of orientation of the particles. An illustration of the modelled clumps along with the SEM micrographs is presented in Figure 3.3. For more information regarding the clump logic in PFC, one may refer to Section 2.3.5.

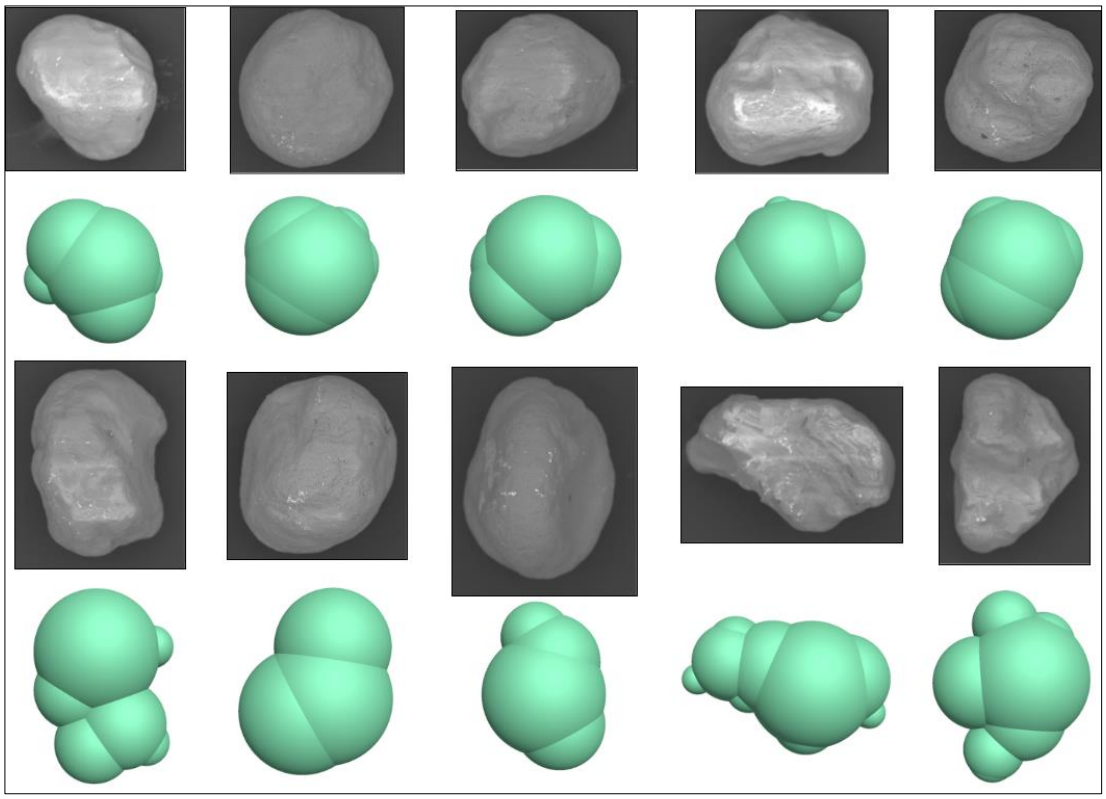

Figure 3.3 A library of generated clumps along with SEM micrographs

3.5 Numerical simulations

In PFC^{3D}, the direct shear box is modelled using rigid walls having the same dimensions as mentioned in Section 3.3. The shear box has two independent boxes namely the 'box top' and 'box bottom' with corresponding planes to cover at both the ends (top and bottom), respectively. Also, two more additional flanges are attached (left and right) either side of the shear box to overcome the particle expulsion during shear. The schematic representation of the direct shear test model in PFC along XZ-plane is shown in Figure 3.4.

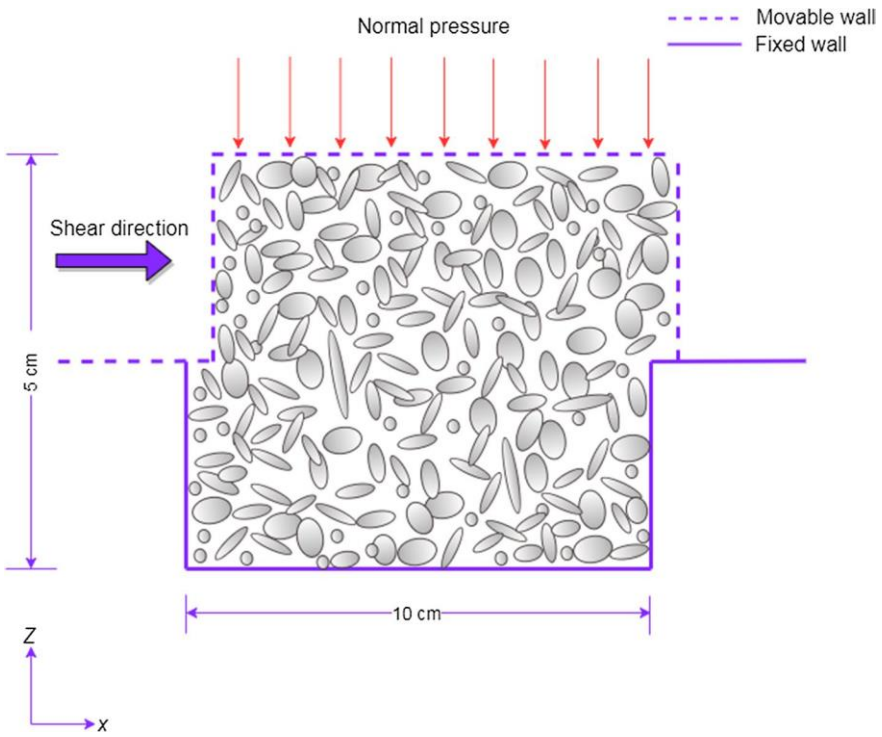

Figure 3.4 Schematic representation of direct shear test along XZ-plane

The particles are randomly distributed using a widely employed random generation approach, which was described by Itasca (2002). A built-in random seed generator is used to define a random size and the location for each particle within the problem domain. If the particle does not fit – in, i.e., where overlapping with an existing particle occurs, the radius is retained but another location is chosen randomly. At the onset, a maximum number of attempts to find a suitable location for any particle is specified. Once the number of attempts has exceeded the maximum value, the generation process is terminated. The limitations of this approach include the computationally expensive contact detection which is required to avoid the overlapping of particles at each insertion attempt. After generating the particles, the assembly is cycled to reach equilibrium through facilitating particles to form a contact with each other. A built-in servo-control mechanism is activated to maintain the desired stress levels during one-dimensional compression under different normal stresses. Moreover, the density scaling based on the auto timestep scaling mode in PFC (Itasca Consulting Group 2018) is also activated to

minimize the computational cost associated with subsequent DEM simulations which were also reported by Cui & O'Sullivan (2006).

3.6 Sensitivity analysis

To understand the sensitivity of microscopic parameters on the DEM simulations of granular materials, a range of parameters are considered as presented in Table 3.1.

Table 3.1 Microscopic parameters for the sensitivity analysis

Properties	Value
Number of particle	926, 2345, 7180 and 11,375
Interparticle friction coefficient	0.3, 0.4, 0.5 and 0.6
Damping constant	0.1, 0.3, 0.5 and 0.7
Particle density (kg/m$^{3)}$	2700
Wall friction	0 (smooth wall)
Shear to normal stiffness ratio	0.1, 0.5, 1 and 2

All numerical assemblies considered for the sensitivity analysis are one-dimensionally compressed at 75 kPa and sheared up to a maximum shear strain of 25%. The sensitivity analysis includes the following:

- Sensitivity to the number of particles
- Sensitivity to the interparticle friction coefficient
- Sensitivity to loading rate
- Sensitivity to damping constant
- Sensitivity to shear to normal stiffness ratio

3.6.1 Sensitivity to the number of particles

For the sensitivity to the number of particles, the number of particles considered as 926, 2345, 7180 and 11,375. The generated assemblies of various

numbers of particles are shown in Figure 3.5. The ratio between mean unbalanced force and the mean contact force against shear strain for different particle numbers are presented in Figure 3.6. It is seen from the figure that the shear strain decreases with the increasing number of particles. Similarly, no much variation is noticed in the plot between stress ratio and vertical strain against shear strain (see Figure 3.7 and Figure 3.8). Following the literature (Huang *et al*. 2014a), and a statement given by Wang & Gutierrez (2010), if the number of particles maintained in between 1170 – 3000, the potential effects of the particle numbers on the simulation results can be avoided. Moreover, it was also mentioned by O'Sullivan (2011) that the computational cost enormously affects the number of particles of granular materials. When realistic gradings are used, as many small numbers of particles must be clumped together to simulate each irregular large particle. The existence of these smaller particles significantly increases the number of degrees of freedom in the system and also necessitates the use of a very small timestep to ensure numerical stability. Hence, taking into account the computational expenses, each assembly is limited to 2,345 discrete particles such that the computation time is within the reasonable limits for a single run (i.e., within 24 hours) except for the sensitivity analysis. In addition, for repeatability of the simulation, the random seed generator is kept constant so that the repeatability of similar results can be achieved.

The particle size distribution of the assembly used is shown in Figure 3.9. This figure indicates that the particle size follows a log-normal distribution. The uniformity coefficient ($C_u = d_{60} / d_{10}$) of the assembly is 1.45 and the coefficient of curvature ($C_c = d_{30}^2 / (d_{60} \times d_{10})$) is 1.04. These values indicate that the assembly is poorly graded. The equivalent diameter of the clumped particles can be obtained as, $d_{eq} = \sqrt{6V / \pi}$, where V is the volume of the clump.

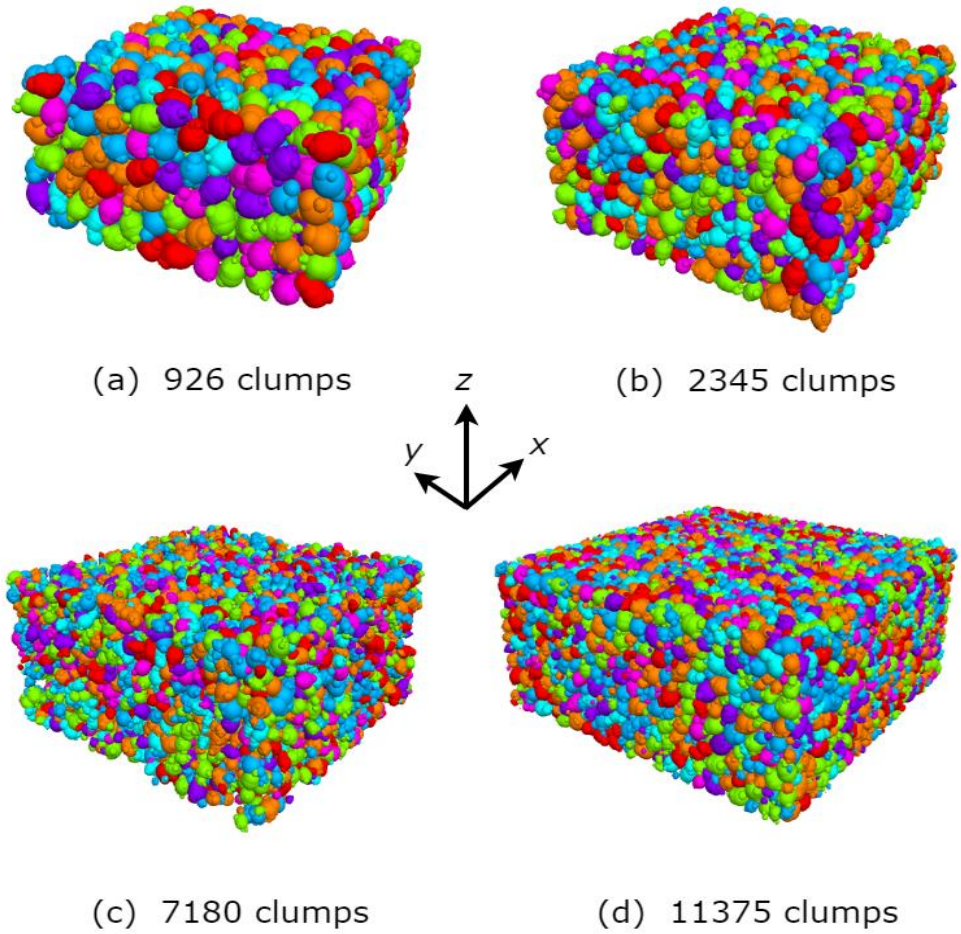

Figure 3.5 Numerical assemblies for different particle numbers

(Walls are omitted)

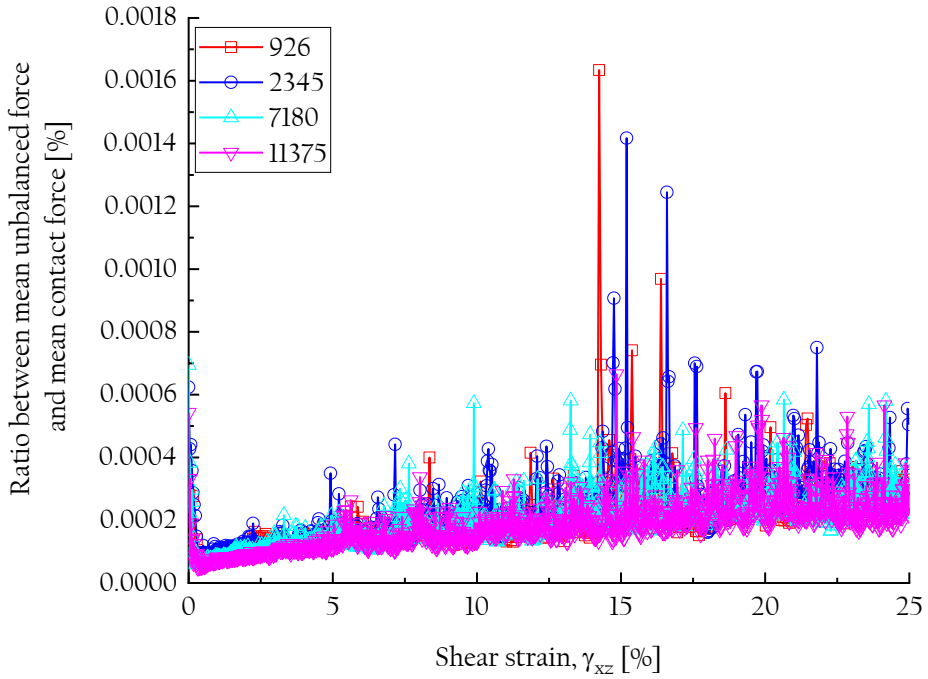

Figure 3.6 Ratio between mean unbalanced force and the mean contact force against shear strain for different particle numbers

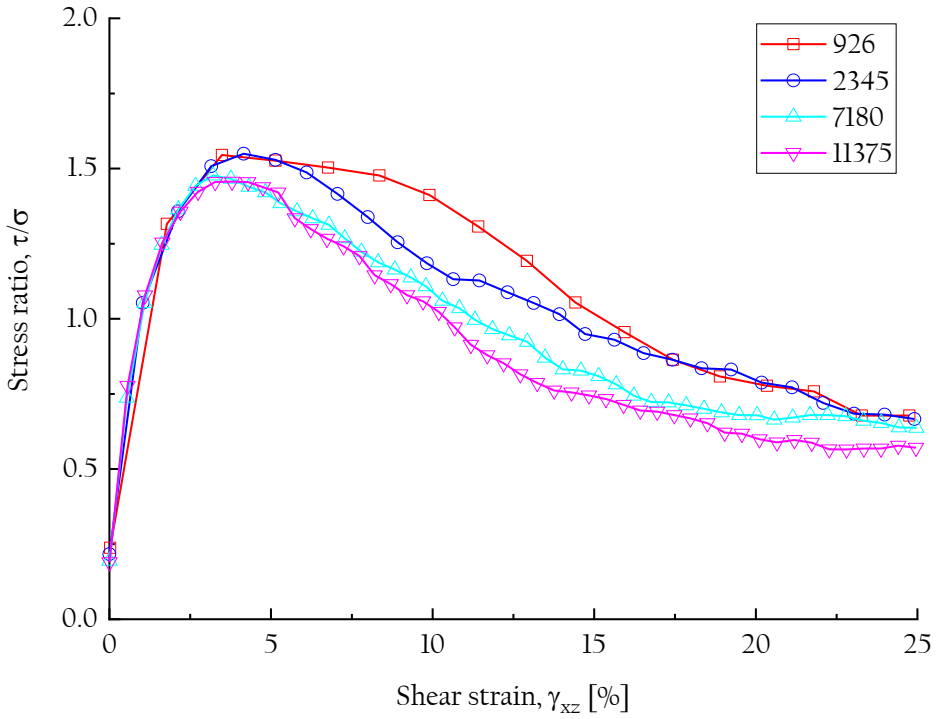

Figure 3.7 Stress ratio against shear strain for different particle numbers

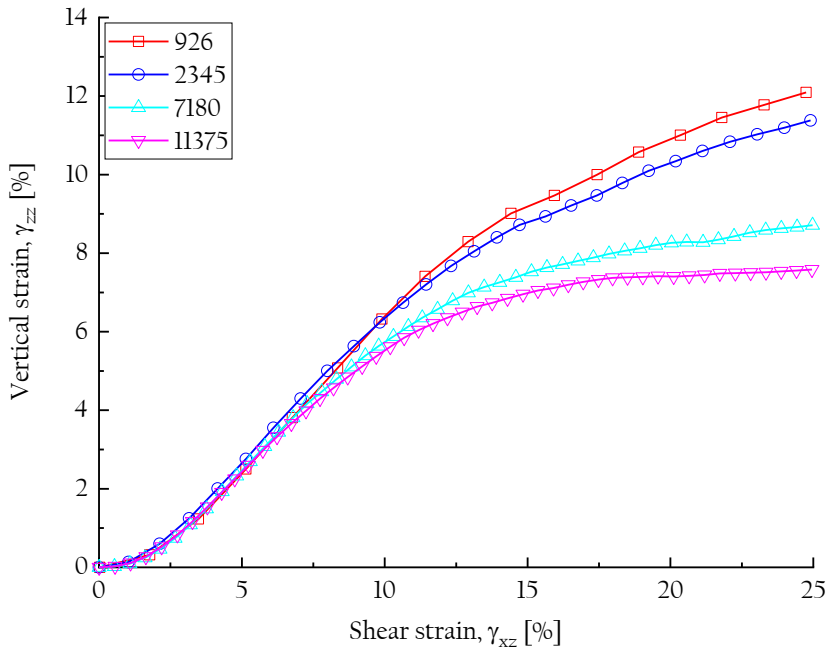

Figure 3.8 Vertical strain against shear strain for different particle numbers

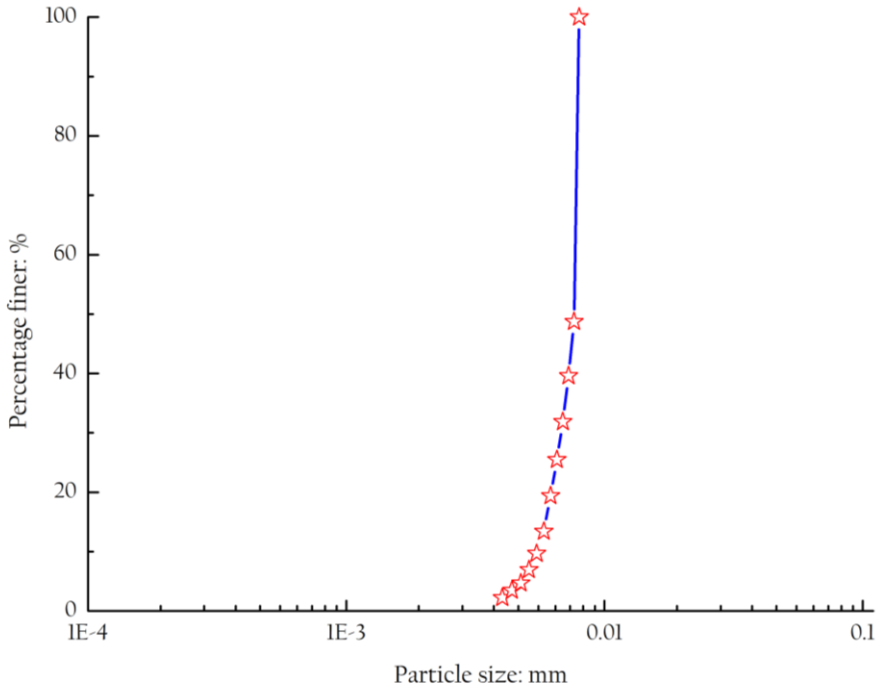

Figure 3.9 Particle size distribution curve used

3.6.2 Sensitivity to the interparticle friction coefficient

The interparticle friction coefficient is one of the intrinsic parameters which significantly affect the DEM simulation results. This is mainly related to the friction between the particles when one particle slides over another. Numerous studies have explored the effect of interparticle friction coefficient theoretically and experimentally (e.g., Rowe & Barden 1964; Skinner 1969). Figure 3.10 and Figure 3.11 show the effect of interparticle friction coefficient on the stress ratio and vertical strain against shear strain for clumped particle systems. It is observed that the strength increases with increase in the interparticle friction coefficient. The angle of internal friction for quartz sand lies in between 21° and 31° which was evaluated based on the experimental observations (Proctor & Barton 1974). The interparticle friction coefficient is taken as 0.5 for the numerical simulations throughout this thesis, which was also commonly employed in most of the simulations.

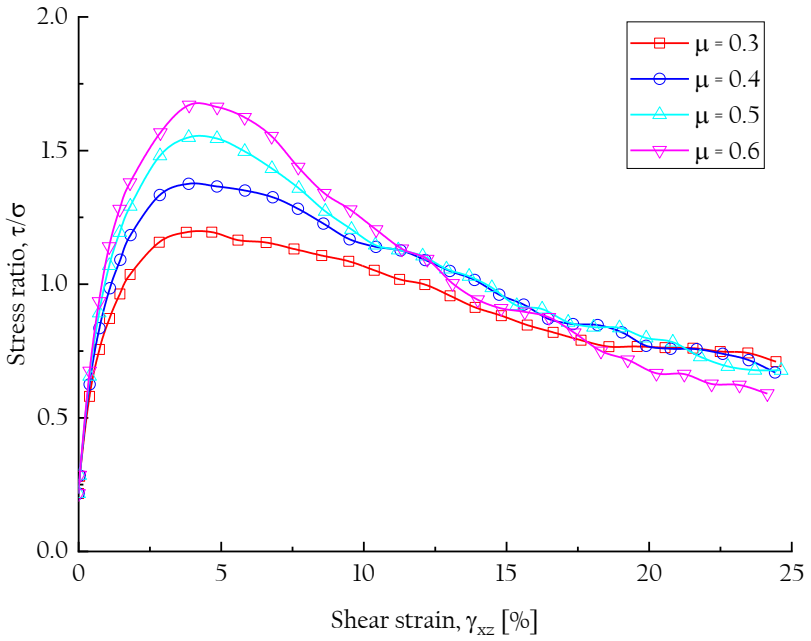

Figure 3.10 Stress ratio against shear strain for different interparticle friction coefficients

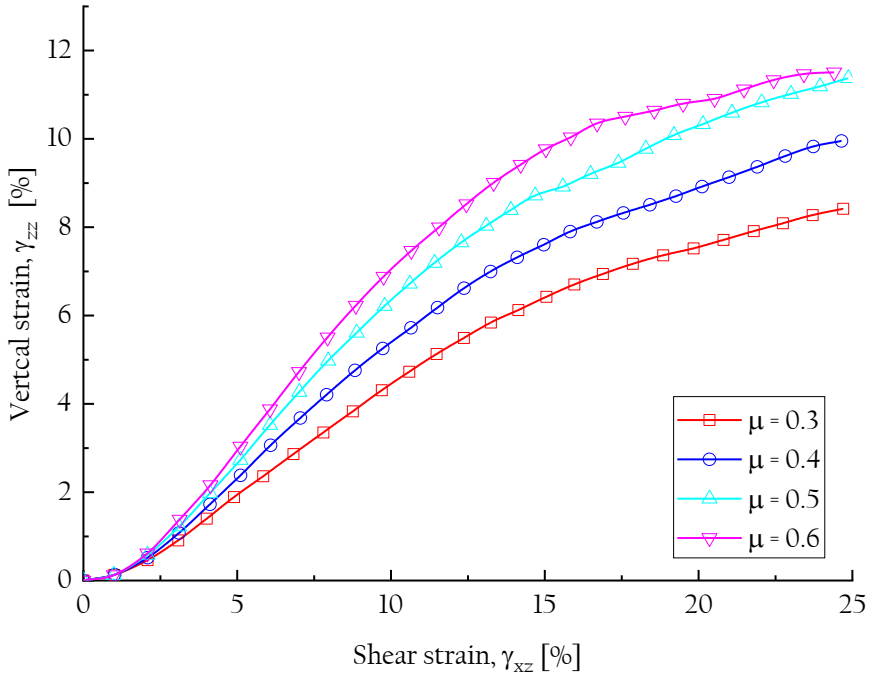

Figure 3.11 Vertical strain against shear strain for different interparticle friction coefficients

3.6.3 Sensitivity to loading rate

In general, most of the simulations and laboratory tests are quasi-static, i.e., inertial effects are assumed to be negligible. Especially in DEM, in addition to the mechanical response of granular materials, the computational cost demands mainly depend on the loading rate (Anitha Kumari 2012). Thus choosing a suitable loading rate is crucial in DEM simulations. To understand the sensitivity to loading rate, a series of numerical direct shear test simulations are performed considering various strain rates (i.e., 6.0×10^{-2}, 6.0×10^{-3}, 6.0×10^{-4} and 6.0×10^{-5}). Figure 3.12 shows the ratio between the mean unbalanced forces to the mean contact force against shear strain for different loading rates. It is seen that except 6.0×10^{-2}, there seems no much variation noticed in the stress ratio, indicating that lower loading rates are showing approximately the same behaviour. Figure 3.13 shows the stress ratio against shear strain for different loading rates. It is also noticed that there is no significant variation in the plot of vertical strain against shear strain (see Figure

3.14). Hence, considering the computational time, the loading rate is taken as 6.0×10^{-4}, for all the DEM simulations throughout this thesis.

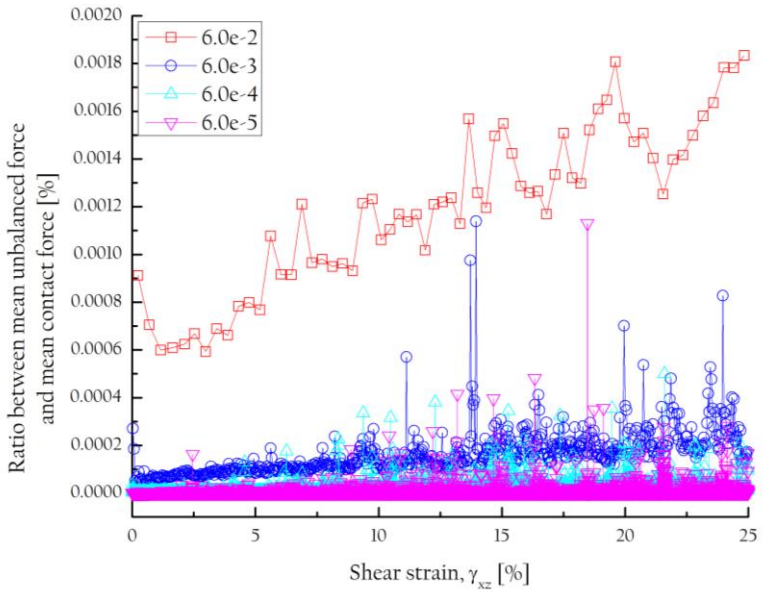

Figure 3.12 Ratio between mean unbalanced force and mean contact force against shear strain for different loading rates

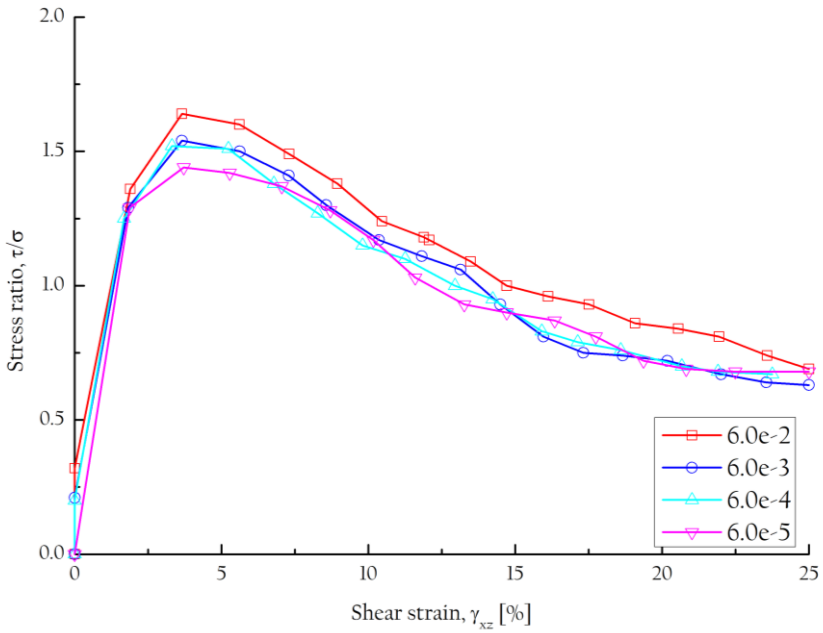

Figure 3.13 Stress ratio against shear strain for different loading rates

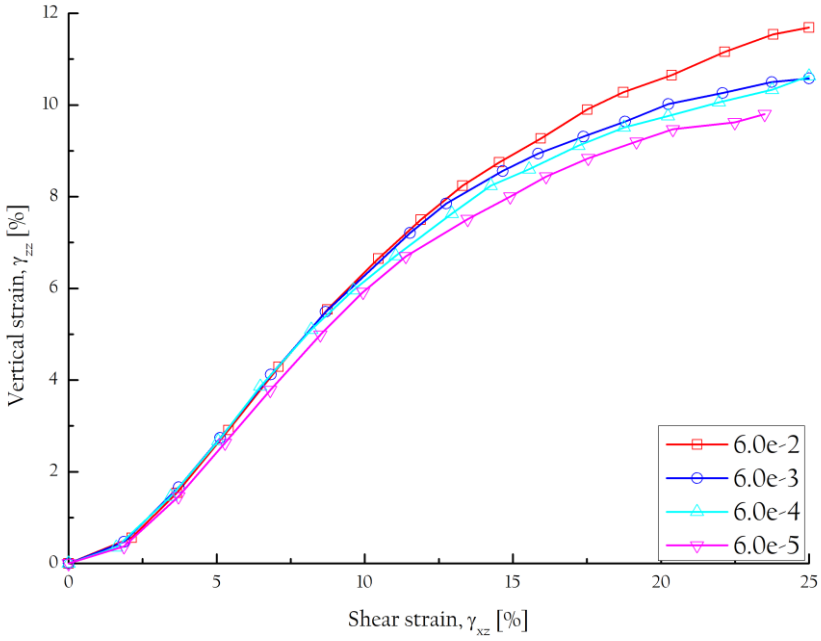

Figure 3.14 Vertical strain against shear strain for different loading rates

3.6.4 Sensitivity to damping constant

In PFC, local damping is activated to dissipate the kinetic energy. The local damping applies a damping force to the particles and the magnitude of the damping force is proportional to the unbalanced force. Figure 3.15 shows the ratio between mean unbalanced forces to the mean contact force against shear strain for different damping constants. It is seen that except d = 0.1, there seems no significant variation observed with different damping constants. Also, the plots of stress ratio and vertical strain against shear strain (see Figure 3.16 and Figure 3.17) show no significant effect for different values of damping constants. To achieve reasonable results, considering the ratio between mean unbalanced forces to the mean contact force, a damping value of 0.7 is used throughout the simulations in this thesis. This value also commonly used by several researchers in the field (e.g., Gong & Liu 2017; Zhu *et al.* 2020).

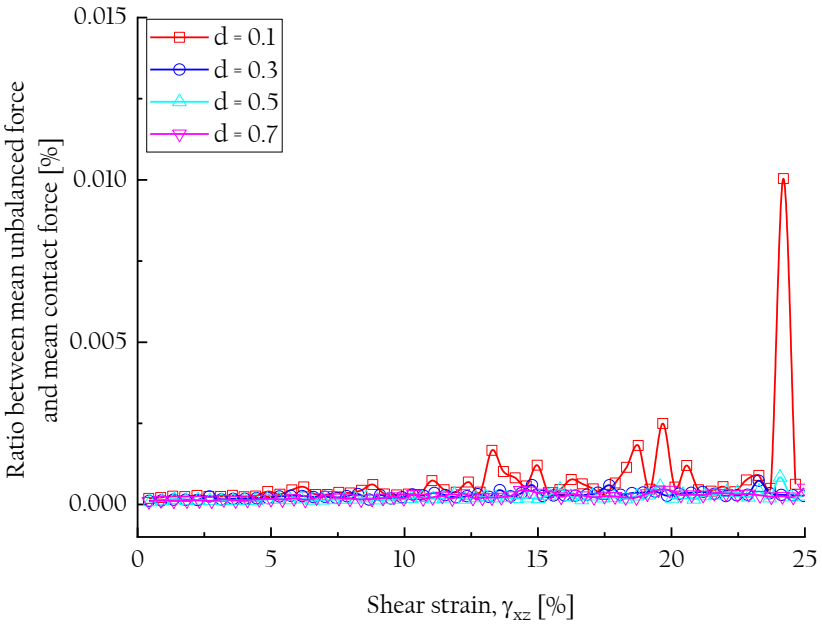

Figure 3.15 Ratio between mean unbalanced force and mean contact force against shear strain for different damping constants

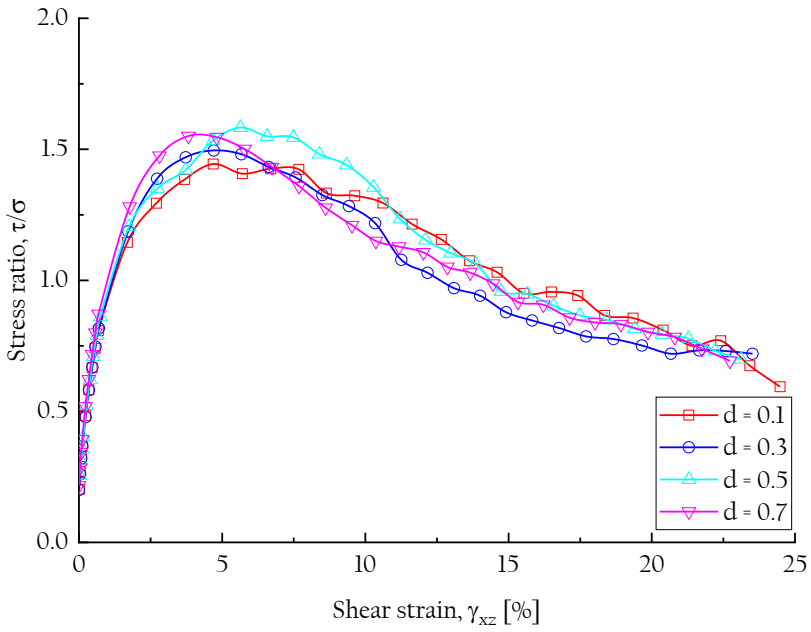

Figure 3.16 Stress ratio against shear strain for different damping constants

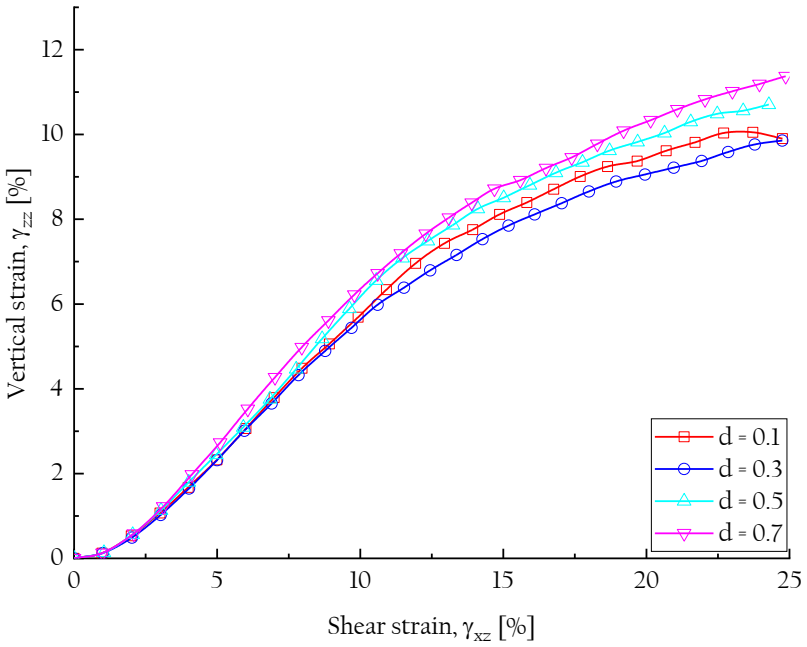

Figure 3.17 Vertical strain against shear strain for different damping constants

3.6.5 Sensitivity to the ratio between normal and shear stiffness

To understand the sensitivity to the ratio between normal and shear stiffness, a series of direct shear test simulations are performed using different values of k* ($\equiv k_n / k_s$) taken as 0.1, 0.5, 1 and 2. Figure 3.18 and Figure 3.19 show the stress ratio and vertical strain against shear strain for different values of contact stiffness ratio. It is seen from the figures that there is no significant variation found for different contact stiffness ratios. According to Goldenberg & Goldhirsch (2005), for realistic granular materials, the value of k_n / k_s typically in the range of $1.0 < k_n / k_s < 1.5$, which correlates well with the Cattaneo–Mindlin model (Johnson 1985). Hence, k_n / k_s = 4/3 is used for all the DEM simulations.

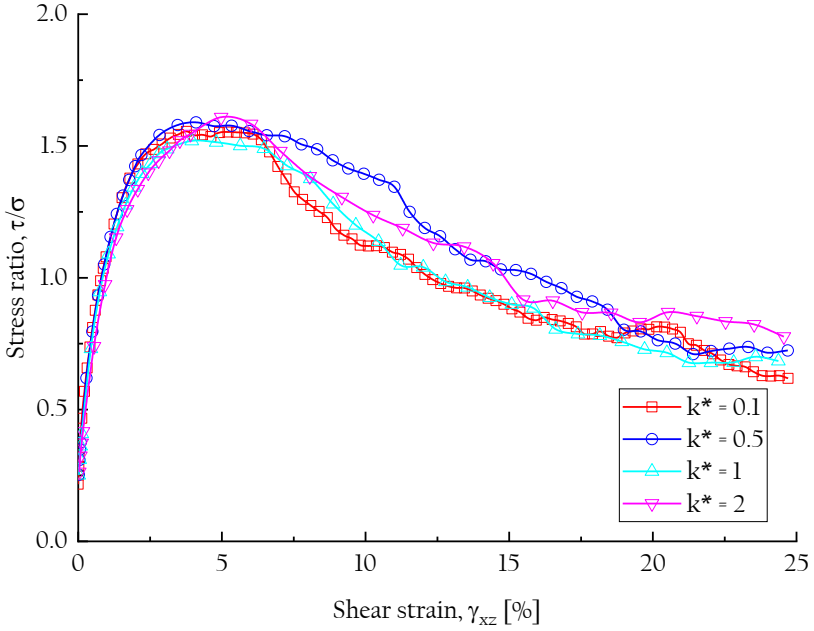

Figure 3.18 Stress ratio against shear strain for varying stiffness ratios

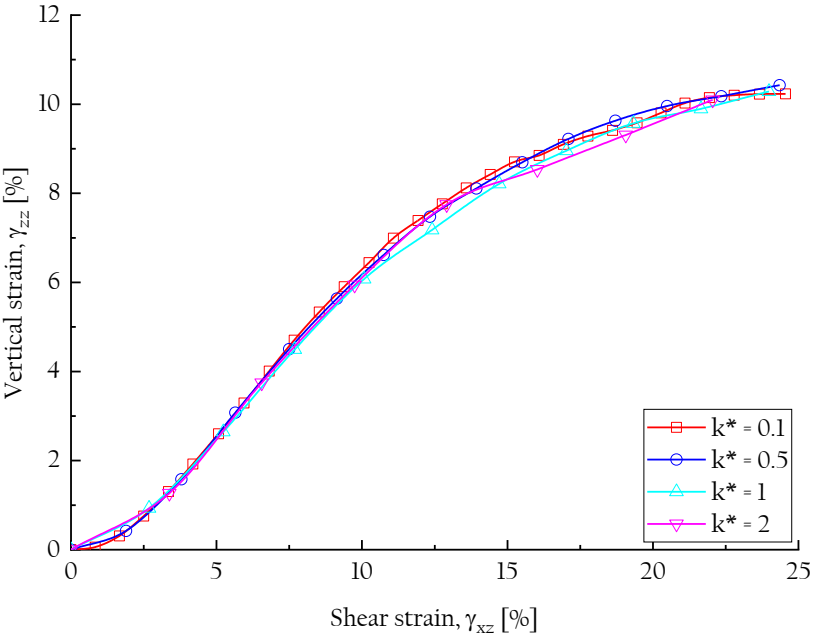

Figure 3.19 Vertical strain against shear strain for varying stiffness ratios

The direct shear test simulations are performed for one-dimensionally compressed granular assemblies. Based on the sensitivity analysis discussed above, the microscopic parameters for the validation of the numerical assembly is chosen such that the ratio between mean unbalanced force and the mean

contact forces are almost negligible. Hence, the system will be in equilibrium state so that a stable solution can be achieved within a reasonable time. Based on the sensitivity analysis, the selected input parameters are chosen for the numerical validation of the direct shear test, as presented in Table 3.2.

Table 3.2 Input parameters for DEM validation

Parameter description	Value
Number of particles	2,345
Notional particle density, ρ $\left(kg/m^3\right)$	2700
Inter-particle friction coefficient	0.4
Wall-particle friction coefficient	0.0
Wall stiffness (N/m)	1.0×10^9
Effective modulus, E^* (Pa)	0.52×10^8
Normal to shear stiffness ratio, $k^*(\equiv k_n/k_s)$	4/3
Local damping constant	0.7

3.7 Comparison between the experimental and DEM results

3.7.1 Stress-strain behaviour

A set of experimental and subsequent DEM simulations are performed under direct shear test conditions to examine the efficiency and applicability of the proposed realistic particle generation approach. The macroscopic behaviour of granular specimens is exposed to three different normal stresses, i.e., σ_n = 75, 179, and 318 kPa and those are kept constant throughout the shearing process.

Figure 3.20 and Figure 3.21 show the comparison of stress ratio and vertical strain against shear strain obtained from the laboratory as well as from DEM simulations. The macroscopic responses of all specimens exhibit stress-dependent and strain-hardening behaviour. The volume change in terms of the vertical strain shows the initial contraction and volumetric dilation, whereby

the higher the normal stress, the higher the peak stress and smaller in the dilation is noticed. These observations are consistent with the study performed by Indraratna *et al.* (2014), for three-dimensional DEM simulations of fresh and fouled railway ballast subjected to direct shear test conditions. Furthermore, it is found that the DEM results are qualitatively in agreement with the laboratory results and minor variations are noticed. These variations could be attributed to the initial conditions and particle breakage during the simulation which is not considered in this investigation.

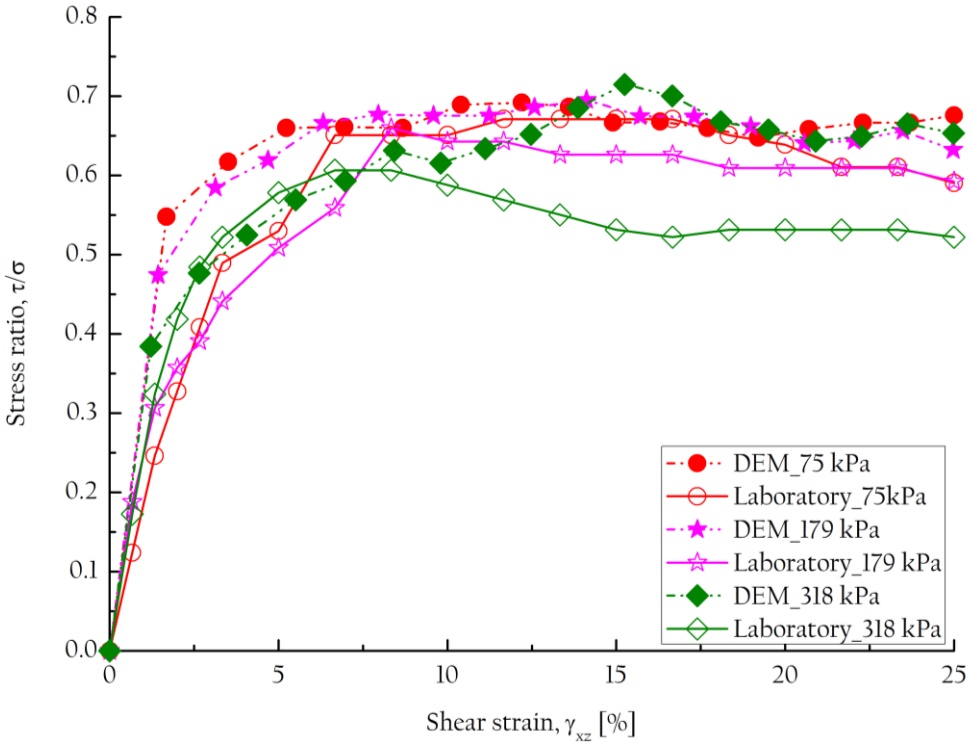

Figure 3.20 Comparison of laboratory and DEM simulation results of stress ratio against the shear strain

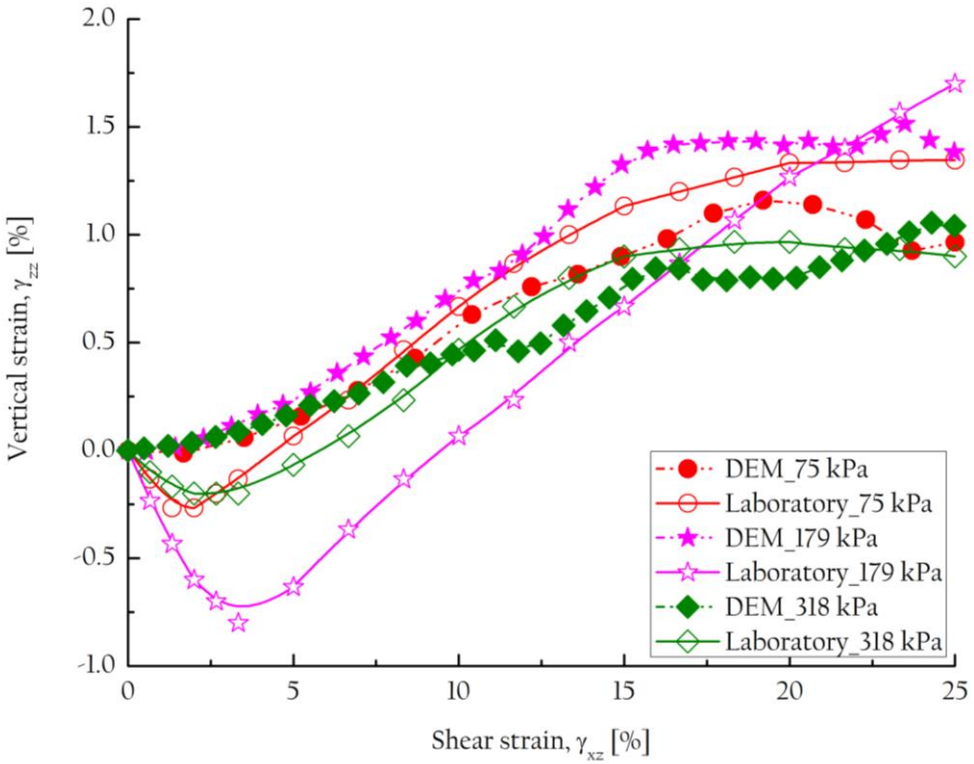

Figure 3.21 Comparison of laboratory and DEM simulation results of vertical strain against shear strains

The peak angle of shearing resistance, ϕ_p, is obtained as the best fit lines between the applied normal stresses and shear stresses at the peak state. It is found from Figure 3.22 that the ϕ_p laboratory and DEM simulations are 31.29° and 35.14°, respectively. As compared to the laboratory test results, the DEM simulation results are overestimated.

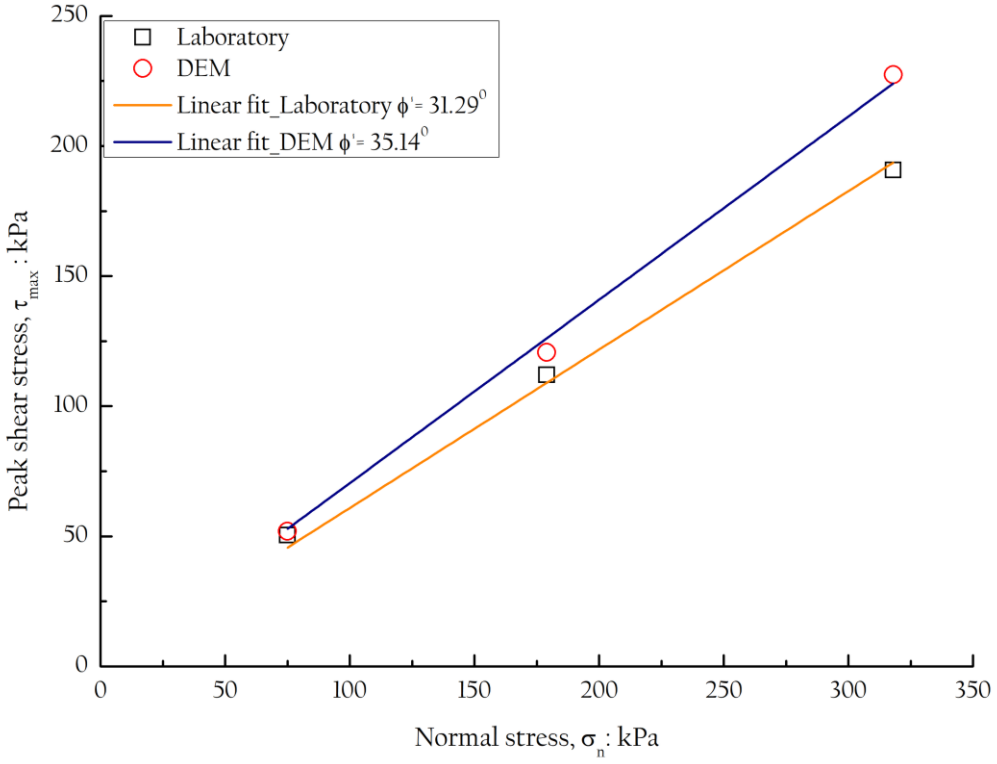

Figure 3.22 Peak stress against normal stress

3.7.2 Coordination number (CN)

For a three-dimensional assembly, considering the friction between the particles, assuming no sliding anywhere, the number of degrees of freedom of a particle is 6, which indicates that a total number of degrees of freedom in the system is $6N_p$. Similarly, the number of constraints at each contact is 3. The total number of constraints in the system is $3N_C$. If the assembly is said to be statically determinate, then the CN is equalled to 4 (i.e., $3N_C = 6N_p$). It was mentioned by Gong (2008) that if the CN is greater than 4, it can be treated as redundant, otherwise, it is structurally unstable. Figure 3.23 presents the variation of CN against shear strain under different normal stresses. As expected, CN increases with increasing normal stress. Moreover, regardless of the applied normal stresses, the CN values are above 4, which indicates structurally stable assembly at any stage during the entire simulation.

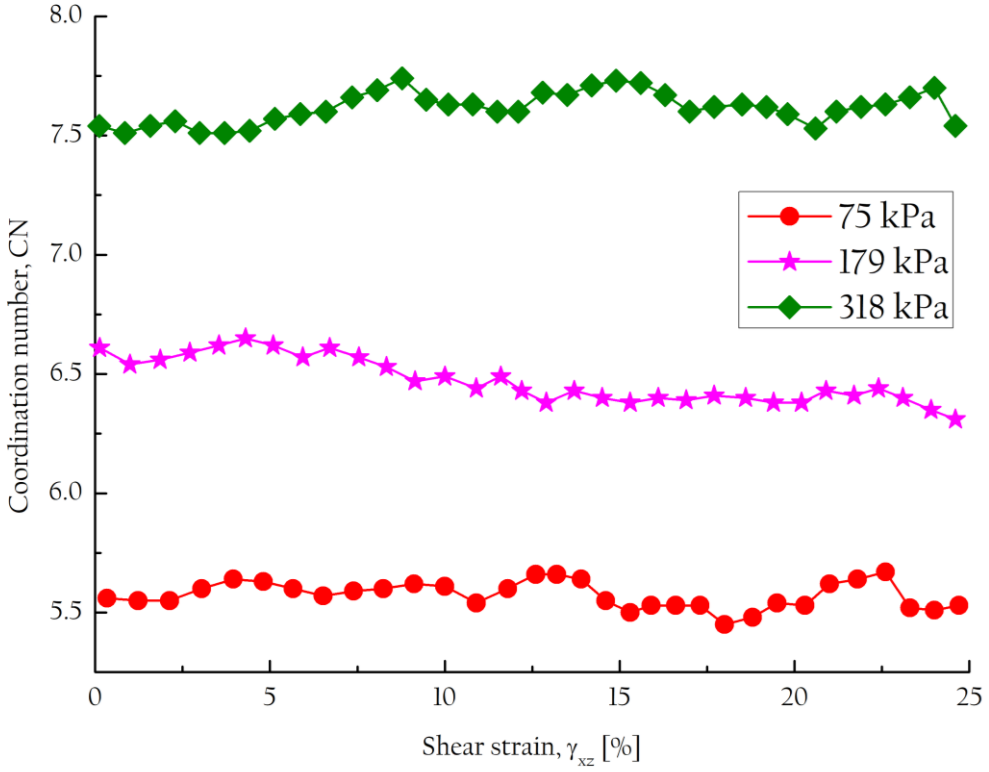

Figure 3.23 CN against the shear strain

Figure 3.24 shows the distribution of contact forces along XZ-plane for the DEM specimen with the applied normal stress of σ_n = 179 kPa. In PFC^{3D}, the inter-particle forces are represented by solid lines with its thickness and colour is proportional to the force magnitudes (Itasca Consulting Group 2018). The lines connecting the particles can form a force chain. It can be seen that at the onset (i.e., γ_{xz} = 0%), the contact forces distributed uniformly and transmitted vertically from top to bottom of the shear box, while as shearing advances, the contact normal forces are intensified in the diagonal direction (see Figure 3.24(b)). This behaviour is attributed to the reduction of contact numbers per particle associated with an increase in the dilation and the corresponding drop in the shear strength.

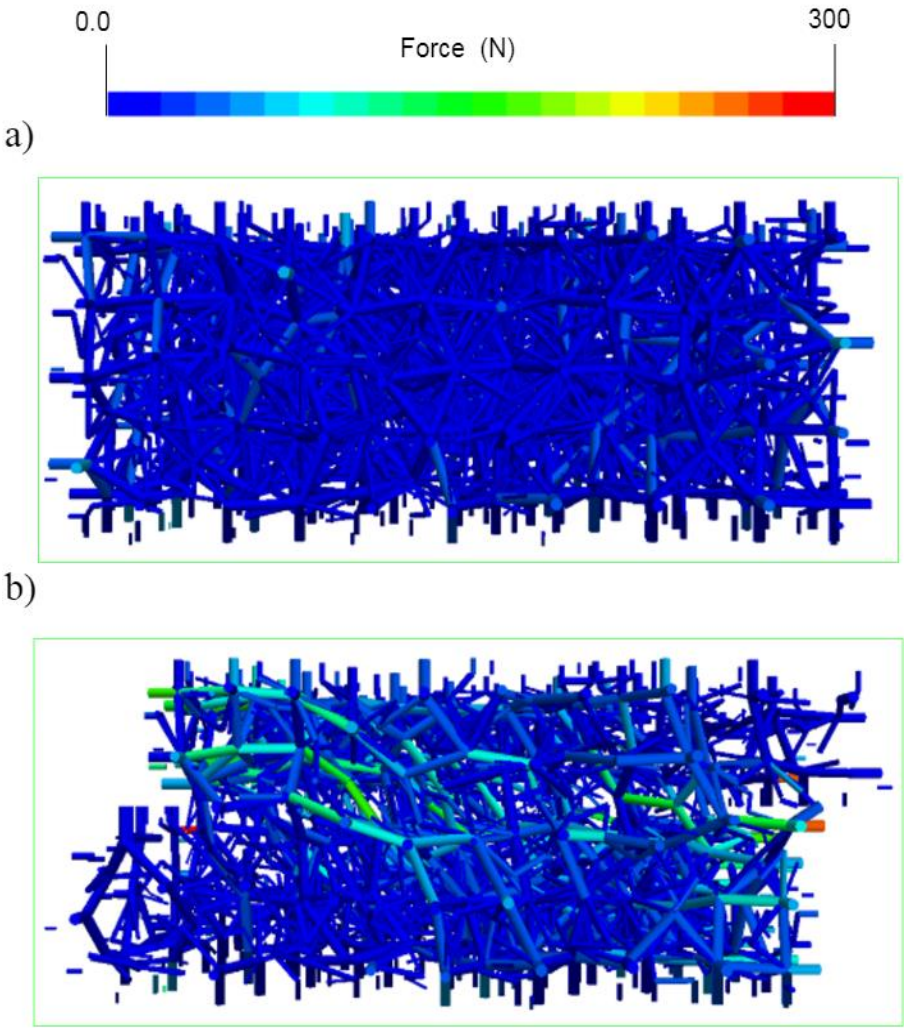

Figure 3.24 Distribution of contact normal force networks for normal stress of 179 kPa: a) end of one-dimensional compression; b) end of the shear

In general, a vector has two independent properties, i.e., magnitude and direction. Each vector represents the displacement of a particle, with the vector start corresponds to the initial position and the length represents the distance travelled. Figure 3.25 shows the displacement vectors of clumped particles for the applied normal stress of σ_n = 179 kPa. As observed from Figure 3.25(a) that at small strain (i.e., $\gamma_{xz} = 1\%$), particles in the 'box top' moved horizontally while particles in the 'box bottom' tended to travel in the downward direction causing a contraction in the assembly. On the other hand, at higher global shear strain (i.e., $\gamma_{xz} = 18\%$), particles in the 'box top' tended to move up or dilate (see Figure 3.25(b)). These microstructural features in DEM clearly illustrate the

likely mechanism for the volumetric changes occurred during the shearing, which may not be possible to capture during the physical experimentation.

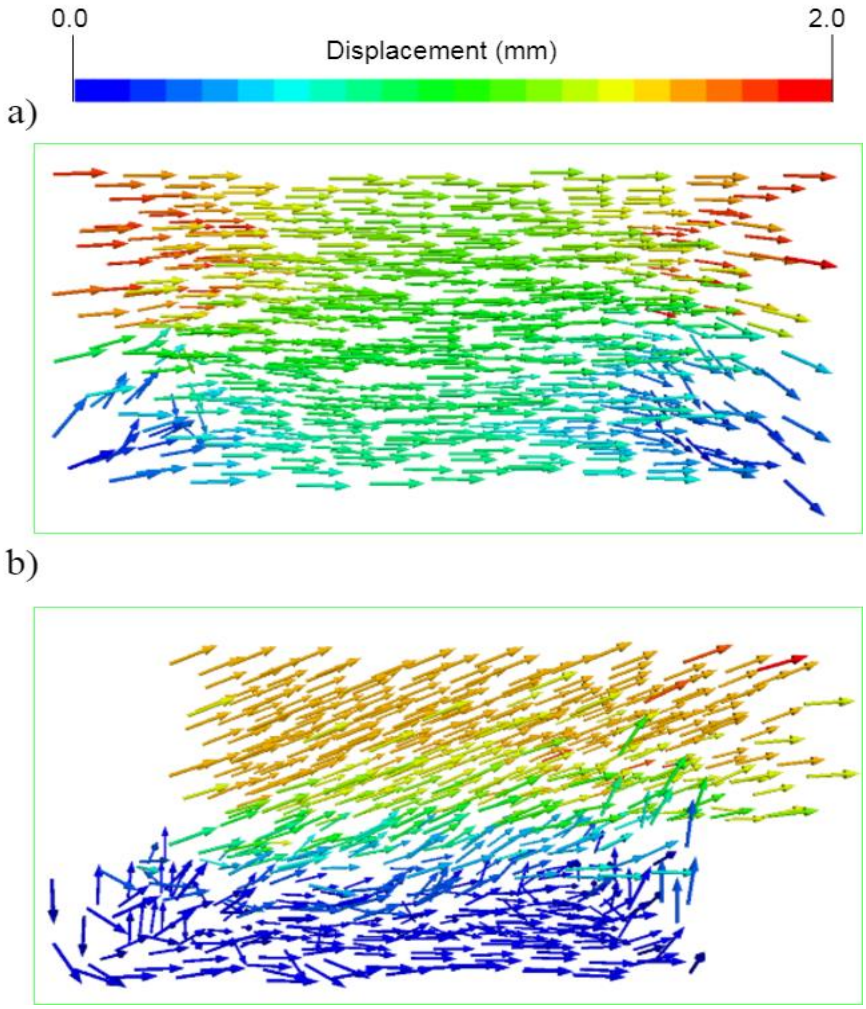

Figure 3.25 Displacement vectors for normal stress of 179 kPa: a) end of one-dimensional compression; b) end of the shear

3.7.3 Evolution of fabric anisotropy

Figure 3.26, Figure 3.27 and Figure 3.28 show the evolution of deviator fabrics of overall, strong and weak subnetworks under different normal stresses during shearing, respectively. A brief description of the fabric tensor is presented in Section 2.5.2. As can be seen from the figures that the overall and subnetworks are developed considerably and the degree of anisotropy increase with an increase in shear strain. It is also found that the increase in normal stress can

limit the development of fabric anisotropy, thereby increase in shear strength. Moreover, in contrast, normal stress has shown a significant effect on the structural anisotropy and higher the normal stress, whereby smaller the deviator fabric.

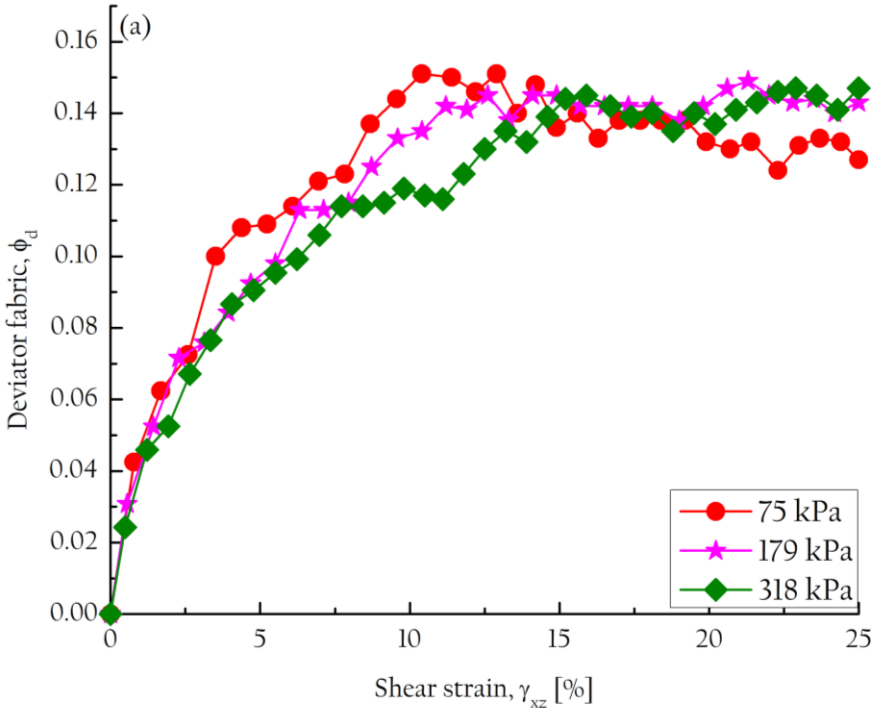

Figure 3.26 Deviator fabric against shear strain for different normal stresses

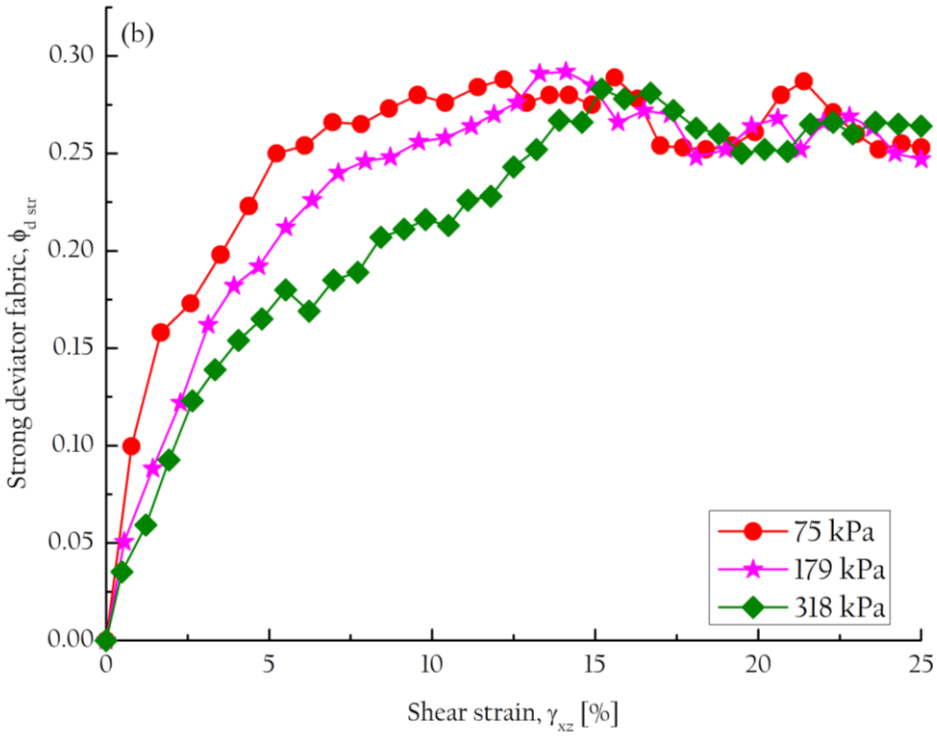

Figure 3.27 Strong deviator fabric against shear strain for different normal stresses

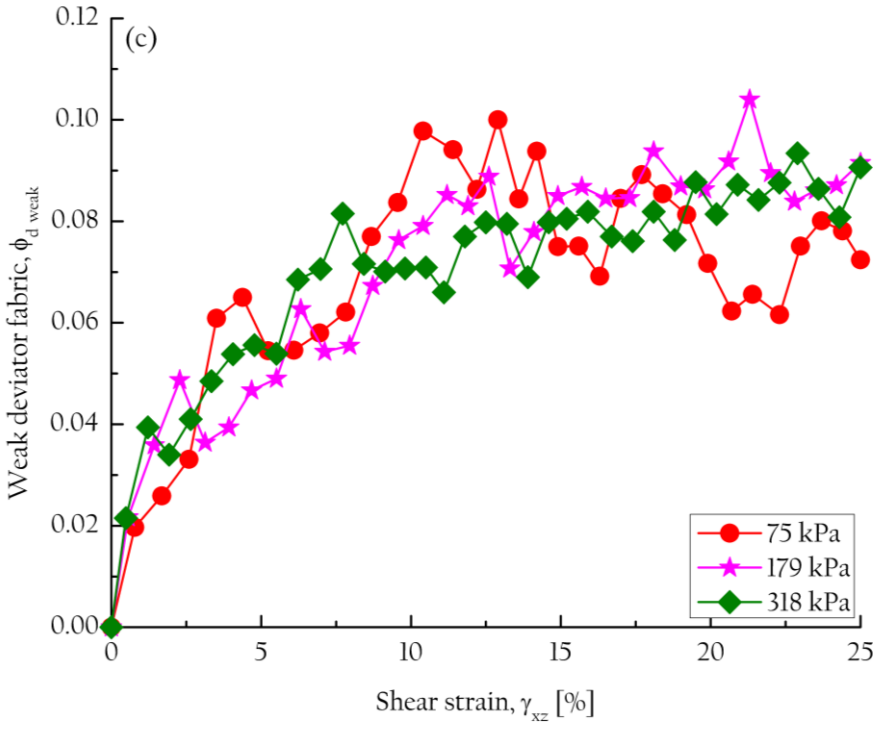

Figure 3.28 Weak deviator fabric against shear strain for different normal stresses

3.8 Summary

In this chapter, a series of laboratory and numerical simulations were performed under direct shear test conditions. A simple and robust approach suggested by Zheng & Hryciw (2015) was employed to generate the realistic particle geometries considering their major plane of orientations. Based on the sensitivity analysis, appropriate microscopic parameters were selected to validate the DEM model with experimental results.

The DEM simulation results were generally in agreement with the laboratory test data; however, the peak angle of shearing resistance observed in the DEM simulations is consistently higher than that of the peak angle of shearing resistance observed in the laboratory tests. It was also noticed that normal stress has a significant effect on the structural anisotropy. Moreover, the simulation results demonstrate the effectiveness of the particle generation method adopted in this investigation. The microscopic results in terms of fabric anisotropy are found to increase with the increase in normal stress and showed a significant effect on the structural anisotropy.

Chapter 4 Influence of particle elongations on the direct shear behaviour

4.1 Introduction

Numerous laboratory experiments have been carried out to explore the particle shape effects on the mechanical response of granular materials (Shinohara *et al.* 2000; Cho *et al.* 2006; Yang *et al.* 2012). Also, in-depth microscopic information of the specimens using photoelasticity (Oda 1974), CT scan (Goudarzy *et al.* 2016) and X-ray (Reimann *et al.* 2017) methods were employed by different researchers. However, the traditional element tests (e.g., direct shear, simple shear and triaxial shear tests) can only provide limited macroscopic information in the laboratory. In general, these methods are extremely laborious and sometimes even more expensive. Instead, DEM based numerical approaches are efficient in exploring the microscopic behaviour of granular materials (e.g., Gong & Liu 2017; Kodicherla *et al.* 2019). The developments in computer technology have provoked the potential possibility to consider realistic particle shapes in DEM. Hence, the desire of obtaining the true behaviour of granular materials could be achieved at reasonable costs.

In this chapter, a general introduction is presented in Section 4.1 and a review of literature related to different particle shapes under direct shear test conditions are reviewed in Section 4.2. In Sections 4.3 and 4.4, the methodology for particle elongation and the simulation details are presented, respectively. The results at macroscopic and microscopic levels are presented in Sections 4.5 and 4.6, correspondingly. Also, the distribution of force chain networks in Section 4.7 and the relationships between stress-dilatancy and critical state lines are furnished in Section 4.8. In the end, a summary of this chapter is presented.

4.2 Review of literature

Extensive numerical investigations have been carried out by employing various particle shapes, such as clumped discs (Maeda *et al.* 2010; Saint-Cyr *et al.* 2011), ellipses (Ting *et al.* 1995), polygons (Tillemans & Heemann 1995; Hosseininia 2012), spheropolygons (Alonso-Marroquin 2008) in 2D cases, and clumped spheres (Hartl & Ooi 2011; Kozicki *et al.* 2012; Azema *et al.* 2013), ellipsoids (Ng 2009), polyhedrons (Zhao *et al.* 2015), spherocylinders (Pournin *et al.* 2005), spheropolyhedra (Boton *et al.* 2013), superellipsoids (Wellmann *et al.* 2008; Cleary 2010) in 3D cases. Besides, some researchers have adopted the particle shape descriptors, e.g., elongation or aspect ratio (Ting *et al.* 1995; Ng 2009; Azema & Radjai 2010), angularity (Azema *et al.* 2013; Zhao *et al.* 2015), eccentricity ratio (Zhao *et al.* 2015) and roughness (Kozicki *et al.* 2012), to quantitatively describe the particle shape effects in their numerical investigations. Moreover, it was mentioned by Anitha Kumar (2012) that the shear strength of clumped particle was found higher than those of spherical particles.

The effect of particle properties on the soil behaviour under three-dimensional direct shear test conditions using bonded spherical particles was explored by Ni *et al.* (2000). The effect of particle shape and particle size under different vertical (normal) loads were explored. It was found that the particle size, when compared with the shear box, affected the bulk shear strength of the sample, but it is dependent on the number of particles used in the simulations. Also, the authors found that as the particle becomes less spherical, the bulk friction angle and volumetric dilation of sample increases. Moreover, the shear strength increased considerably by the particle shape changes from a pure sphere.

Zhang & Thornton (2007) performed a numerical examination of the direct shear test using a two-dimensional DEM. The authors found that the dilation inside the shear zone was much greater than that deduced from the boundary

measurements. The stress ratio obtained from the boundary force was about 10% greater than that calculated in the shear zone. The coaxiality of stress and strain rate exists at the critical state. Also, it was suggested that the previously published simulation results in the context of both stress ratio and dilation would be obtained easily if the shear box aspect ratio was reduced below the value of 1:2, which was commonly adopted in the traditional Casagrande shear box test.

The interplay between contact friction and particle interlocking arising from the geometric interaction between the particles to produce the bulk behaviour of granular friction in DEM simulations using a Jenike direct shear test was explored by Hartl & Ooi (2011). The authors considered two different particle shapes, i.e., spherical particle and non-spherical particle. The full range of interparticle contact friction values was considered and explored numerically. To separate the influence of sample packing density from interparticle contact friction on the bulk shearing response, the same initial packing was used for each particle shape in the simulations. It was found that particle interlocking has a greater effect than the packing density on bulk friction and for each particle shape. Moreover, a good quantitative match of the limiting bulk friction as long as similar initial packing density was achieved.

Yan (2011) explored the particle elongation and decomposition effect to the macroscopic and microscopic response under numerical direct shear test assemblies using PFC3D. The elongated particles were modelled by joining primary spherical balls together, and no particle breakage was allowed. The global measurements appreciably conclude that the higher ultimate shear strength of the assemblage as compared to the local ones from the measurement spheres, regardless of the particles aspect ratio and packing. Also, it was found that only particles close to the shear plane exhibit significant rotation and consequently a noticeable change in the fabric was observed.

Zhao *et al.* (2015) explored the effect of particle angularity under direct shear test using a modified version of the open-source DEM code, i.e., YADE. Four categories of assemblies with different angularities using convex polyhedra were generated and sheared under different vertical (normal) stresses. It was found that the macroscopic shear strength and dilatancy characteristics were in agreement with the results reported in the literature.

Tian *et al.* (2018) studied the influence of particle shapes on the microstructure evolution of granular materials under two-dimensional direct shear test conditions using PFC2D. The authors considered three different particle shapes including circular, triangular and elongated particles. The results show that the peak shear stress ratio and the ultimate dilatancy increases when decreasing the value of overall regularity. Moreover, it was also reported that particle shape has a remarkable influence on the fabric evolution of granular assemblies.

4.3 Methodology for particle elongation

The particle elongation methodology is adopted from Azema & Radjai (2011). The elongated particles are generated using a commonly adopted multi-spherical (MS) approach, as suggested by Taghavi (2000). The elongated particles are modelled as a juxtaposition of three spheres of the radius R' with an imaginary rectangle of length, L and width, $2R'$, as shown in Figure 4.1. Assuming that R is the radius of a circle circumscribing the particle, the radius R' is also that of the inscribed circle. Hence, the change of a particle from a circular shape is considered to be $\Delta R = R - R' = L/2$. A dimensionless elongation parameter, Λ is defined as:

$$\Lambda = \Delta R / R \tag{4.1}$$

where ΔR is the deviation from the circular shape which is equal to a half of the imaginary length (L) of the rectangle. For better visualization, the portrayal of the generated elongated particles with different Λ values is presented in Figure 4.2. Alternatively, the aspect ratio (A_R) of the elongated particle can also be calculated by $(L+2\Delta R)/(2R')$.

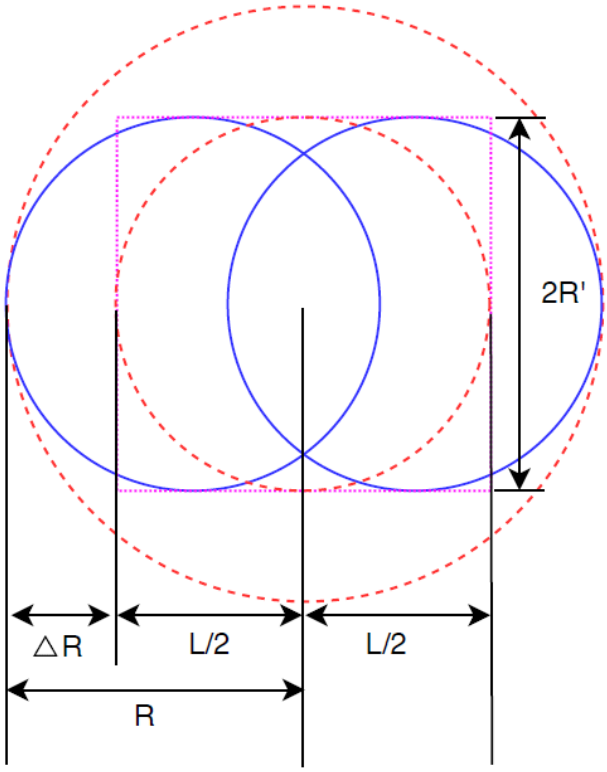

Figure 4.1 Methodology for particle elongation

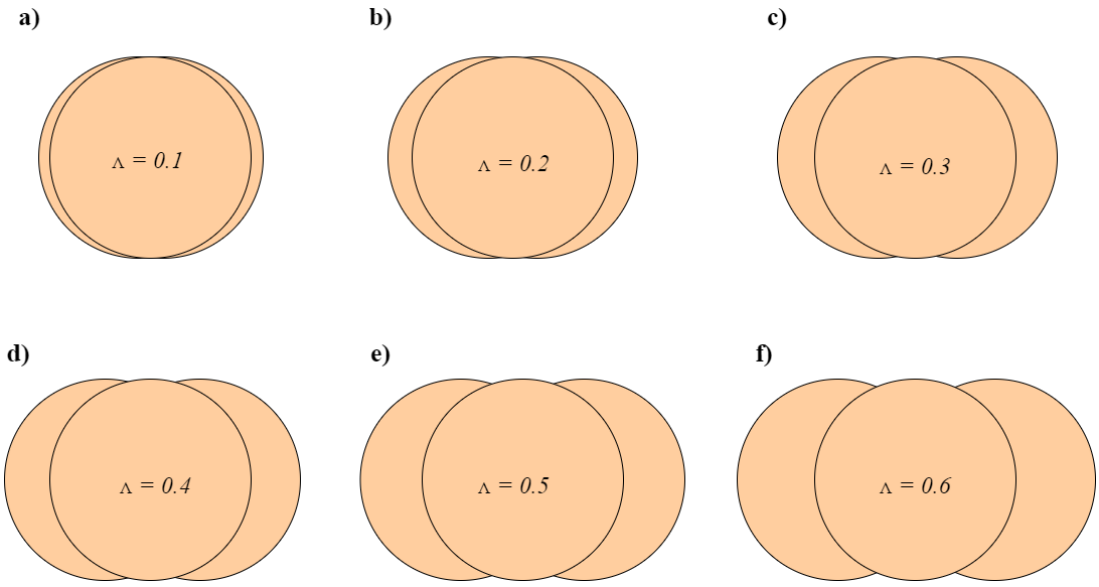

Figure 4.2 Elongated particles with different Λ

4.4 Simulation details

A built-in clump logic is used to generate the elongated particles, i.e., an approach for creating elongated particle by joining and overlapping three spheres of the same size and by allocating the corresponding radii and coordinates. More details regarding the clump logic are given in Section 2.3.5. In total, six consolidated specimens with a target void ratio (e) of 0.5, represented as S1, S2, S3, S4, S5 and S6 are generated. All input parameters are the same as mentioned in Section 3.6, except for E^*. For simplicity, the E^* is taken as 10^8 Pa which is same as used by Gong *et al.* (2019) and approximately equal to that used by Guo & Zhao (2013, 2014) and Gu *et al.* (2014). The initial characteristics of the specimens are presented in

Table 4.1. The initial states of generated packings with different Λ are presented in Figure 4.3. It should be noted that all assemblies are prepared at their densest states, ensuring that they all had the same relative density. To achieve the densest state, a zero clump friction coefficient was temporarily used during the specimen generation stage and changed back to 0.5 while shearing. This routine approach was also used by many investigators in the field (e.g., Deluzarche & Cambou 2006; Abbireddy & Clayton 2010; Gong & Liu 2017; Zhao & Zhao 2019).

Table 4.1 Initial characteristics of the numerical specimens

Specimen ID	Λ	e_o	CN_o
S1	0.1	0.49	14.5
S2	0.2	0.43	12.4
S3	0.3	0.41	11.9
S4	0.4	0.40	11.7
S5	0.5	0.43	11.5
S6	0.6	0.48	11.5

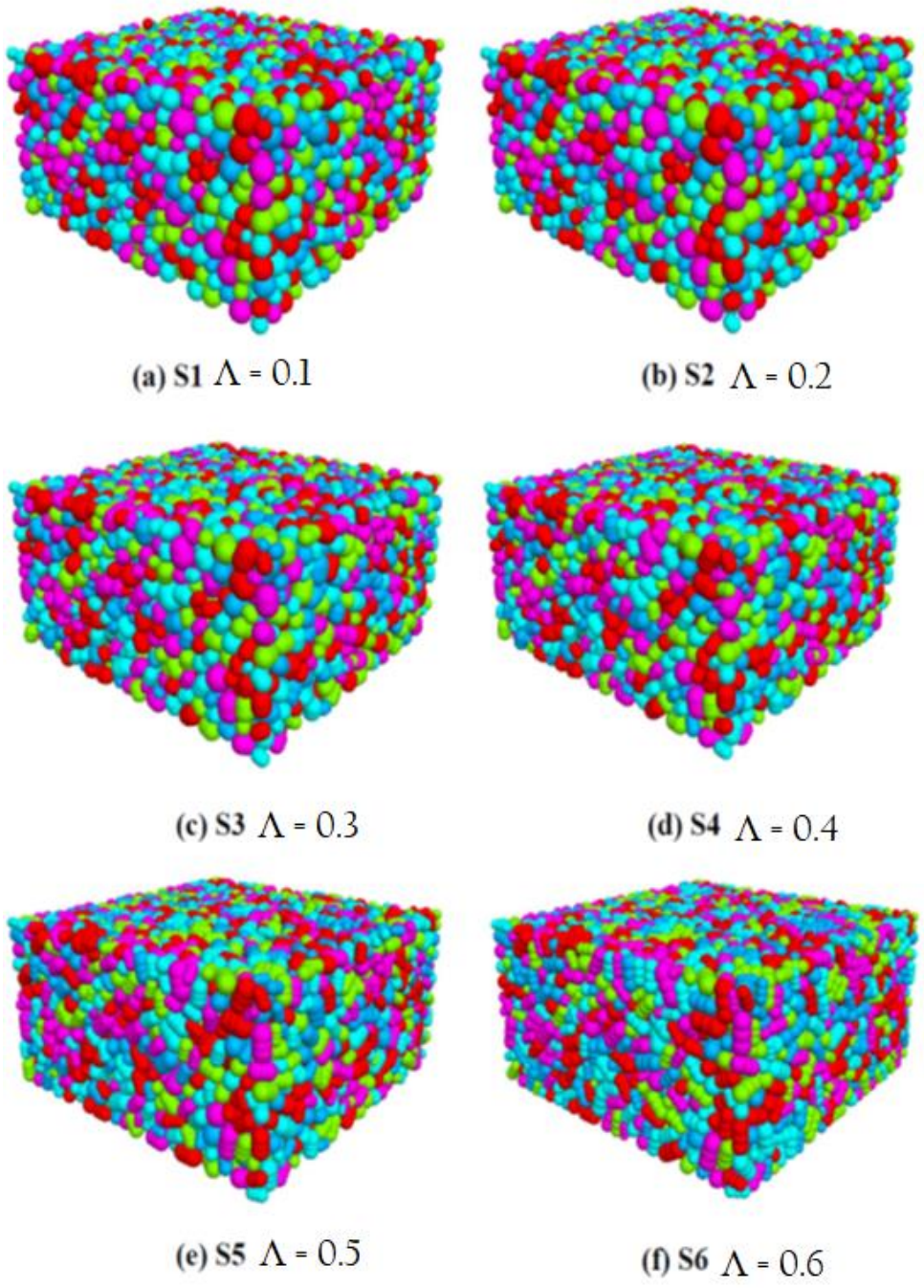

Figure 4.3 The initial states of generated packings with different Λ

(wall are omitted)

4.5 Macroscopic behaviour

All numerical samples are sheared to a maximum shear strain (γ_{xz}) of 30%, which are expected to reach the critical state. It should be stated that the average stresses are obtained directly from the wall forces instead of each contact (e.g., Thornton & Zhang 2003; Thornton 2015). Figure 4.4 presents the influence of Λ on the direct shear behaviour of samples one-dimensionally compressed at σ_n = 200 kPa. It is found that all samples exhibit an initial strain-hardening and post-peak softening behaviour, then eventually attaining a critical value at maximum shear strain, manifested by no further changes in both the stress ratio and vertical strains. Also, the evolution of vertical strain against shear strain (γ_{xz}) (see Figure 4.5) shows a dilative response in all the samples.

The influence of Λ on the direct shear friction angles at peak state (ϕ_p) and critical state (ϕ_c), respectively are presented in Figure 4.6. The error bars in Figure 4.6 indicates the standard deviation of direct shear friction angles at the critical state. Moreover, the values of ϕ_p initially increases, i.e., attaining an extreme value at Λ = 0.2 and stays stable as Λ increases. It was mentioned by Azema & Radjai (2010) that ϕ_c monotonically increases with Λ (for biaxial simulations), while Ng (2009) mentioned that ϕ_c monotonically decreases with increasing aspect ratios (for triaxial simulations) using ellipsoids. The results from this study supported the former one. These differences may be attributed to the surface textures and resultant interaction mechanisms between the particles during shear.

Figure 4.7 presents the influence of normal stress on the shear behaviour of granular material (for the sample S3). Interestingly, it is found that after ~25% of shear strain, independent of the applied normal stresses, all samples reach the critical state with a unique value of normalized stress ratio (i.e., $\tau / \sigma = 0.51$), which is obtained from the slopes of linear fitting by plotting

the shear stress against the normal stress at the critical state. However, the peaks are slightly varied owing to the inhibited rotations of particles which are highly compressed during the one-dimensional compression with the applied incremental normal stresses. These results are generally in agreement with the physical experiments conducted by Charles & Watts (1980) and numerical simulations performed by Abedi & Mirgasemi (2011).

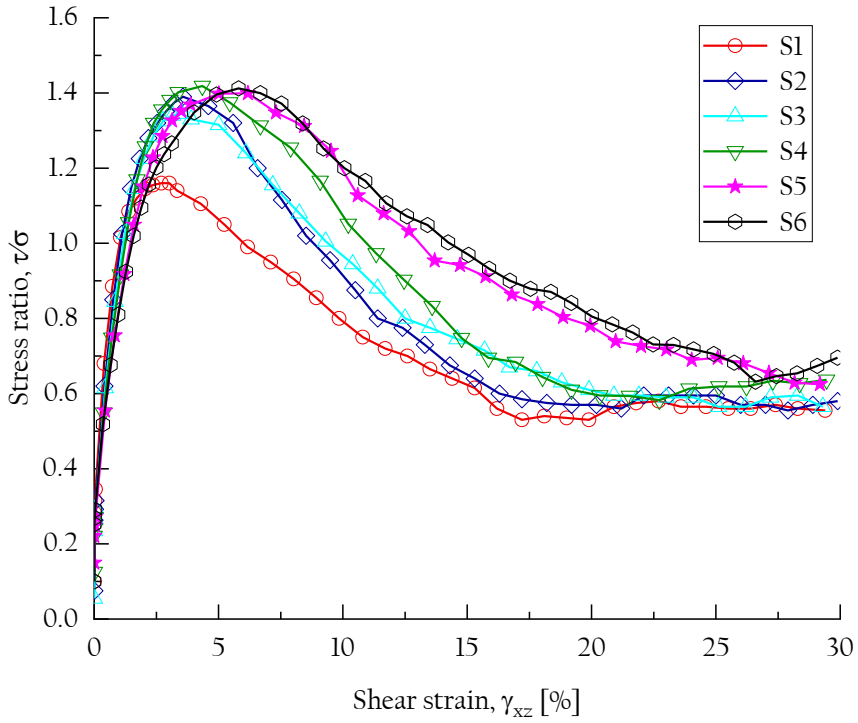

Figure 4.4 Stress ratio against shear strain for different samples

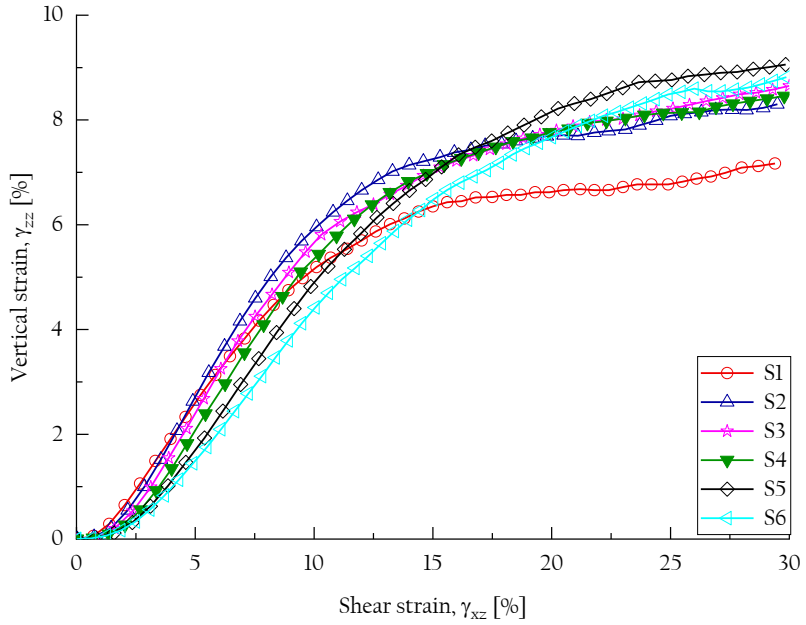

Figure 4.5 Vertical strain against shear strain for different samples

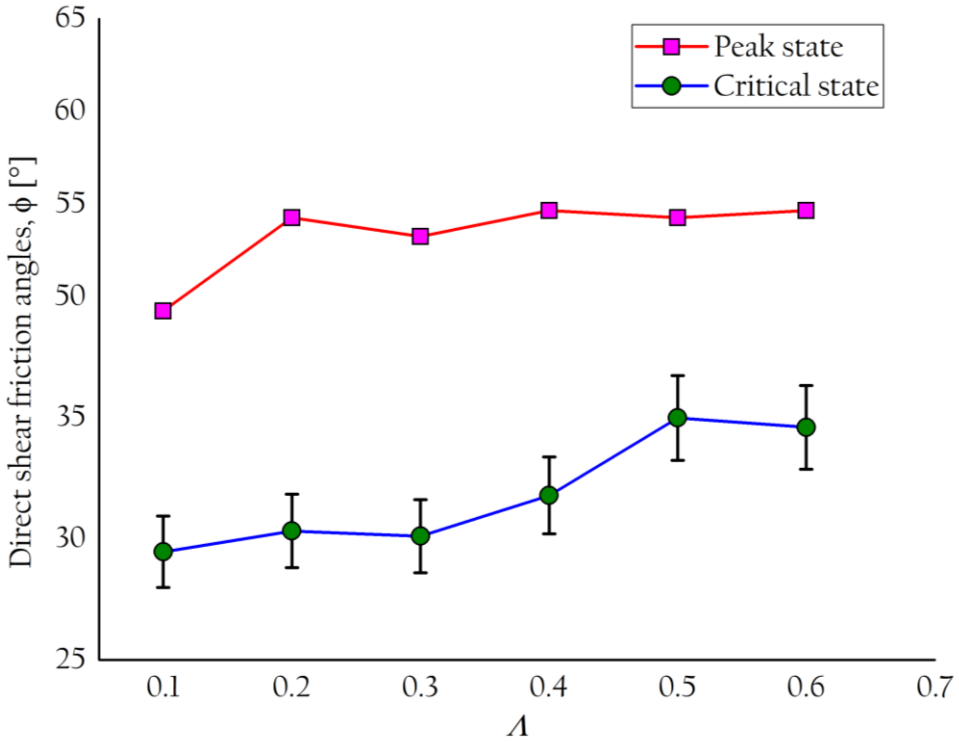

Figure 4.6 Influence of Λ on the peak and critical state friction angles

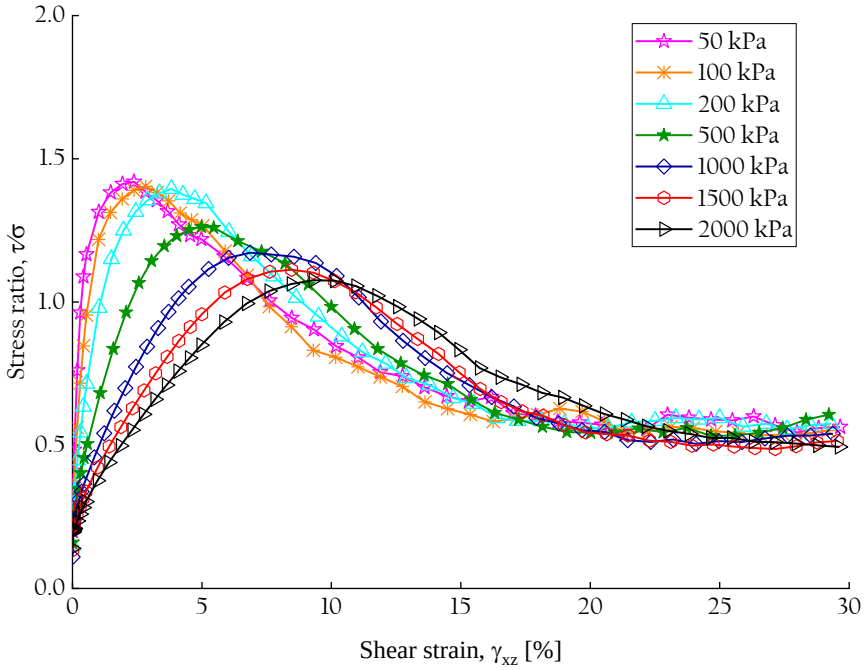

Figure 4.7 Influence of normal stresses on the shear behaviour of granular assembly (sample S3)

4.6 Evolution of fabric anisotropy and microscopic behaviour

The evolution of CN against shear strain (γ_{xz}) for samples one-dimensionally compressed at σ_n = 200 kPa are presented in Figure 4.8. The basic formulation and the description of the CN are presented in Section 2.5.1. It is observed that CN decreases quickly at the onset and slowly attains almost steady value at the critical state. This rapid decrement of onset CN may be due to the sudden transformation of the state of the assembly in addition to the contribution of volume increase as a result of dilatancy. Except for sample S1, there seems no big variation is found with increasing Λ.

Figure 4.9 shows the evolution of deviator fabric ϕ_d against shear strain for all the numerical samples. The description of deviator fabric is furnished in Section 2.5.2. For large strains, the trends in Figure 4.9 is generally comparable to that observed in Figure 4.4, whereas for small strains, the deviator fabric is governed by the volume change and it agrees with that for the volume change showed in

Figure 4.5. It can also be understood that for small strains, the deviator fabric depends on both the stress and volume change, whereas for large strains, the volume approaches to a steady value and the deviator fabric mainly depends on the stress only.

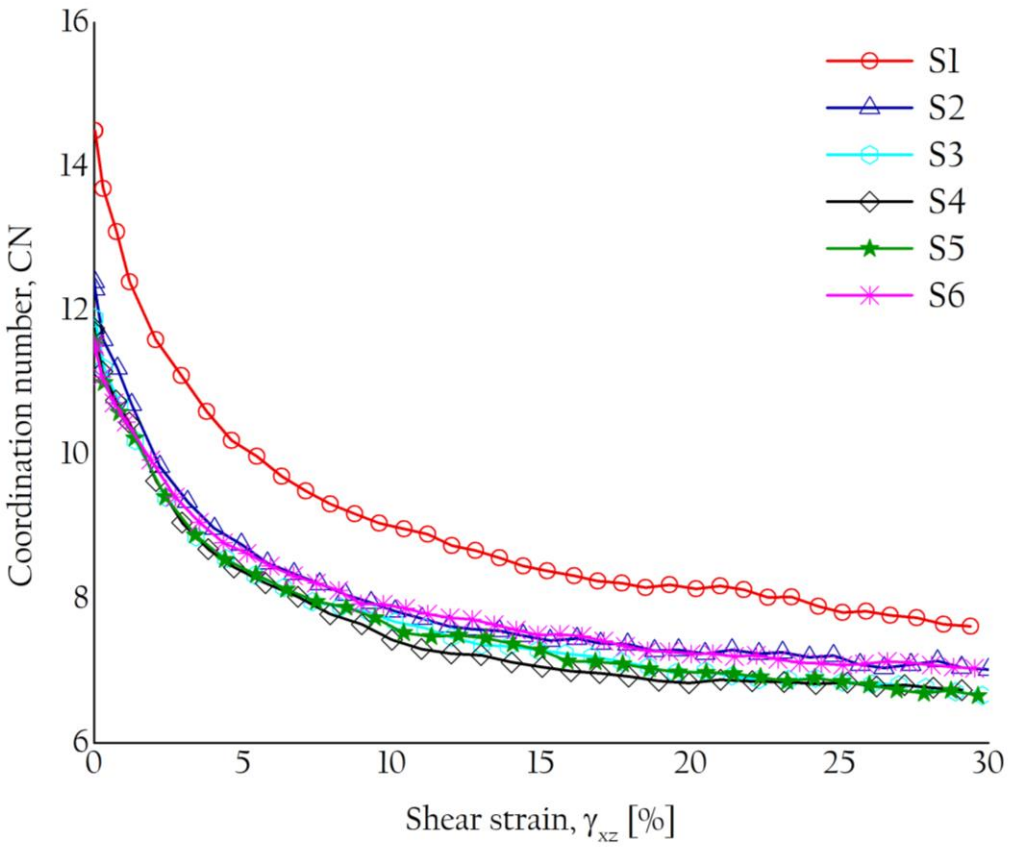

Figure 4.8 Influence of Λ on the CN

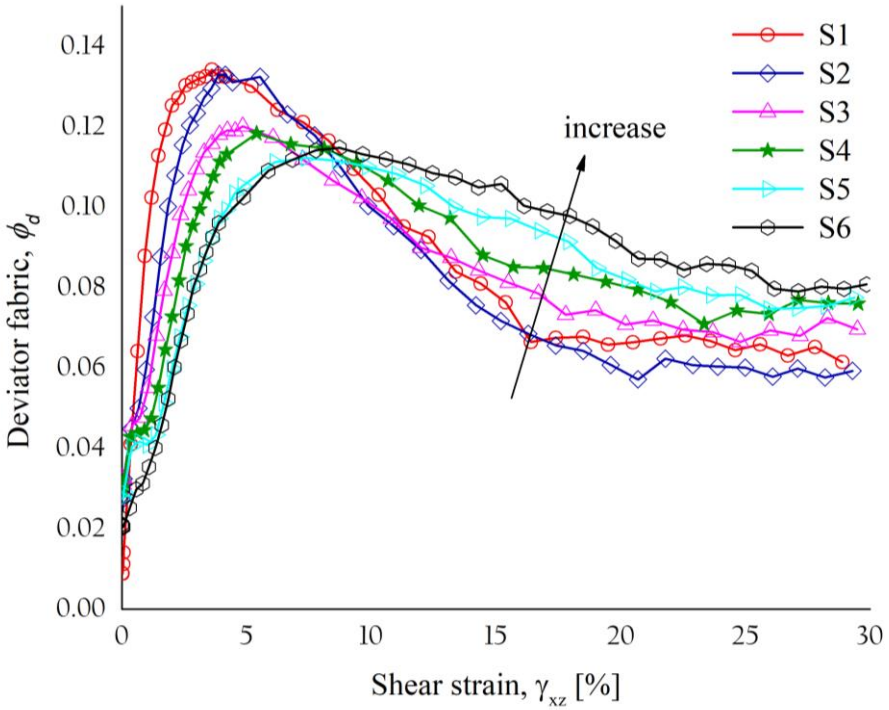

Figure 4.9 Influence of Λ on the deviator fabric

The evolution of principal fabrics for strong force subnetworks (ϕ_1^s and ϕ_3^s) and weak force subnetworks (ϕ_1^w and ϕ_3^w) are presented correspondingly in Figure 4.10 and Figure 4.11. The description of the subnetworks is presented in Section 2.5.3. It is observed that the strong subnetwork becomes highly anisotropic (see Figure 4.10) and the ϕ_1^s shows a similar trend as seen in Figure 4.4. Moreover, there is a stiffer response as Λ increases for ϕ_1^s and the peak principal values of the strong fabric tensor occur at the same range of shear strain (i.e., about 3.5%). The weak force subnetwork (ϕ_i^w) also exhibits anisotropy during the entire shearing process (see Figure 4.11), but with a smaller in magnitude as compared with the strong force subnetwork shown in Figure 4.10. It is also noted from Figure 4.11 that there is no obvious variation of ϕ_1^w as Λ increases. The trends of strong force sub-network (major principal value)(see Figure 4.10), are similar to the evolutions of stress ratios given in Figure 4.4, which describes the major contribution to the stress-fabric relationship which is

mainly governed by the strong force components. The trends of the weak force sub-network are, however, very different from the evolutions of the stress ratio.

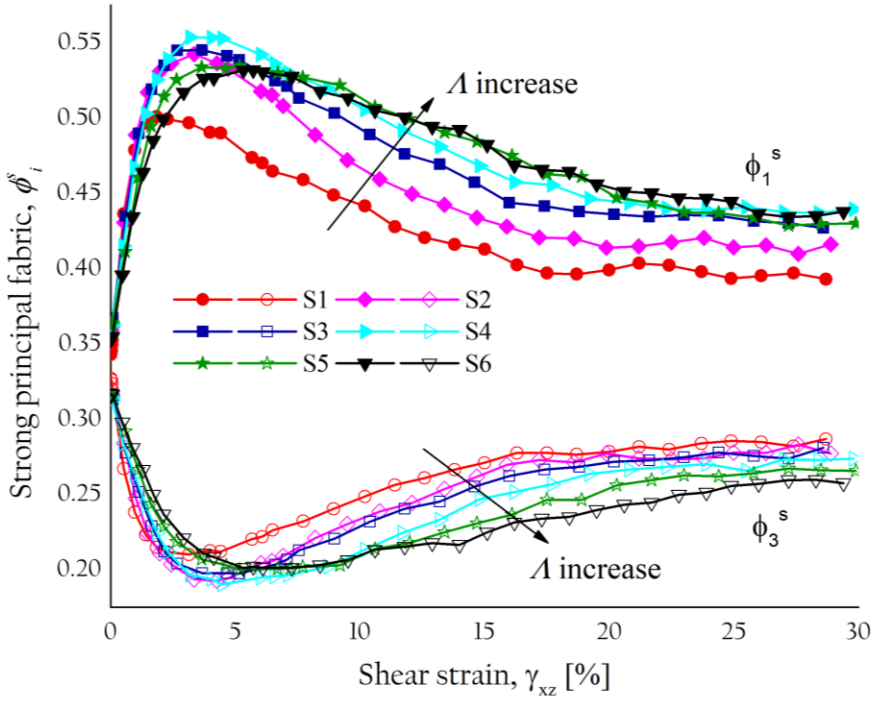

Figure 4.10 Influence of major and minor principal fabrics in the strong subnetwork

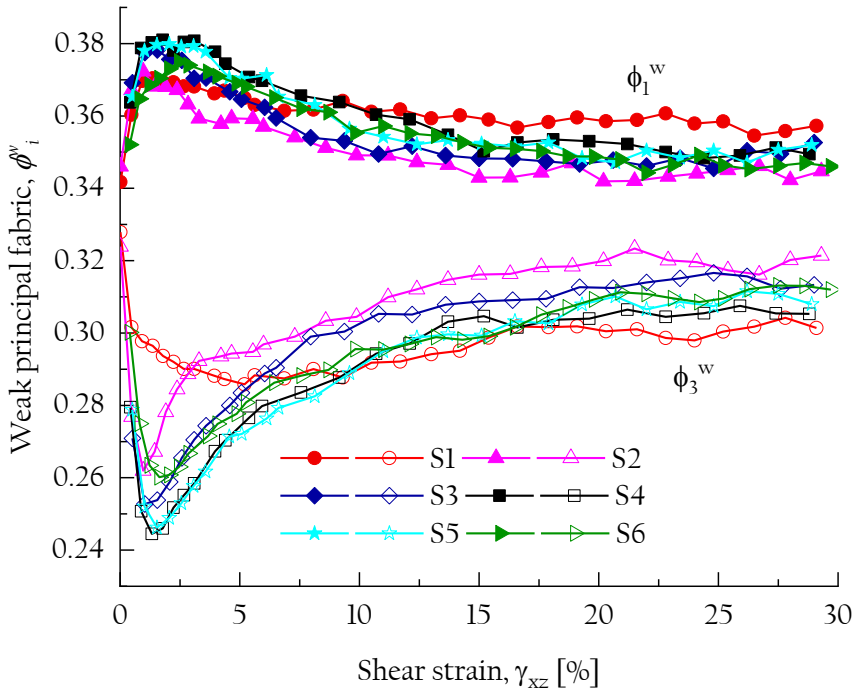

Figure 4.11 Influence of major and minor principal fabrics in the weak subnetwork

4.7 Distribution of force chain networks

In the force chain system, each force is characterized by a colour line fragment joining the particles which are in contact, and the line is proportional to the magnitude of the contact normal forces. Figure 4.12 presents the distribution of contact normal force chain network along XZ-plane at different strains. For a better comparison, samples S1 and S6 are taken into account. Comparing these two specimens, the sample S6 has greater force in magnitudes than those of sample S1 at the same shear strain. It was mentioned by Zhao & Zhou (2017) that the contact normal forces contribute significantly more to the shear strength than contact tangential (shear) forces in the assembly. This indicates that the sample S6 is expected to have a higher shear strength than that of the sample S1, which is in agreement with the trend as seen in Figure 4.4.

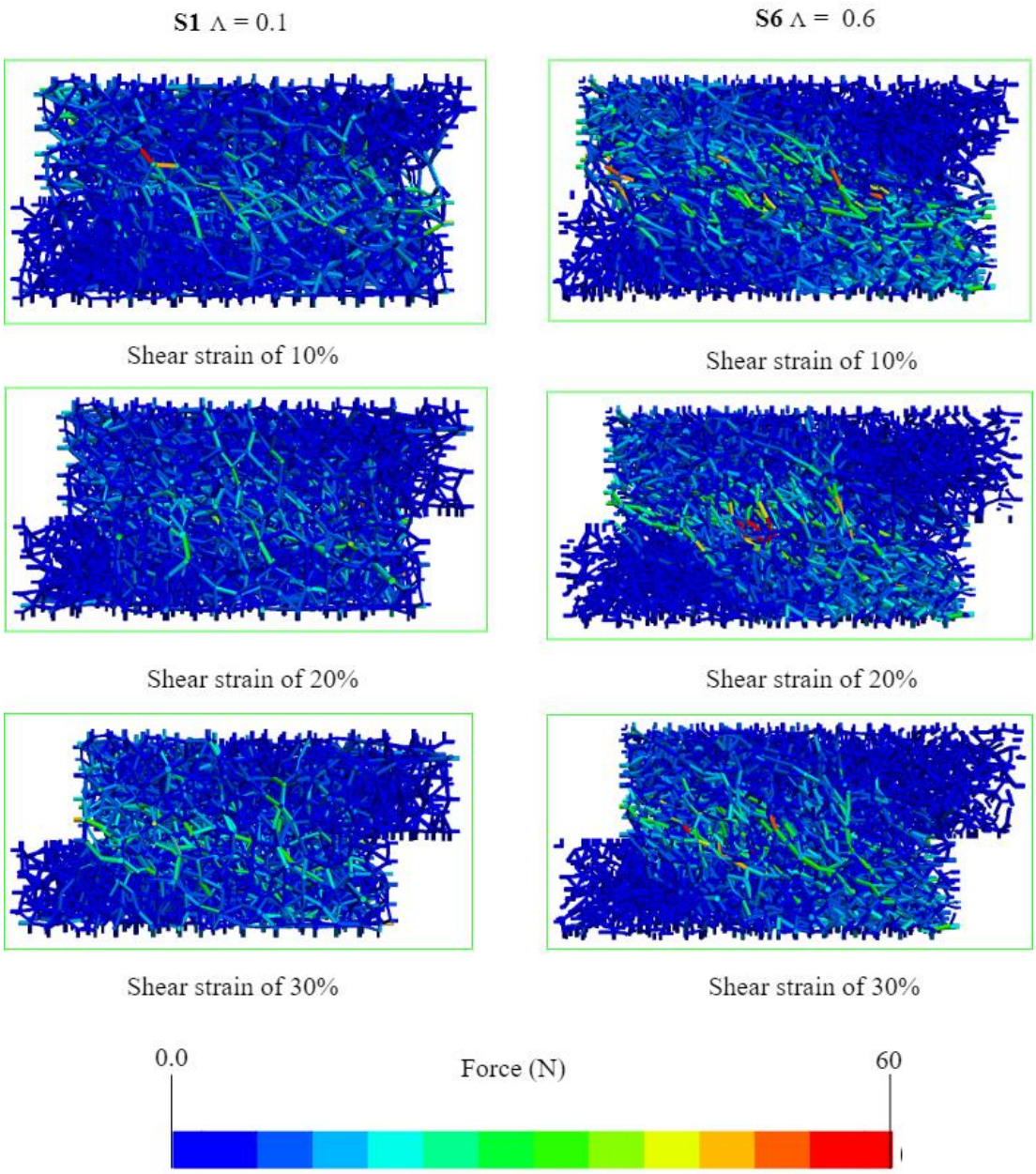

Figure 4.12 Distribution of contact force chain networks along XZ-plane

4.8 Stress- dilatancy relationship

Simony & Houlsby (2006) mentioned that the horizontal plane in the direct shear test is presumed to be a zero extension line, the angle of dilation, Ψ can be derived from Mohr's circle of strain increments, which is given as:

$$\tan(\Psi) = -d\varepsilon_{zz} / d\gamma_{xz} = dv / du \qquad (4.2)$$

where ε_{zz} and γ_{xz} are the vertical strain and shear strain, respectively. The vertical deformation (v) and the shear displacement (u) can be used to evaluate the rate of dilation (dv/du). Figure 4.13 shows the angle of dilation against shear strain for the samples one-dimensionally compressed at σ_n = 200 kPa. In all samples, Ψ originates from zero reaches a peak value (Ψ_p) and slowly decreases to the critical value with fluctuations lesser than 5°.

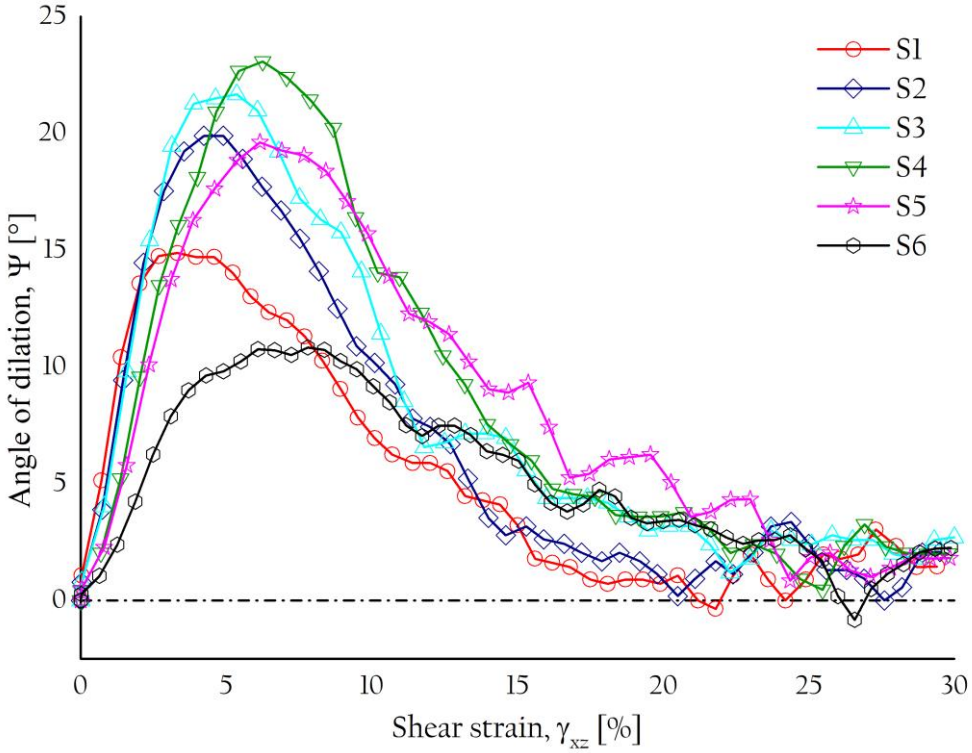

Figure 4.13 Angle of dilation against the shear strain

To explore the relationship between the peak angle of dilation, Ψ_p and peak angle of internal friction, ϕ_p, Bolton (1986) has simplified the Rowe's (1969) stress-dilatancy relationship which is given as:

$$\phi_p = \phi_c + k\Psi_p \tag{4.3}$$

where k is the fitting parameter. An attempt has been made in this investigation to see how best these parameters are in relationship with each other. A relationship between $\phi_p - \phi_c$ and Ψ_p is shown in Figure 4.14. Moreover, the literary data points from various researchers are superimposed (Bolton 1986; Guo & Su 2007 (angular & rounded sand); Gong & Liu 2017; Gong *et al*. 2019). The data from this study is well-fitted (R^2 = 0.96) by the following mathematical expression:

$$\phi_p = \phi_c + 1.182 \pm 0.09 \Psi_p \tag{4.4}$$

It is observed that the k obtained in this study is higher than those reported in the literature. According to Gong & Liu (2017), the value of k for 2D elongated planar particles is smaller than those of 3D multi-sphere ellipsoids. It is also mentioned by Rothenburg & Bathurst (1992) that this variation could be attributed to the planar nature of the 2D granular assembly.

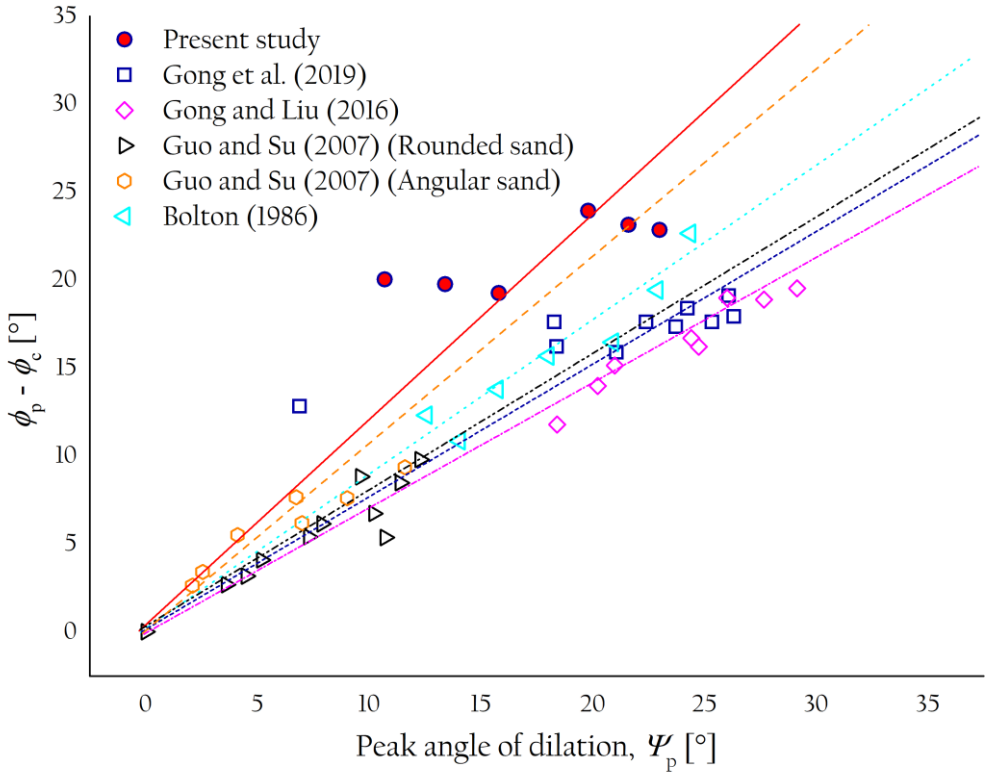

Figure 4.14 Relationship between $\phi_p - \phi_c$ and Ψ_p

4.9 Critical State Soil Mechanics (CSSM) framework

The critical state is a reference state and its uniqueness has evoked increasing debate for many years. However, reaching the critical state in physical shear tests is a difficult task. It is a fact that due to highly non-uniform deformation in the specimen, very limited attention has been given to the critical state properties of granular materials in the direct shear tests.

A pioneer work by Casagrande (1936) is to describe a popular state for sands at which prevention of volume change leads to no further strength. Later, a unified approach by Roscoe *et al.* (1958) to form the concept of a unique critical void ratio line in the $e - p' - q$ space considering the behaviour of Weald clay. This key concept formed as the cornerstone for the framework of the critical state soil mechanics (CSSM) (Schofield & Wroth 1968). The position of the critical state line (CSL) is a unique representation of granular materials.

A methodology to linearize the CSL in the $e-\left(p'/p_a\right)^{\varsigma}$ space for sand, which is given as:

$$e_c = e_\Gamma - \lambda_c \left(p'/p_a\right)^{\varsigma} \tag{4.5}$$

where p_a is the atmospheric pressure (=101.325 kPa), which is used for normalization, e_Γ is the intercept on the x-axis (i.e., critical state void ratio, e_c), λ_c is the slope of CSL, and ς is a material constant parameter (i.e., taken as $\varsigma = 0.7$, which is a typical value for Toyoura sand (Li & Wang 1998)). Figure 4.15 shows the CSLs fitted by Eq. (4.5) for the samples considered. The CSL parameters for each sample indicating almost parallel and a minor slope ranging between -0.011 and -0.021 is noticed. This variation could be attributed to the deviation in the particle geometric shape (Xie *et al.* 2017 and Jiang *et al.* 2018). Also, it is observed that as particles elongate, the downward shifting of CSL is noticed and the intercept values are slightly increased initially and then decreases to the minimum value.

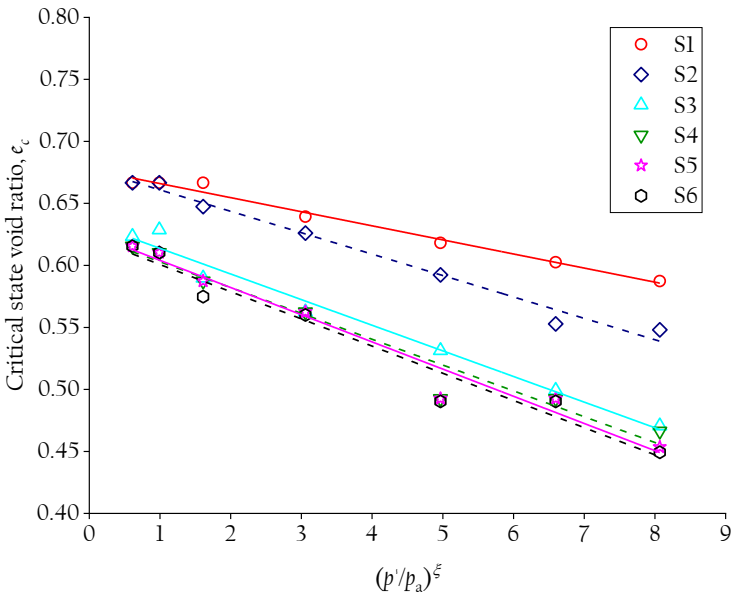

Figure 4.15 Critical state lines in the $e-\left(p'/p_a\right)^{\varsigma}$ space for all samples

The two critical state parameters, i.e., the slope of the critical state line (λ_c) and the intercept of critical state lines on the y-axis (e_Γ) are correlated against Λ as shown in Figure 4.16 and Figure 4.17, respectively. Both critical state parameters are well-fitted by a unique second-order polynomial function with accepted regression value. The developed mathematical expressions can be seen at the inset of the plots.

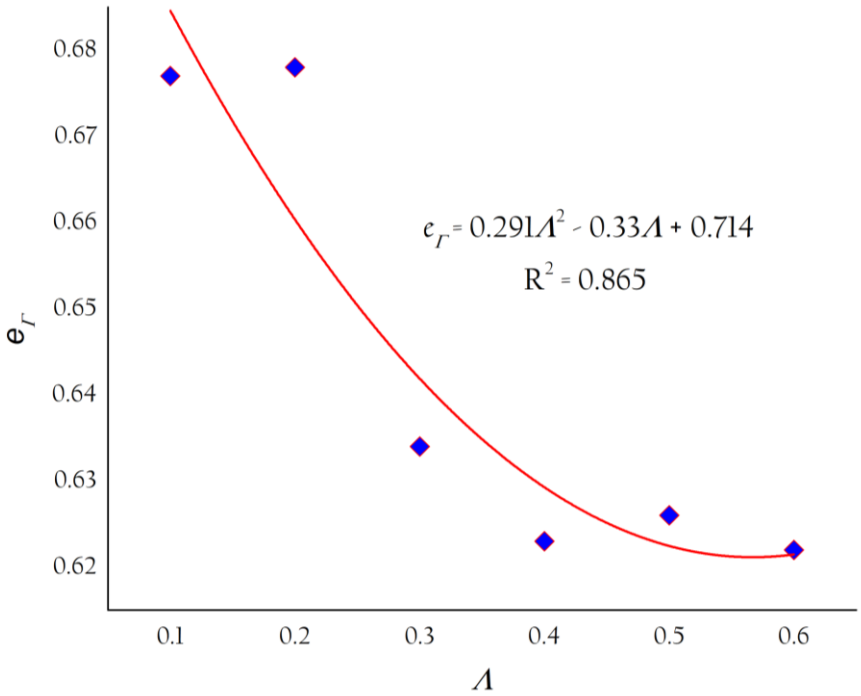

Figure 4.16 Correlation between e_Γ against Λ

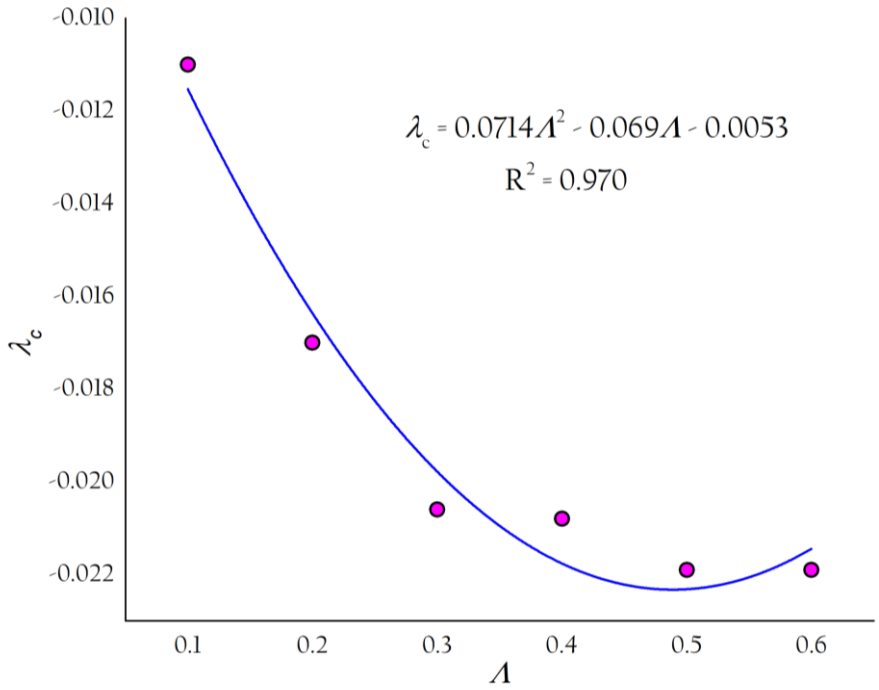

Figure 4.17 Correlation between λ_c against Λ

4.10 Summary

This chapter has presented the results of three-dimensional DEM-based analysis of how elongated particles influence the mechanical behaviour of granular assemblies under direct shear test conditions. The stress-strain response of elongated particles exhibits an initial strain - hardening followed by post-peak softening behaviour, and thereafter eventually attained a critical state. The peak state direct shear friction angles initially increase and stay stable as Λ increases, whereas the critical state direct shear friction angles increase with the increase of Λ. It was also observed that independent of the applied normal stresses, all samples reached critical state at a unique normalized stress ratio at the large shear strain.

The stress-fabric relationship was found to be mainly governed by the strong force subnetwork. The strong force subnetwork is more affected by the change of Λ than the weak force subnetwork. The behaviour of ϕ_p concerning to Λ depends on the mutual influence of ϕ_c and Ψ_c. As particle elongates, the

downward shifting of CSLs was noticed. The correlation between the critical state parameters and particle elongations were well-fitted by a unique second-order polynomial function with acceptable regression value.

Chapter 5 Influence of particle elongations on triaxial behaviour

5.1 Introduction

The complexity in granular soils originates from particulate nature and the key characteristics include particle size, gradation analysis, particle shape and mineralogy. Among the various grain-scale characteristics, particle size and gradation analysis can be routinely used in the soil mechanics. In the past decade, the influence on these characteristics has received relatively more attention rather than the particle shape due to the difficulties involved in quantifying the grain shape characteristics. An accurate evolution of the particle shape may not be required and the information on particle shape is usually provided in qualitative terms using routinely used approach proposed by Krumbein & Sloss (1963). The chart was arranged as a 4×5 matrix of 2D images of standard particles. In each row, five particles with the same sphericity but different values of roundness and each column includes four particles with the same roundness but different values of sphericity. For a given particle, roundness and sphericity values are assessed by visual comparison with the reference particle shapes in the chart. In general, this approach is tedious and the accuracy in predicting the shape characteristics may not be high. Thus, to improve the accuracy, one can choose to evaluate the roundness of the particle from the measurements on the particle image suggested by Wadell (1932) method. However, the direct measurements remain time-consuming and may need sophisticated instrumentation for obtaining accurate results.

In this chapter, a general introduction is presented in Section 5.1 and relevant review of the literature is presented in Section 5.2. The basic definitions for the particle shape characteristics are presented in Section 5.3. In Section 5.4,

simulation details and input parameters are presented. In Sections 5.5 and 5.6, the evolution of macroscopic and microscopic behaviours are discussed. In Section 5.7, relationships between critical state parameters and shape parameters are presented. In the end, in Section 5.8, a summary of the overall chapter is provided.

5.2 Review of literature

The relationship between critical state and particle shape of the mechanics of granular materials was explored by Yang & Luo (2015). They used spherical glass beads and crushed angular glass beads of different percentages mixed with a uniform quartz sand (Fujian sand). The mixtures of Fujian sand and spherical glass beads were deemed to be markedly more susceptible to liquefaction than the mixtures of Fujian sand and crushed angular glass beads. The geometry of particle was measured using a laser scanning technique and was characterized by aspect ratio, sphericity and convexity. Considering these three shape parameters, a new shape index, i.e., overall regularity was proposed. Moreover, it was noticed that the change in liquefaction susceptibility was shown to be consistent with the change in the position of the critical state locus (CSL) in the compression space. This was manifested by a decrease in the intercept and gradient of the CSL due to the presence of spherical glass beads.

The effect of particle shape on the strength, dilatancy, and stress-dilatancy relationship through a series of drained triaxial compression tests on sands mixed with angular and rounded glass beads of different proportions (0%, 25%, 50%, 75%, and 100%) were studied by Xiao *et al.* (2019). The overall regularity was maintained from 0.844 to 0.971 to define the particle shape of these mixtures. It was found from the results that at an initial relative density of 0.6, all samples exhibit strain-softening and volume-expansion behaviour. The peak-state deviatoric stress, peak-state axial strain, and peak-state friction angle at a given confining pressure decreased with increasing overall regularity.

Due to the changes in the particle shape, the maximum differences in the peak-state deviator stress, peak-state axial strain, peak-state friction angle, excess friction angle, and maximum dilation angle could be as much as 0.61 MPa, 5.4%, 8.6, 1.5, and 3° at a given confining pressure of 0.4 MPa, respectively. It was also found that the slope of the relationship between the peak-state friction angle and maximum dilation angle was independent of the particle shape, whereas the intercept (i.e., the critical state friction angle) was significantly influenced by the particle shape.

The influence of grading on the undrained behaviour of granular materials was explored by Liu *et al.* (2014). The authors considered two different materials, i.e., glass balls and Hostun sand. For each material, samples with different grading's and similar relative densities were prepared. The experimental results confirm that the undrained shear strength decreases when the coefficient of uniformity increases from 1.1 to 20. The results demonstrate a significant influence of the grading, i.e., increasing the coefficient of uniformity heightens the potential of static liquefaction, and the materials become more unstable. Moreover, the DEM simulation results show similar behaviours as compared to the experimental tests and confirmed the influence of the grain size distribution on the stress-strain relationship and instability phenomena.

The influence of particle characteristics on the index void ratios of granular materials was explored by Sarkar *et al.* (2019). The effects of particle and specific gravity characteristics such as shape, size, and specific gravity on the limiting void ratios e_{max} and e_{min} of the granular matter were investigated. To assess the effect of specific gravity, two different types of materials, i.e., glass beads and natural sands were considered. Particle characteristics such as roundness, sphericity and regularity, the average of roundness and sphericity, were calculated through image analysis techniques after obtaining high-quality microscopic images of individual grains. The German DIN standards were

strictly followed to determine the extremities of the void ratio. Experimental data were used to investigate the effects of the particle characteristics on the relative density of soils. The results show the significant effect of the mean grain size (D_{50}) on the extreme void ratios of poorly graded glass as well as the significant effect of C_u but the negligible effect of D_{50} on the extreme void ratios of sand.

Gong & Liu (2017) explored the effect of aspect ratio on triaxial compression of multi-sphere ellipsoid assemblies simulated using DEM. The authors found that the stress–dilatancy relationship of ellipsoids with different aspect ratios were expressed as a linear function. In particular, the aspect ratio influenced the position of the critical state lines for these assemblies. Particle-scale characteristics at the critical state indicate that particles tend to be flat lying, and the obstruction of particle rotation that occurs with longer particles affects their contact mechanics.

Fu *et al.* (2012) studied the effect of particle shape and size on flow properties of lactose powders. The influence of particle shape/size of three different lactose powders on their respective flow and bulk characteristics were explored. Two of the samples differ in size but have similar shapes; the third sample was more spherical but similar in size to one of the other two samples. In addition to particle size, particle shape significantly affect the flow characteristics of powder over a wide range of stress conditions.

Shinohara *et al.* (2000) explored the effect of particle shape on the angle of internal friction was investigated by the triaxial compression test. The angular stainless steel powder was processed toward increasing sphericity by a rotational impact-type surface modification apparatus. The angle of internal friction was found to increase with the increasing angularity of particles and

decreasing initial voidage of the specimen owing to increase in the interlocking effect.

Zhao & Zhou (2017) investigated the effects of particle asphericity on the macro and micro-mechanical behaviours of granular assemblies. They proposed a shape descriptor, i.e., asphericity, to isolate the effect of aspect ratio and angularity. It was found that particle asphericity can enhance the particle-particle inter-locking with higher locked-in forces, showing an increasing proportion of sliding contacts, thereby making a granular assembly stiffer and stronger. Also, weak contacts have a dominant proportion in the overall contact networks, positively correlated with asphericity. However, asphericity has an insignificant effect on the mean coordination number at the critical state. Furthermore, it was found that anisotropy of granular fabric is strongly determined by anisotropy sources in strong contact networks, where a larger asphericity results in a more anisotropic granular fabric.

Xie *et al.* (2017) investigated the influence of particle geometry and the intermediate stress ratio, $b=(\sigma_2-\sigma_3)/(\sigma_1-\sigma_3)$ on the shear behaviour of granular materials. They investigated samples with different particle aspect ratios and a unique particle size distribution (PSD). At the macroscopic level, the shear strength decreases with an increase in both aspect ratio and b values, whereas at the microscopic level, the fabric evolution was also affected by both aspect ratio and b. The results from DEM analyses qualitatively agree with the available experimental data. The position of the critical state loci in the compression ($e-p'$) space is slightly affected by aspect ratio while the critical stress ratio is dependent on both aspect ratio and b. Moreover, it was understood that for a given stress path, a unique critical state fabric norm is dependent on the particle shape but is independent of critical state void ratio.

Zhao *et al*. (2017) investigated the particle shape effects on the fabric of granular random packing. A broad range of particle shapes controlled by two shape parameters (i.e., aspect ratio and blockiness) were taken into account. A series of random packing of non-cohesive, frictional monodisperse superellipsoids was conducted under gravitational forces in the simulations. The effects of particle shape on packing density and mean coordination number was in agreement with the reported literature. The distribution of particle orientations was much more sensitive to blockiness than aspect ratio. The anisotropy of both particle orientations and contact normals shows a similar M-type relationship with aspect ratio, two times larger than that of branch vectors. Interestingly, the particle shape has an insignificant effect on the probability distribution of normalized contact forces which shows a clear exponential distribution.

Ng (2009) investigated the particle shape effect on macro- and micro-behaviours of monodisperse ellipsoids. The evolution of three vector-typed micromechanical arguments with strain including the particle orientation, branch vector, and normal contact force was investigated. The normal contact force (micromechanical argument) was found to have a direct relationship with the principal stress ratio (macroscopic parameter). It was also found that the maximum angle between vectors was related to particle shape, distributions and the maximum values of these angles do not change with loading.

Katagiri *et al*. (2010) explored a simple shear simulation of 3D irregularly shaped particles by image-based DEM. The particle shape was modelled by a cluster of several spherical elements using dynamic optimization method. It was found that the 10-element model can quantitatively reproduce the shear behaviour of relatively-dense specimens, whereas, for loose specimens, the 10-element model was found to be insufficient. This result implies that the overall grain shape that was relevant to the moment transmission between grains is important in

densely-packed granular assembly, while small surface angularity plays a considerable role in the loosely-packed granular assembly.

5.3 Particle shape characteristics

The same approach, i.e., as discussed in Section 4.3, is used for generating elongated particles. In general, particle shapes can be characterized by three key shape parameters, i.e., the aspect ratio (A_R), convexity (C_X) and sphericity (S_W) (Wadell 1932; Krumbein 1941; Powers 1953; Krumbein & Sloss 1963; Barrett 1980). The definitions of these parameters are given as:

- Aspect ratio (A_R): The ratio between minimum Feret diameter ($D^F_{\min}$) and the maximum Feret diameter ($D^F_{\max}$).

$$A_R = \frac{Diameter_{\min.Feret}}{Diameter_{\max.Feret}} = \frac{D^F_{\min}}{D^F_{\max}} \tag{5.1}$$

- Convexity (C_X): The measure of the compactness of a particle. It is the ratio between the particle volume V_p and the volume of the particle's convex hull, V_{CH} . In general, the range of C_X values typically vary between 0 and 1, and mainly depends on the shape of the particle.

$$C_X = \frac{Volume_{particle}}{Volume_{Convex\ hull}} = \frac{V_p}{V_{CH}} \tag{5.2}$$

- Sphericity (S_W): It describes how closely a particle resembles a sphere. According to Wadell (1932), it is the ratio between the surface area of a sphere which is believed to have the same volume and surface area of that particle.

$$S_W = \frac{\pi^{1/3}\left(6V_p\right)^{2/3}}{S_p} \tag{5.3}$$

where V_P and S_P are the volume and surface area of a particle respectively. The range of S_W vary from 0 to 1 $(0 < S_W \leq 1)$ and the value of S_W for a spherical particle equals to 1.

- Overall regularity (O_R): It is considered as the impacts of three particle shape parameters (i.e., A_R, C_X and S_W), which is used for characterizing particle shape in an integrated manner (Yang & Luo 2015).

$$O_R = \frac{\left(A_R + C_X + S_W\right)}{3} \tag{5.4}$$

It should be noted that A_R, C_X, S_W and O_R can only reflect the shape characteristics of a particle but not the whole assembly. The generated elongated particles with different shape parameters are presented in Figure 5.1.

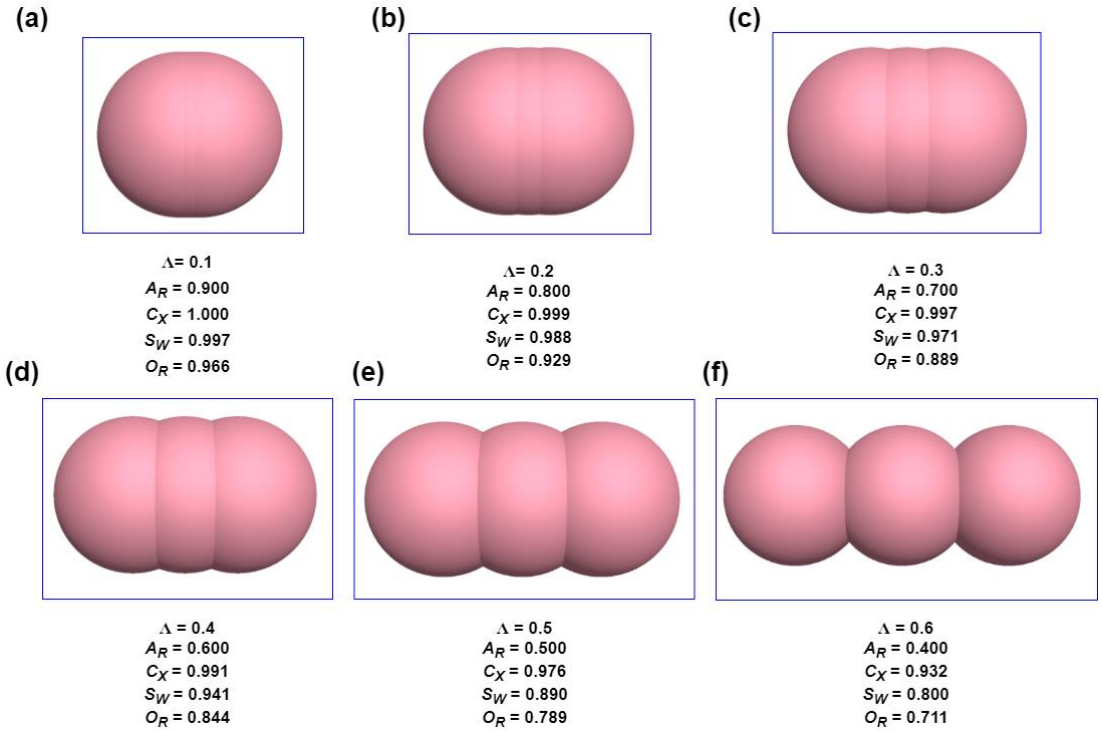

Figure 5.1 Elongated particles with varying shape parameters

5.4 Simulation details

The triaxial test specimen in three-dimensions is modelled using six independent rigid walls formed as a cubic box. The particles are allowed to distribute randomly and there is no gravitational force is applied to the particles. A built-in servo-mechanism is activated to maintain the desired stress levels within the assembly during isotropic compression. While shearing the sample, both the top and bottom walls are permitted to move towards each other at a constant loading strain rate which is sufficiently small enough to ensure the quasi-static conditions, whereas the remaining walls hold the same confining pressure using a stress-controlled servo mechanism (Zhao & Zhao 2019). To investigate the particle elongation effects, all samples generated at their densest state by imposing a zero interparticle friction coefficient during the sample preparation stage. The input parameters used here are the same as those used in the previous chapter (see Section 4.4).

5.5 Macroscopic behaviour

The axial strain ε_1 and volumetric strain ε_v can be obtained from the displacements of the rigid walls (boundaries), as:

$$\varepsilon_1 = -\int_{H_0}^{H} \frac{\mathrm{d}h}{h} = \ln\left(\frac{H_0}{H}\right) \tag{5.5}$$

$$\varepsilon_v = -\left(\varepsilon_1 + \varepsilon_2 + \varepsilon_3\right) = \int_{V_0}^{V} \frac{\mathrm{d}v}{v} = \ln\left(\frac{V}{V_0}\right) \tag{5.6}$$

where H and V are the height and volume of the specimen at the current time, respectively, H_0 and V_0 are their initial values at the onset of shear. Similarly, the strains ε_2 and ε_3, in x and y - directions can be obtained accordingly.

It should be mentioned that all samples are isotropically compressed at 200 kPa. Figure 5.2 shows the evolution of stress ratio (q/p) against axial strain for different values of Λ. It is observed that all specimens deemed to exhibit similar behaviour, i.e., post-peak strain-softening, which is obvious in the dense granular assemblies. The stress ratio flattens off and tends to follow a steady-state after an axial strain of 40%. According to Schofield & Wroth (1968), this state is believed to have reached a critical state.

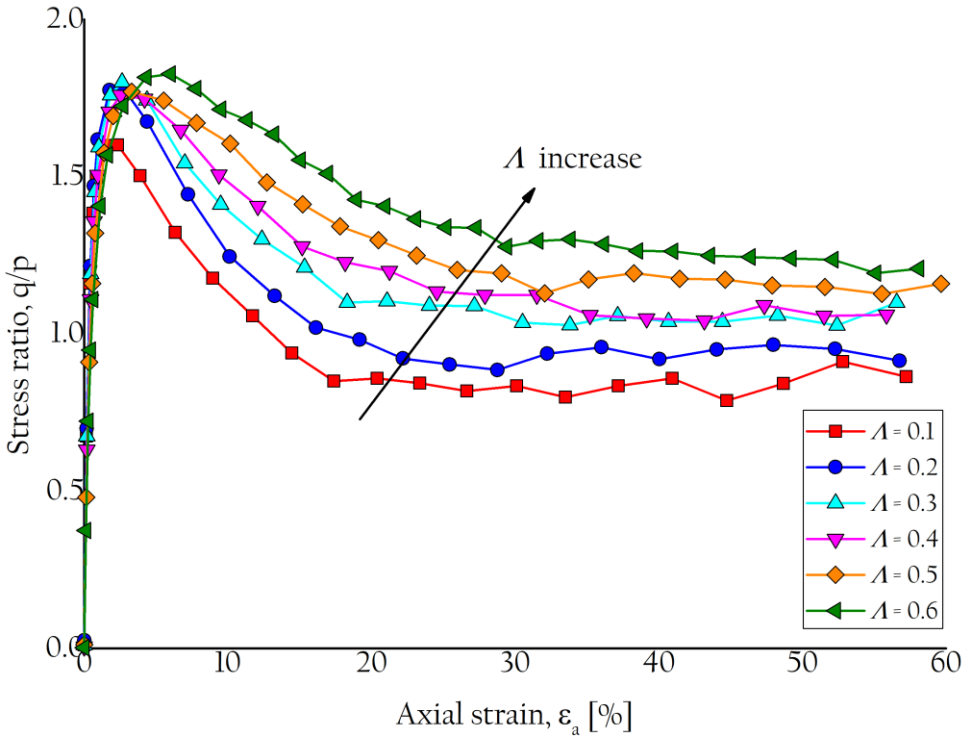

Figure 5.2 Stress ratio against axial strain for different Λ

In the triaxial shear test, the mobilised shear strength of granular assembly can be represented by the angle of internal friction ϕ, which is given as:

$$\phi = \arcsin\left\{\frac{\sigma_1 - \sigma_3}{\sigma_1 + \sigma_3}\right\} = \arcsin\left\{\frac{3q/p'}{q/p' + 6}\right\} \tag{5.7}$$

where σ_1 = major principle effective stress; σ_3 = minor principle effective stress. The influence of Λ on the angle of internal frictions at both peak and critical states is presented in Figure 5.3. The peak state is recognised as the state at which the stress ratio reaches the peak against axial strain, whereas the critical state is considered to be the one at which the granular assembly is continuously sheared under a constant volume and stresses. The error bars represent the standard deviation of the friction angles at the critical state. It is found that the

peak state friction angles reached a peak value at Λ = 0.2 and almost stabilized as a further increase in Λ. According to Gong & Liu (2017), as aspect ratio increases, the value of peak state friction angles exhibited a unimodal peak, whereas the critical state friction angle was monotonically increased. Although the same approach (i.e., MS approach) was used in both the investigations, the variations at both peak and critical state friction angles are noticed. This might be due to different initial conditions and the number of spheres in each clump.

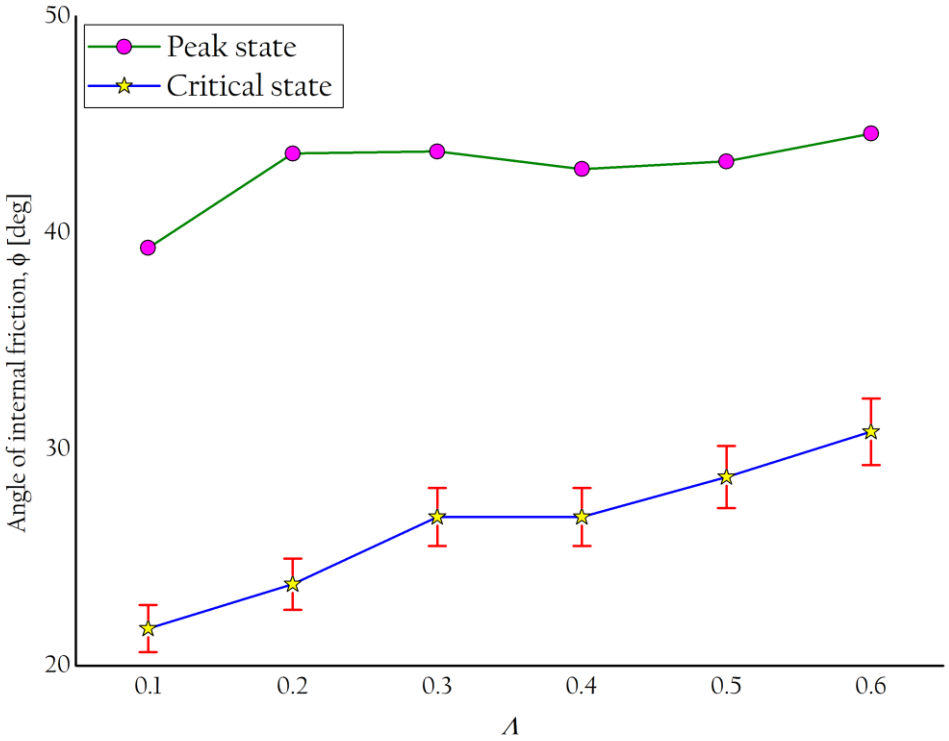

Figure 5.3 Effect of Λ on the angle of internal frictions

Figure 5.4 presents the effect of confining stresses on the triaxial shear behaviour of granular materials for Λ = 0.3. As it is found that all assemblies reach the critical state at the same stress ratio (i.e., $\sim q/p'$ = 1.0), which indicates that the residual shear strength of the assemblies is dependent on the confining stress. However, the peak stress ratio of the assemblies with different confining stresses is slightly varied. These findings are in agreement with the results reported by Gong & Liu (2017) and Kodicherla *et al.* (2019). Furthermore, the

ellipsoids generated using MS approach has multiple contacts resulting in a stronger interlocking, enhancing the shear strength of the granular assembly. In the case of true ellipsoids, the effect of interlocking may be limited because of the smooth surface, consequently lesser shear strength was achieved by Ng (2009).

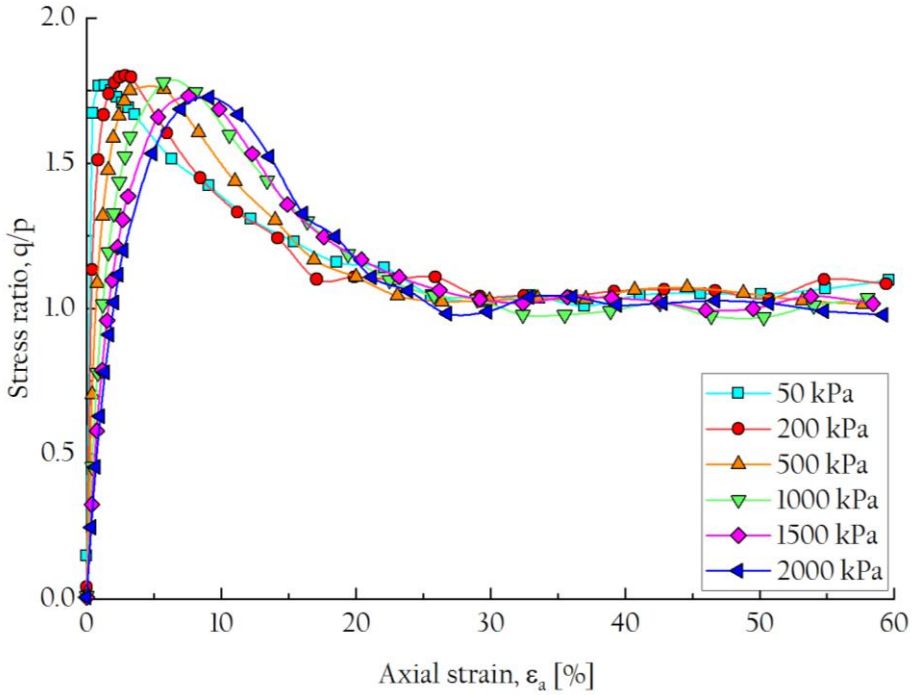

Figure 5.4 Stress ratio against axial strain for different isotropic stresses

Figure 5.5 shows the evolution of volumetric strains and void ratios against axial strain and Λ. The evolution of volumetric strain against axial strain for different Λ values is shown in Figure 5.5(a). It is observed from the figure that all assemblies exhibit initial contraction and continuous dilation until reaching the critical state. Also, it is clearly understood that Λ has a significant impact on the volumetric behaviour of granular assemblies. For instance, the sample for Λ = 0.1 reaches a critical state of about ~ 30% of axial strain, whereas for the case Λ = 0.6, about ~ 45% of axial strain was required to reach the critical state. The void ratio (e) initially decrease up to Λ = 0.3 but increase further with the

increase in Λ (see Figure 5.5(b)). This observation is somewhat different from the behaviour of granular materials obtained using the multi-sphere (MS) approach by Gong & Liu (2017). It may be because the method of particle generation has a noticeable influence on the spatial arrangement and the critical state void ratio (e_c) of granular assemblies. The relationship between the void ratios against Λ at different stages of axial strains in Figure 5.5(c) shows that the values of e reach a minimum value at Λ = 0.4 while increase with the increase in Λ, for different percentages of axial strains.

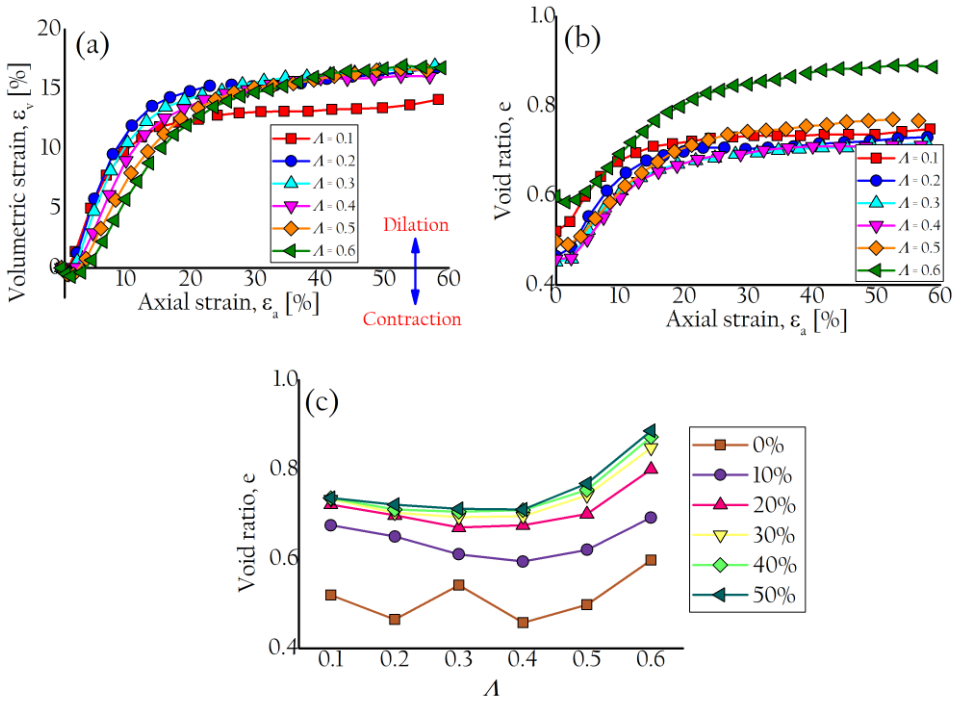

Figure 5.5 (a) Evolution of volumetric strain against axial strain; (b) Evolution of void ratio against axial strain; (c) Relationship between void ratio against Λ at different stages of axial strains

5.6 Microscopic behaviour

5.6.1 Coordination number (CN)

Figure 5.6 presents the evolution of CN against axial strain for different Λ values. It is observed that all samples follow an exponential decay against the axial strain. The inset (see Figure 5.6) shows the initial and steady-state CN of the samples with different Λ values. The onset of CN decreases with increasing Λ, while the steady-state CN is found to increase with the increase in Λ values.

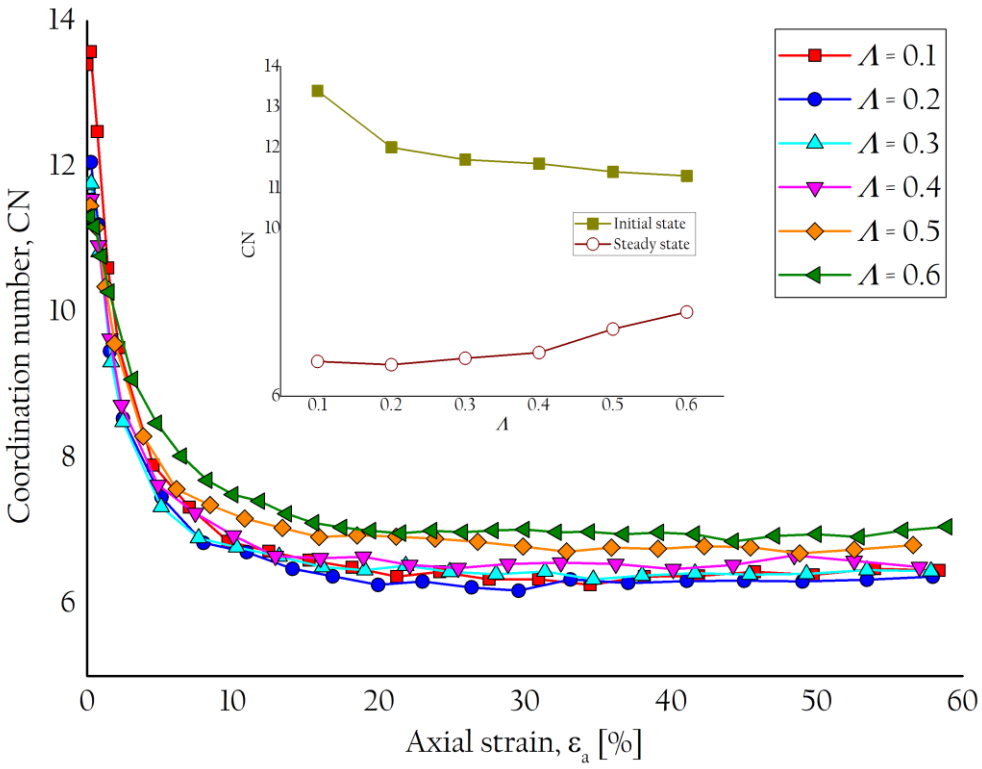

Figure 5.6 CN against axial strain for different Λ

5.6.2 Evolution of deviator fabric

The evolution of deviator fabric against axial strain for different Λ values is shown in Figure 5.7. The trend of ϕ_d follows same as the stress-strain response (see Figure 5.2), which was also reported by Kodicherla *et al.* (2019) that the deviator fabric at small strains mainly depends on both the stress and volume

change, while at large strains the volume approaches a steady value and depend only on the stress.

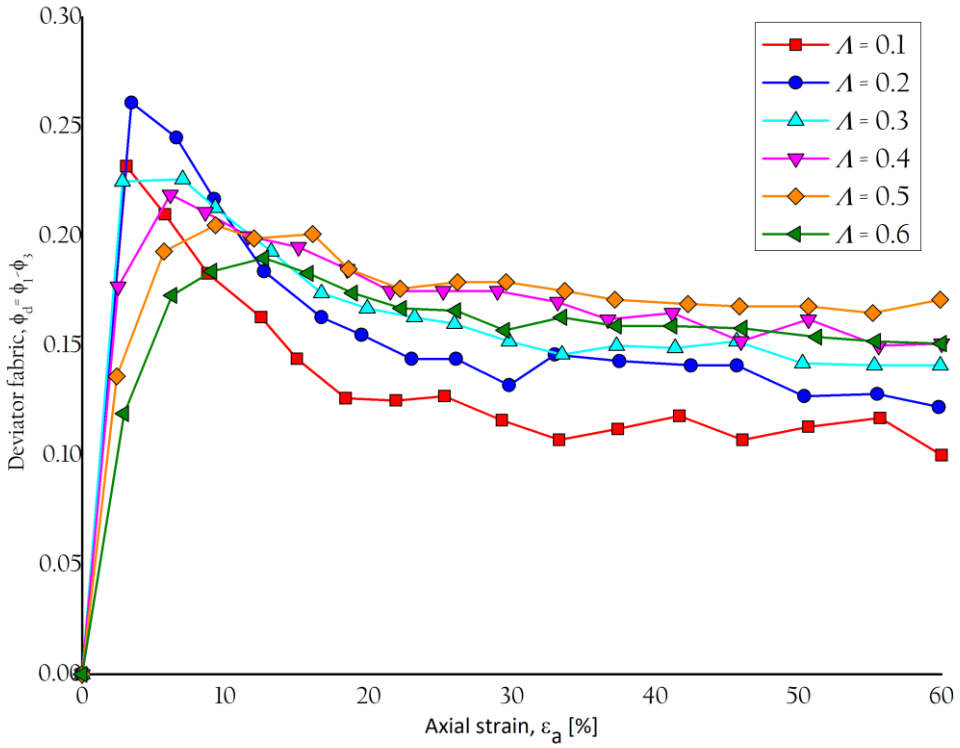

Figure 5.7 Evolution of deviator fabric against axial strain for different Λ

5.7 Relationships between critical state and shape parameters

According to Yang & Luo (2015), the position of CSL may change its position by the transformation of particle shape in the stress space. From Figure 5.8(a), it is found that a strong linear relationship between two quantities ($R^2 = 0.974$), indicating that the M values decreasing with increasing A_R. A strong correlation between M and C_χ (see Figure 5.8(b)) and M and S_W (see Figure 5.8(c)), both show an approximately linear and a second order exponential relationship with acceptable regression coefficient values, respectively. Also, it is noted that the M values decreasing with increasing C_χ and S_W, respectively.

Although the C_X is almost insensitive in my case, it is also one of the important parameters to consider in correlating the relationship between critical state parameters and particle shape characteristics. Moreover, the key shape parameter O_R defines based on the impacts of all three shape parameters (i.e., A_R , C_X and S_W). Hence, C_X also is considered in this analyses. Similar observations were also reported by Yang & Luo (2015), for Fujian sand and Glass beads. Furthermore, considering the impacts of three shape parameters (i.e., A_R,C_x, and S_w), the correlation between M and O_R can be given as:

$$M = 2.197 - 1.384 O_R \tag{5.8}$$

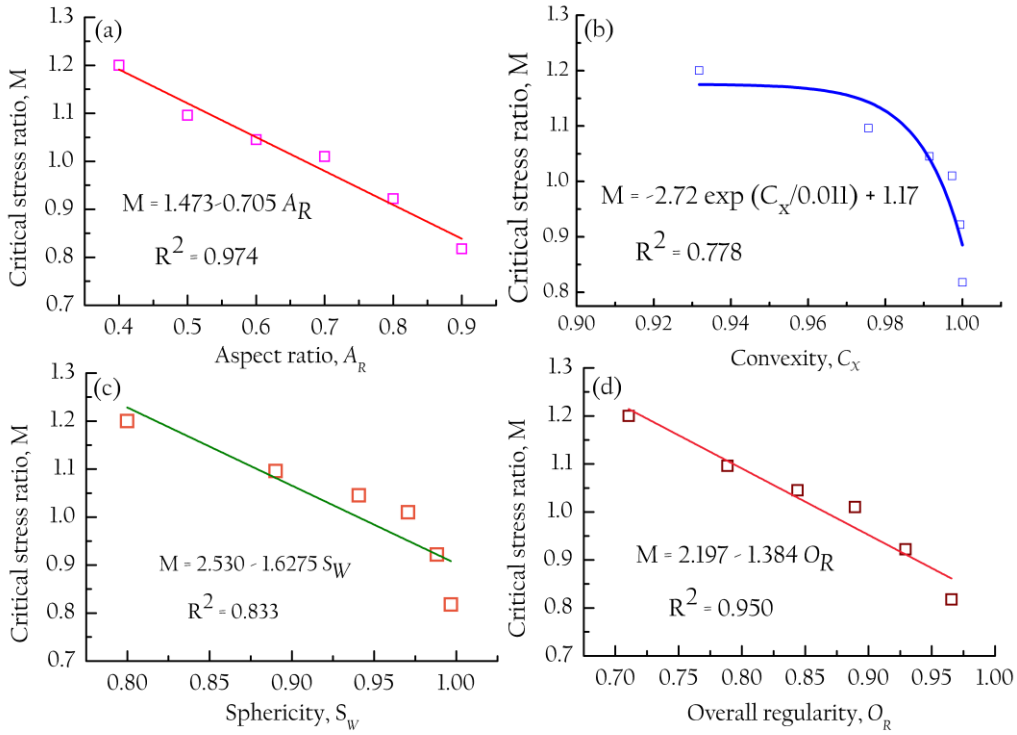

Figure 5.8 Relationships between M and shape parameters

The correlations between the critical state parameters (i.e., e_Γ and λ_c) and the shape parameters (i.e., A_R,C_x,S_w *and* O_R) are presented in Figure 5.9. It is noticed that the e_Γ correlate with these shape parameters fairly well, giving a

linear relationship with acceptable regression values. Amongst the relationships, C_χ correlate well with the e_Γ (i.e., R^2 = 0.981). The shape effect between the intercept e_Γ and O_R, is given as:

$$e_\Gamma = 1.435 - 0.747(O_R) \tag{5.9}$$

The gradient of the CSL against the shape parameters is shown in Figure 5.10. A fair correlation is established between λ_c and the shape parameters. The effect of the shape parameter λ_c can be well represented by O_R, given as:

$$\lambda_c = 0.0946 - 0.0862(O_R) \tag{5.10}$$

The above equation can well predict that the slope of the CSL in the stress space tends to decrease as particle O_R increases. These findings are in agreement with the study conducted by Yang & Luo (2015).

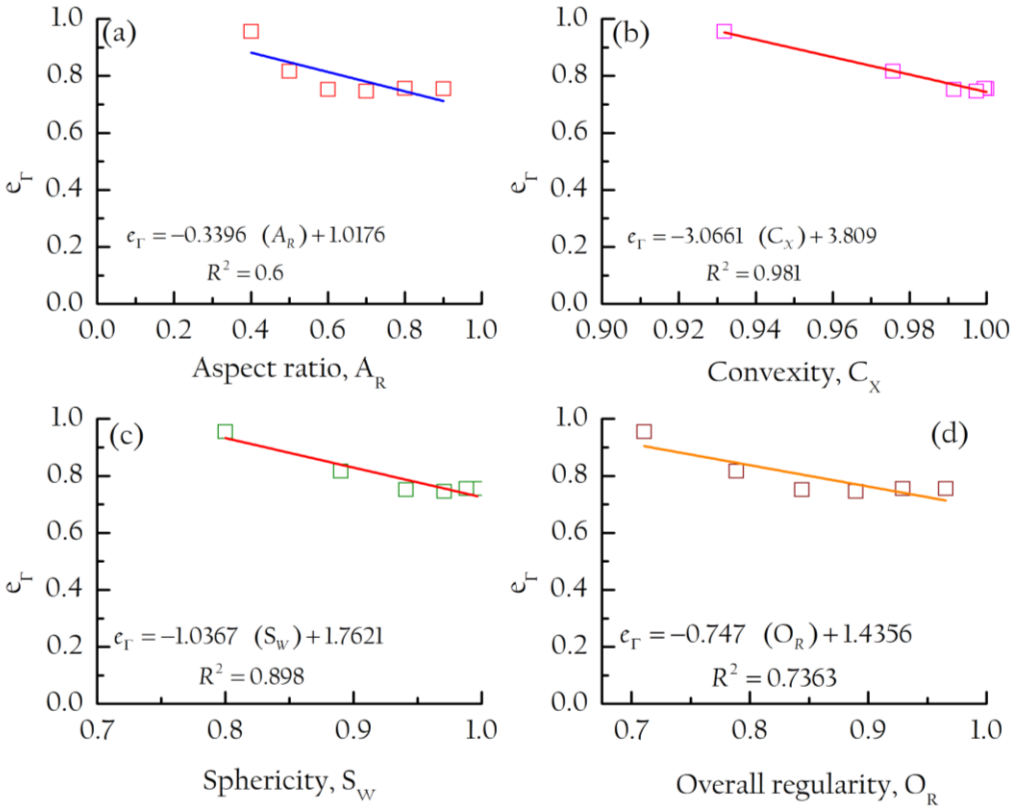

Figure 5.9 Relationships between e_Γ and shape parameters

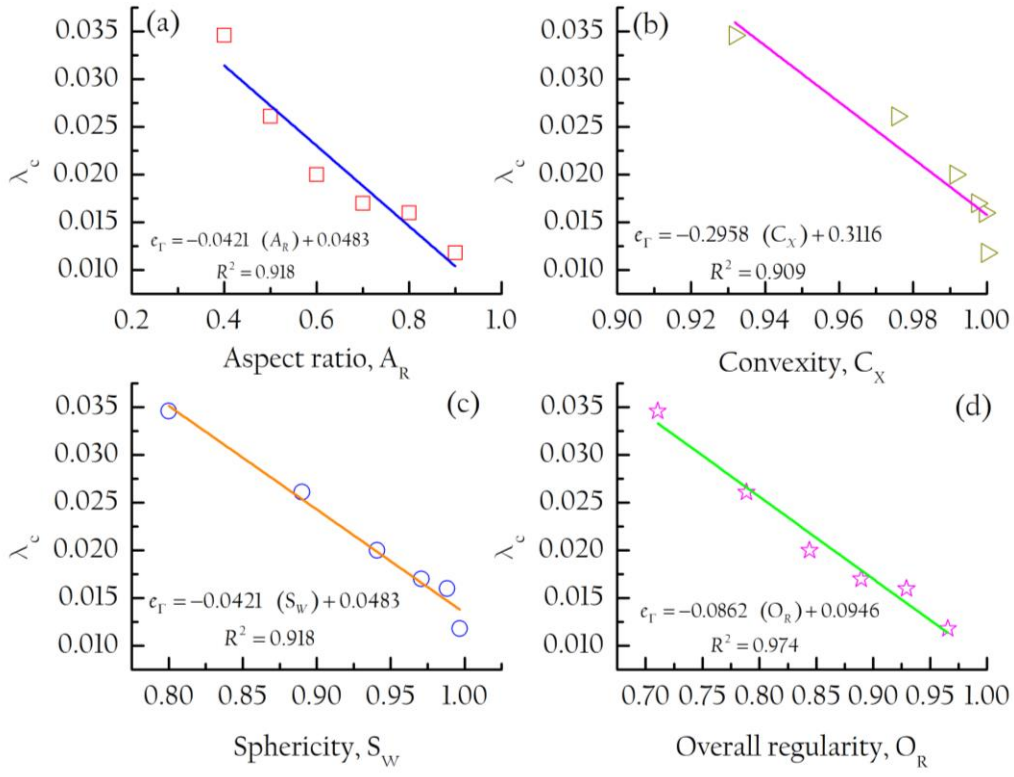

Figure 5.10 Relationships between λ_c and shape parameters

5.8 Summary

A series of DEM based drained triaxial simulations were performed considering different values of Λ. The macroscopic behaviour of granular materials exhibits post-peak strain-softening response, the stress ratio flattens off and tends to follow a steady-state after an axial strain of ~ 40%. It was also found that the residual shear strength of the assemblies depends on the applied confining stress. The microscopic behaviour in terms of CN shows an exponential decay against the axial strain, the deviator fabric followed a similar trend as observed in the macroscopic behaviour of granular materials.

The quantitative relationships were established between the critical state parameters and shape parameters. Furthermore, it should be highlighted that a critical stress ratio (M) and critical state parameters (i.e., e_Γ and λ_c) decrease with increasing shape parameters (i.e., A_R, C_x, and S_w). The relationship between the shape index (O_R) and the shape parameters (A_R, C_x, and S_w) was also established to provide a collective description of the particle geometry.

Chapter 6 Influence of particle morphology on triaxial behaviour

6.1 Introduction

To understand the true mechanical behaviour, numerous particle shapes have been considered in the literature. For non-spherical particle shapes whose surface equations are more complicated, the multi-sphere (MS) method and polyhedron method can be generally used to reconstruct the 3D particles. Using the MS method, complex non-spherical particle shape can be approximately constructed via clumping small spheres and the resolution of the particle shape is determined by both the number and size of the component spheres. Using the polyhedron method, the surface of a particle can be constructed using polygons. As long as the component spheres or polygons are sufficient, any complex shape can be well represented using either of the above methods. Nevertheless, in practice, this is unrealistic due to computational cost, especially in processing the contact detection.

In addition to the above-mentioned particle generation methods, particle irregularity and roughness also were found to have a significant influence on the shear strength and volume change of granular materials (Kozicki *et al*. 2012; Kozicki *et al*. 2014; Araujo *et al*. 2017). Moreover, among the various particle shapes considered in DEM simulations, it was confirmed that ellipsoid-shaped particles can offer a realistic behaviour of the mechanical behaviour of granular materials (Bagherzadeh-khalkhali & Mirghasemi 2009; Zhou *et al*. 2013). Moreover, the effects of particle morphology on the macroscopic and microscopic responses of granular materials are not yet fully explored or understood.

A general introduction is presented in Section 6.1 and a review of literature related to particle morphology is discussed in Section 6.2. In Sections 6.3, a methodology for particle morphology is presented. In Section 6.4 and Section 6.5, simulation details and simulations results are presented correspondingly. In Section 6.6, the relationship between macro- and micro-scale parameters are furnished. In the end, a summary of this chapter is also presented.

6.2 Review of literature

It was mentioned by Zhao & Zhao (2019) that the particle morphology is an indispensable factor in affecting the mechanical behaviours of granular materials. Several researchers have attempted to study granular material behaviour at different scales including shear strength, crushability, dilatancy, shear-induced localization and instability (Sukumaran & Aishmawy 2003; Guo & Su 2007; Tsomokos & Georgiannou 2010). However, it is a challenging task to quantitatively relate the morphological features of soil particles to the mechanical behaviour of granular materials using physical experimentation. Instead, micromechanics based numerical models, such as discrete element method (DEM), have been widely applied across many disciplines for capturing the microscopic insights of granular materials (Radjai *et al*. 1998; Thornton 2000; Nicot & Darve 2007; Wang *et al*. 2012; Guo & Yu 2015; Nicot *et al*. 2017; Jiang *et al*. 2018).

During the past two decades, the developments in X-ray micro-computed tomography (μCT) technology has allowed three-dimensional (3D) visualization and characterisation capabilities at the micro-scale enhancing significantly the insights into micromechanical behaviour of granular materials. Nevertheless, the number of scanned particles is usually restricted because of the limitations in costs and resolutions of μCT scanning. The DEM framework allows reconstruction of particle surfaces and realistic particle shapes that can be modelled using advanced clump template logics (Ferellec & McDowell 2008; Gao *et al*. 2012; Zheng & Hryciw 2015). Although the limitation of the

number of particles exists for DEM simulations, the samples for describing the particle morphologies of DEM are repetitive and can represent the realistic particles to the least.

Wei *et al.* (2018) proposed a method for generating realistic sand particles with fractal nature using an improved spherical harmonic analysis. Based on the X-ray micro-computed tomography images of natural sand particles, a set of spherical harmonic descriptors and an associated fractal dimension were introduced to characterize the multi-scale particle morphology. A powerful correlation between the spherical harmonic descriptors and the spherical harmonic degree in log-log scales was found for natural sand particles, which indicates a clear fractal nature between the multi-scale morphological features of sand particles. The visual inspection of 3D printed particles and the statistical distributions of the shape parameters (i.e., sphericity, roundness, convexity and elongation index) of the generated particles were consistent with those measured for the real sand particles from the μCT images.

Li *et al.* (2015) proposed a new algorithm to approximate real particles for DEM simulation based on a modified greedy heuristic algorithm. The authors proposed three different solution schemes based on a modified greedy heuristic algorithm, namely, a body-covering scheme, a surface-covering scheme and a triangular surface-covering scheme. The parameters were used to evaluate the precision of three different schemes indicate that all three schemes are excellent. It was understood that different schemes offer different levels of precision for different particles with different numbers of multiple spheres. Therefore, it was important to choose the scheme best suited to represent a particular objective. Also, the computational time was considered as the efficiency of the algorithm.

Jerves *et al.* (2015) investigated the effects of grain morphology on critical state using a computational analysis approach. To enable the inclusion of real grain

shapes, a new DEM scheme (LS-DEM) was employed. Using LS-DEM, the experimental results were calibrated and validated for real experimental results. Also, the potentiality of LS-DEM, the dependency of critical state parameters (CSP) such as critical state line (CSL) slope k, CSL intercept λ, and critical state friction angle of unconfined compressive strength on the grain's morphology, i.e., sphericity, roundness, and regularity, were exploited. Moreover, the authors found that the critical state friction angles show less sensitiveness to idealization and for ϕ_{cs} the CSPs computed from real grain shapes show more dependency on the grain's regularity than their counterparts from idealized grains. The authors investigated the importance that the amount of accuracy used in capturing a real grain's shape can have on the values of the critical state parameters.

A numerical investigation of particle shape effects on the fabric of granular packing was carried out using the three-dimensional discrete element method with a superellipsoid model by Zhao *et al.* (2017). A broad range of particle shapes controlled by two shape parameters (i.e., aspect ratio and blockiness) were taken into account. A series of random packing of non-cohesive, frictional monodisperse superellipsoids was conducted under gravitational forces in simulations. The fabric of a granular packing was quantified in terms of packing density, coordination number, distribution of particle orientations, the anisotropy of three types of fabric vectors (i.e., particle orientation, contact normal and branch vector), and distribution of normalized contact forces. It was shown that the effects of particle shape on packing density and coordination number were in agreement with the reported literature. Moreover, ellipsoids show the lowest packing density in the family of superellipsoids. The distribution of particle orientations was much more sensitive to blockiness than aspect ratio. Interestingly, it was found that particle shape has an insignificant effect on the probability distribution of normalized contact forces which shows a clear exponential distribution.

The influence of particle morphology on the friction and dilatancy of sand was investigated by Alshibli & Cil (2018). The stress-strain response and volume change behaviour, as well as peak state and critical state (CS) friction and dilatancy angles, was examined and the triaxial test results of Toyoura and Hostun RF sands collected from the literature were included in the analyses. Simple statistical models capable of predicting the peak and CS friction angles as well as dilatancy angle by providing particle surface texture, roundness, sphericity, relative density, and initial mean stress as input parameters were developed. The results show that morphology parameters highly influence dilatancy angle, CS, and peak state friction angles.

An experimental investigation of the kinematics of sand particles under triaxial compression was explored by Cheng & Wang (2017). A particle-tracking method based on the particle volume was employed and applied to the acquisition of particle kinematics of uniformly graded sand undergoing shearing in a mini triaxial apparatus using the X-ray synchrotron radiation technique. It was found that the particle tracking based on the two tracking criteria's i.e., particle volume and particle surface area, provides consistent results of particle kinematics with high accuracy.

Lee *et al.* (2012) studied the simulation of triaxial compression tests with polyhedral discrete elements to simulate drained and undrained triaxial compression tests. A series of DEM simulations were performed to replicate nine isotropically consolidated drained triaxial compression (CIDC) tests on sand specimens. The DEM micro-mechanical parameters of the inter-particle friction angle, normal and shear contact stiffness were calibrated using a single test in the series. The calibrated DEM model was then used to compute the response of the other eight tests. The deviatoric stress and volumetric strains obtained in each CIDC test simulation show good agreement with the corresponding experimental data. The major source of error in the simulations was the use of larger particle sizes necessary to keep the computational cost

manageable. The computed undrained triaxial compression (CIUC) responses, presented in terms of the stress path, deviatoric stress, and shear-induced pore water pressure, were consistent with the sand behaviour.

Ngo *et al.* (2016) explored a micromechanics-based investigation of fouled ballast using large-scale triaxial tests and discrete element modelling. Monotonically loaded and drained triaxial tests were carried out on ballast with levels of clay fouling that varied from 10 to 50% void contamination index (VCI) subjected to three confining pressures of 10, 30, and 60 kPa. The results show that an increase in the level of fouling decreased the mobilized friction angle and increased the ballast dilation. Ballast fouling was approximately simulated in DEM by adding 1-mm particles into the pore spaces of the fresh ballast. The predicted mobilized friction angles and volumetric changes obtained from the DEM simulations agreed well with those measured in the laboratory, indicating that the peak friction angle of fouled ballast and dilation decreased as the degree of fouling increased.

6.3 Methodology

The elliptical particles are modelled using a commonly adopted multi-sphere (MS) approach in PFC. In three-dimensions, the Voronoi diagram of a closed surface may be approximated by calculating a constrained Delaunay tetrahedralization of the ellipsoid mesh representing the surface (Chew 1989; Dey 2003; George 2003). For an ellipsoid surface enclosing a volume, a Delaunay tetrahedralization is initially constructed and then for each tetrahedron, the centre and radius of its circumscribed sphere are noted as the balls or pebbles of a clump. This approach can be implemented in the Kubrix automatic mesh generation software package (Taghavi 2000; Simulation Works 2009) as an option called BubblePack which automatically generates clump templates for PFC^{3D}. The ellipsoid surface in the form of an STL file (see Figure 6.1), and two morphological descriptors of which ξ represents the particle geometry and β represents the surface texture of the particle, should be identified. The

BubblePack outputs a file containing a surface description of the clump template that is compatible to read in PFC^{3D} as shown in Figure 6.2.

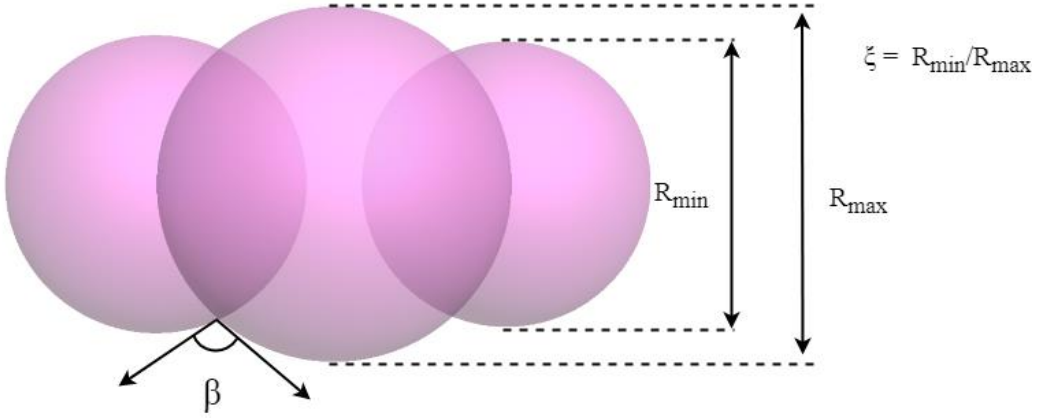

Figure 6.1 Clump representing an ellipsoid generated by MS approach

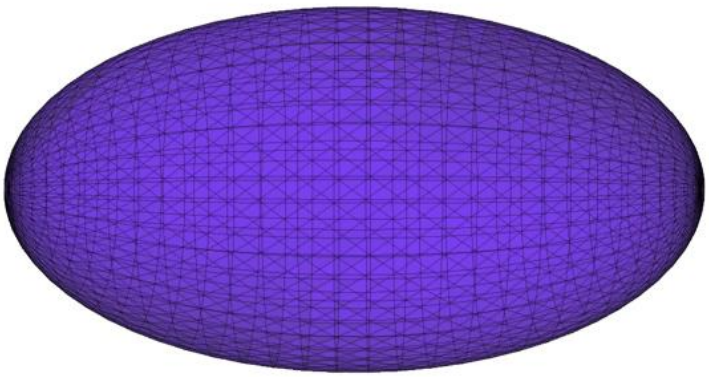

Figure 6.2 A surface representing an ellipsoid

To optimize these two parameters, Figure 6.3 shows the effects of ellipsoid clump templates for different values of ξ and β. The present DEM model can present the total range of ellipsoids as controlled by two morphological descriptors. However, due to the computational limitations and associated costs, we herein focus on the following cases: β = 150° with ξ = 0.4, 0.6 and 0.8; and ξ = 0.4 with β = 100°, 130° and 160°. The initial configurations of ellipsoidal assemblies with various β and ξ are presented in Figure 6.4.

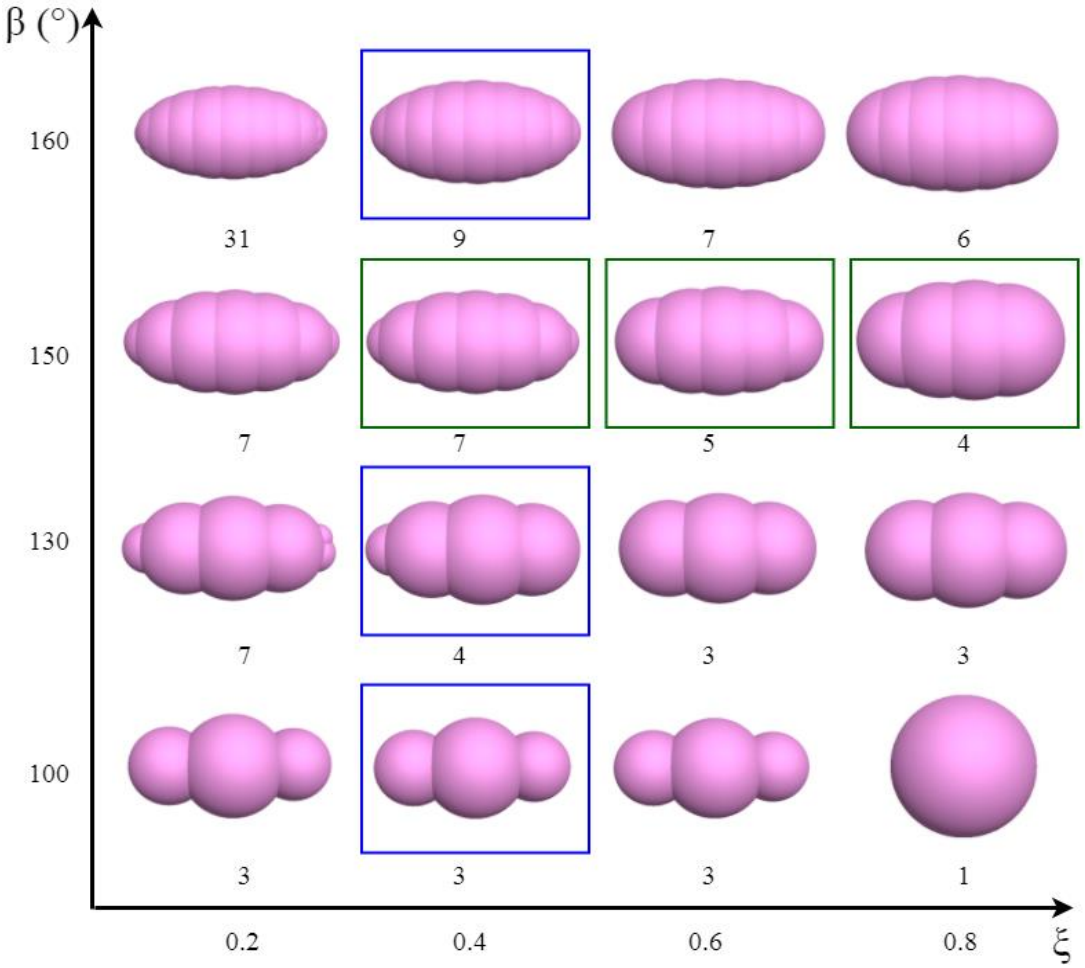

Figure 6.3 The effects of varying β and ξ for the ellipsoid clump templates

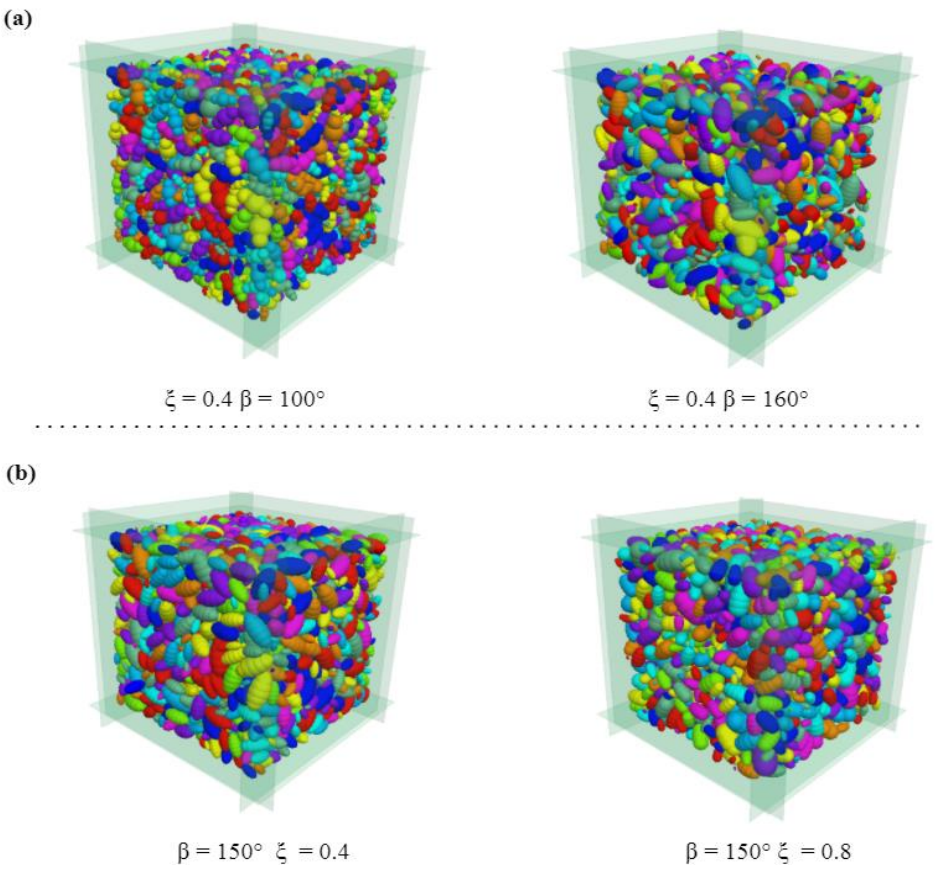

Figure 6.4 Initial configurations of ellipsoidal assemblies for triaxial simulations

6.4 Simulation details

It should be mentioned that all samples are prepared at their densest states. The input parameters used and simulation procedure remain same as reported in the previous chapter (see Section 5.4).

6.5 Simulation results

The simulation results include the evolution of macro and microscopic response of ellipsoid particles for various morphological descriptors under drained triaxial test conditions. The macroscopic behaviour includes the evolution of normalized stress, volumetric strain, void ratio and shear strength. The microscopic behaviour includes the evolution of coordination number, deviator fabric for strong force and weak force subnetworks. Moreover, the relationship between macro and macro-level quantities are established.

6.5.1 Macroscopic behaviour

Figure 6.5 and Figure 6.7 show the stress ratio against axial strain for the specimens with different ξ and β, respectively. All specimens exhibit very similar behaviour, i.e., post-peak strain-softening, which is associated with dilatancy in terms of volumetric strain as shown in Figure 6.6 & Figure 6.8. This typical behaviour is quite obvious for dense granular assembly. Also, the normalized deviator stress and volumetric strains flatten off and tend to reach a steady value after an axial strain of 40%, which shows that all samples have attained a critical state (Schofield & Wroth 1968).

The peak shear strength is found to depend on the morphological descriptors, i.e., the lower value of β tend to higher shear strength, and the higher value of ξ tend to higher shear strength. This is due to the rough surface of a particle where multiple contacts exist around the particle, a limited number of contacts in-between the smoother particles. As mentioned by Ludewig & Vandewalle (2012) and Shamsi & Mirghasemi (2012) that multiple contacts between rough surfaces of the particles would result in stronger interlocking, and as such, lead to higher shear strength within the granular assembly.

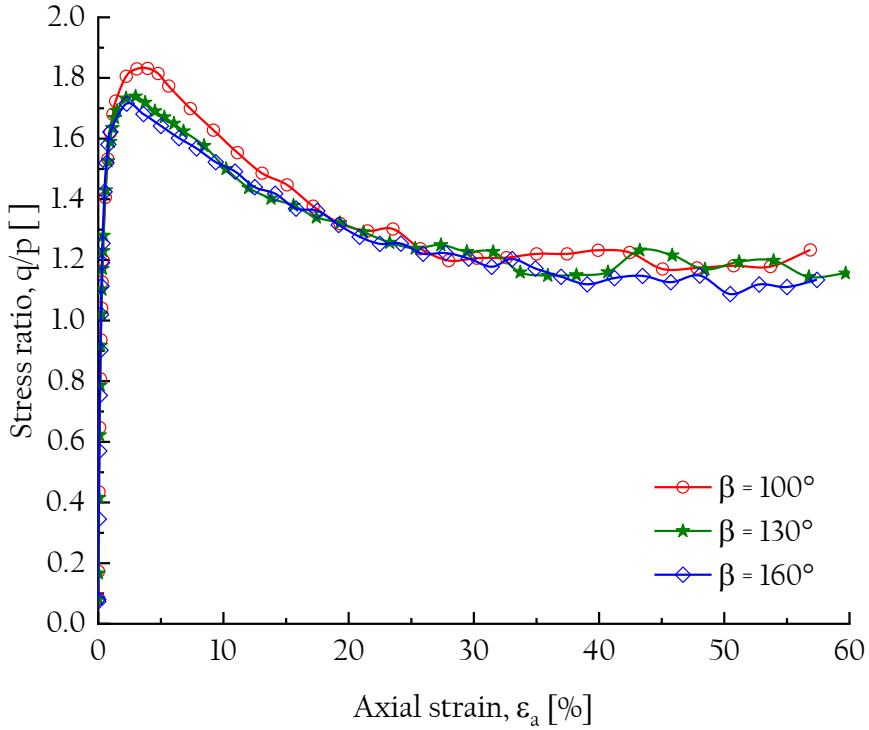

Figure 6.5 Evolutions of stress ratio against axial strain for the specimens ξ = 0.4 with different β

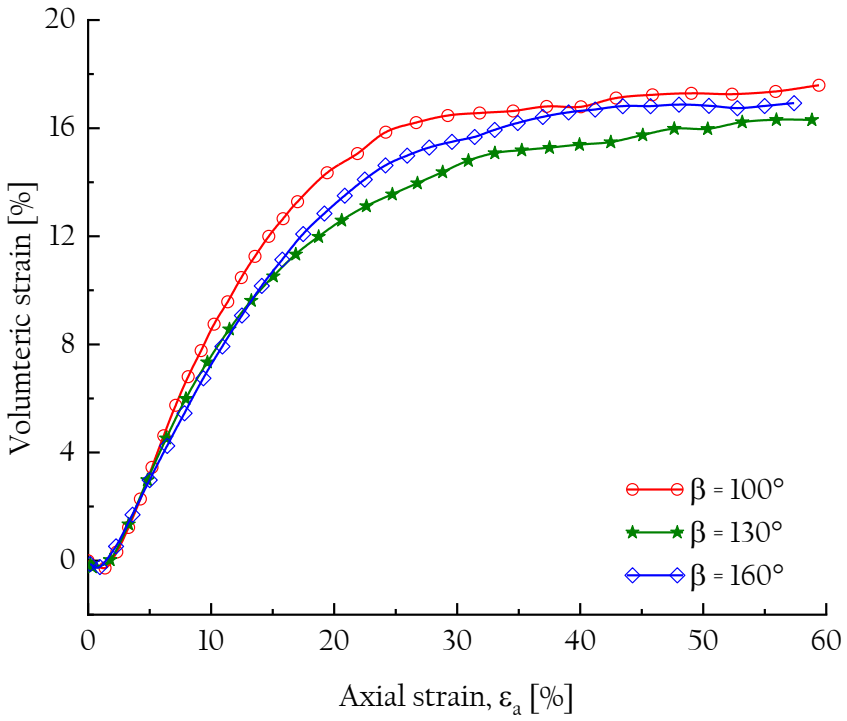

Figure 6.6 Evolutions of volumetric strain against axial strain for the specimens ξ = 0.4 with different β

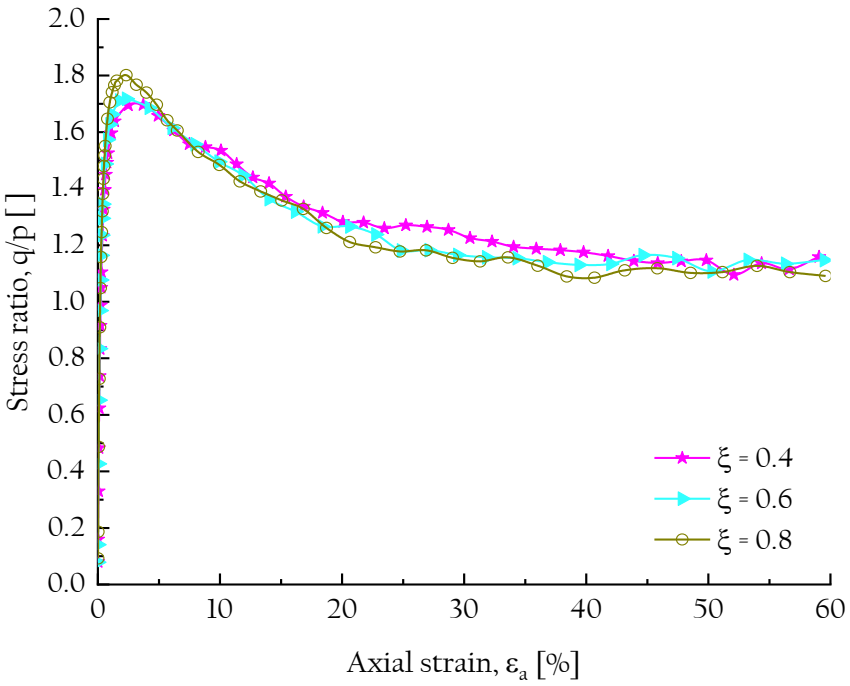

Figure 6.7 Evolutions of stress ratio against axial strain for the specimen's β $=150^{\circ}$ with different ξ

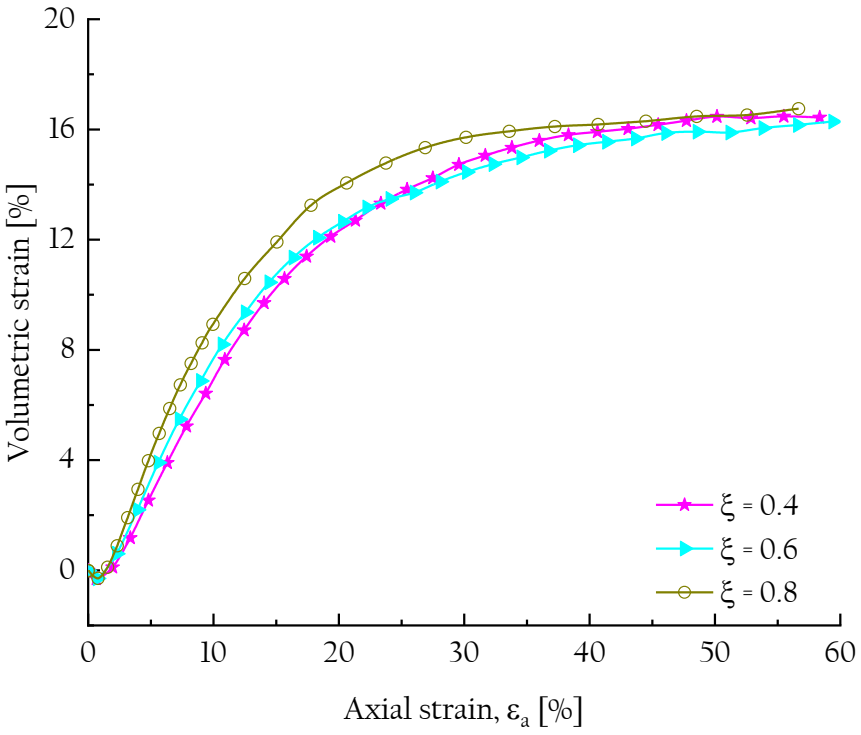

Figure 6.8 Evolutions of volumetric strain against axial strain for the specimens β $=150^{\circ}$ with different ξ

Figure 6.9 and Figure 6.10 show the evolution of void ratio (e) against axial strain for the specimens with different values of β and ξ, respectively. These curves follow a similar trend as obtained for the volumetric behaviour of granular assembly (see Figure 6.6 and Figure 6.8). Also, it is observed that the onset void ratios increase with an increase of β and decrease with an increase of ξ. These variations could be attributed to the transformation of particle geometry and surface textures with corresponding changes in the morphological descriptors.

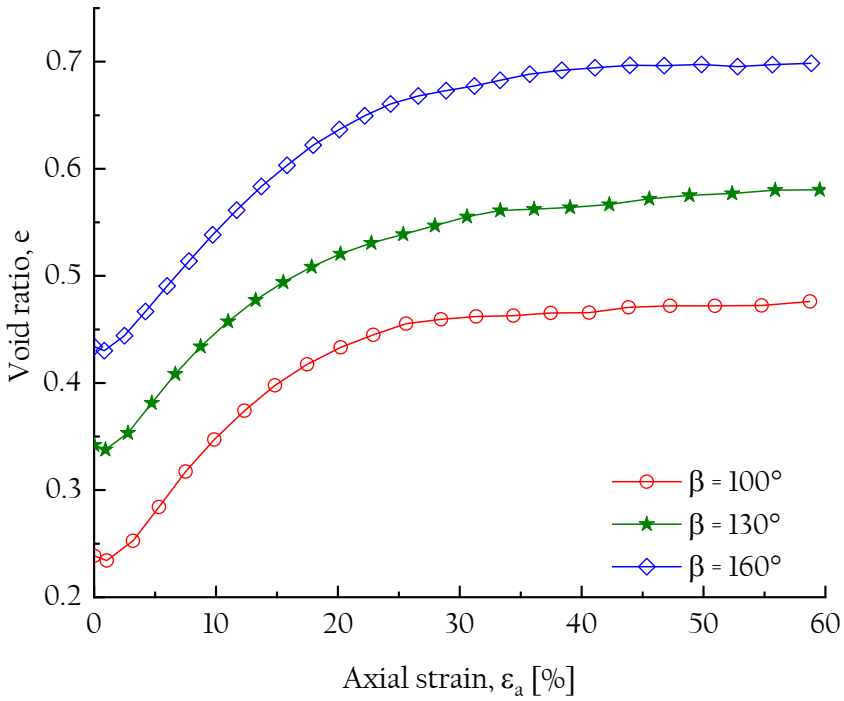

Figure 6.9 Evolutions of the void ratio against axial strain for the specimens ξ = 0.4 with different β

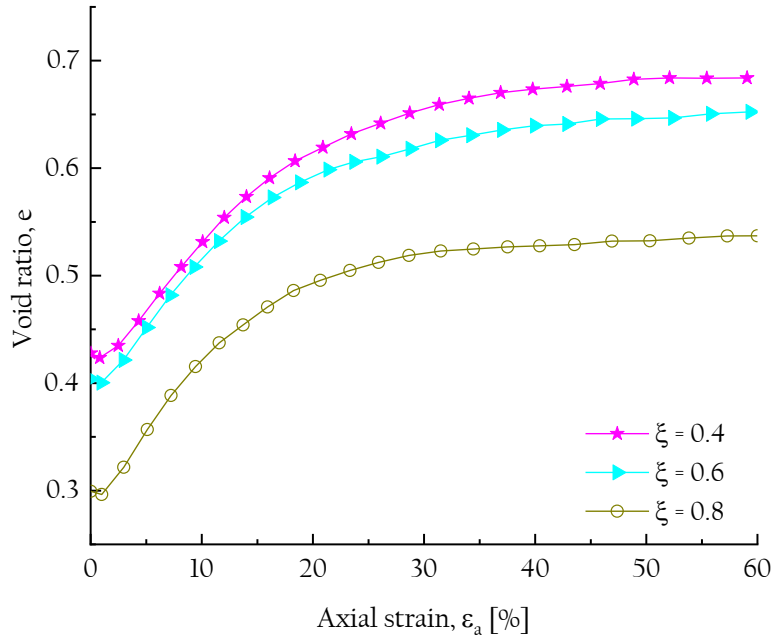

Figure 6.10 Evolutions of the void ratio against axial strain for the specimens β = 150° with different ξ

6.5.2 Evolution of the angles of internal friction

Figure 6.11 and Figure 6.12 show the influence of β and ξ on the angle of internal frictions, respectively. The error bars in these figures represent the standard deviation of the angles of friction at the critical state. It is found that the friction angles are reliant on the morphological descriptors at both peak states and critical states. However, at the critical state, such effects are less significant as compared to the peak state. Also, the peak state angles of friction decrease with an increase of β and increase with an increase of ξ. Moreover, the deviation between angles of friction at peak state and critical state appears to have an increasing trend as ξ increases, which suggests an increase in dilation angle. The same observations were reported by Zhao & Zhou (2017) under drained triaxial test simulations.

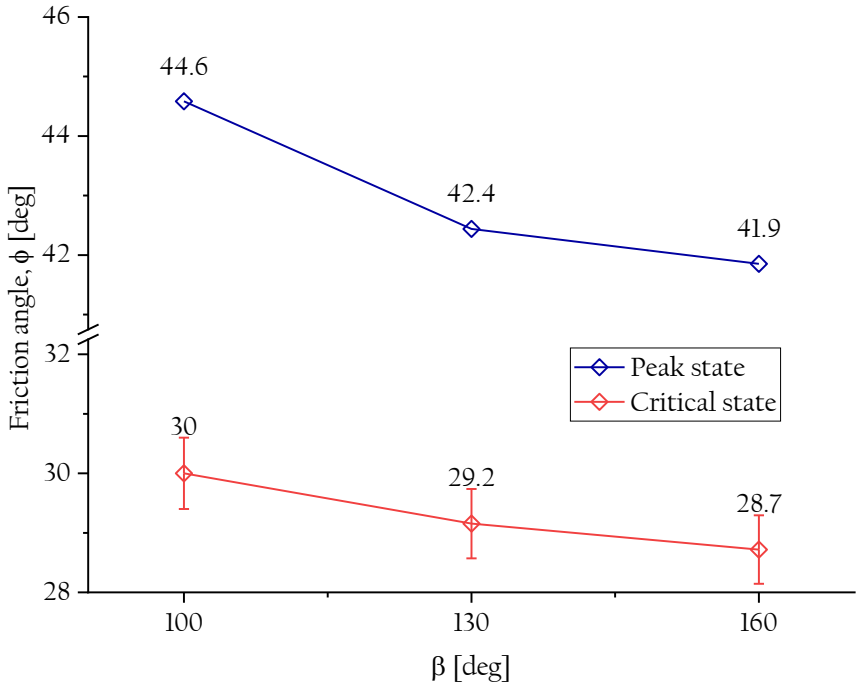

Figure 6.11 Effect of β on the angle of internal frictions

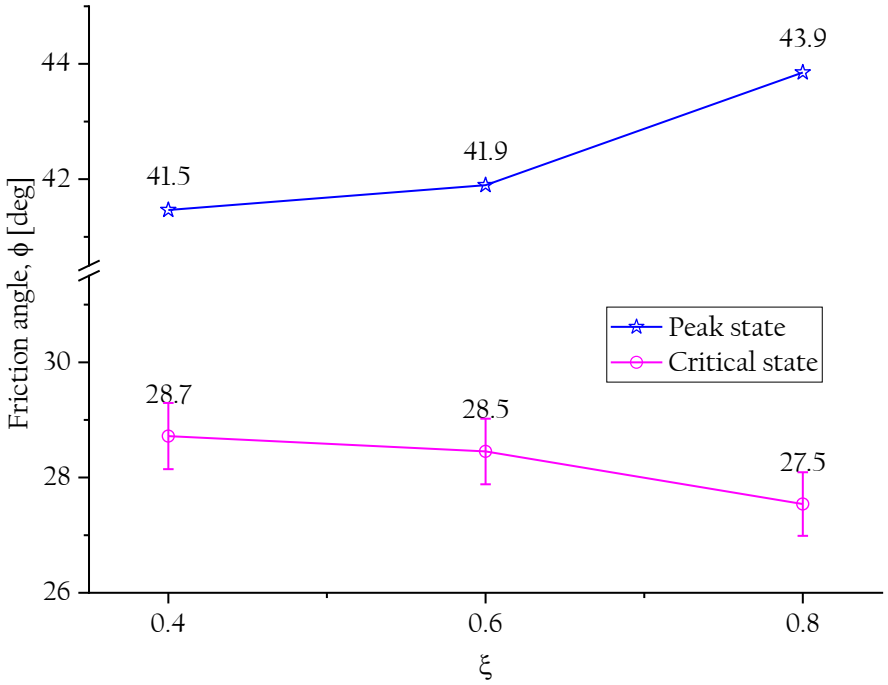

Figure 6.12 Effect of ξ on the angle of internal frictions

6.5.3 Microscopic behaviour

Figure 6.13 and Figure 6.14 show the evolutions of coordination number (CN) for the specimens with different β and ξ respectively. It is found that the CN experiences a significant exponential decay before reach $\varepsilon_1 = 15\%$ and it stabilizes during a further increase in the axial strain.

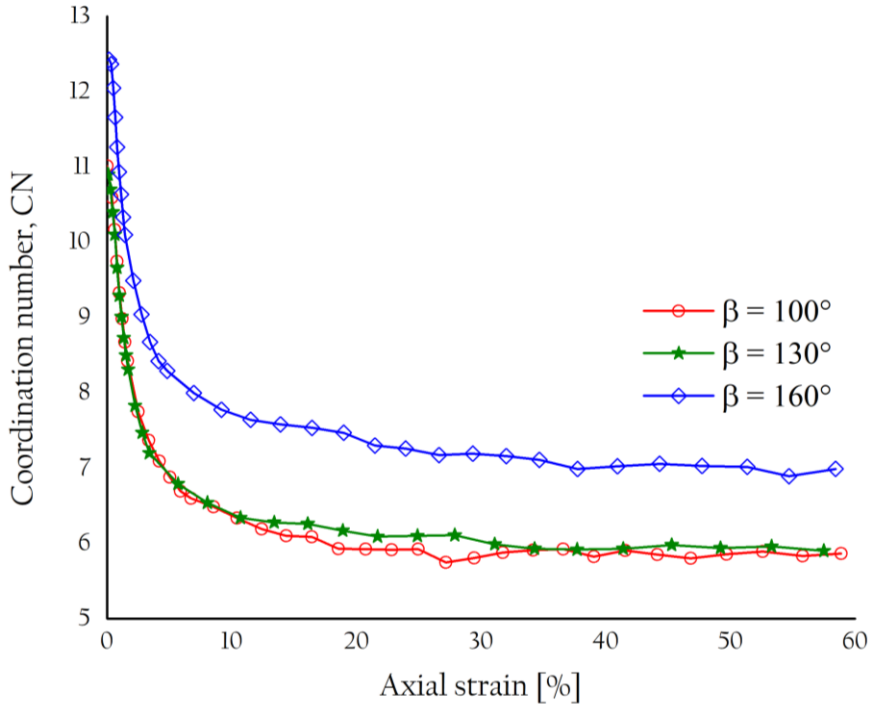

Figure 6.13 Evolutions of CN for the specimens ξ = 0.4 with different β

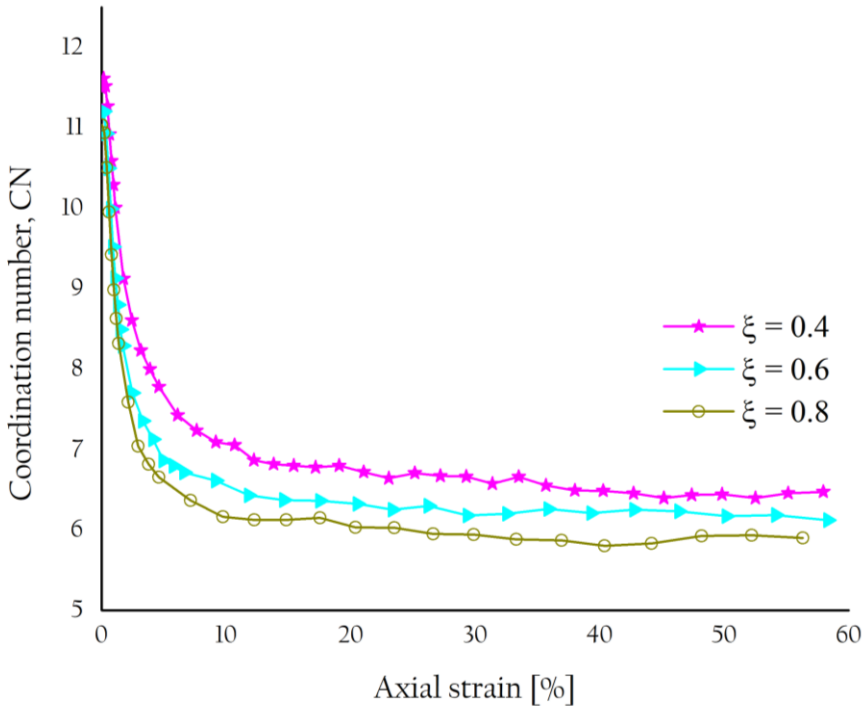

Figure 6.14 Evolutions of CN for the specimens β = 150° with different ξ

Figure 6.15 and Figure 6.16 show the probability distributions of CN for the specimens with different β and ξ, respectively. These curves are well-fitted by the Gaussian distribution function and there appears to be a systematic skewness to the distributions. Although there is no big variation between the specimens with β = 100° and β = 130°, the distribution shifts to the right as both β increases and as ξ decreases. The peaks are within the range of 6.0 to 8.0, an increase in β or decrease in ξ leads to a decrease in CN.

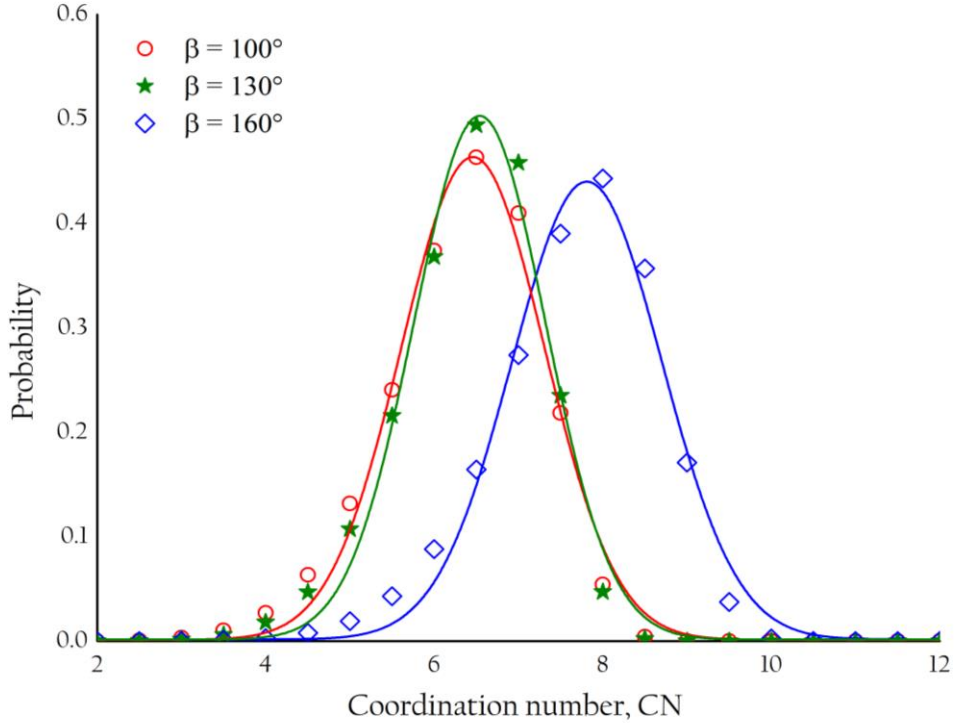

Figure 6.15 Probability distributions of coordination numbers for the specimens ξ = 0.4 with different β

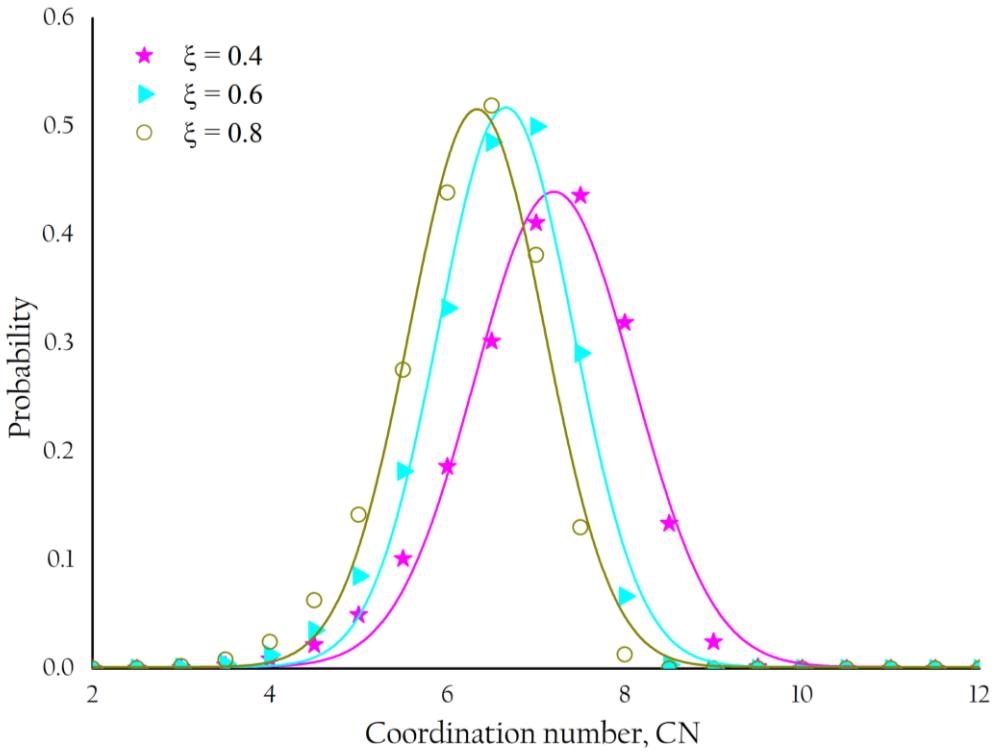

Figure 6.16 Probability distributions of coordination numbers for the specimens β = 150° with different ξ

Figure 6.17 and Figure 6.18 show the force chain networks corresponding to the initial, peak and critical states with different β and ξ respectively. In both the figures, before shearing the sample, i.e., at the initial stage or end of isotropic compression (see left columns in figures), contact forces are approximately distributed uniformly throughout the specimen, because the sample was under a state of isotropic compression. At the peak state (see middle figure), the strong contact forces (i.e., red-coloured spots) are transmitted through the top to bottom of the specimen. Also, it seems that there are limited strong contacts, however, they are deemed to be adequate to take up the external loads as pillars. Meanwhile, the weak contact force chains contributed to the stability of the strong contact force chains to a much less degree. Furthermore, as β increases or ξ decreases, the strong contact force chains are found to become stronger, corresponding to higher peak stresses. For the remaining shear process, the contacts gradually disappeared and lead to sparser contact force networks before attaining the critical state.

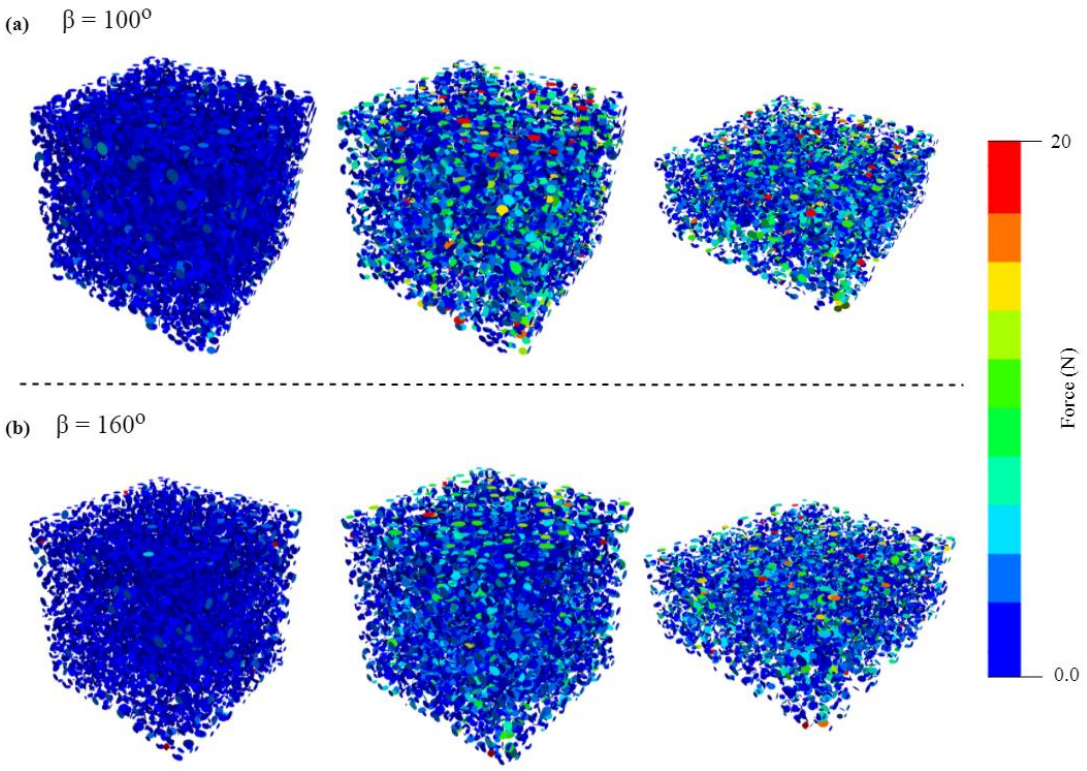

Figure 6.17 The contact force chain networks at initial (left), peak (centre) and critical (right) states for β = 100° and β = 160°

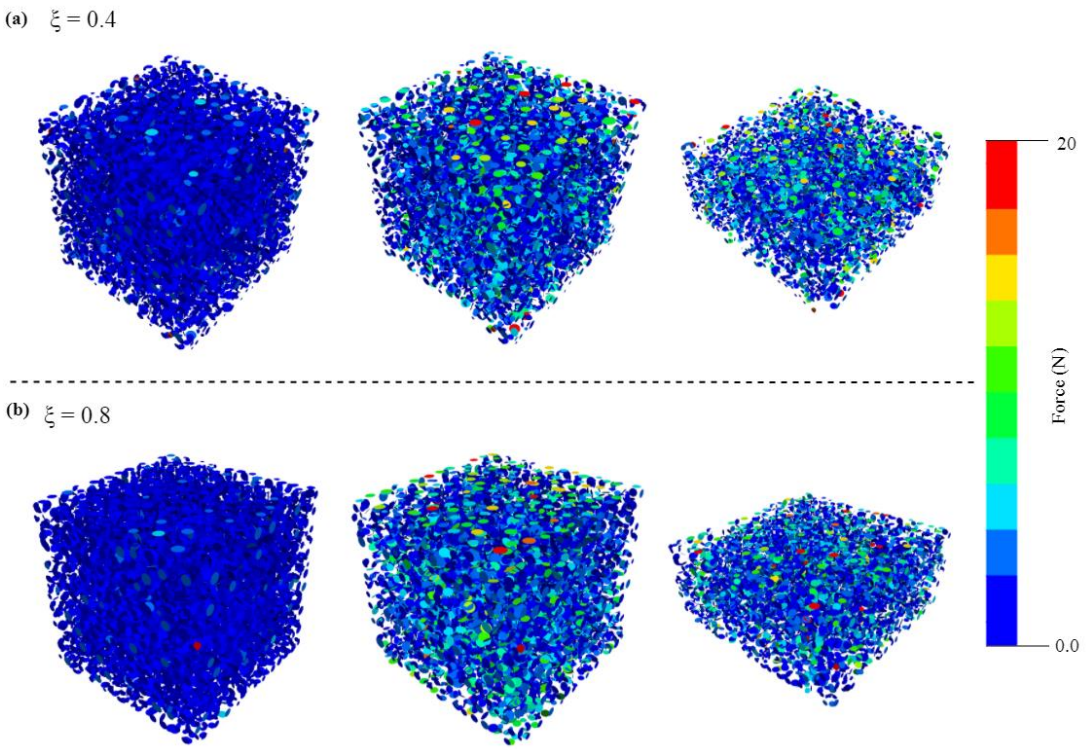

Figure 6.18 The contact force chain networks at the initial (left), peak (middle) and critical (right) states for ξ = 0.4 and ξ = 0.8

In DEM simulations, the Coulomb's friction law is commonly applied to track the proportions of sliding fractions in the assembly. According to Gong & Liu (2017), the sliding is governed by a sliding index $s_c = |f_t| / (\mu f_n)$, where f_t is the tangential contact force at the contact, μ is the internal friction coefficient, and f_n is the normal force at the contact. In general, it is assumed that the sliding is assumed to occur when s_c is greater than 0.999.

The evolution of proportions of sliding contacts for the specimens with different β and ξ, respectively are presented in Figure 6.19 and Figure 6.20. It is found that independent of β and ξ, the sliding contacts increases sharply to the peak and reaches a steady value at a higher axial strain. These observations were also reported by Gu *et al.* (2014) and Gong & Liu (2017) for the dense granular assemblies under triaxial test conditions. Moreover, ξ has a significant effect on the sliding contacts as compared to β, which indicates the increase of ξ can improve the interlocking between particles.

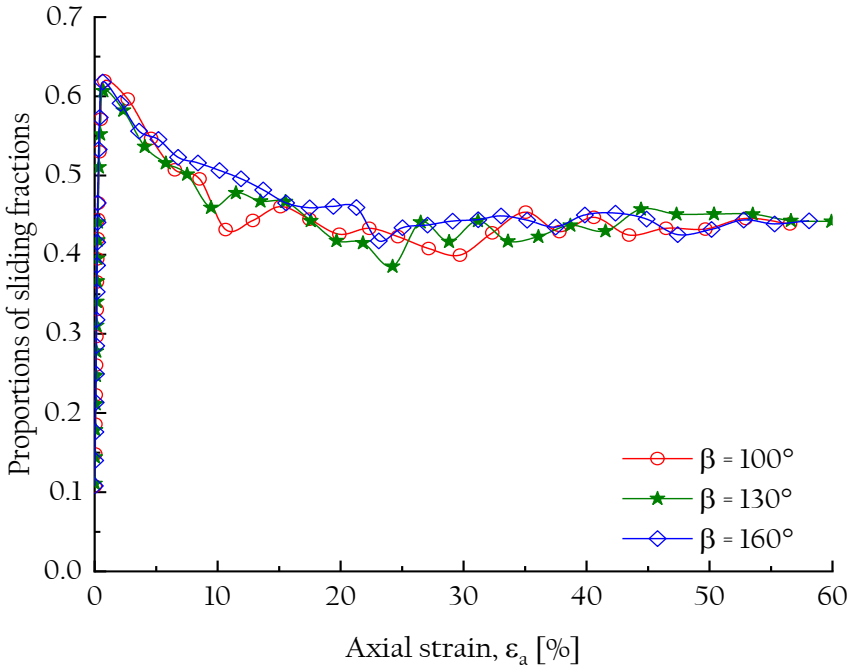

Figure 6.19 Proportions of sliding fractions for the specimens ξ = 0.4 with different β

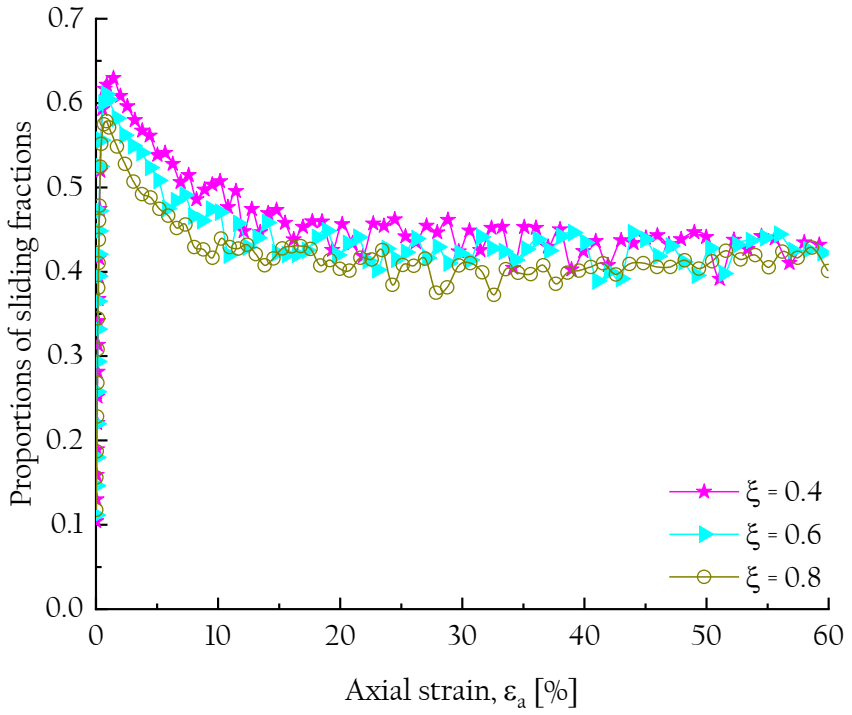

Figure 6.20 Proportions of sliding fractions for the specimens β = 150° with different ξ

6.6 Establishing the micro-macro relationship

Several investigators have tried to establish the relationship between the micro-macro relationship for granular materials (e.g., Radjai *et al.* 1998; Alonso-Marroquin *et al.* 2005; Sazzad & Suzuki 2013). Figure 6.21 to Figure 6.24, the overall and strong fabric measures of ϕ_d / ϕ_m and $\phi^s{}_d / \phi^s{}_m$ against axial strain for the specimens with different β and ξ, respectively are presented. Both overall and strong fabric measures behave similarly with higher in magnitudes for the strong fabrics. Moreover, it is found that the increase in β or ξ leads to an increase in the fabric measures for the same axial strain. Figure 6.25 presents a relationship between the macro and micro scale quantities for different morphological descriptors. Regardless of β and ξ, the relationships are approximately linear before their peaks.

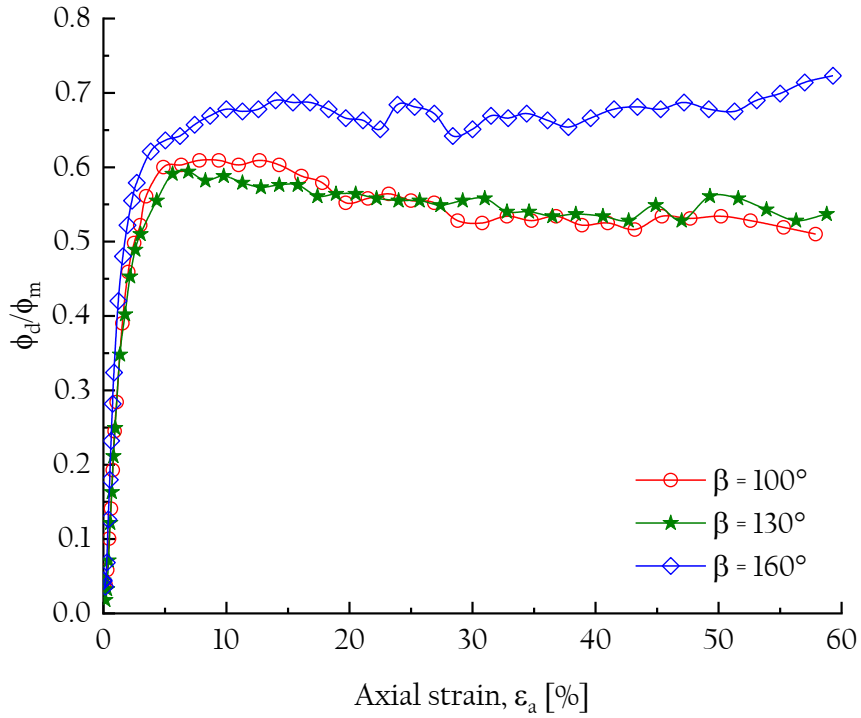

Figure 6.21 Evolutions of ϕ_d / ϕ_m against axial strain for the specimens ξ = 0.4 with different β

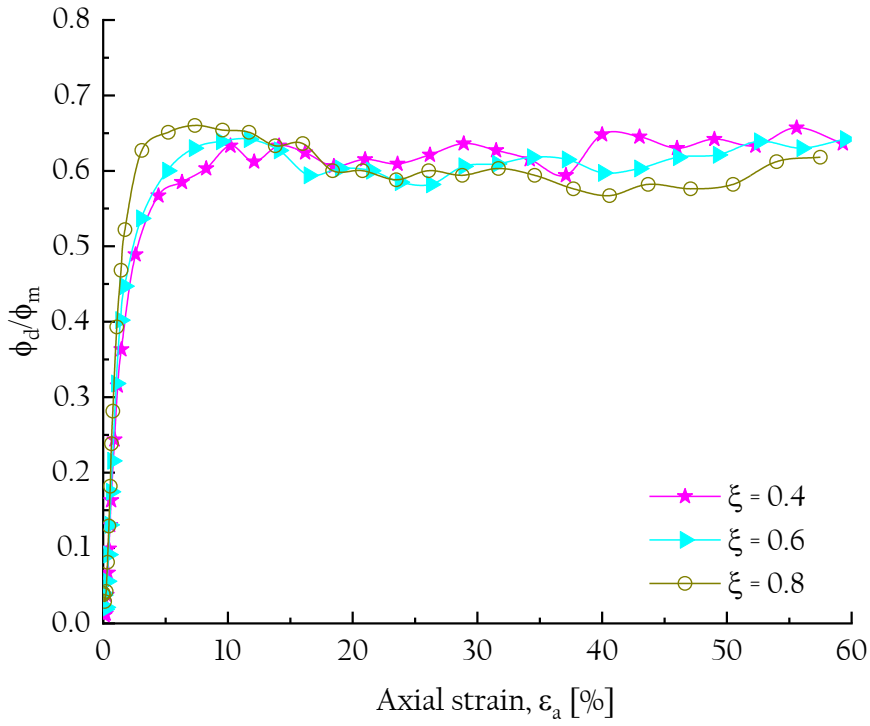

Figure 6.22 Evolutions of ϕ_d / ϕ_m against axial strain for the specimens β = 150° with different ξ

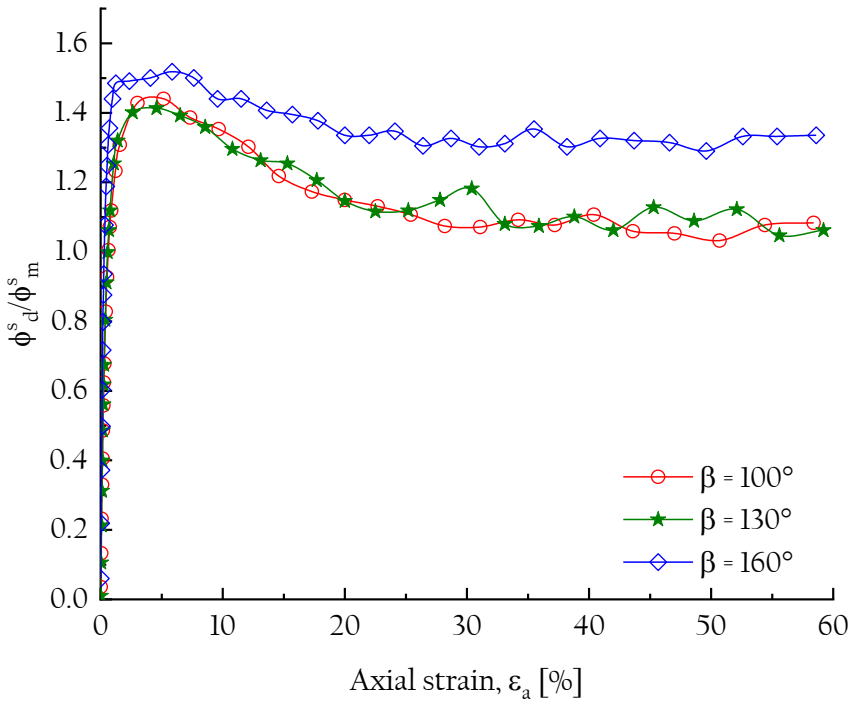

Figure 6.23 Evolutions of ϕ^s_d / ϕ^s_m against axial strain for the specimens ξ = 0.4 with different β

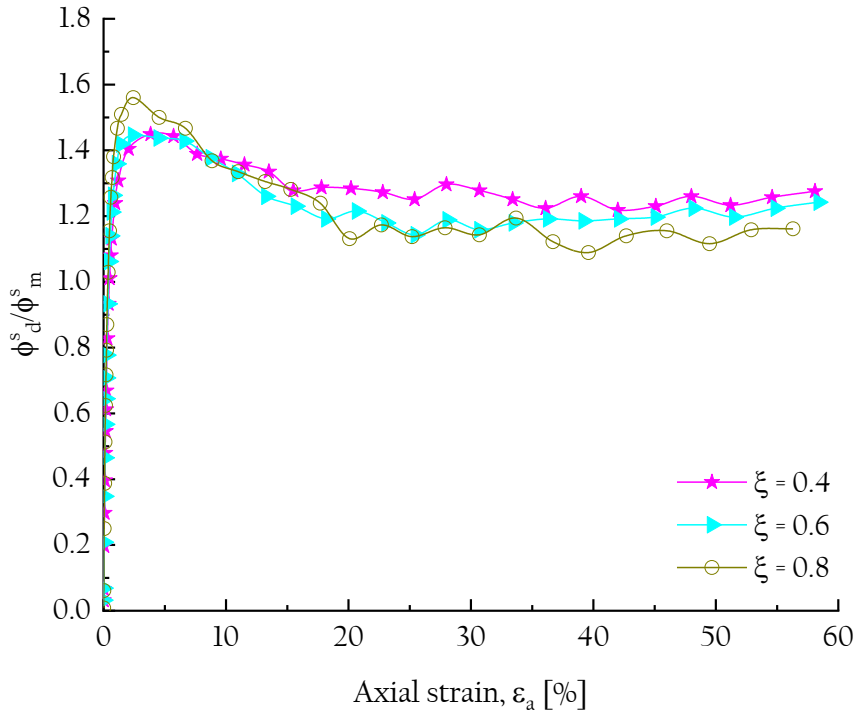

Figure 6.24 Evolutions of ϕ^s_d / ϕ^s_m against axial strain for the specimens β = 150° with different ξ

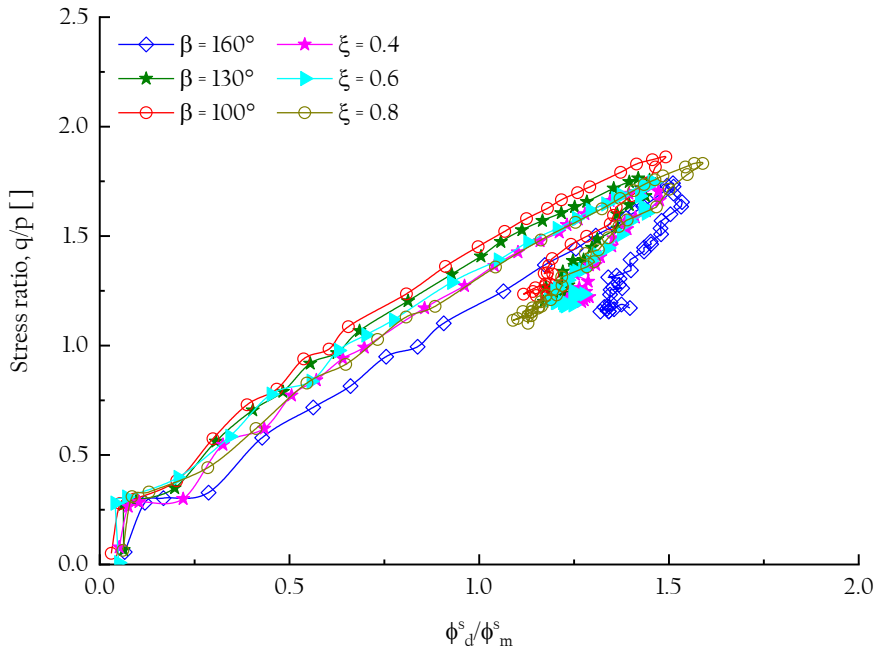

Figure 6.25 Relationship between strong fabric parameter ϕ^s_d / ϕ^s_m and stress ratio q / p'

6.7 Summary

The macroscopic behaviour of numerical assemblies with different morphological descriptors was deemed to be comparable in trends. The difference between angles of internal friction at the peak state and the critical state appears to increase with increasing ξ, which corresponds to an increase in the dilation angle. The coordination numbers exhibit significant exponential decay before reaching an axial strain of about 15% and eventually stabilizes with a further increase in the axial strain. Moreover, irrespective of the morphological descriptors, an approximately linear relationship is found between the stress ratio and the strong fabric parameter $\phi^s{}_d / \phi^s{}_m$ before reaching the peak.

Chapter 7 Influence of loading paths on critical state behaviour

7.1 Introduction

The development of critical state soil mechanics (CSSM) framework was initiated in the 1950s and 1960s by Roscoe *et al.* (1958) and Schofield & Wroth (1968). The key assumption of the CSSM framework is that the soil is continuously sheared to a large strain where both the constant volume and constant stress states occur. Although the CSSM framework was based on the experimental observations and theoretical derivations, the conflicting findings regarding some key issues, such as the uniqueness of the critical state line (CSL) and achieving the critical state, have been discussed for a long time (Chu 1995; Mooney *et al.* 1998; Zhao & Gao 2013). Notwithstanding this, the uniqueness of critical state has evoked increasing debate for many years and remains an unresolved issue. The central difficulty lies in how to integrate fabric anisotropy into the delineation of the critical-state failure. Some experimental investigations indicated that the CSL in the void ratio (e) and mean normal effective stress (p') space is non-unique (Been *et al.* 1991; Verdugo & Ishihara 1996), while others show a unique CSL regardless of the initial conditions (Ng 2009; Sitharam & Vinod 2009; Salvatore *et al.* 2017).

Critical-state failure is a salient feature for particular materials, whereas the critical-state theory (CST) is widely accepted for understanding and interpreting the behaviour of a range of materials under complex loading conditions. In elasto-plastic soil modelling, the critical state is also a favourable reference state for capturing and simulating the soils responses, and thus many constitutive models have been developed within the CST framework.

A critical state void ratio (e_c) alone cannot well represent the comprehensive state of the soil sample. Been & Jefferies (1985) introduced a state parameter $\psi = e - e_c$, where e is the current void ratio and e_c is the void ratio at the critical state for the current p' value. A positive value of ψ signifies a looser state while the negative value ψ indicates a denser state of the assembly. In the recent past, numerous constitutive models for soils have been developed which explicitly take ψ into account in their formulation (e.g., Jefferies 1993; Jefferies and Shuttle 2002). However, there is a lack of large-strain laboratory test data for three-dimensional generalized loading conditions, which bounds the ability to develop and to apply these models to field applications where the stress state is not axisymmetric (Huang *et al*. 2014b).

An overview of the relevant literature regarding the loading paths is presented in Section 7.2. In Sections 7.3 and 7.4, evaluation of I_D and introduction on the loading paths are presented. The simulation details and results are presented in Sections 7.5 and 7.6, respectively. In the end, a summary of the chapter is presented.

7.2 Review of literature

The experimental results on critical state behaviour of granular materials under true triaxial test conditions is rarely reported because the loss of homogeneity in deformation at large strain levels. Thus computer-based numerical simulations are gained much weightage in which the loading paths and simulation parameters can be appropriately controlled and the stress-strain responses can be analyzed thoroughly. In the literature, many researchers have been dedicated to studying the critical-state behaviour of granular materials (e.g., Ng 2009; Sitharam & Vinod 2009; Maeda *et al*. 2010; Yan & Dong 2011; Guo & Zhao 2013; Gu *et al*. 2014). Nevertheless, many DEM studies have investigated the effects of b on the load-deformation response (Thornton 2000; Barreto & O'Sullivan 2012; Ng 2004; Sazzad & Suzuki 2013). These studies

have considered the influence of b mainly on comparing the behaviour of sands under triaxial compression (b = 0.0) and triaxial extension loading conditions (b = 1.0). Been *et al.* (1991) reported that the CSL obtained from triaxial compression tests and that determined from triaxial extension tests are identical, a consensus has been formed among other researchers that the CSL for triaxial extension lies below that of triaxial compression (Vaid *et al.* 1990; Riemer & Seed 1997; Carrera *et al.* 2011). Yet there is no clear justification made in this regard.

Huang *et al.* (2014) explored the critical-state response of granular assemblies composed of elastic spheres under generalised three-dimensional loading conditions using DEM. The simulations were performed with a simplified Hertz–Mindlin contact model using a modified version of the LAMMPS code. Initially, isotropic samples were subjected to three-dimensional stress paths controlled by the intermediate stress ratio, $b=(\sigma_2-\sigma_3)/(\sigma_1-\sigma_3)$, where σ_1, σ_2 and $\sigma_3$are the major, intermediate, and minor principal stresses, respectively. The data show that, while shearing, the dilatancy at post-peak increases with increasing b. Thus at a given mean effective stress, the void ratio at the critical state increases systematically with b. Four commonly used three-dimensional failure criteria were shown to give a better match to the simulation results at the critical state than at the peak state. The variation in the critical state void ratios at the same mean effective stress, p' value is related to the directional fabric anisotropy which is sensitive to b.

Zhou *et al.* (2016) studied the macroscopic and microscopic behaviours of granular materials under proportional strain paths. A contact model considering rolling friction was adopted to account for the effects of particle shape. The mechanical responses indicate that loose assemblies without the rolling resistance were more vulnerable to static liquefaction. A sample with a

smaller initial void ratio or larger rolling friction coefficient will reinforce the stability of the structure and reduce the likelihood of failure.

Xie *et al.* (2017) explored the influence of particle geometry and the intermediate stress ratio on the shear behaviour of granular materials. The numerical experiments employ samples with different particle aspect ratios and a unique particle size distribution (PSD). The test results show that both the particle aspect ratio (A_R) and intermediate stress ratio (b) affect the macro- and micro-scale responses. At the macro-scale, the shear strength decreases with an increase in both aspect ratio and intermediate stress ratio, b values. At the micro-scale level, the fabric evolution was also affected by both A_R and b. The results from DEM analyses qualitatively agree with available experimental data. It is observed that the position of the critical state loci in the compression ($e-p'$) space is only slightly affected by A_R while the critical stress ratio is dependent on both A_R and b. It was also demonstrated that the influence of the aspect ratio and the intermediate stress can be captured by micro-scale fabric evolutions that can be well understood within the framework of existing critical state theories. For a given stress path, a unique critical state fabric norm is dependent on the particle shape but is independent of critical state void ratio.

Yang & Wu (2017) studied critical state behaviour for anisotropic granular materials using DEM. Samples with different degrees of initial fabric anisotropy were sheared up to the critical state under both triaxial compression and extension conditions. Based on the numerical simulations with varying densities and confining pressures, a unique critical-state line was approximately obtained in the $e-p'$ plane and was found to be independent of initial fabrics and shearing modes or Lode angles. The fabric anisotropy and its evolution during the loading process were quantified by a deviatoric fabric tensor defined based on the statistical distribution of the contact normal vectors within the granular assemblies. The most prominent observation is that the principal direction of the fabric tensor is codirectional with the stress at the

critical state, whereas its norm was having a unique value pertinent to the shear mode or Lode angle.

Jiang *et al*. (2018) studied the influence of particle-size distribution on critical state behaviour of spherical and non-spherical particle assemblies. A series of DEM based triaxial test simulations were performed to examine the influence of particle-size distribution (PSD) and particle shape, which were independently assessed. Samples were composed of particles with varying shapes characterized by overall regularity (O_R) and different PSDs. The samples were subjected to the axial compression through different loading schemes: constant volume, constant mean effective stress, and constant lateral stress. All samples were sheared to large strains to ensure that a critical state was reached. For a given PSD, both the shear strength and fabric norm decrease with an increase in O_R. It was found that the critical state angle of shearing resistance was highly dependent on particle shape. In terms of PSD, uniformly distributed assemblies mobilize higher shear strength and experience more dilative responses than specimens with a greater variety of particle sizes. The position of the critical state line in the $e-p'$ space was also affected by PSD. However, the effects of PSD on critical strength and evolution of fabric were negligible.

Yang *et al*. (2018) studied the unified modelling of the influence of consolidation conditions on monotonic soil response considering the evolution of fabric. An anisotropic plasticity model to address the effect of consolidation conditions on the responses of soils within the framework of the anisotropic critical state theory (ACST) was proposed. Double-yield surfaces were employed to describe the plastic deformation caused by both deviatoric shear and compression. A fabric tensor was defined to quantify the internal structure of soils and its evolution during the plastic deformation under both loading mechanisms was explicitly proposed. The novel expression of the fabric evolution rules allows for both 'hardening' and 'softening' types of variation in the fabric norm that is manifested by discrete element method simulations. A modified anisotropic

variable was proposed, engaging with the effect of the anisotropic consolidation and the subsequent loading path and rendering the combined dilation–contraction deformation patterns being simulated, which are exclusively pertinent to the anisotropic consolidation conditions. The predictive capacity of the model was demonstrated by triaxial tests on both sand and clay. A satisfactory comparison was found between the model response and test results.

7.3 Evaluation of density index (I_D)

In DEM simulations, the application of interparticle friction during the isotropic compression will play a key role in controlling the state of granular assembly. In soil mechanics, the state of soil can be well – represented by relative density $D_r = (e_{max} - e)/(e_{max} - e_{min})$, where e_{max} and e_{min} are the maximum and minimum void ratios, respectively. However, the evaluation of limiting void ratios are challenging in DEM simulations. Therefore, an alternative measure D_r is the densification index (I_D), which is used to capture the state of the numerical assembly. The expression I_D is defined as (Zhang *et al.* 2018):

$$I_D = \frac{e_{up} - e}{e_{up} - e_{low}} \tag{7.1}$$

where e_{up} and e_{low} are the corresponding void ratios on upper and lower consolidation lines, respectively. The upper boundary is the isotropic consolidation line (ICL) of the loosest sample and the lower boundary is the ICL of the sample exposed to the densest state or maximum densification (see Figure 7.1). It should be emphasised that the state of the sample in DEM mainly depends on the application of the interparticle friction coefficient during the specimen generation or isotropic compression phase. To achieve the densest

state, the zero interparticle friction coefficient should be assigned to the particles during the specimen generation phase, and then the e obtained at the end of the isotropic compression phase will be considered as e_{min}. Similarly, for the loosest state, the interparticle friction coefficient in the successive isotropic compression phase shall be gradually increased until the e becomes almost stable even though the change is imposed in the interparticle friction coefficient. The e obtained at this particular isotropic compression phase will be regarded as e_{max}. Although, the D_r and I_D are slightly different as I_D is dependent on p_o', and therefore, its value for the same e can change with p_o'.

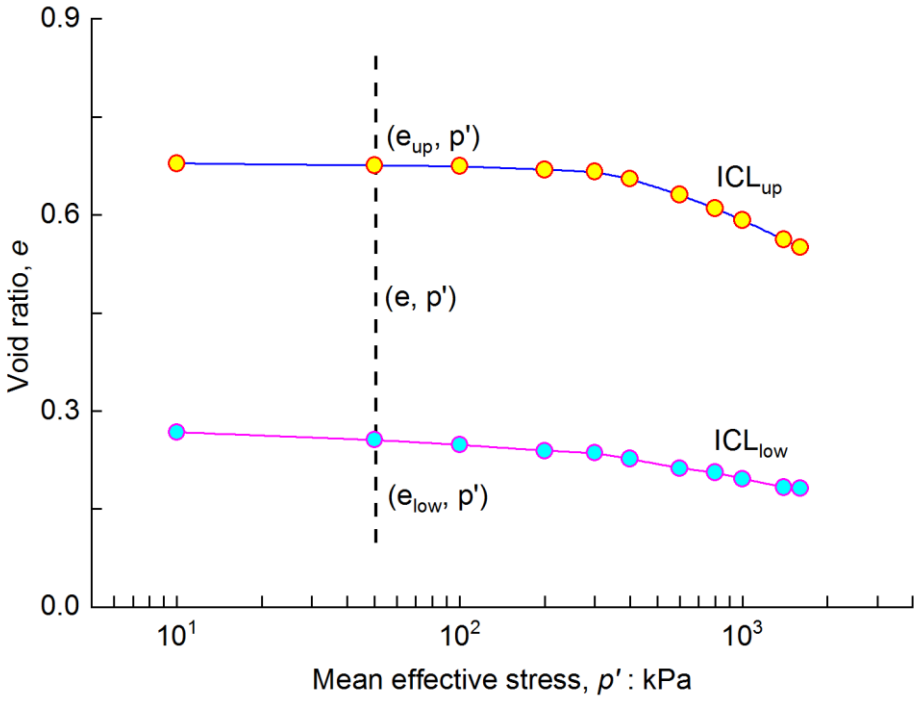

Figure 7.1 Evaluation of densification index (I_D)

7.4 Triaxial loading paths

Several investigators worked on the DEM simulations for analysing the mechanical response of granular materials under various loading conditions, together with identifying their critical-state behaviour (Ng 2004, 2009; Fu & Dafalias 2015; Yang & Wu 2016). However, the mechanical response of granular

materials are not only closely related to the loading environment but also be contingent to the stress paths or loading paths (Jiang *et al*. 2013; Gutierrez *et al*. 2009; Rodriguez & Lade 2013).

In general, standard triaxial stress loading path tests are performed based on engineering practice and more generalised three-dimensional stress state taking into account the fact that the intermediate and minor principal stresses can be attained using true triaxial apparatus (TTA) (Ko & Scott 1967; Green & Bishop 1969; Head 1986). Each stress path has a critical field significance. However, the stress paths with lateral stress greater than the vertical stress are thought to represent more critical field cases.

The triaxial drained loading and unloading stress paths can be classified into four types: axial compression (AC), axial extension (AE), lateral compression (LC) and lateral extension (LE). The schematic representation of the stress paths is shown in Figure 7.2. For the case of AC and AE tests, the specimen is loaded axially ($\Delta\sigma_a \uparrow$) and unloaded axially ($\Delta\sigma_a \downarrow$) while the lateral pressure is kept constant ($\Delta\sigma_r = 0$), respectively. Similarly, for the case of LC and LE tests, the specimen is loaded laterally ($\Delta\sigma_r \uparrow$) and unloaded laterally ($\Delta\sigma_r \downarrow$) while the axial pressure kept constant ($\Delta\sigma_a = 0$), respectively. The illustration of drained triaxial loading paths considered in the $q - p'$ space for isotropically consolidated specimens at 400 kPa is shown in Figure 7.3.

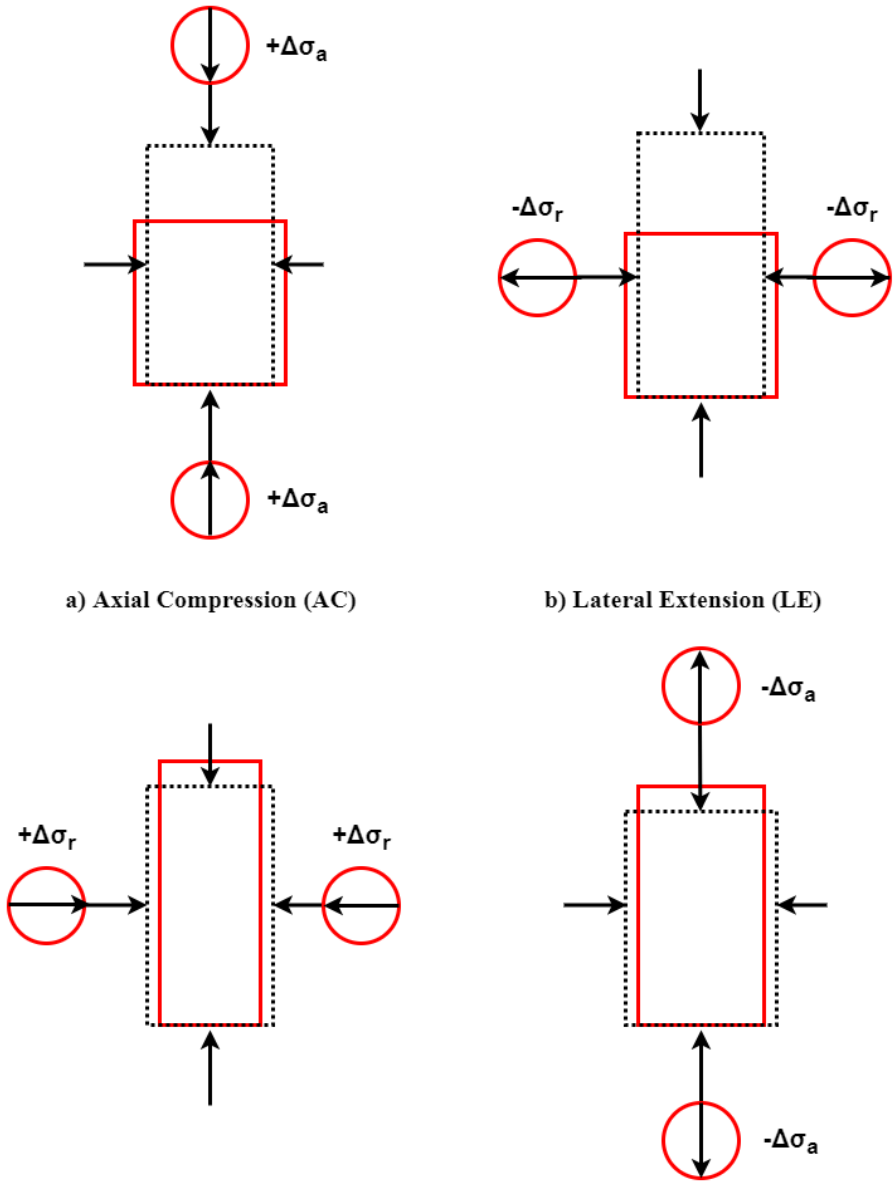

Figure 7.2 Illustration of three-dimensional triaxial drained loading paths (after Springman *et al.* 2013)

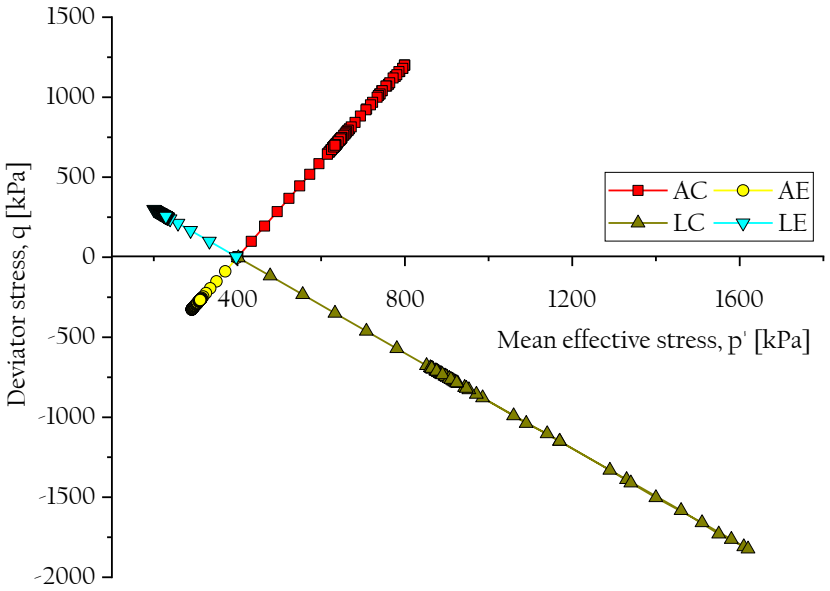

Figure 7.3 Triaxial drained loading paths in the $q-p'$ space

7.5 Simulation details

A random sand particle in the form of an STL file (clump template file) using the MS approach is modelled. More information regarding the MS approach can be found in Section 3.4. In clump template, each constituent particle is formed by joining and overlapping individual spheres (called pebbles in PFC) at different coordinates, which then behave as a rigid body that does not break apart, regardless of the magnitude of forces acting upon it (Li & Yu 2010; Yang *et al.* 2013). In PFC, modelling the clump template pebbles can occur via the BubblePack algorithm (Taghavi 2000). A triangulated surface must be specified with geometry, and no manual generation of pebbles is allowed. These pebbles are filtered based on their morphological descriptors such as ξ which is the ratio of the smallest to the largest pebble within the clump ($0<\xi<1$) and β corresponds to an angular measure of smoothness ($0°<\beta<180°$). Taking computational limitations and associated costs into account, the following parameters are adopted: $\xi=0.5$ and $\beta=150°$. The main effects of the morphological descriptors (i.e., ξ and β) on the macro- and the micro-scale

response of granular materials were described by Kodicherla *et al.* (2020). A map of clumps with a different plane of orientations is presented in Figure 7.4. In total, 60 numerical simulations are performed for 12 different series of numerical simulations. Each series has 5 simulations with different confining pressures (p_o' = 100, 200, 400, 800 and 1600 kPa), under four different stress paths. For example, Series I – III involve AC stress path tests on three different states of assemblies, i.e., AC_L, AC_M and AC_D. These states of assemblies typically represent loose, medium and dense states based on theirs I_D. All samples are sheared to a maximum ε_a of 60%, at which the critical state failure can be identified. A summary of the DEM simulation results under different stress paths is considered, where the subscript '0' denotes the onset shear or end of isotropic compression as presented in Appendix - A.

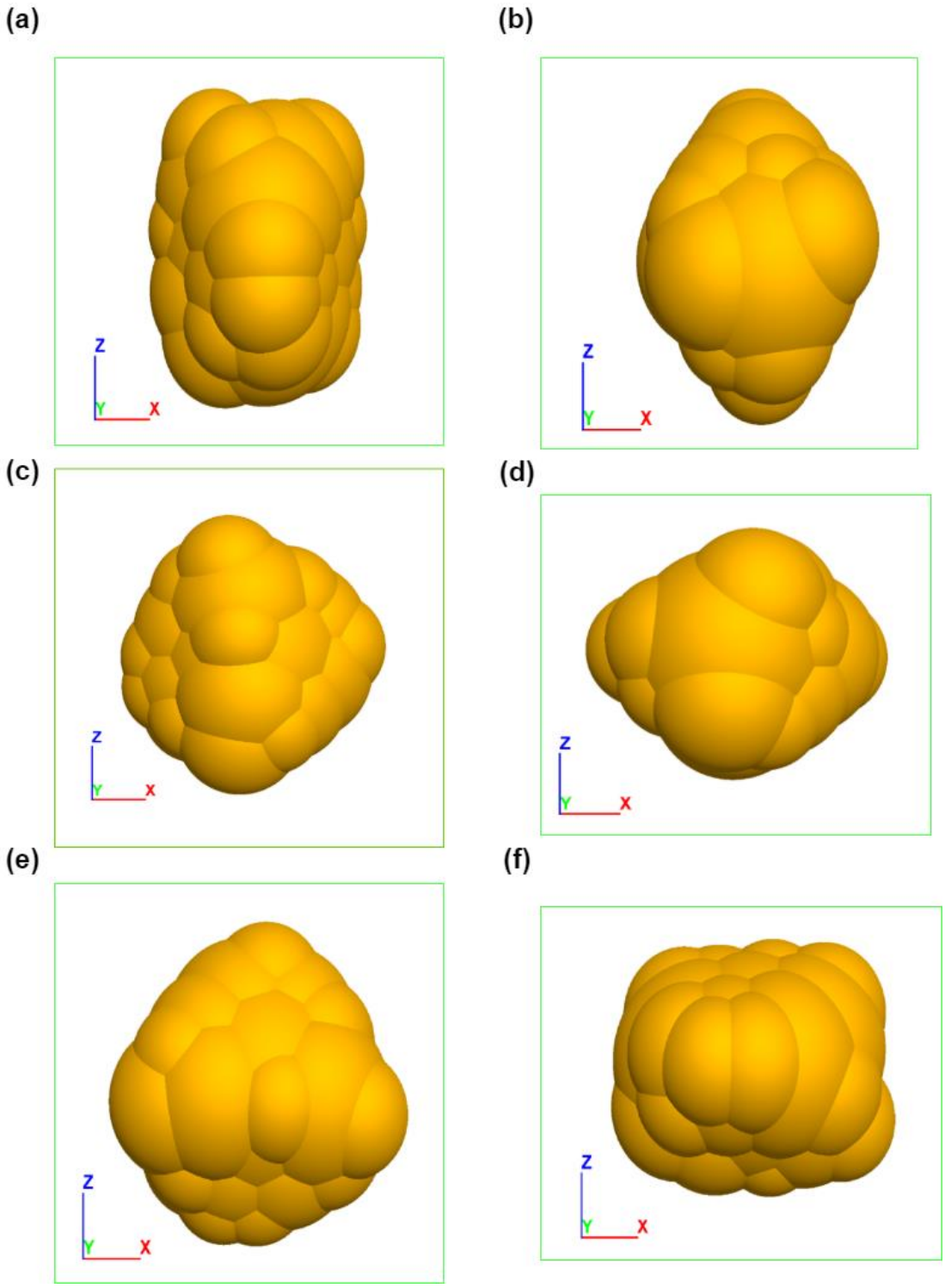

Figure 7.4 Map of clumps along the different plane of orientations: (a) XYZ (b) XZY (c) YXZ (d) YZX (e) ZXY and (f) ZYX

7.6 Simulation results

7.6.1 Macroscopic behaviour

The macroscopic evolution of stress ratio ($\eta = q/p'$) against axial strain (ε_a) for the two extreme values of p_0' and three different states of assemblies under AC and AE stress path tests are presented in Figure 7.5(a) and Figure 7.6(a), respectively. It is observed that independent of the applied p_0', dense samples exhibit post-peak strain-softening behaviour, whereas loose samples show a strain hardening response. Also, the medium dense samples exhibit initial hardening with minor post-peak strain-softening behaviour. Independent of stress paths, in all samples, the critical states are attained after $\varepsilon_a > \sim$ 50%.

In terms of volumetric responses, it is observed that dense samples are more dilative while loose samples exhibited extreme contractive responses. For medium dense samples, initial contraction followed by dilation behaviour is identified (see Figure 7.5(b) and Figure 7.6(b)). These behaviours are irrespective of the stress path tests considered. Moreover, these characteristics well represent the typical behaviour of granular materials, which are well documented in the literature (Gong *et al.* 2012; Gong & Zha 2013).

Figure 7.5(c) and Figure 7.6(c) present the evolution of void ratio (e) against ε_a for AC and AE stress paths, respectively. The e increases with increasing ε_a in dense samples, whereas e decreases with increasing ε_a in loose samples. For both the cases, e flattens off after $\varepsilon_a \sim$ 50% and reaches a critical value. A unique value e_c is achieved for a given p_0'. Moreover, the e_c decrease with increasing p_0'.

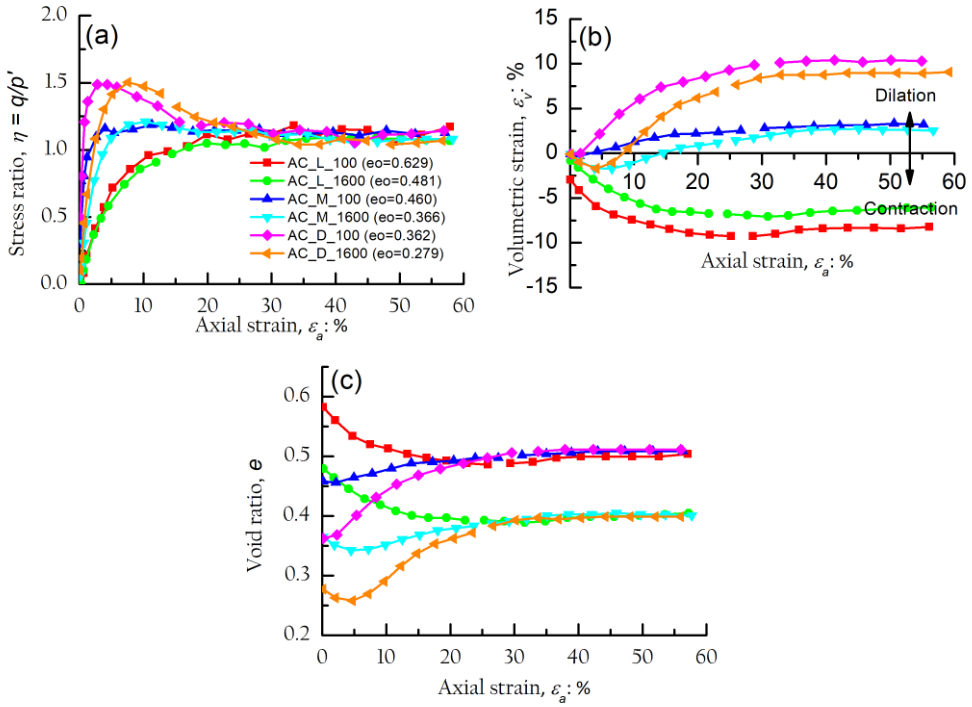

Figure 7.5 Macroscopic results of AC test: (a) $\varepsilon_a - \eta$; (b) $\varepsilon_a - \varepsilon_v$; (c) $\varepsilon_a - e$

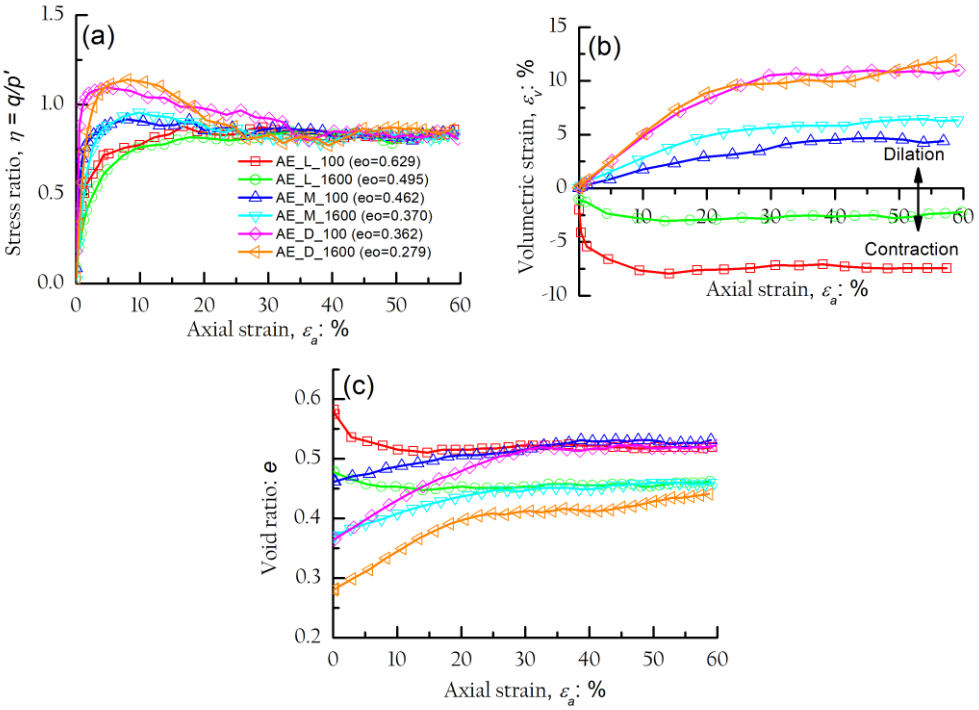

Figure 7.6 Macroscopic results of AE test: (a) $\varepsilon_a - \eta$; (b) $\varepsilon_a - \varepsilon_v$; (c) $\varepsilon_a - e$

Figure 7.7 illustrates the comparison of loading path tests results for medium dense samples with different confining pressures (i.e., 100, 200, 400, 800, and 1600 kPa) for Series - II and Series - V, respectively. For both AC and AE tests, the η exhibits minor post-peak strain-softening behaviour and reaches a critical value after $\varepsilon_a > \sim 50\%$ (see Figure 7.7(a)). The volumetric behaviour for the AC test showed considerable initial contraction (i.e., up to $\varepsilon_a \sim$ 10%) whereas, for the AE test, a well-represented dilation is noticed from the onset shear (see Figure 7.7(b)). Interestingly, it is found that irrespective of the stress path tests, the confining stresses showed a significant influence on e_o (i.e., $0.366 \sim 0.460$). Moreover, the critical state stress-ratio for the AC test ($M_c = q/p' = 1.08$) is higher than that obtained for the AE test ($M_e = q/p' = 0.83$) (see Figure 7.7(c)). The ratio of M_c / M_e = 1.30 is very close to the typical range of the standard Toyoura sands evaluated from laboratory experiments (Lade & Duncan 1975; Kulhawy & Mayne 1990; Yoshimine *et al.* 1998; Yang *et al.* 2008). A numerical investigation by Ng (2004) was found that relative value of stress ratio of 1.12 and 1.09 for two different aspect ratios of ellipsoids (i.e., 1.2 and 1.5) respectively, which are slightly smaller than those obtained in this investigation. This may be attributed to the fact that particle morphological features can affect the critical state stress ratios of granular materials (Kodicherla *et al.* 2020).

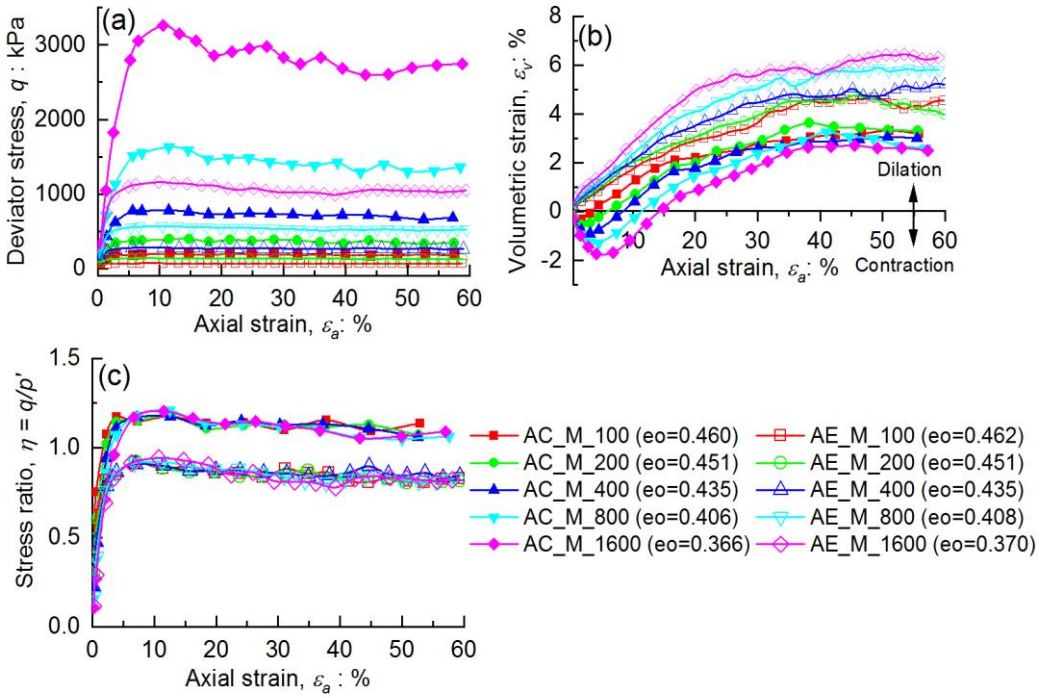

Figure 7.7 Comparison of triaxial stress path results for Series - II and Series - V: (a) $q-\varepsilon_a$; (b) $\varepsilon_v-\varepsilon_a$; (c) $\eta-\varepsilon_a$

7.6.2 Comparison of drained triaxial loading paths

Figure 7.8 compares the stress-strain response of DEM samples sheared under different loading paths isotropically compressed at $p_o = 400kPa$. The q for AC and LE are positive, while for LC and AE are negative. Moreover, the volumetric strain for the LE sample followed that of the AE sample while the volumetric strain for the AC sample is similar to that of the LC sample. It is confirmed that isotropic samples sheared in the same loading mode yield the same behaviour regardless of loading directions (see Figure 7.8), which is in line with the reported results by Huang *et al.* (2014).

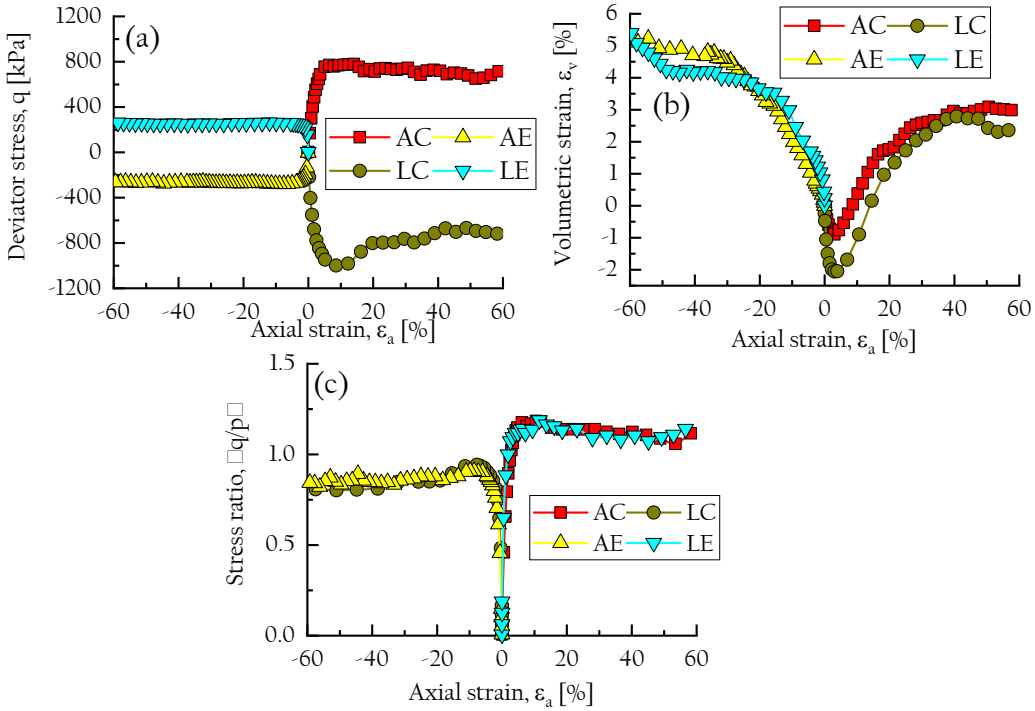

Figure 7.8 Stress-strain behaviour of DEM samples sheared under different loading paths ($p_o' = 400\ kPa$)

7.6.3 Evolution of critical state characteristics

A brief overview of the CSSM framework is presented in Chapter 4 (see Section 4.9). The CSSM framework can be described by two unique relationships, given as:

$$q = Mp' \tag{7.2}$$

$$e_c = \Gamma - \lambda\left(p' / p_a\right)^{\varsigma} \tag{7.3}$$

where M is a critical stress ratio, Γ is the intercept of the CSL and λ is the slope of the CSL in the $e - p'$ space and ς are the material constants and p_a is the atmospheric pressure for normalization.

Figure 7.9 presents the critical state characteristics for AC and AE loading paths. Referring to Figure 7.9(a), it is observed that the CSLs show an obvious

dependency on the loading paths. The CSL of AE path is located above than that of AC path in the $e-p'$ space, which is in agreement with the simulated results reported by Li (2006). Also, these CSLs collapses into two different trend lines with a unique independent critical state parameter (see Figure 7.9(b)). The AC loading path test has $\Gamma_c = 0.522$ and $\lambda_c = 0.0133$, while the AE has $\Gamma_e = 0.534$ and $\lambda_e = 0.0139$. Irrespective of the loading paths, both CSLs fit into very-well with considerable spacing between them and has a regression value greater than $R^2 = 0.98$. As noticed in Figure 7.9(c), the critical state data points in the $q-p'$ space are linearly fitted and considered to pass through the origin with slopes of $M_c = 1.106$ and $M_e = 0.838$, respectively. Moreover, the critical strength of the AC loading path test is found to be higher than that obtained from the AE loading path. These findings are in agreement with a study conducted by Yang & Wu (2016) for undrained loading paths using clumped particles with an aspect ratio of 0.6.

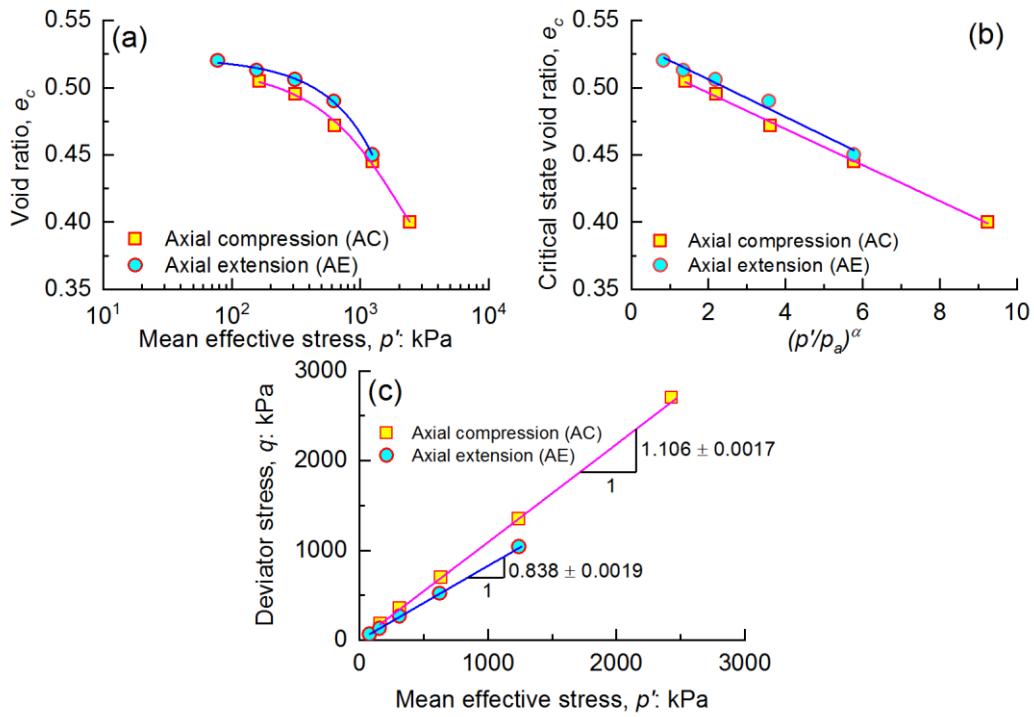

Figure 7.9 Critical state characteristics of AC and AE loading paths:

(a) $e_c - p'$ (b) $e_c - (p'/p_a)^{\varsigma}$ (c) $q-p'$

7.6.4 DEM analysis of the state parameter

Been & Jefferies (1985) introduced a scalar quantity called as the state parameter, i.e., $\psi = e - e_c$ where e is the current state void ratio and e_c is the critical state void ratio on the critical state line in the $e - p'$ space corresponding to the current p'_o as shown in Figure 7.10. A positive value of ψ signifies a loose state while a negative value ψ represents a dense state of the system. The ψ is chosen to be the state-dependent variable that is represented as (Li & Wang 1998):

$$\psi = e - e_c = e - [e_\Gamma - \lambda_c \left(p' / p_a \right)^\varsigma] \tag{7.4}$$

where e_Γ, λ_c and ς are the material constants determining the critical state line in the $e - p'$ space, p_a is the atmospheric pressure for normalization. Been & Jefferies (1985) observed from the triaxial test data that a clear link between ψ and the strength and dilatancy of sand. In the literature, recently developed constitutive models for soils have explicitly considered ψ in their formulation, e.g., NorSand (Jefferies 1993; Jefferies & Shuttle 2002; Wood *et al.* 1994), Severn–Trent sand (Gajo & Wood 1999) and the model proposed by Li & Dafalias (2000).

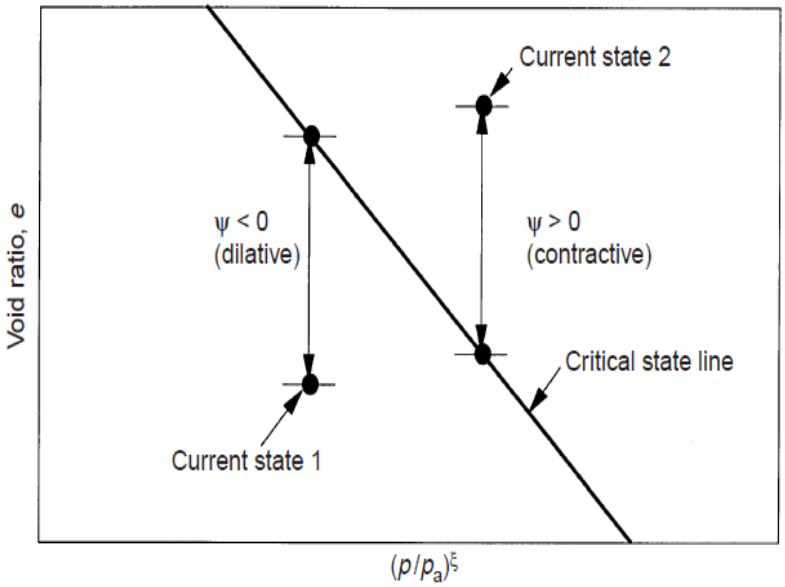

Figure 7.10 Critical state line and state parameter (ψ) (after Li & Dafalias 2000)

7.6.5 Relationship between the strength and state parameter

Many researchers (e.g., Castro 1969; Lade 1972; NGI 1982; Jefferies & Been 2006) struggled to have a quantitative comparison between the strength and the state-dependent response of granular materials. Figure 7.11 compares the peak angle of shearing resistance (ϕ_p) against the initial state parameter (ψ_o). The DEM results of the AC loading path results are generally in agreement with those of experimental triaxial compression tests performed on sands. However, the AE loading path tests data are consistently below the experimental values of sands, which do not compare well with the compression results. As it is difficult to achieve the densest state in experimental tests, the ϕ_p values of dense samples lied as an outlier to the right. Moreover, an experimental study conducted by Cho *et al.* (2006) and a DEM study executed by Maeda *et al.* (2009) confirmed that the shear strength of granular materials depends mainly on particle geometry, whereas a numerical study by Huang *et al.* (2014b) found that the shear strength of spherical particles is consistently below the experimental values, attributing to the particle geometry and interlocking.

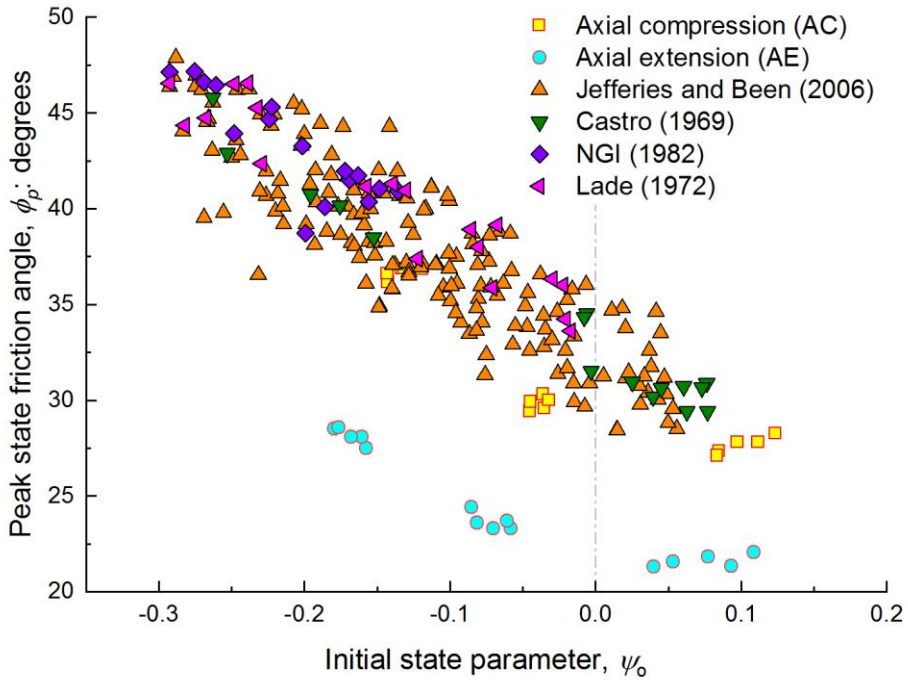

Figure 7.11 Relationship between ϕ_p and ψ_0

Following the approach suggested by Been & Jefferies (1985), the stress dilatancy angle of shearing resistance ($\phi_p - \phi_c$) against the ψ_0 is shown in Figure 7.12. The simulations results under both loading path tests are compared with experimental datasets reported in the literature (see Figure 7.12). Using this approach the responses observed in the DEM simulations well matched with those in the literature (e.g., Castro 1969; Lade 1972; NGI 1982; Jefferies & Been 2006).

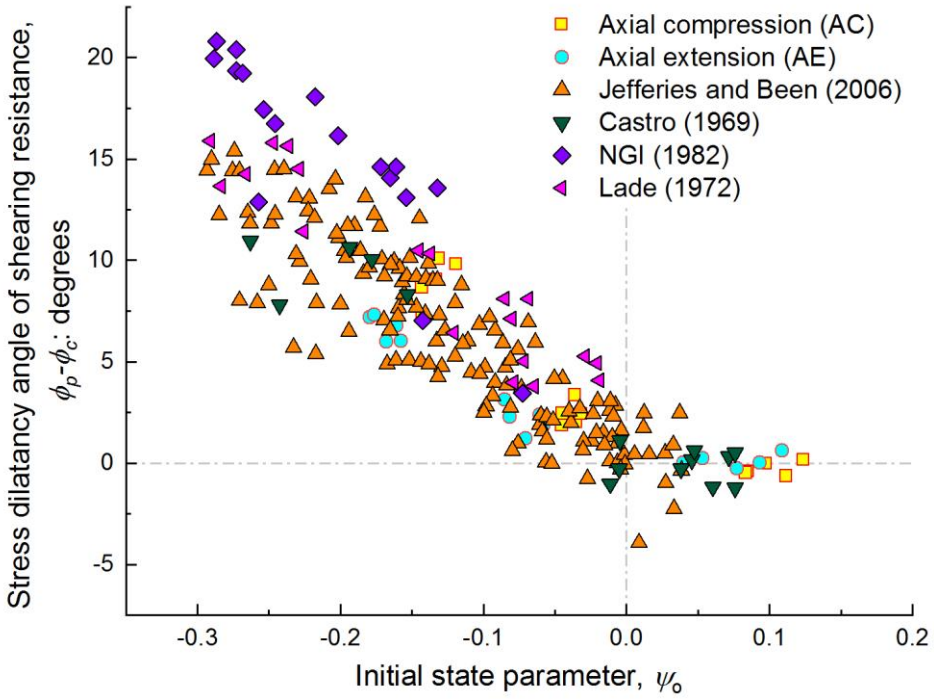

Figure 7.12 Relationship between $\phi_p - \phi_c$ and ψ_0

7.6.6 Relationship between dilatancy and state parameter

It was mentioned by Rowe (1962) that a similarity between friction angle (ϕ) and dilation rate (D) may be forecasted theoretically and the difference between ϕ_p and ϕ_c is directly related to the dilation rate. In practice, it is preferable to relate individual behaviours to the fundamental parameters of the state instead of relating derived behaviours to each other. According to Taylor (1948), the strength of soil can be distinguished into a dilational and intrinsic component. Consequently, the developments of this decomposition led to the stress-dilatancy theory suggested by Rowe (1962). Been & Jefferies (1985) introduced that the dilation rate ($D = -d\varepsilon_v / d\varepsilon_a$) at the peak ($D_p$) was related to the ψ_0. Figure 7.13 shows the relationship between D_p and ψ_0 for both the loading path tests. Besides, for a better comparison, the experimental data from Jefferies & Been (2006) is also superimposed in the plot. A unique relationship

is found between D_p and ψ_0 which is path-dependent and the DEM data lie within the range of the experimental values.

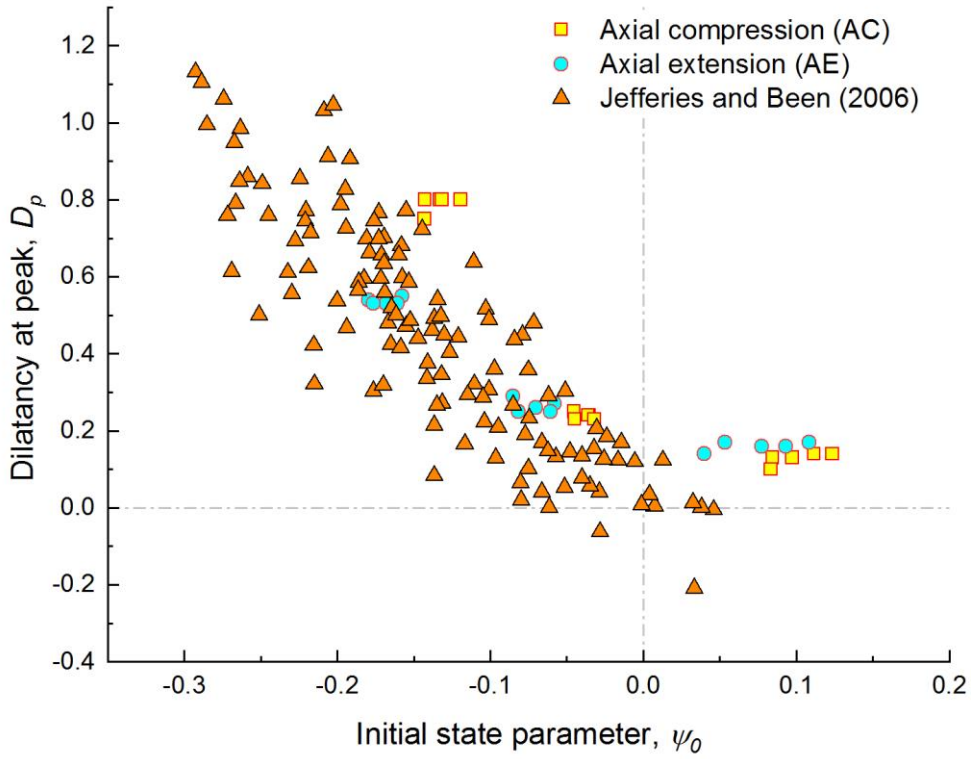

Figure 7.13 Relationship between D_p and ψ_0

Figure 7.14 illustrates the relationships among the strength in terms of ϕ_p, η_p and D_p. A linear relationship is observed between ϕ_p - D_p and η_p - D_p (see Figure 7.14(a) and (b)), which is typical for the standard sands as reported by Vaid & Sasitharan (1991). It is also found that the slope and the position of best-fit lines appear to be path-dependent. It was also reported in the literature that the dependency of strength parameters on the intermediate stress ratio of numerical simulations by Ng (2004) and Huang *et al.* (2014a).

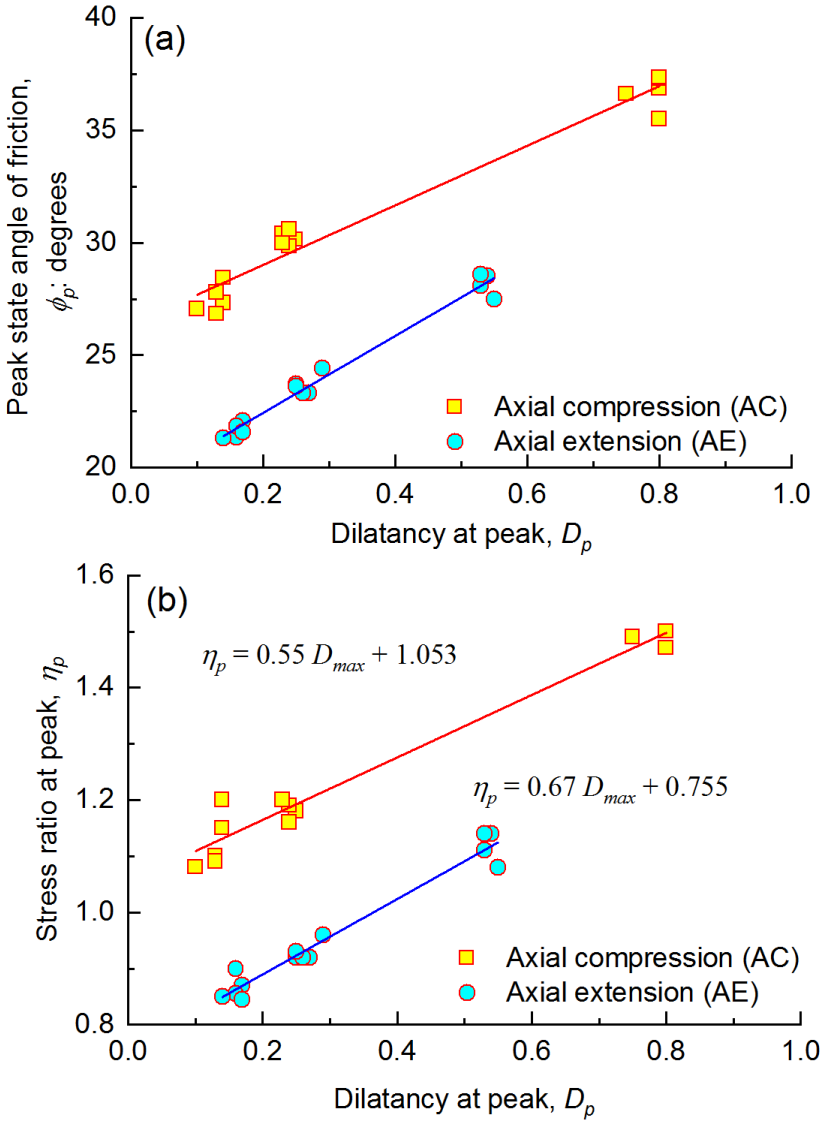

Figure 7.14 Relationship between peak strength and peak dilatancy: (a) $\phi_p - D_p$; (b) $\eta_p - D_p$

7.6.7 Evolution of microscopic quantities

From Figure 7.15(a) and (b), it is observed that for the onset shearing, i.e., $\varepsilon_a \sim$ < 10%, the *CN* increases for the *AC* loading path while decreases for the *AE* loading path, which is because contraction induces the formation of new contacts whereas dilation induces more contact disruptions. These behaviours are well represented by the volumetric responses for both loading paths considered (see Figure 7.15(b)). Also, for all the samples, *CN* reaches a critical value at large ε_a. Figure 7.15(c) shows the relationship of $p' - CN$ at the critical

state, which shows that the *CN* increases with increasing p_o', reflecting a decrease in the *e*. The data presented in Figure 7.15(d) indicates that these relationships are non-linear and dependent on the loading paths. Furthermore, it should be highlighted that the *CN* for the *AC* is higher than that obtained for *AE*.

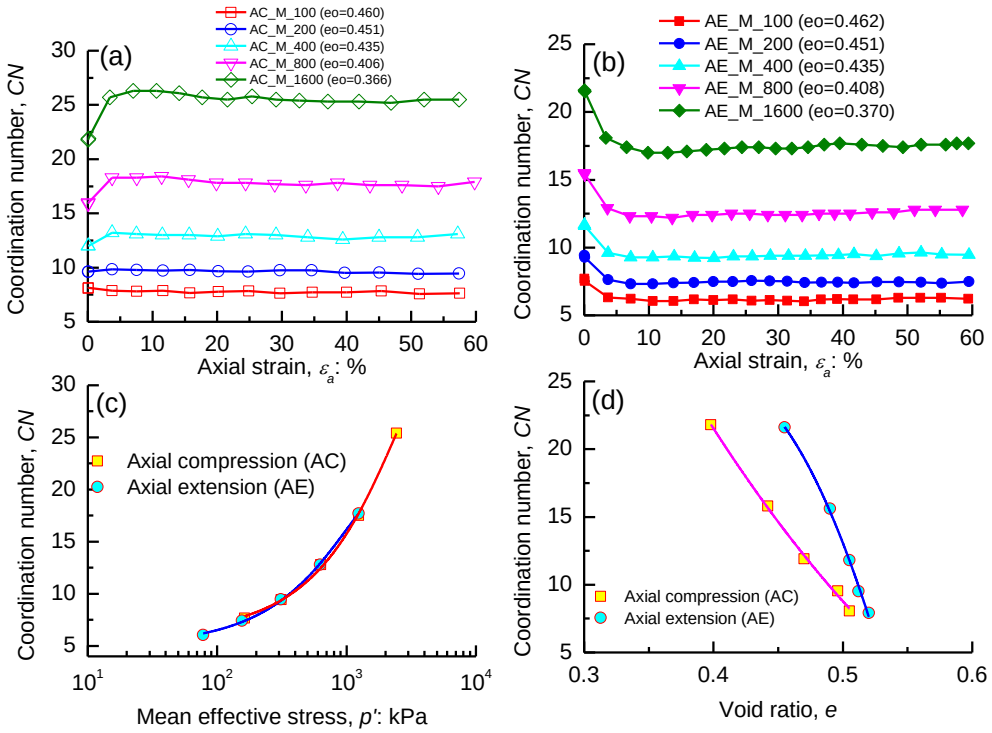

Figure 7.15 Evolution of *CN* for Series - II and Series - V: (a) $\varepsilon_a - CN$ for *AC* loading path; (b) $\varepsilon_a - CN$; (c) $p' - CN$ at critical state; (d) $p' - CN$ at a critical state.

Figure 7.16 shows the evolution of deviator fabrics for medium dense samples under the *AC* and *AE* loading paths. For both overall and strong deviator fabrics, it is found that the structural anisotropy increased to the peak and stabilized as ε_a further increased and finally reaches a critical value. Also, the strong force subnetworks generally follow the trend of the stress-strain behaviour as observed in Figure 7.5 and Figure 7.6, which supports the initiation of the strong force chain buckling that can be characterized by the appearance of peak structural anisotropy (Tordesillas & Muthuswamy 2009; Huang *et al.* 2014c).

Figure 7.16(c) and (d) show the relationships between the overall and strong deviator fabrics against p', respectively for Series - II and Series - V at the critical states. As it is noticed that the *AC* loading path results are found to be more anisotropic than the *AE* loading path. Moreover, the structural anisotropy at the critical state decreases with increasing p_o', which is significantly modified, especially in the strong deviator fabric $\phi_{d,str}$ in comparison to the overall deviator fabric ϕ_d.

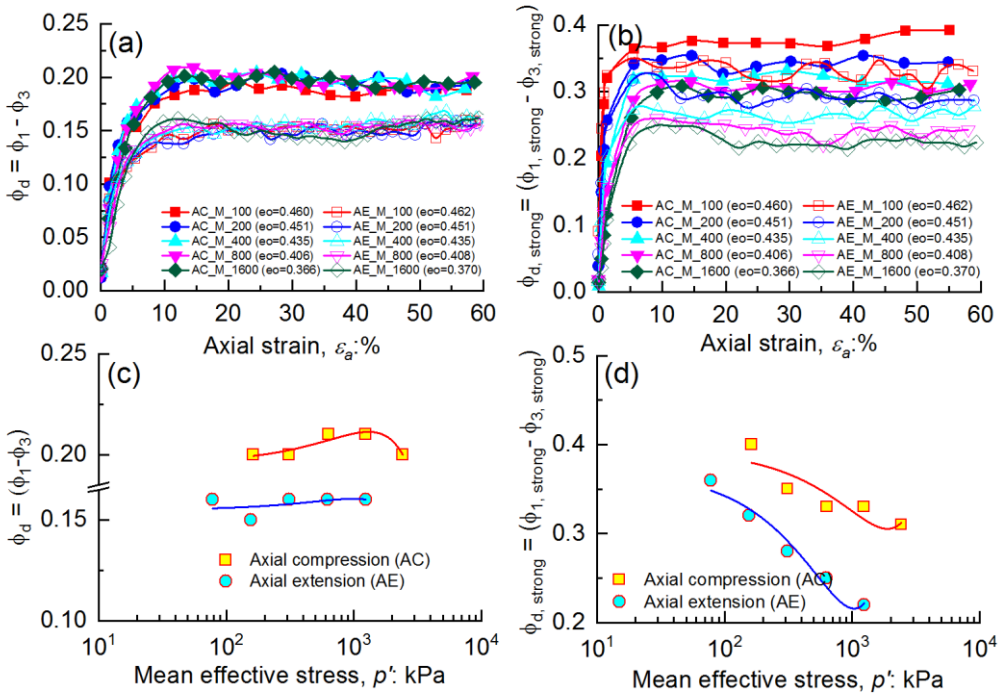

Figure 7.16 Evolution of deviator fabrics for Series - II and Series - V: (a) $\varepsilon_a - \phi_d$; (b) $\varepsilon_a - \phi_{d,strong}$; (c) $p' - \phi_d$ at the critical state; (d) $p' - \phi_{d,strong}$ at the critical state

7.7 Summary

This chapter has presented the results of strength and critical state behaviour of granular materials under different drained triaxial loading paths using DEM. In total, sixty numerical simulations are performed by considering the different states of assemblies based on their density index and sheared to the maximum value to achieve critical states. The numerical results are analyzed at the macro

and micro scale levels, examining the uniqueness of the critical state lines and relationships among strength, dilation and state parameters.

It is found that all samples have reached critical values after an axial strain of $\sim$ 50%. A unique critical state void ratio is achieved for a given mean effective stress, which is confirmed to be path-dependent. The critical void ratios are found to decrease with increasing mean effective stress. For medium dense samples, independent of loading paths, the mean effective stress affected the onset void ratio. Moreover, at a critical state, the value of the critical stress ratio for the axial compression loading path is higher than that obtained for the axial extension. It is also confirmed that the samples sheared under the same loading mode yield the same behaviour regardless of loading directions.

The critical state lines in the $e-p'$ space are found to be path-dependent and the critical strengths of granular materials in the axial compression loading path is higher than that of axial extension. The coordination numbers increase with increasing mean effective stress showing a decrement in the void ratio. The relationships between coordination number and void ratio are found to be non-linear and mainly depends on the stress paths. Moreover, the structural anisotropy at the critical state decreases with increasing mean effective stress.

Chapter 8 Summary and Conclusions

8.1 Summary

The principal objective of the current research is to explore the mechanical behaviour of granular materials considering particle shape characteristics using discrete element modelling (DEM). Two commonly used fundamental geotechnical laboratory tests, i.e., the direct shear test and triaxial test, were chosen for consideration into this research.

8.1 Principal findings

8.1.1 Direct shear test

A series of physical direct shear tests were conducted on natural sand and subsequent numerical simulations were also performed. Based on the analysis of results and discussions, the following conclusions are drawn:

1. A series of numerical direct shear test simulations were performed to investigate the sensitivity to microscopic parameters. All samples were one-dimensionally compressed at 75 kPa. The particle numbers were not sensitive to the macroscopic behaviour, whereas the ratio between mean unbalanced force and the mean contact force against shear strain for different particle numbers were found to be sensitive. The specimen response was found to be sensitive to the interparticle friction coefficient. Except for 6.0×10^{-2} mm/s, the macroscopic response of the specimen was not sensitive to the loading rate. Moreover, the specimen was also not sensitive to the damping and stiffness ratios.

2. The DEM results of direct shear test employing generated realistic clumps were generally in agreement with the laboratory test data. This shows the capability of the particle generation approach. However, the

peak angle of shearing resistance was found to be consistently higher than those obtained from the laboratory tests. The microscopic results in terms of fabric anisotropy were found to increase with the increase in normal stress and showed a significant influence on the structural anisotropy.

3. For elongated particles, the peak state direct shear friction angles were initially increased and stay stable as Λ further increases. The critical state direct shear friction angles were found to increase with the increase in Λ. Also, it was found that independent of applied normal stresses, all samples reached a unique normalized stress ratio at the critical state.

4. The trend of coordination numbers of elongated particles under the direct shear test was found to decrease rapidly at the onset and slowly attains almost steady value at the critical state. There seems no significant variation was noticed among the evolution of coordination numbers, except for sample S1. For small strains, it was found that the deviator fabric depends on both the stress and volume change, whereas for large strains, the volume approaches to a stable value and found to mainly depend on the stress only. The trends of strong force sub-network (major principal value), were similar to the evolutions of stress ratios which describes the major contribution to the stress-fabric relationship was mainly governed by the strong force components.

5. A relationship between $\phi_p - \phi_c$ and Ψ_p was found to be well-fitted with acceptable regression value. Also, it was observed that as particles elongate, the downward shifting of critical state lines was noticed. The intercept values were slightly increased initially and then decreases to

the minimum value. Besides, the critical state parameters for each sample indicating almost parallel and minor slope was noticed.

8.1.2 Triaxial shear test

A series of numerical simulations were performed considering particle elongations, morphology and various loading paths under drained triaxial test conditions. Based on the simulation results, the following conclusions are drawn:

1. The same particle elongation methodology (i.e., see in Chapter 4) was used to investigate the critical state behaviour under drained triaxial test conditions. At the macroscopic level, similar observations were noticed.

2. At the microscopic level, the onset of coordination number decreases with increasing Λ, while at the steady-state coordination numbers found to increase with the increase in Λ values. The trend of deviator fabric followed as same as the stress-strain response.

3. The relationship between critical stress ratio and critical state parameters were found to decrease with increasing particle shape parameters. Moreover, irrespective of the critical state parameters, acceptable regression values were achieved.

4. Two morphological descriptors, i.e., ξ represents the particle geometry and β represents the surface texture of the particle, were considered to investigate the particle morphology at the macroscopic and microscopic level. The peak state angles decrease with an increase of β and increase with an increase of ξ. Moreover, the deviation between angles of friction

at peak state and critical state was found to have an increasing trend as ξ increases, which was believed to increase in the dilation angle.

5. The coordination numbers experience a significant exponential decay before reach $\varepsilon_1 = 15\%$ and stabilize as a further increase in the axial strain. The probability distributions were found to be well-fitted by a Gaussian distribution function and found to be a systematic skewness to the distributions. The relationships were found to be approximately linear before their peaks.

6. Notwithstanding the loading paths, independent of the applied initial mean effective stresses, dense samples show post-peak strain-softening behaviour while loose samples were found to exhibit strain hardening response. Also, the medium dense samples exhibit initial hardening with minor post-peak strain-softening behaviour.

7. The deviator stress for AC and LE are positive while for LC and AE are negative. Moreover, it was found that the isotropic samples sheared in the same loading mode yield the same behaviour regardless of loading directions.

8. For AC and AE loading paths, irrespective of the loading paths, critical state lines were found to fit into a very-well and considerable spacing between them. For a given mean effective stress, a unique critical state void ratio was found to be path-dependent.

9. A linear relationship was found between ϕ_p - D_p, the slope and the position of best-fit lines appeared to be path-dependent. Also, a unique relationship was found between D_p - ψ_0 which was also believed to be path-dependent.

10. The microscopic parameters in terms of coordination numbers found to increase with increasing mean effective stress and a decrement were noticed in the void ratio. The relationships between coordination number and void ratio were found to be non-linear and mainly depends on the loading paths. Moreover, the structural anisotropy at the critical state decreases with increasing mean effective stress.

8.2 Future perspectives

In the current research, the influences of particle shape characteristics on the macro- and micro-scale behaviour of granular materials were explored under the direct shear test and triaxial test conditions using DEM. To further advance the findings of the current research, a few suggestions for future research are given below.

1. Although an attempt was made to investigate and validate the experimental results from direct shear test considering the major plane of orientation of realistic sand particles, the future research needs to consider an improved version of 3D geometric reconstruction approaches to track the true mechanical behaviour of granular materials.

2. The macroscopic response of numerical assembly under the direct shear test was quantitatively in agreement with experimental results. However, there seems minor deviations were noticed, which could be pertinent to the sensitivity to the particle numbers and initial conditions of the sample. Therefore, in future research, these aspects need to be taken into account to fully enhance the DEM capabilities.

3. Even though a random clumped particle was used to explore the effects of loading path tests, the stress level considered seemed to be beyond the normal range that would be considered in laboratory tests. At that high-

stress level, particle crushing is unavoidable and may dominate the overall stress-deformation response. However, such a mechanism was absent in the current study which must be considered in future research.

4. One more issue which could be possibly explored in the future research is that very limited attention has been made in the literature to fluid coupling with DEM employing different particle shapes (e.g., Liu *et al.* 2015; Foroutan & Mirghasemi 2020). Future research needs to consider the particle shapes along with fluid coupled DEM to understand the mechanical behaviour of saturated soils.

5. The future research will also focus on true triaxial stress paths considering different intermediate principal stress values and undrained test conditions. Also the evolution of the rotation of principal stress direction under direct shear test conditions.

Bibliography

[1]. Abbireddy, C. O. R. & Clayton, C. R. I. (2010) Varying initial void ratios for DEM simulations. *Geotechnique*. 60(6), 497–502.

[2]. Abedi, S. & Mirghasemi, A.A. (2011) Particle shape consideration in numerical simulation of assemblies of irregularly shaped particles. *Particuology*. 9(4), 387–397.

[3]. Alonso-Marroquin, F. (2008) Spheropolygons: a new method to simulate conservative and dissipative interactions between 2d complex shaped rigid bodies. *Europhysics Letters*. (EPL) 83(1), 14001.

[4]. Alonso-Marroquin, F. Luding, S. Herrmann, H.J. & Vardoulakis, I. (2005) Role of the anisotropy in the elastoplastic response of a polygonal packing. *Physical Review E*. 71, 051304.

[5]. Alshibli, K. A. & Cil, M. B. (2018) Influence of Particle Morphology on the Friction and Dilatancy of Sand. *Journal of Geotechnical and Geoenvironmental Engineering*. 144(3), 04017118.

[6]. Amirpour Harehdasht, S., Roubtsova, V., Chekired, M., Hussien, M.N. & Karray, M. (2018) Micromechanics-based assessment of reliability and applicability of boundary measurements in symmetrical direct shear test. *Canadian Geotechnical Journal*. 55(3), 397-413.

[7]. Ando, E., Hall, S.A., Viggiani, G., Desrues, J. & Besuelle, P. (2012) Experimental micromechanics: grain-scale observation of sand deformation. *Geotechnique Letters*. 2(3), 107–112.

[8]. Andrade, J.E. & Mital, U. (2019) Multiscale and Multiphysics modeling of soils. *Geotechnical Fundamentals for Addressing New World Challenges*. 141-168.

[9]. Andrade, J.E., Lim, K.W., Avila, C.F. & Vlahinić, I. (2012) Granular element method for computational particle mechanics. *Computer Methods in Applied Mechanics and Engineering*. 241–244, 262–274.

[10]. Anitha Kumari, S.D. (2012) *Effect of particle shape on the mechanical behaviour of granular media: Discrete element simulations*. PhD thesis.

[11]. Araujo, G.S. Bicalho, K.V. & Tristao, F.A. (2017) Use of digital image analysis combined with fractal theory to determine particle morphology and surface texture of quartz sands. *Journal of Rock Mechanics and Geotechnical Engineering*. 9, 1131-1139.

[12]. Azéma, E. & Radjaï, F. (2010) Stress–strain behavior and geometrical properties of packings of elongated particles. *Physical Review E*. 81, 051304.

[13]. Azéma, E. & Radjaï, F. (2011) Force chains and contact network topology in packings of elongated particles. *Physical Review E*. 85, 031303.

[14]. Azéma, E., Radjaï, F. & Dubois, F. (2013) Packings of irregular polyhedral particles: strength, structure, and effects of angularity. *Physical Review E*. 87, 062203.

[15]. Bagherzadeh-Khalkhali, A. & Mirghasemi, A. (2009) Numerical and experimental direct shear tests for coarse-grained soils. *Particuology*. 7, 83-91.

[16]. Barreto, D. & O'Sullivan, C. (2012) The influence of inter-particle friction and the intermediate stress ratio on soil response under generalised stress conditions. *Granular Matter*. 14, 505–521.

[17]. Barrett, P. J. (1980) The shape of rock particles, a critical review. *Sedimentology*. 27, 291–303.

[18]. Bathe, K.J. & Wilson, E.L. (1976) *Numerical Methods in Finite Element Analysis*. Englewood Cliffs: Prentice-Hall.

[19]. Been, K. & Jefferies, M.G. (1985) A state parameter for sands. *Géotechnique*. 35 (2), 99–112.

[20]. Been, K., Jefferies, M. G. & Hachey, J. (1991) The critical state of sands. *Geotechnique*. 41(3), 365-181.

[21]. Bjerrum, L. & Landva, A. (1966) Direct simple-shear tests on a norwegian quick clay. *Géotechnique*. 16 (1), 1–20.

[22]. Bolton, M.D. (1986) The strength and dilatancy of sands. *Geotechnique*. 36(1), 65–78.

[23]. Boton, M., Azéma, E., Estrada, N., Radjai, F. & Lizcano, A. (2013) Quasistatic rheology and microstructural description of sheared granular materials composed of platy particles. *Physical Review E*. 87, 032206.

[24]. Carrera, A., Coop, M.R. & Lancellotta, R. (2011) Influence of sample preparation techniques and stress path followed on the location of the Critical State Line : an example of a silty-sandy tailing. *In: International Symposium on Deformation Characteristics of Geomaterials*. 526–532.

[25]. Casagrande, A. (1936) Characteristics of cohesionless soils affecting the stability of earth fills. *Journal of Boston Society of Civil Engineering. Reprinted in Contributions to soil mechanics*. 1925-1940.

[26]. Castro, G. (1969) *Liquefaction of sand*. PhD thesis. Division of Engineering and Applied Physics, Harvard University.

[27]. Cavarretta, I., Coop, M. & O'Sullivan, C. (2010) The influence of particle characteristics on the behavior of coarse grained soils. *Geotechnique*. 60(6), 413-423.

[28]. Charles, J. A. & Watts, K. S. (1980) The influence of confining pressure on the shear-strength of compacted rockfill. *Geotechnique*. 30(4), 353–367.

[29]. Cheng, Z. & Wang, J. (2018) Experimental investigation of inter-particle contact evolution of sheared granular materials using X-ray micro-tomography. *Soils and Foundations*. 58, 1492-1510.

[30]. Chew, L.P. (1989) Constrained Delaunay triangulations. *Algorithmica*. 4, 97-108.

[31]. Cho, G.C., Dodds, J. & Santamarina, J.C. (2006) Particle Shape Effects on Packing Density, Stiffness, and Strength: Natural and Crushed Sands. *Journal of Geotechnical and Geoenvironmental Engineering*. 132, 591–602.

[32]. Christoffersen, J., Mehrabadi, M. & Nemat-Nasser, S. (1981) A micro-mechanical description of granular material behaviour. *Journal of Applied Mechanics*. 48(2), 339–344.

[33]. Chu, J. (1995) An experimental examination of the critical state and other similar concepts for granular soils. *Canadian Geotechnical Journal*. 32(6), 1065–1075.

[34]. Cleary, P.W. (2010) DEM prediction of industrial and geophysical particle flows. *Particuology*. 8, 106–118.

[35]. Cui, L. & O'Sullivan, C. (2006) Exploring the macro- and micro-scale response of an idealised granular material in the direct shear apparatus. *Geotechnique*. 56(7), 455-468.

[36]. Cundall, P. A. & Strack, O.D.L. (1979c) *The discrete element method as a tool for research in granular media*. Part II. Report to National Science Foundation, Department of Civil & Mineral Engineering. University of Minnesota, Minneapolis, Minnesota.

[37]. Cundall, P. A. (1971) A computer model for simulating progressive, large-scale movements in blocky rock systems. *Proc. Symp. Int. Soc. Rock Mech*. Nancy, 2, 132-150.

[38]. Cundall, P.A. & Strack, O.D.L. (1979) The development of constitutive laws for soil using the distinct element method. *Third International Conference on Numerical Methods in Geomechanics, Wittke (Eds), Balkema, Aachen*, 289-298.

[39]. Cundall, P.A. & Strack, O.D.L. (1979b) A discrete numerical model for granular assemblies. *Geotechnique*. 29(1), 47-65.

[40]. Cundall, P.A. (1974) A computer model for rock-mass behaviour using interactive graphics for the input and output of geometrical data. *Report for the Missouri River Division*. U.S. Army Corps of Engineers, University of Minnesota.

[41]. Cundall, P.A. (1978) *BALL-A computer program to model granular media using the distinct element method*. Technical note TN-LN-13. *Advance Technology Group*. Dames and Moore, London.

[42]. Cundall, P.A. (1988) *Computer simulations of dense sphere assemblies*. Micromechanics of granular materials, Satake and Jenkins (eds), Elsevier Science Publishers, Amsterdam, Netherlands, 113-123.

[43]. Cundall, P.A. (2001) A discontinuous future for numerical modelling in geomechanics? *Proceedings of the Institution of Civil Engineers, Geotechnical Engineering*. 149(1), 41 – 47.

[44]. Deluzarche, R. & Cambou, B. (2006) Discrete numerical modelling of rockfill dams. *International Journal for Numerical and Analytical Methods in Geomechanics*. 30(11), 1075–1096.

[45]. Deresiewicz, H. (1958a) Mechanics of granular matter. *Advances in mechanics*. 5, 233-306.

[46]. Deresiewicz, H. (1958b) Stress-strain relations for a simple model of a granular medium. *Journal of Applied Mechanics*. 25, 402-406.

[47]. Dey, T.Z.W. (2003) Approximating the medial axis from the Voronoi diagram with a convergence guarantee. *Algorithmica*. 38, 179-200.

[48]. Dubois, F., Jean, M., Renouf, M., Mozul, R., Martin, A. & Bagneris, M. (2011) LMGC90. *Engineering Sciences [physics] /Mechanics [physics.med-ph]*. In: 10e colloque national en calcul des structures. p Clé USB.

[49]. Duffy, J. & Mindlin, R.D. (1957) Stress strain relationships and vibrations of a granular medium. *Journal of Applied Mechanics*. 24, 585-593.

[50]. Duffy, J. (1959) A differential stress-strain relation for the hexagonal close packed array of elastic spheres. *Journal of Applied Mechanics*. 26, 88-94.

[51]. Favier, J.F., Abbaspour-Fard, M.H. & Kremmer, M. (2001) Modeling Nonspherical Particles Using Multisphere Discrete Elements. *Journal of Engineering Mechanics*. 127, 971–977.

[52]. Ferellec, J.F. & McDowell, G.R. (2008) A simple method to create complex particle shapes for DEM. *Geomechanical and Geoengineering: An International Journal*. 3(3), 211–216.

[53]. Foroutan, T. & Mirghasemi, A. (2020) CFD-DEM model to assess stress-induced anisotropy in undrained granular material. *Computers and Geotechnics*. 119, 103318.

[54]. Fu, P. & Dafalias, Y.F. (2015) Relationship between void-and contact normal-based fabric tensors for 2D idealized granular materials. *International Journal of Solids and Structures*. 63, 68–81.

[55]. Fu, X., Huck, D., Makein, L., Armstrong, B., Willen, U. & Freeman, T. (2012) Effect of particle shape and size on flow properties of lactose powders. *Particuology*. 10(2), 203–208.

[56]. Gajo, A. & Muir Wood, D. (1999) A kinematic hardening constitutive model for sands: the multiaxial formulation. *International Journal for Numerical and Analytical Methods in Geomechanics*. 23(9), 925–965.

[57]. Gander, W., Golub, G.H. & Strebel, R. (1994) Least-squares fitting of circles and ellipses. *BIT Numerical Mathematics*. 34(4), 558-578.

[58]. Gao, R., Du, X., Zeng, Y., Li, Y. & Yan, J. (2012) A new method to simulate irregular particles by discrete element method. *Journal of Rock Mechanics and Geotechnical Engineering*. 4(3), 276-281.

[59]. Garboczi, E.J. & Bullard, J.W. (2016) 3D analytical mathematical models of random star-shape particles via a combination of X-ray computed microtomography and spherical harmonic analysis. *Advanced Powder Technology*. 28(2), 325-339.

[60]. George, P.L. (2003) *Triangulation de Delaunay et Maillage*. Paris: Editions Hermes.

[61]. Goldenberg, C. & Goldhirsch, I. (2005) Friction enhances elasticity in granular solids. *Nature*. 435(7039), 188–191.

[62]. Gong, G. & Zha, X. (2013) DEM simulation of undrained behaviour with preshearing history for saturated granular media. *Modelling and Simulation in Materials Science and Engineering*. 21, 025001.

[63]. Gong, G. (2008) *DEM Simulations of Drained and Undrained Behaviour*. Ph.D. thesis, University of Birmingham, UK.

[64]. Gong, G., Zha, X. & Wei, J. (2012) Comparison of granular material behaviour under drained triaxial and plane strain conditions using 3D DEM simulations. *Acta Mechanica Solida Sinica*. 25(2), 186-195.

[65]. Gong, H., Song, W., Huang, B., Shu, X., Han, B., Wu, H. & Zou, J. (2019) Direct shear properties of railway ballast mixed with tire derived aggregates: Experimental and numerical investigations. *Construction and Building Materials*. 200, 465-473.

[66]. Gong, J. & Liu, J. (2017) Effect of aspect ratio on triaxial compression of multi-sphere ellipsoid assemblies simulated using a discrete element method. *Particuology*. 32, 49–62.

[67]. Gong, J., Liu, J. & Cui, L. (2019) Shear behaviors of granular mixtures of gravel-shaped coarse and spherical fine particles investigated via discrete element method. *Powder Technology*. 353, 178–194.

[68]. Gong, J., Nie, Z., Zhu, Y., Liang, Z. & Wang, X. (2019) Exploring the effects of particle shape and content of fines on the shear behaviour of sand-fines mixtures via the DEM. *Computers and Geotechnics*. 106, 161–176.

[69]. Goudarzy, M., König, D. & Schanz, T. (2016) Small strain stiffness of granular materials containing fines. *Soils and Foundations*. 56, 756–764.

[70]. Green, G.E. & Bishop, A.W. (1969) A note on the drained strength of sand under generalized strain conditions. *Geotechnique*. 19, 144–149.

[71]. Gu, X., Huang, M. & Qian, J. (2014) DEM investigation on the evolution of microstructure in granular soils under shearing. *Granular Matter*. 16 (1), 91–106.

[72]. Guo, N. & Zhao, J. (2013) The signature of shear-induced anisotropy in granular media. *Computers and Geotechnics*. 47, 1-15.

[73]. Guo, N. & Zhao, J. (2014) Local fluctuations and spatial correlations in granular flows under constant-volume quasistatic shear. *Physical Review E*. 89.

[74]. Guo, P. & Su, X. (2007) Shear strength interparticle locking, and dilatancy of granular materials. *Canadian Geotechnical Journal*. 44(5), 579–591.

[75]. Guo, Y. & Yu, X. (2015) Understanding the microscopic moisture migration in pore space using DEM simulation. *Journal of Rock Mechanics and Geotechnical Engineering*. 7, 171-177.

[76]. Gutierrez, M., Wang, J. & Yoshimine, M. (2009) Modeling of the simple shear deformation of sand: effects of principal stress rotation. *Acta Geotechnica*. 4, 193–201.

[77]. Hart, R., Cundall, P.A. & Lemos, J. (1988) Formulation of a three-dimensional distinct element model—Part II. Mechanical calculations for motion and interaction of a system composed of many polyhedral blocks. *International Journal Rock Mechanics and Mining Sciences & Geomechanics Abstracts*. 25, 117–125.

[78]. Hartl, J. & Ooi, J. (2011) Numerical investigation of particle shape and particle friction on limiting bulk friction in direct shear tests and comparison with experiments. *Powder Technology*. 212(1), 231-239.

[79]. Head, K.H. (1986) *Manual of soil laboratory testing*. Pentech Press, London.

[80]. Hertz, H. (1882) Über die berührung fester elastischer Körper. *Journal f¨ur die Reine und Angewandte Mathematik*. 29, 156–171.

[81]. Hohner, D., Wirtz, S. & Sherer, V. (2015) A study on the influence of particle shape on the mechanical interactions of granular media in a hopper using the Discrete Element Method. *Powder Technology*. 278, 286-305.

[82]. Hosseininia, E.S. (2012) Investigating the micromechanical evolutions within inherently anisotropic granular materials using discrete element method. *Granular Matter*. 14, 483–503.

[83]. Huang, X., Hanley, K.J., O'Sullivan, C. & Kwok, C.Y. (2014c) Exploring the influence of interparticle friction on critical state behaviour using DEM. International Journal for Numerical and Analytical Methods in Geomechanics, 38, 1276-1297.

[84]. Huang, X., Hanley, K.J., O'Sullivan, C. & Kwok, F.C.Y. (2014a) Effect of sample size on the response of DEM samples with a realistic grading. *Particuology*. 15, 107–115.

[85]. Huang, X., O'Sullivan, C., Hanley, K.J. & Kwok, C.Y. (2014b) Discrete-element method analysis of the state parameter. *Geotechnique*. 64(12), 954-965.

[86]. Indraratna, B., Ngo, T.N., Rujikiatkamjorn, C. & Vinod, J.S. (2014) Behavior of fresh and fouled railway ballast subjected to direct shear testing: Discrete element simulation. *International Journal of Geomechanics*. 14, 34-44.

[87]. Itasca (2002) *Itasca Manual, Theory and Backround. Itasca, second edition*.

[88]. *Itasca Consulting Group: Particle Flow Code in Three Dimensions (PFC3D)*. (2018) Itasca Consulting Group, Minneapolis.

[89]. Iwashita, K. & Oda, M. (1998) Rolling resistance at contacts in simulation of shear band development by DEM. *Journal of Engineering Mechanics*. 124(3), 285-292.

[90]. Jefferies, M.G. & Been, K. (2006) *Soil liquefaction: a critical state approach*. London, UK: Taylor and Francis.

[91]. Jefferies, M.G. & Shuttle, D.A. (2002) Dilatancy in general Cambridge-type models. *Géotechnique*. 52 (9), 625–638.

[92]. Jefferies, M.G. (1993) Nor-Sand: a simple critical state model for sand. *Geotechnique*. 43(1), 91–103.

[93]. Jerves, A.X., Kawamoto, R. Y. & Andrade, J. E (2015) Effects of grain morphology on critical state: a computational analysis. *Acta Geotechnica*. 11(3), 493-503.

[94]. Jerves, A.X., Kawamoto, R.Y. & Andrade, J.E. (2016) Effects of grain morphology on critical state: a computational analysis. *Acta Geotechnica*. 11(3), 493–503.

[95]. Jiang, M.D., Yang, Z.X., Barreto, D. & Xie, Y.H. (2018) The influence of particle-size distribution on critical state behavior of spherical and non-spherical particles assemblies. *Granular Matter*. 20(4), 80.

[96]. Jiang, M.J., Li, L. & Yang, Q. (2013) Experimental investigation on deformation behavior of TJ-1 lunar soil simulant subjected to principal stress rotation. *Advanced Space Research*. 52, 136–146.

[97]. Johnson, K. (1985) *Contact mechanics*. London: Cambridge University Press.

[98]. Katagiri, J., Matsushima, T. & Yamada, Y. (2010) Simple shear simulation of 3D irregularly-shaped particles by image-based DEM. *Granular Matter*. 12(5), 491–497.

[99]. Kawamoto, R., Andò, E., Viggiani, G. & Andrade, J.E. (2016) Level set discrete element method for three-dimensional computations with triaxial case study. *Journal of the mechanics and Physics of Solids*. 91, 1–13.

[100]. Kloss, C. & Goniva, C. (2011) LIGGGHTS - Open Source Discrete Element Simulations of Granular Materials Based on Lammps. *In: Supplemental Proceedings*. John Wiley & Sons, Inc., Hoboken, NJ, USA. 781–788.

[101]. Ko, H.Y. & Scott, R.F. (1967) A new soil testing apparatus. *Géotechnique*. 17, 40–57.

[102]. Kodicherla, S.P.K., Gong, G., Fan, L., Moy, C.K.S. & He, J. (2018) Effects of preparation methods on inherent fabric anisotropy and packing density of reconstituted sand. *Cogent Engineering*. 5(1), 1–14.

[103]. Kodicherla, S.P.K., Gong, G., Fan, L., Wilkinson, S. & Charles K.S. Moy (2020). DEM investigations of the effects of particle morphology on granular material behaviour using a multi-sphere approach. *Journal of Rock mechanics and Geotechnical Engineering*.

[104]. Kodicherla, S.P.K., Gong, G., Yang, Z.X., Krabbenhoft, K., Fan, L., Charles K.S. Moy. & Wilkinson, S. (2019) The influence of particle elongations on direct shear behaviour of granular materials using DEM. *Granular Matter*. 21(4).

[105]. Kozicki, J. & Donzé, F.V. (2009) YADE-OPEN DEM: an open-source software using a discrete element method to simulate granular material. *Engineering Computations.* 26(7), 786–805.

[106]. Kozicki, J., Tejchman, J. & Mróz, Z. (2012) Effect of grain roughness on strength, volume changes, elastic and dissipated energies during quasi-static homogeneous triaxial compression using DEM. *Granular Matter*. 14, 457–468.

[107]. Kozicki, J., Tejman, J. & Muhlhaus, H.B. (2014) Discrete simulations of a triaxial compression test for sand by DEM. *International Journal for Numerical and Analytical Methods in Geomechanics*. 38(18), 1923-1952.

[108]. Krumbein, W.C. & Sloss, L.L. (1963) *Stratigraphy and Sedimentation second ed*ition. Freeman and Company, San Francisco.

[109]. Krumbein, W.C. (1941) Measurement and geological significance of shape and roundness of sedimentary particles. *Journal of Sedimentary Research*. 11, 64–72.

[110]. Kuhn, M.R. (1999) Structured deformation in granular materials. *Mechanics of Materials*. 31(6), 407-429.

[111]. Kuhn, M.R. (2003) Smooth Convex Three-Dimensional Particle for the Discrete-Element Method. *Journal of Engineering Mechanics*. 129,539–547.

[112]. Kulhawy, F.H. & Mayne, P.W. (1990) *Manual on estimating soil properties in foundation design*. Palo Alto, CA: EPRI.

[113]. Kuo, C.Y., Rollings, R.S. & Lynch, L.N. (1998) Morphological study of coarse aggregates using image analysis. *Journal of Materials in Civil Engineering*. 10(3), 135-142.

[114]. Lade, P.V. & Duncan, J.M. (1975) Elastoplastic stress-strain theory for cohesionless soil. *Journal of Geotechnical Engineering Division*. 101(10), 1037–1053.

[115]. Lade, P.V. (1972) *The stress-strain and strength characteristics of cohesionless soils*. PhD thesis, University of California at Berkeley.

[116]. Lee, S. J., Hashash, Y. M. A. & Nezami, E. G. (2012) Simulation of triaxial compression tests with polyhedral discrete elements. *Computers and Geotechnics*. 43, 92–100.

[117]. Li, C.Q., Xu, W.J. & Meng, Q.S. (2015) Multi-sphere approximation of real particles for DEM simulation based on a modified greedy heuristic algorithm. *Powder Technology*. 286, 478–487.

[118]. Li, H. & McDowell, G.R. (2018) Discrete element modelling of under sleeper pads using a box test. *Granular Matter*. 20.

[119]. Li, X. & Yu, H.S. (2010) Numerical investigation of granular material behaviour under rotational shear. *Geotechnique*. 60(5), 381–394.

[120]. Li, X. (2006) *Micro-scale investigation on the quasi-static behavior of granular material*. Doctorial Dissertation, Hong Kong University of Science and Technology.

[121]. Li, X. S. & Dafalias, Y. F. (2000) Dilatancy for cohesionless soils. *Geotechnique*. 50(4), 449–460.

[122]. Li, X.S. & Wang, Y. (1998) Linear representation of steady-state line for sand. *Journal of Geotechnical and Geoenvironmental Engineering*. 124(12), 1215–1217.

[123]. Lim, K.W., Kawamoto, R., Andò, E., Viggiani, G. & Andrade, J.E. (2016) Multiscale characterization and modeling of granular materials through a computational mechanics avatar: a case study with experiment. *Acta Geotechnica*. 11, 243–253.

[124]. Lim, K.W., Krabbenhoft, K. & Andrade, J.E. (2014) On the contact treatment of non-convex particles in the granular element method. *Computational Particulate Mechanics*. 1, 257–275.

[125]. Lin, C.L. & Miller, J.D. (2005) 3D characterization and analysis of particle shape using X-ray microtomography (XMT). *Powder Technology*.154(1), 61–69.

[126]. Lin, X. & Ng, T.T (1997) A three-dimensional discrete element model using arrays of ellipsoids. *Géotechnique*. 47(2), 319–329.

[127]. Liu, G., Rong, G., Peng, J. & Zhou, C. (2015) Numerical simulation on undrained triaxial behavior of saturated soil by a fluid coupled-DEM model. *Engineering Geology*. 193, 256-266.

[128]. Liu, Y.J., Li, G., Yin, Z.Y., Dano, C., Hicher, P.Y., Xia, X.-H. & Wang, J.H. (2014) Influence of grading on the undrained behavior of granular materials. *Comptes Rendus Mécanique*. 342(2), 85–95.

[129]. Ludewig, F. & Vandewalle, N. (2012) Strong interlocking of nonconvex particles in random packings. *Physical Review E*. 85(5), 051307.

[130]. Maeda, K., Fukuma, M. & Nukudani, E. (2009) Macro and micro critical states of granular materials with different grain shapes. *AIP Conference Proceedings*. 1145(1), 829–832.

[131]. Maeda, K., Sakai, H., Kondo, A., Yamaguchi, T., Fukuma, M. & Nukudani, E. (2010) Stress–chain based micromechanics of sand with grain shape effect. *Granular Matter*. 12, 499–505.

[132]. Masson, S. & Martinez, J. (2001) Micromechanical analysis of the shear behavior of a granular material. *Journal of Engineering Mechanics*. 127(10), 1007.

[133]. Matsuoka, E. & Geka, H. (1983) A stress-strain model for granular materials considering mechanism of fabric changes. *Soils and Foundations*. 23(2), 83-97.

[134]. McDowell, G.R. & Harireche, O. (2002) Discrete element modelling of soil particle fracture. *Géotechnique*. 52, 131–135.

[135]. Mehrabadi, M.M. & Nemat-Nasser, S. (1983) Stress, dilatancy and fabric in granular materials. *Mechanics of Materials*. 2(2), 155-161.

[136]. Mehrabadi, M.M., Nemat-Nasser, S. & Oda, M. (1982) On statistical description of stress and fabric in granular materials. *International Journal of Numerical and Analytical Methods in Geomechanics*. 6, 95-108.

[137]. Mindlin, R.D. & Deresiewicz, H. (1953) Elastic spheres in contact under varying oblique force. *Journal of Applied Mechanics*. 20, 327–344.

[138]. Mindlin, R.D. (1949) Compliance of elastic bodies in contact. *Journal of Applied Mechanics*. 16, 259-268.

[139]. Mollon, G. & Zhao, J. (2013) Generating realistic 3D sand particles using Fourier descriptors. *Granular Matter*. 15(1), 95–108.

[140]. Mooney, M. A., Finno, R. J. & Viggiani, M. G. (1998) A unique critical state for sand? *Journal of Geotechnical and Geoenvironmental Engineering*. 124(11), 1100-1108.

[141]. Nezami, E.G., Hashash, Y.M.A., Zhao, D. & Ghaboussi, J. (2004) A fast contact detection algorithm for 3-D discrete element method. *Computers & Geotechnics*. 31(7), 575–587.

[142]. Ng, T.T. (2004) Shear strength of assemblies of ellipsoidal particles. *Geotechnique*. 54(10), 659–669.

[143]. Ng, T.T. (2009) Discrete element method simulations of the critical state of a granular material. *International Journal of Geomechanics*. 9(5), 209–216.

[144]. Ngo, N.T., Indraratna, B. & Rujikiatkamjorn, C. (2017) Micromechanics-Based Investigation of Fouled Ballast Using Large-Scale Triaxial Tests and Discrete Element Modeling. *Journal of Geotechnical and Geoenvironmental Engineering*. 143(2), 04016089.

[145]. Ni, Q., Powrie, W., Zhang, X. & Harkness, R. (2000) Effect of particle properties on soil behaviour: 3-D numerical modelling of shear box tests. *In Geotechnical special publication*. 58.

[146]. Nicot, F. & Darve, F. (2007) A micro-mechanical investigation of bifurcation in granular materials. *International Journal of Solids and Structures*. 44(20), 6630–6652.

[147]. Nicot, F., Xiong, H., Wautier, A., Lerbet, J. & Darve, F. (2017) Force chain collapse as grain column buckling in granular materials. *Granular Matter*. 19(2), 18.

[148]. Norwegian Geotechnical Institute (NGI). (1982) *Results of triaxial tests on Hokksund sand*. Internal Report 52108-12.

[149]. Nouguier-Lehon, C. (2010) Effect of the grain elongation on the behaviour of granular materials in biaxial compression. *Comptes Rendus Mécanique*. 338(10-11), 587-59.

[150]. O'Donovan, J., O'Sullivan, C. & Marketos, G. (2012) Two-dimensional discrete element modelling of bender element tests on an idealised granular material. *Granular Matter*. 14, 733–747.

[151]. O'Donovan, J., O'Sullivan, C., Marketos, G. & Muir Wood, D. (2015) Analysis of bender element test interpretation using the discrete element method. *Granular Matter*. 17, 197–216.

[152]. O'Sullivan, C. & Cui, L. (2009) Micromechanics of granular material response during load reversals: Combined DEM and experimental study. *Powder Technology*. 193(3), 289–302.

[153]. O'Sullivan, C. (2011) Particle-Based Discrete Element Modeling: Geomechanics Perspective. *International Journal of Geomechanics*. 11, 449–464.

[154]. O'Sullivan, C. (2014) *Advancing geomechanics using DEM. In: Kenichi Soga (ed.).* The International Symposium on Geomechanics from Micro to Macro (IS-Cambridge 2014). Cambridge, UK, CRC Press/Balkema.

[155]. Oda, M. (1972) Initial fabrics and their relations to mechanical properties of granular material. *Soils and Foundations*. 12(1), 17-36.

[156]. Oda, M. (1974) A mechanical and statistical model of granular material. *Soils and Foundations*. 14(1), 13–27.

[157]. Oda, M. (1978) *Significance of fabric in granular mechanics*. Proceedings U.S. – Japan Seminar on Continuum-Mechanical and Statistical Approaches

in the Mechanics of Granular Materials. Cowin and Satake (eds.), Tokyo, 7-26.

[158]. Oda, M. (1999) *Fabric tensor and its geometrical meaning*. An introduction: Mechanics of Granular Materials, Oda and Iwashita (eds.), Balkema, Rotterdam, 27-33.

[159]. Oda, M., Nemat Nasser, S. & Konishi, J. (1985) Stress induced anisotropy in granular masses. *Soils and Foundations*. 25(3), 85-97.

[160]. O'Sullivan, C. (2002) *The Application of Discrete Element Modelling to Finite Deformation Problems in Geomechanics*. PhD thesis, University of California, Berkeley.

[161]. O'Sullivan, C., Bray, J. & Riemer, M. (2004) An examination of the response of regularly packed specimens of spherical particles using physical tests and discrete element simulations. *Journal of Engineering Mechanics*. 130(10), 1140-1150.

[162]. Pournin, L., Weber, M., Tsukahara, M., Ferrez, J.A., Ramaioli, M. & Liebling, ThM. (2005) Three-dimensional distinct element simulation of spherocylinder crystallization. *Granular Matter*. 7(2–3), 119–126.

[163]. Powers, M.C. (1953) A new roundness scale for sedimentary particles. *Journal of Sedimentary Research*. 23, 117–119.

[164]. Proctor, D.C. & Barton, R.R. (1974) Measurement of the angle of interparticle friction. *Geotechnique*. 24(4), 581-604.

[165]. Radjai, F., Wolf, D.E., Jean, M. & Moreau, J.J. (1998) Bimodal character of stress transmission in granular packings. *Physical Review Letters*. 80, 61.

[166]. Reimann, J., Vicente, J., Brun, E., Ferrero, C., Gan, Y. & Rack, A. (2017) X-ray tomography investigations of mono-sized sphere packing structures in cylindrical containers. *Powder Technology*. 318, 471–483.

[167]. Riemer, M.F. & Seed, R.B. (1997) Factors affecting apparent position of steady-state line. *Journal of Geotechnical and Geoenvironmental Engineering*. 123 (3), 281–288.

[168]. Rodriguez, N.M. & Lade, P.V. (2013) Effects of principal stress directions and mean normal stress on failure criterion for cross-anisotropic sand. *Journal of Engineering Mechanics*. 139(11), 1592–1601.

[169]. Roscoe, K. (1953) An apparatus for the application of simple shear to soil samples. *In: 3rd International Conference on Soil Mechanics*. Zurich, 186–191.

[170]. Roscoe, K.H., Schofield, A.N. & Wroth, C.P. (1958) On the yielding of soils. *Geotechnique.* 8(1), 22–53.

[171]. Rothenburg, L. & Bathurst, R. J. (1989) Analytical study of induced anisotropy in idealized granular materials. *Geotechnique*. 39(4), 601-614.

[172]. Rothenburg, L. & Bathurst, R.J. (1991) Numerical simulation of idealized granular assemblies with plane elliptical particles. *Computers and Geotechnics*. 11(4), 315–329.

[173]. Rothenburg, L. & Bathurst, R.J. (1992) Micromechanical features of granular assemblies with planar elliptical particles. *Geotechnique*. 2(1), 79–95.

[174]. Rothenburg, L. & Kruyt, N.P. (2004) Critical state and evolution of coordination number in simulated granular materials. *International Journal of Solids and Structures*. 41, 5763-5774.

[175]. Rowe, P. W. & Barden, L. (1964) Importance of free ends in triaxial testing. *Journal of Terramechanics*. 1(2), 97.

[176]. Rowe, P.W. (1962) The stress dilatancy relation for static equilibrium of an assembly of particles in contact. *Proceedings of Royal Society A: Mathematical, Physical and Engineering Sciences*. 269(1339), 500-527.

[177]. Rowe, P.W. (1969) The relation between the shear strength of sands in triaxial compression, plane strain and direct shear. *Geotechnique*. 19(1), 75–86.

[178]. Saint-Cyr, B., Delenne, J.Y., Voivret, C., Radjai, F. & Sornay, P. (2011) Rheology of granular materials composed of nonconvex particles. *Physical Review E*. 84, 041302.

[179]. Salazar, A., Saez, E. & Pardo, G. (2015) Modeling the direct shear test of a coarse sand using the 3D Discrete Element Method with a rolling friction model. *Computers and Geotechnics*. 67, 83-93.

[180]. Salvatore, E., Modoni, G., Andò, E., Albano, M. & Viggiani, G. (2017) Determination of the critical state of granular materials with triaxial tests. *Soils and Foundations*. 57(5), 733–744.

[181]. Sarkar, D., König, D. & Goudarzy, M. (2019) The influence of particle characteristics on the index void ratios in granular materials. *Particuology*. 46, 1-13.

[182]. Satake, M. (1978) *Constitution of mechanics of granular materials through the graph theory*. Proceedings U.S-Japan Seminar on continuum-mechanical and statistical approaches in the mechanics of granular materials. Tokyo, 47-62.

[183]. Sazzad, M.M. & Suzuki, K. (2013) Density dependent macro-micro behavior of granular materials in general triaxial loading for varying intermediate principal stress using DEM. *Granular Matter*. 15 (5), 583–593.

[184]. Schneider, C.A., Rasband, W.S. & Eliceiri, K.W. (2012) NIH Image to Image J: 25 years of image analysis. *Nature Methods*. 9(7), 671-675.

[185]. Schofield, A. & Wroth, P. (1968) *Critical state soil mechanics*. McGraw-Hill London.

[186]. Shamsi, M.M.M. & Mirghasemi, A.A. (2012) Numerical simulation of 3D semi-real- shaped granular particle assembly. *Powder Technology*. 221, 431–446.

[187]. Shinohara, K., Oida, M., & Golman, B. (2000) Effect of particle shape on angle of internal friction by triaxial compression test. *Powder Technology*. 107(1-2), 131–136.

[188]. Simony, A. & Houlsby, G.T. (2006) The direct shear strength and dilatancy of sand–gravel mixtures. *Geotechnical and Geological Engineering*. 24, 523–549.

[189]. Simulation Works, Inc. (2009) *Kubrix, Version 11.6 Manual. St. Paul: Simulation Works*.

[190]. Sitharam, T.G. & Vinod, J.S. (2009) Critical state behaviour of granular materials from isotropic and rebounded paths: DEM simulations. *Granular Matter*. 11 (1), 33–42.

[191]. Skinner, A. (1969) A note on the influence of interparticle friction on the shearing strength of a random assembly of spherical particles. *Geotechnique*. 19(1), 150-157.

[192]. Springman, S.M., Yamamoto, Y., Buchli, T., Hertrich, M., Maurer, H., Merz, K., Gartner-Roer, I. & Seward, L. (2013) *Rock glacier degradation and instabilities in the European Alps: a characterisation and monitoring experiment in the Turtmanntal, CH*. In Landslide Science and Practice. Edited by C. Margottini, P. Canuti, and K. Sassa. Springer, Berlin, Heidelberg, 5–13.

[193]. Strack, O.D.L. & Cundall, P. A. (1978) The discrete element method as a tool for research in granular media. *Part I. Report to National Science Foundation*. NSF Grant ENG76-20711.

[194]. Sukumaran, B. & Ashmaway, A.K. (2003) Influence of inherent particle characteristics on hopper flow rate. *Powder Technology*. 138, 46–50.

[195]. Sun, Y., Indraratna, B. & Nimbalkar, S. (2014) Three-dimensional characterisation of particle size and shape for ballast. *Geotechnique Letters*. 4(3), 197–202.

[196]. Taghavi, R. (2000) Automatic Block Decomposition Using Fuzzy Logic Analysis. *Proceedings of the 9th International Meshing Roundtable (pp. 187-192)*. New Orleans: Sandia National Laboratories.

[197]. Taylor, D.W. (1948) *Fundamentals of soil mechanics*. New York, NY, USA: Wiley.

[198]. Thornton, A.R., Krijgsman, D., Fransen, R.H.A., Briones, S.G., Tunuguntla, D.R., Voortwis, A., Luding, S., Bokhove, O. & Weinhart, T. (2013) Mercury-DPM: fast particle simulations in complex geometries. *EnginSoft Newsletter Simulation Based Engineering & Sciences*. 10, 48–53.

[199]. Thornton, C. & Antony, S. J. (1998) Quasi-static deformation of particulate media. *Proceedings of Royal Society A*. 356, 2763-2782.

[200]. Thornton, C. & Sun, G. (1993) Axisymmetric compression of 3D polydisperse systems of spheres. Thornton (ed.). *Powders and Grains*. 93, 129-134.

[201]. Thornton, C. & Zhang, L. (2003) Numerical simulations of direct shear test. *Chemical Engineering Technology*. 26(2), 153-156.

[202]. Thornton, C. & Zhang, L. (2005) On the elastic response of granular media. In: Garcia-Rojo, R., Herrmann, H.J., McNamara, S. (eds.). *Powders and Grains*. 235–238. Balkema, Leiden.

[203]. Thornton, C. (2000) Numerical simulations of deviatoric shear deformation of granular media. *Geotechnique*. 50(1), 43-53.

[204]. Thornton, C. (2015) *Granular Dynamics, Contact Mechanics and Particle System Simulations (Particle Technology Series)*. Hardcover – 15 September 2015.

[205]. Tian, J., Liu, E., Jiang, L., Jiang, X., Sun, Y. & Xu, R. (2018) Influence of particle shape on the microstructure evolution and the mechanical properties of granular materials. *Comptes Rendus Mécanique*. 346(6), 460–476.

[206]. Tillemans, H.J. & Herrmann, H.J. (1995) Simulating deformations of granular solids under shear. *Physica A: Statistical Mechanics and its Applications*. 217, 261–288.

[207]. Ting, J.M., Meachum, L. & Rowell, J.D. (1995) Effect of particle shape on the strength and deformation mechanisms of ellipse-shaped granular assemblages. *Engineering Computations*. 12(2), 99–108.

[208]. Tordesillas, A. & Muthuswamy, M. (2009) On the modeling of confined buckling of force chains. *Journal of the Mechanics and Physics of Solids*. 57, 706–727.

[209]. Tsomokos, A. & Georgiannou, V.N. (2010) Effect of grain shape and angularity on the undrained response of fine sands. *Canadian Geotechnical Journal*. 47(5), 539–551.

[210]. Vaid, Y. P. & Sasitharan, S. (1991) The strength and dilatancy of sand. *Canadian Geotechnical Journal*. 29(10), 522–526.

[211]. Vaid, Y.P., Chung, E.K.F. & Kuerbis, R.H. (1990) Stress path and steady state. *Canadian Geotechnical Journal*. 27, 1–7.

[212]. Vangla, P., Roy, N. & Gali, M. (2018) Image based shape characterization of granular materials and its effect on kinematics of particle motion. *Granular Matter*. 20(6).

[213]. Verdugo, R. & Ishihara, K. (1996) The steady state of sandy soils. *Soils and Foundations*. 36 (2), 81–91.

[214]. Verlet, L. (1967) Computer 'Experiments' on Classical Fluids. I. Thermodynamical Properties of Lennard-Jones Molecules. *Physical Review*. 159, 98-103.

[215]. Wadell, H. A. (1932) Volume, shape, and roundness of rock particles. *The Journal of Geology*. 40(5), 443–451.

[216]. Wang, C., Deng, A. & Taheri, A. (2018) Three-dimensional discrete element modeling of direct shear test for granular rubber–sand. *Computers and Geotechnics*. 97, 204-216.

[217]. Wang, J. & Gutierrez, M. (2010) Discrete element simulations of direct shear specimen scale effects. *Geotechnique*. 60(5), 395–409.

[218]. Wang, L., Xu, W. & Xu, A. (2012) Three-dimensional cellular automata based particle flow simulations of mechanical properties of talus deposit. *Journal of Rock Mechanics and Geotechnical Engineering*. 4(4), 375-384.

[219]. Wang, Z., Jing, G., Yu, Q. & Yin, H. (2015) Analysis of ballast direct shear tests by discrete element method under different normal stress. *Measurement*. 63, 17-24.

[220]. Weatherley, D., Boros, V. & Hancock, W. (2011) ESyS-Particle Tutorial and User's Guide Version 2.1. *Earth Syst Sci Comput Cent Univ Qld.*

[221]. Wei, D., Wang, J., Nie, J. & Zhou, B. (2018) Generation of realistic sand particles with fractal nature using an improved spherical harmonic analysis. *Computers and Geotechnics*. 104, 1–12.

[222]. Wellmann, C., Lillie, C. & Wriggers, P. (2008) Comparison of the macroscopic behavior of granular materials modeled by different constitutive equations on the microscale. *Finite Elements in Analysis and Design*. 44, 259–271.

[223]. Wood, M. D., Belkheir, K. & Liu, D. F. (1994) Strain softening and state parameter for sand modelling. *Geotechnique*. 44(2), 335 -339.

[224]. Xiao, Y., Long, L., Mathew Evans, T., Zhou, H., Liu, H. & Stuedlein, A.W. (2019) Effect of Particle Shape on Stress-Dilatancy Responses of Medium-Dense Sands. *Journal of Geotechnical and Geoenvironmental Engineering*. 145(2), 04018105.

[225]. Xie, Y. H., Yang, Z. X., Barreto, D. & Jiang, M.D. (2017) The influence of particle geometry and the intermediate stress ratio on the shear behavior of granular materials. *Granular Matter*. 19(2), 35.

[226]. Yan, B., Regueiro, R.A. & Sture, S. (2010) Three-dimensional ellipsoidal discrete element modeling of granular materials and its coupling with finite element facets. *Engineering Computations*. 27(4), 519–550.

[227]. Yan, W. (2011) Particle Elongation and Deposition Effect to Macroscopic and Microscopic Responses of Numerical Direct Shear Tests. *Geotechnical Testing Journal*. 34(3), 238-249.

[228]. Yan, W.M. & Dong, J. (2011) Effect of particle grading on the response of an idealized granular assemblage. *International Journal of Geomechanics*. 11 (4), 276–285.

[229]. Yang, J. & Luo, X.D. (2015) Exploring the relationship between critical state and particle shape for granular materials. *Journal of the Mechanics and Physics of Solids*. 84, 196–213.

[230]. Yang, Z. X. & Wu, Y. (2017) Critical State for Anisotropic Granular Materials: A Discrete Element Perspective. *International Journal of Geomechanics*. 17(2), 04016054.

[231]. Yang, Z. X., Xu, T. T. & Chen, Y.N. (2018) Unified Modeling of the Influence of Consolidation Conditions on Monotonic Soil Response Considering Fabric Evolution. *Journal of Engineering Mechanics*. 144(8), 04018073.

[232]. Yang, Z.X. & Wu, Y. (2016) Critical state for anisotropic granular materials: A discrete element perspective. *International Journal of Geomechanics*. 17(2), 04016054.

[233]. Yang, Z.X., Li, X.S. & Yang, J. (2008) Quantifying and modelling fabric anisotropy of granular soils. *Geotechnique*. 58(4), 237–248.

[234]. Yang, Z.X., Yang, J. & Wang, L. Z. (2012) On the influence of inter-particle friction and dilatancy in granular materials: a numerical analysis. *Granular Matter*. 14 (3), 433–447.

[235]. Yang, Z.X., Yang, J. & Wang, L.Z. (2013) Micro-scale modelling of anisotropy effects on undrained behaviour of granular soils. *Granular matter*. 15(5), 557-572.

[236]. Yoshimine, M., Ishihara, K. & Vargas, W. (1998) Effects of principal stress direction and intermediate principal stress on undrained shear behavior of sand. *Soils and Foundations*. 38(3), 179–188.

[237]. Zhang, J., Lo, S.C.R., Rahman, M.M. & Yan, J. (2018) Characterizing monotonic behavior of pond ash within critical state approach. *Journal of Geotechnical and Geoenvironmental Engineering*. 144(1), 04017100.

[238]. Zhang, L. & Thornton, C. (2002) DEM simulations of the direct shear test. *In Proceeding of 15th ASCE Engineering Mechanics Conference*. New York.

[239]. Zhang, L. & Thornton, C. (2007) *Numerical probing of the mechanical response of granular material in general 3D stress/strain space*. In-house report, Civil Engineering Department, University of Birmingham, UK.

[240]. Zhao, J. & Guo, N. (2013) Unique critical state characteristics in granular media considering fabric anisotropy. *Geotechnique*. 63(8), 695-704.

[241]. Zhao, S. & Zhao, J. (2019) A poly-superellipsoid-based approach on particle morphology for DEM modeling of granular media. *International Journal for Numerical and Analytical Methods in Geomechanics*. 43(13), 2147-2169.

[242]. Zhao, S. & Zhou, X. (2017) Effects of particle asphericity on the macro- and micro-mechanical behaviours of granular assemblies. *Granular Matter*. 19, 38.

[243]. Zhao, S., Zhang, N., Zhou, X. & Zhang, L. (2017) Particle shape effects on fabric of granular random packing. *Powder Technology*. 310, 175–186.

[244]. Zhao, S., Zhang, N., Zhou, X. & Zhang, L. (2017) Particle shape effects on fabric of granular random packing. *Powder Technology*. 310, 175–186.

[245]. Zhao, S., Zhou, X. & Liu, W. (2015) Discrete element simulations of direct shear tests with particle angularity effect. *Granular matter*. 17, 793-806.

[246]. Zheng, J. & Hryciw, R.D. (2015) Traditional soil particle sphericity, roundness and surface roughness by computational geometry. *Geotechnique*. 65(6), 494-506.

[247]. Zhou, W., Liu, J., Ma, G., Yuan, W. & Chang, X. (2016) Macroscopic and microscopic behaviors of granular materials under proportional strain path: a DEM study. *International Journal for Numerical and Analytical Methods in Geomechanics*. 40(18), 2450–2467.

[248]. Zhou, W., Ma, G., Chang, X. & Zhou, C. (2013) Influence of particle shape on behavior of rockfill using a three-dimensional deformable DEM. *Journal of Engineering Mechanics*. 139(12), 1868–1873.

[249]. Zhu, H.P., Zhou, Z.Y., Yang, R.Y. & Yu, A.B. (2007) Discrete particle simulation of particulate systems: Theoretical developments. *Chemical Engineering Science*. 62(13), 3378–3396.

[250]. Zhu, Y., Gong, J. & Nie, Z. (2020) Shear behaviours of cohesionless mixed soils using the DEM: The influence of coarse particle shape. Particuology.

Appendix - A: Summary of DEM results for different loading paths

Series designation	Simulation ID	e_0	I_D	ψ_0	CN_o
Series - I	AC_L_100	0.629	0.109	0.124	5.6
	AC_L_200	0.608	0.143	0.112	7.1
	AC_L_400	0.567	0.204	0.097	9.8
	AC_L_800	0.527	0.206	0.085	13.5
	AC_L_1600	0.481	0.186	0.083	19.1
Series - II	AC_M_100	0.460	0.504	-0.045	8.1
	AC_M_200	0.451	0.506	-0.045	9.6
	AC_M_400	0.435	0.514	-0.035	11.9
	AC_M_800	0.406	0.505	-0.036	15.8
	AC_M_1600	0.366	0.500	-0.032	21.8
Series - III	AC_D_100	0.362	0.733	-0.143	10.7
	AC_D_200	0.353	0.735	-0.143	12.3
	AC_D_400	0.337	0.741	-0.133	14.8
	AC_D_800	0.311	0.741	-0.131	18.9
	AC_D_1600	0.279	0.737	-0.119	25.5
Series - IV	AE_L_100	0.629	0.109	0.109	5.6
	AE_L_200	0.608	0.143	0.093	7.1
	AE_L_400	0.567	0.204	0.077	9.8
	AE_L_800	0.527	0.206	0.053	13.5
	AE_L_1600	0.481	0.186	0.040	19.1
Series - V	AE_M_100	0.460	0.504	-0.058	8.1
	AE_M_200	0.451	0.506	-0.061	9.6
	AE_M_400	0.435	0.514	-0.070	11.9
	AE_M_800	0.406	0.505	-0.082	15.8
	AE_M_1600	0.366	0.500	-0.085	21.8
Series - VI	AE_D_100	0.362	0.733	-0.158	10.7
	AE_D_200	0.353	0.735	-0.161	12.3
	AE_D_400	0.337	0.741	-0.168	14.8
	AE_D_800	0.311	0.741	-0.179	18.9
	AE_D_1600	0.279	0.737	-0.176	25.5
Series - VII	LC_L_100	0.631	0.103	0.121	5.1
	LC_L_200	0.613	0.130	0.108	6.5
	LC_L_400	0.585	0.164	0.115	9.1
	LC_L_800	0.546	0.159	0.116	12.6
	LC_L_1600	0.495	0.150	0.110	19.1
Series VIII	LC_M_100	0.461	0.502	-0.049	7.9
	LC_M_200	0.451	0.506	-0.054	9.5
	LC_M_400	0.435	0.514	-0.035	11.8
	LC_M_800	0.408	0.499	-0.022	15.7

	LC_M_1600	0.368	0.495	-0.017	21.7
Series - IX	LC_D_100	0.359	0.741	-0.151	10.7
	LC_D_200	0.351	0.739	-0.154	12.3
	LC_D_400	0.337	0.741	-0.133	14.8
	LC_D_800	0.311	0.741	-0.119	19.0
	LC_D_1600	0.279	0.737	-0.106	25.5
Series - X	LE_L_100	0.631	0.103	0.124	5.1
	LE_L_200	0.613	0.130	0.105	6.5
	LE_L_400	0.585	0.164	0.090	9.1
	LE_L_800	0.546	0.159	0.061	12.6
	LE_L_1600	0.495	0.150	0.035	19.1
Series - XI	LE_M_100	0.461	0.502	-0.048	7.9
	LE_M_200	0.451	0.506	-0.057	9.5
	LE_M_400	0.435	0.514	-0.060	11.8
	LE_M_800	0.408	0.499	-0.077	15.7
	LE_M_1600	0.368	0.495	-0.090	21.7
Series -XII	LE_D_100	0.359	0.741	-0.151	10.7
	LE_D_200	0.351	0.739	-0.157	12.3
	LE_D_400	0.337	0.741	-0.158	14.8
	LE_D_800	0.311	0.741	-0.174	19.0
	LE_D_1600	0.279	0.737	-0.181	25.5

Appendix - B: Servo-mechanism in PFC

The PFC[3D] code used for this thesis provides an in-built servo-mechanism in order to maintain the desired stress levels. The servo function is called once per cycle. The function of a servo-control mode is to permit any desired stress path to be followed approximately in incremental steps. With the servo-control mode, the applied strain field is continuously adjusted according to the difference between the desired stress state and the measured stress state. The servo-mechanism uses a proportional controller with adaptive gain as follows.

Let $\mathbf{F}^t$ be the target force (input by the user), and F^c be the reaction force exerted by all pieces in the model on a wall. The wall velocity $\mathbf{v}$ is decomposed in to two components:

$$\mathbf{v} = \nu_n \hat{\mathbf{n}} + (\mathbf{v} - \nu_n \hat{\mathbf{n}})$$

where ν_n is the signed magnitude of the velocity in direction $\hat{\mathbf{n}}$,

$$\nu_n = (\mathbf{v}.\hat{\mathbf{n}})$$

where $\hat{\mathbf{n}} = \mathbf{F}^t / \|\mathbf{F}^t\|$ is a unit vector in the direction of the target force. The value of ν_n is adjusted as:

$$\nu_n = G(F^t + F^c)$$

where G is the controller gain and $F^t = \mathbf{F}^t.\hat{\mathbf{n}}$ and $F^c = \mathbf{F}^c.\hat{\mathbf{n}}$ are the signed magnitudes of the target servo force and of the reaction force, respectively.

To ensure stability, the gain is automatically evaluated as

$$G = \frac{\alpha}{K^c \Delta t}$$

where α is a relaxation factor that can be set by user with the gainfactor keyword (default to 0.8), K^c is the sum of the effective transitional stiffness of all mechanical contacts involving the wall, and Δt is the current timestep.

Appendix - C: Direct shear test – PFC code

```
%% Geometry creation %%
new
;;;define the size of sample
[mv_W=0.100]
[mv_D=0.100]
[mv_H=0.05]

;[clumpFric = 0.3]
;[wallFric = 0.0]

domain extent [-0.8*mv_W] [0.8*mv_W] [-0.8*mv_D] [0.8*mv_D] [-
0.8*mv_H] [0.8*mv_H] condition destroy
;;;;supposing that the center of the model is at position (0,0,0)

cmat default model linear method deformability emod 1.0e8 kratio 1.33

;cmat default model linear prop kn 1e9 ks 1e9 fric 0.0 type pebble-pebble
;cmat default model linear prop kn 1e9 ks 0.0 fric 0.0 type pebble-facet
;;;;Pre-define contact model and properties

wall generate name 'walltop' box [-0.5*mv_W] [0.5*mv_W] [-0.5*mv_D]
[0.5*mv_D] 0.0 [0.6*mv_H]
wall generate name 'wallbot' box [-0.5*mv_W] [0.5*mv_W] [-0.5*mv_D]
[0.5*mv_D] [-0.6*mv_H] 0.0

wall delete range set name 'walltopBottom'
wall delete range set name 'walltopTop'
wall delete range set name 'wallbotBottom'
```

```
wall delete range set name 'wallbotTop'

wall generate name 'walltopTop'     plane dip 0.0 dd 0.0 position 0.0 0.0 [
0.5*mv_H]
wall generate name 'wallbotBottom' plane dip 0.0 dd 0.0 position 0.0 0.0 [-
0.5*mv_H]
;;;wall generation

wall generate name 'wallLeft' ...
   group polygons ...
   polygon ...
      [-0.5*mv_W] [0.5*mv_D] [0.0] ...
      [-0.5*mv_W] [-0.5*mv_D] [0.0] ...
      [-0.7*mv_W] [0.5*mv_D] [0.0] ...
      [-0.7*mv_W] [-0.5*mv_D] [0.0]

wall generate name 'wallRight' ...
   group polygons ...
   polygon ...
      [0.5*mv_W] [0.5*mv_D] [0.0] ...
      [0.5*mv_W] [-0.5*mv_D] [0.0] ...
      [0.7*mv_W] [0.5*mv_D] [0.0] ...
      [0.7*mv_W] [-0.5*mv_D] [0.0]

set random 10001   ;;;;reset the random seed

[rmin =
clump template create ...
    pebcalculate ...
    name three_peb ...
    pebbles 3 ...
```

```
        0.0007 0.0 0.0 0.0 ...
        0.0007 5.56e-5 0.0 0.0 ...
        0.0007 -5.56e-5 0.0 0.0

clump distribute ...
        porosity 0.35 ...
        resolution 1.0 ...
        numbin 5 ...
        diameter ...
        bin 1 ...
          volumefraction 0.2 ...
          template three_peb ...
          size 0.004 0.006 ...
          azimuth 0.0 360 ...
          elevation 0.0 360 ...
          tilt 0.0 360 ...
          density 100.0 ...
          gauss ...
          group bin1 ...
        bin 2 ...
          volumefraction 0.2 ...
          template three_peb ...
          size 0.004 0.006 ...
          azimuth 0.0 360 ...
          elevation 0.0 360 ...
          tilt 0.0 360 ...
          density 100.0 ...
          gauss ...
          group bin2 ...
        bin 3 ...
          volumefraction 0.2 ...
```

```
92          template three_peb ...
93          size 0.004 0.006 ...
94          azimuth 0.0 360 ...
95          elevation 0.0 360 ...
96          tilt 0.0 360 ...
97          density 100.0 ...
98          gauss ...
99          group bin3 ...
100       bin 4 ...
101         volumefraction 0.2 ...
102         template three_peb ...
103         size 0.004 0.006 ...
104         azimuth 0.0 360 ...
105         elevation 0.0 360 ...
106         tilt 0.0 360 ...
107         density 100.0 ...
108         gauss ...
109         group bin4 ...
110       bin 5 ...
111         volumefraction 0.2 ...
112         template three_peb ...
113         size 0.004 0.006 ...
114         azimuth 0.0 360 ...
115         elevation 0.0 360 ...
116         tilt 0.0 360 ...
117         density 100.0 ...
118         gauss ...
119         group bin5 ...
120     box [-0.5*mv_W] [0.5*mv_W] [-0.5*mv_D] [0.5*mv_D] [-0.5*mv_H]
121 [0.5*mv_H]
122
```

```
123  measure create id 1 radius 0.2 ...
124                  bins 100 @dmin [table.x(exptab,10)]
125  measure dump id 1 table 'numerical'
126
127  pause key
128
129  clump attribute density 2700 damp 0.7
130  ;clump prop fric @clumpFric
131  ;wall prop fric @wallFric
132  cyc 2000 calm 10
133  set timestep scale
134  cyc 5000
135  set timestep auto
136  cyc 1000
137  calm
138  clump attribute displacement multiply 0.0
139  save MakeSpecimen
140  return
141
142  %% one-dimensional compression phase %%
143
144  rest MakeSpecimen
145
146  def wszz
147     wszz = wall.force.contact.z(wall.find('walltopTop'))/(mv_W*mv_D)
148  end
149
150  def servo_walls
151     wall.servo.force.z(wall.find('walltopTop')) = -szz*mv_W*mv_D
152  end
153  set fish callback 9.0 @servo_walls
```

```
154
155 wall servo activate on zforce [-szz*mv_W*mv_D] vmax 0.1 range set name
156 'walltopTop'
157
158 [szz = 2.0e5]  ;;;positive indicates compression, which is self-defined
159 [tol=0.001]
160
161 def stop
162    if math.abs((wszz-szz)/szz) > tol
163       exit
164    endif
165    if mech.solve('aratio') > 1e-4
166       exit
167    endif
168    stop = 1
169 end
170
171 [stop = 0]
172
173 history id 1 @wszz
174 history id 101 mech solve aratio
175
176 solve fishhalt @stop
177
178 calm
179 clump attribute displacement multiply 0.0
180
181 wall attri disp mult 0.0
182
183 save Compact
184 %% Shear phase %%
```

```
rest Compact

[vel=1.0e-2]

wall attri xvel [vel] range set name 'walltopLeft'
wall attri xvel [vel] range set name 'walltopRight'
wall attri xvel [vel] range set name 'walltopFront'
wall attri xvel [vel] range set name 'walltopBack'
wall attri xvel [vel] range set name 'wallLeft'

def shear_disp
    shear_disp = wall.disp.x(wall.find('walltopLeft'))
end

def shear_str
    lz0 = wall.pos.z(wall.find('walltopTop'))-
wall.pos.z(wall.find('wallbotBottom'))
    shear_str = (shear_disp/lz0)*100
end

def shear_stress
    shear_stress = -
(wall.force.contact.x(wall.find('walltopLeft'))/(mv_W*mv_D))*0.001
end

def ver_disp
    ver_disp = wall.disp.z(wall.find('walltopTop'))
end

def ver_str
    ver_str = (ver_disp/lz0)*100
```

```
end

hist id 11 @shear_stress
hist id 12 @shear_disp
hist id 13 @shear_str
hist id 14 @ver_disp
hist id 15 @ver_str

; Fabric anisotropy

; Contact normal anisotropy

def Contact_normal_aniso
  local sum_xx = 0.0
  local sum_yy = 0.0
  local sum_zz = 0.0
  local sum_xy = 0.0
  local sum_xz = 0.0
  local sum_yz = 0.0
  local count_contacts = 0.0
  loop foreach local ct contact.list
  local e1 = contact.end1(ct)
  local e2 = contact.end2(ct)
  local nx = contact.normal.x(ct)
  local ny = contact.normal.y(ct)
  local nz = contact.normal.z(ct)
  if type.pointer(e1) = 'pebble'
    local cp1 = clump.pebble.clump(e1)
  endif
  if type.pointer(e2) = 'pebble'
    local cp2 = clump.pebble.clump(e2)
```

```
247     endif
248     count_contacts = count_contacts + 1
249     sum_xx = sum_xx + nx*nx
250     sum_yy = sum_yy + ny*ny
251     sum_zz = sum_zz + nz*nz
252     sum_xy = sum_xy + nx*ny
253     sum_xz = sum_xz + nx*nz
254     sum_yz = sum_yz + ny*nz
255     endloop
256     Fxx = sum_xx/count_contacts
257     Fyy = sum_yy/count_contacts
258     Fzz = sum_zz/count_contacts
259     Fxy = sum_xy/count_contacts
260     Fxz = sum_xz/count_contacts
261     Fyz = sum_yz/count_contacts
262     end
263
264 hist @Contact_normal_aniso
265 hist @Fxx
266 hist @Fyy
267 hist @Fzz
268 hist @Fxy
269 hist @Fxz
270 hist @Fyz
271 ; Evolution of coordination number
272
273 def Coordination
274   local count_contacts = 0.0
275   loop foreach local ct contact.list
276   local e1 = contact.end1(ct)
277   local e2 = contact.end2(ct)
```

```
278     if type.pointer(e1) = 'pebble'
279       local cp1 = clump.pebble.clump(e1)
280     endif
281     if type.pointer(e2) = 'pebble'
282       local cp2 = clump.pebble.clump(e2)
283     endif
284     count_contacts = count_contacts + 1.0
285     count_clump = clump.num
286     endloop
287     count_contacts_1 = count_contacts
288     count_clump_1 = count_clump
289     CN = 2.0*count_contacts_1/count_clump_1
290     end
291
292   hist @Coordination
293
294   hist @CN
295   hist @count_contacts_1
296   hist @count_clump_1
297   hist @count_clump_contact_num
298
299   hist @x0
300   hist @x1
301   hist @x3
302   hist @MCN
303
304   ; Sliding contacts
305
306   def hist_slip
307    local i = 0.0
308    local j = 0.0
```

```
 loop foreach local cp contact.list
   aa = contact.prop(cp,'lin_slip')
   if aa = true then
     i = i + 1
   else
     j = j + 1
    endif
    endloop
    slip_ratio = i/(i+j)
 end
hist @hist_slip
hist @slip_ratio
;Porosity Evolution
measure create id 1 rad [0.4*(math.min(mv_W, mv_H))]
[porosity = measure.porosity(measure.find(1))]

history id  6   measure porosity id 1

; average force

def compute_average_normal
   local average_normal = 0.0
   local num= 0.0
   loop foreach local ct contact.list
   local e1 = contact.end1(ct)
   local e2 = contact.end2(ct)
   if type.pointer(e1) = 'pebble'
     local cp1 = clump.pebble.clump(e1)
    endif
    if type.pointer(e2) = 'pebble'
     local cp2 = clump.pebble.clump(e2)
```

```
340     endif
341       average_normal = average_normal + math.abs(contact.force.normal(ct))
342       num = num + 1
343     endloop
344     average_normal_1 = average_normal/num
345   end
346
347   hist @compute_average_normal
348   hist @average_normal_1
349
350   ; strong and weak force
351
352   def check_strong_force
353     local Fxx_s = 0.0
354     local Fyy_s = 0.0
355     local Fzz_s = 0.0
356     local Fxy_s = 0.0
357     local Fxz_s = 0.0
358     local Fyz_s = 0.0
359     local Fxx_w = 0.0
360     local Fyy_w = 0.0
361     local Fzz_w = 0.0
362     local Fxy_w = 0.0
363     local Fxz_w = 0.0
364     local Fyz_w = 0.0
365           local num_strong = 0.0
366           local num_weak  = 0.0
367     loop foreach local cp contact.list
368     local e1 = contact.end1(cp)
369     local e2 = contact.end2(cp)
370     local nx = contact.normal.x(cp)
```

```
371          local ny = contact.normal.y(cp)
372      local nz = contact.normal.z(cp)
373      if type.pointer(e1) = 'pebble'
374       local cp1 = clump.pebble.clump(e1)
375      endif
376      if type.pointer(e2) = 'pebble'
377       local cp2 = clump.pebble.clump(e2)
378      endif
379      if math.abs(contact.force.normal(cp)) >= average_normal_1 then
380                                  num_strong = num_strong + 1
381          Fxx_s = Fxx_s + nx*nx
382          Fyy_s = Fyy_s + ny*ny
383          Fzz_s = Fzz_s + nz*nz
384          Fxy_s = Fxy_s + nx*ny
385          Fxz_s = Fxz_s + nx*nz
386          Fyz_s = Fyz_s + ny*nz
387        else
388                                  num_weak = num_weak + 1
389                                  Fxx_w = Fxx_w + nx*nx
390          Fyy_w = Fyy_w + ny*ny
391          Fzz_w = Fzz_w + nz*nz
392          Fxy_w = Fxy_w + nx*ny
393          Fxz_w = Fxz_w + nx*nz
394          Fyz_w = Fyz_w + ny*nz
395        endif
396     endloop
397      Fxx_s1 = Fxx_s/num_strong
398      Fyy_s1 = Fyy_s/num_strong
399      Fzz_S1 = Fzz_s/num_strong
400      Fxy_s1 = Fxy_s/num_strong
401      Fxz_s1 = Fxz_s/num_strong
```

```
402       Fyz_sl = Fyz_s/num_strong
403       Fxx_wl = Fxx_w/num_weak
404       Fyy_wl = Fyy_w/num_weak
405       Fzz_wl = Fzz_w/num_weak
406       Fxy_wl = Fxy_w/num_weak
407       Fxz_wl = Fxz_w/num_weak
408       Fyz_wl = Fyz_w/num_weak
409     end
410
411   hist @check_strong_force
412   hist @Fxx_sl
413   hist @Fyy_sl
414   hist @Fzz_sl
415   hist @Fxy_sl
416   hist @Fxz_sl
417   hist @Fyz_sl
418   hist @Fxx_wl
419   hist @Fyy_wl
420   hist @Fzz_wl
421   hist @Fxy_wl
422   hist @Fxz_wl
423   hist @Fyz_wl
424
425   hist purge
426
427   def stop
428     if math.abs(shear_str) > 30 then
429       stop = 1
430     endif
431   end
432   [stop=0]
```

```
433
434  clump prop fric 0.5
435  wall prop fric 0.0
436
437  set hist_rep 500
438
439  solve fishhalt @stop
440
441  save Shear_Test
442
443  return
444
445
446
447
448
449
450
451
452
```

Appendix -D: Triaxial shear test – PFC code

```
%% Geometry generation %%
new
;;;define the size of sample
[mv_W=0.050]
[mv_D=0.050]
[mv_H=0.050]

;[clumpFric = 0.3]
;[wallFric = 0.0]

domain extent [-0.8*mv_W] [0.8*mv_W] [-0.8*mv_D] [0.8*mv_D] [-
0.8*mv_H] [0.8*mv_H] condition destroy
;;;;supposing that the center of the model is at position (0,0,0)

cmat default model linear method deformability emod 1.0e8 kratio 1.33

;cmat default model linear prop kn 1e9  type ball-ball
;cmat default model linear prop kn 1e10 type ball-facet
;;;;Pre-define contact model and properties

wall generate name 'box' box [-0.5*mv_W] [0.5*mv_W] [-0.5*mv_D]
[0.5*mv_D] [-0.5*mv_H] [0.5*mv_H] expand 1.2
;;;wall generation

set random 10001   ;;;;reset the random seed
[rmin=0.006]
[rmax=0.008]
```

```
geometry import ellipsoid.stl

clump template create name ellipsoid ...
        geometry ellipsoid        ...
        bubblepack ratio 0.6 distance 100 ...
        surfcalculate

pause key

clump distribute ...
      porosity 0.4 ...
      resolution 1.0 ...
      numbin 10 ...
      diameter ...
      bin 1 ...
        volumefraction 0.1 ...
        template Ellipsoid ...
        size [rmin] [rmax] ...
        azimuth 0.0 360 ...
        elevation 0.0 360 ...
        tilt 0.0 360 ...
        density 100.0 ...
        gauss ...
        group bin1 ...
      bin 2 ...
        volumefraction 0.1 ...
        template Ellipsoid ...
        size [rmin] [rmax] ...
        azimuth 0.0 360 ...
        elevation 0.0 360 ...
        tilt 0.0 360 ...
```

```
513         density 100.0 ...
514         gauss ...
515         group bin2 ...
516       bin 3 ...
517         volumefraction 0.1 ...
518         template Ellipsoid ...
519         size [rmin] [rmax] ...
520         azimuth 0.0 360 ...
521         elevation 0.0 360 ...
522         tilt 0.0 360 ...
523         density 100.0 ...
524         gauss ...
525         group bin3 ...
526       bin 4 ...
527         volumefraction 0.1 ...
528         template Ellipsoid ...
529         size [rmin] [rmax] ...
530         azimuth 0.0 360 ...
531         elevation 0.0 360 ...
532         tilt 0.0 360 ...
533         density 100.0 ...
534         gauss ...
535         group bin4 ...
536       bin 5 ...
537         volumefraction 0.1 ...
538         template Ellipsoid ...
539         size [rmin] [rmax] ...
540         azimuth 0.0 360 ...
541         elevation 0.0 360 ...
542         tilt 0.0 360 ...
543         density 100.0 ...
```

```
544         gauss ...
545         group bin5 ...
546       bin 6 ...
547         volumefraction 0.1 ...
548         template Ellipsoid ...
549         size [rmin] [rmax] ...
550         azimuth 0.0 360 ...
551         elevation 0.0 360 ...
552         tilt 0.0 360 ...
553         density 100.0 ...
554         gauss ...
555         group bin6 ...
556       bin 7 ...
557         volumefraction 0.1 ...
558         template Ellipsoid ...
559         size [rmin] [rmax] ...
560         azimuth 0.0 360 ...
561         elevation 0.0 360 ...
562         tilt 0.0 360 ...
563         density 100.0 ...
564         gauss ...
565         group bin7 ...
566       bin 8 ...
567         volumefraction 0.1 ...
568         template Ellipsoid ...
569         size [rmin] [rmax] ...
570         azimuth 0.0 360 ...
571         elevation 0.0 360 ...
572         tilt 0.0 360 ...
573         density 100.0 ...
574         gauss ...
```

```
575          group bin8 ...
576        bin 9 ...
577          volumefraction 0.1 ...
578          template Ellipsoid ...
579          size [rmin] [rmax] ...
580          azimuth 0.0 360 ...
581          elevation 0.0 360 ...
582          tilt 0.0 360 ...
583          density 100.0 ...
584          gauss ...
585          group bin9 ...
586        bin 10 ...
587          volumefraction 0.1 ...
588          template Ellipsoid ...
589          size [rmin] [rmax] ...
590          azimuth 0.0 360 ...
591          elevation 0.0 360 ...
592          tilt 0.0 360 ...
593          density 100.0 ...
594          gauss ...
595          group bin10 ...
596      box  [-0.5*mv_W]  [0.5*mv_W]  [-0.5*mv_D]  [0.5*mv_D]  [-0.5*mv_H]
597  [0.5*mv_H]
598
599  pause key
600
601  clump attribute density 2700 damp 0.7
602
603  ;ball prop fric @clumpFric
604  ;wall prop fric @wallFric
605
```

```
606  cycle 2000 calm 10
607  set timestep scale
608  cyc 5000
609  set timestep auto
610  cyc 1000
611  calm
612  clump attribute displacement multiply 0.0
613  save MakeSpecimen
614  return
615
616  %% Isotropic compression %%
617
618  rest MakeSpecimen
619
620  [wp_top=wall.find('boxTop')]
621  [wp_bot=wall.find('boxBottom')]
622  [wp_lef=wall.find('boxLeft')]
623  [wp_rig=wall.find('boxRight')]
624  [wp_fro=wall.find('boxFront')]
625  [wp_bac=wall.find('boxBack')]
626
627  def wlx
628     wlx = wall.pos.x(wp_rig) - wall.pos.x(wp_lef)
629  end
630
631  def wly
632     wly = wall.pos.y(wp_bac) - wall.pos.y(wp_fro)
633  end
634
635  def wlz
636     wlz = wall.pos.z(wp_top) - wall.pos.z(wp_bot)
```

```
end

def wsxx
    wsxx = 0.5*(wall.force.contact.x(wp_rig)-
wall.force.contact.x(wp_lef))/(wly*wlz)
end

def wsyy
    wsyy = 0.5*(wall.force.contact.y(wp_bac)-
wall.force.contact.y(wp_fro))/(wlx*wlz)
end

def wszz
    wszz = 0.5*(wall.force.contact.z(wp_top)-
wall.force.contact.z(wp_bot))/(wlx*wly)
end

def servo_walls
    wall.servo.force.z(wp_top) = -szz*wlx*wly
    wall.servo.force.z(wp_bot) =  szz*wlx*wly
    wall.servo.force.x(wp_rig) = -sxx*wlz*wly
    wall.servo.force.x(wp_lef) =  sxx*wlz*wly
    wall.servo.force.y(wp_bac) = -syy*wlx*wlz
    wall.servo.force.y(wp_fro) =  syy*wlx*wlz
end

set fish callback 9.0 @servo_walls

wall servo activate on zforce [-szz*wlx*wly] vmax 0.10 range set name
'boxTop'
```

```
667 wall servo activate on zforce [ szz*wlx*wly] vmax 0.10 range set name
668 'boxBottom'
669 wall servo activate on xforce [-sxx*wlz*wly] vmax 0.10 range set name
670 'boxRight'
671 wall servo activate on xforce [ sxx*wlz*wly] vmax 0.10 range set name
672 'boxLeft'
673 wall servo activate on yforce [-syy*wlx*wlz] vmax 0.10 range set name
674 'boxBack'
675 wall servo activate on yforce [ syy*wlx*wlz] vmax 0.10 range set name
676 'boxFront'
677
678 [szz = 1.0e5]  ;;;positive indicates compression, which is self-defined
679 [sxx = 1.0e5]
680 [syy = 1.0e5]
681
682 [tol=0.001]
683
684 def stop
685    if math.abs((wszz-szz)/szz) > tol
686       exit
687    endif
688    if math.abs((wsxx-sxx)/sxx) > tol
689       exit
690    endif
691    if math.abs((wsyy-syy)/syy) > tol
692       exit
693    endif
694    if mech.solve('aratio') > 1e-4
695       exit
696    endif
697    stop = 1
```

```
698  end
699
700  [stop = 0]
701
702  history id 1 @wszz
703  history id 2 @wsxx
704  history id 3 @wsyy
705
706  history id 101 mech solve aratio
707
708  solve fishhalt @stop
709
710  calm
711  clump attribute displacement multiply 0.0
712
713  save Compact
714
715  %% Shear phase %%
716
717  rest Compact
718
719  [vel=0.03]
720
721  wall attri zvel [-vel] range set name 'boxTop'
722  wall attri zvel [ vel] range set name 'boxBottom'
723
724  wall servo activate off
725
726  wall servo activate on xforce [-sxx*wlz*wly] vmax 1.00 range set name
727  'boxRight'
```

```
wall servo activate on xforce [ sxx*wlz*wly] vmax 1.00 range set name
'boxLeft'
wall servo activate on yforce [-syy*wlx*wlz] vmax 1.00 range set name
'boxBack'
wall servo activate on yforce [ syy*wlx*wlz] vmax 1.00 range set name
'boxFront'

[lx0=wlx]
[ly0=wly]
[lz0=wlz]

def wexx
    wexx = math.ln(wlx/lx0)*100.0    ;;;positive indicates contraction
end

def weyy
    weyy = math.ln(wly/ly0)*100.0
end

def wezz
    wezz = math.ln(wlz/lz0)*100.0
end

def wevol    ; Volumetric strain
    wevol = wexx + weyy + wezz
end

def wsd     ; deviator stress q
    wsd = (wszz - 0.5*(wsxx + wsyy))*0.001
end

```

```
hist id 10 @wsd
hist id 11 @wexx
hist id 12 @weyy
hist id 13 @wezz
hist id 14 @wevol

; porosity

def get_poros
   local lx0 = wlx
   local ly0 = wly
   local lz0 = wlz
   local sum = 0.0
   loop foreach local bp clump.list
     sum = sum + clump.vol(bp)
   endloop
   global get_poros = 1.0 - sum / (lx0*ly0*lz0)
end

@get_poros

hist @get_poros

; Evolution of coordination number

def Coordination
  local count_contacts = 0.0
  loop foreach local ct contact.list
  local e1 = contact.end1(ct)
  local e2 = contact.end2(ct)
  if type.pointer(e1) = 'pebble'
```

```
790       local cp1 = clump.pebble.clump(e1)
791     endif
792     if type.pointer(e2) = 'pebble'
793       local cp2 = clump.pebble.clump(e2)
794     endif
795     count_contacts = count_contacts + 1.0
796     count_clump = clump.num
797     endloop
798     CN = 2.0*count_contacts/count_clump
799     end
800
801   hist @Coordination
802   hist @CN
803
804   ; Contact normal anisotropy
805
806   def Contact_normal_aniso
807     local sum_xx = 0.0
808     local sum_yy = 0.0
809     local sum_zz = 0.0
810     local sum_xy = 0.0
811     local sum_xz = 0.0
812     local sum_yz = 0.0
813     local count_contacts = 0.0
814     loop foreach local ct contact.list
815     local e1 = contact.end1(ct)
816     local e2 = contact.end2(ct)
817     local nx = contact.normal.x(ct)
818     local ny = contact.normal.y(ct)
819     local nz = contact.normal.z(ct)
820     if type.pointer(e1) = 'pebble'
```

```
821       local cp1 = clump.pebble.clump(e1)
822     endif
823     if type.pointer(e2) = 'pebble'
824       local cp2 = clump.pebble.clump(e2)
825     endif
826     count_contacts = count_contacts + 1
827     sum_xx = sum_xx + nx*nx
828     sum_yy = sum_yy + ny*ny
829     sum_zz = sum_zz + nz*nz
830     sum_xy = sum_xy + nx*ny
831     sum_xz = sum_xz + nx*nz
832     sum_yz = sum_yz + ny*nz
833     endloop
834     Fxx = sum_xx/count_contacts
835     Fyy = sum_yy/count_contacts
836     Fzz = sum_zz/count_contacts
837     Fxy = sum_xy/count_contacts
838     Fxz = sum_xz/count_contacts
839     Fyz = sum_yz/count_contacts
840     Phi_1 = 0.5*(Fxx + Fyy) + 0.5*((math.sqrt((Fxx-Fzz)^2+(4*Fxz)^2)))
841     Phi_2 = 0.5*(Fxx + Fyy) - 0.5*((math.sqrt((Fxx-Fzz)^2+(4*Fxz)^2)))
842     Phi_d = Phi_1 - Phi_2
843     end
844
845   hist @Contact_normal_aniso
846   hist @Fxx
847   hist @Fyy
848   hist @Fzz
849   hist @Fxy
850   hist @Fxz
851   hist @Fyz
```

```
hist @Phi_d

; slip state

def slip_ratio
  local i = 0.0
  local j = 0.0
  loop foreach local cp contact.list
    aa = contact.prop(cp,'lin_slip')
     if aa = true then
       i = i+1
     else
       j = j+1
     endif
  endloop
  Roll_ratio = i/(i+j)
end
hist @slip_ratio
hist @Roll_ratio

; Average normal force

def compute_average_normal
  local average_normal = 0.0
  local num = 0.0
  loop foreach local ct contact.list('pebble-pebble')
    average_normal = average_normal + math.abs(contact.force.normal(ct))
    num = num + 1
  endloop
  average_normal_1 = average_normal/num
  end
```

```
883
884  hist @compute_average_normal
885  hist @average_normal_1
886
887  hist purge
888
889  def stop
890     if math.abs(wezz) > 50 then
891        stop = 1
892     endif
893  end
894
895  [stop=0]
896
897  clump prop fric 0.5
898  wall prop fric 0.0
899
900  solve fishhalt @stop
901  save Trixial_Load1
902  return
```